IMPERIAL

# Joint-Velocity-Scalar Probability Density Function Method for Modelling High-Speed Turbulent Combustion

Tin-Hang (Enson) Un

Department of Mechanical Engineering
Imperial College London

Thesis submitted for the degree of Doctor of Philosophy
October 2025

# Abstract

This thesis presents a joint-velocity-scalar probability density function (VSPDF) model aimed at improving dual-mode ramjet engine simulations. This model stands out as a unified closure for sub-grid turbulence interactions in large eddy simulations (LES), requiring minimal coefficients and making no assumptions about specific flame structure or combustion regime. The VSPDF is transported using a conservative and thermodynamically consistent stochastic fields (SF) formulation, ensuring stability in shocked turbulent flows. The Eulerian nature of SF allows direct implementation of a high-order numerical scheme and adaptive mesh refinement (AMR). Various cases showcase the model's unique capabilities, such as the ability to distinguish between laminar shear and turbulence, and to capture extreme events such as autoignition.

Two improvements to the model are proposed. The first uses a tensor-based neural network to replace existing sub-grid mixing model. By respecting physical symmetries and dimensional consistency, this approach outperforms both the original simplified Langevin model and a conventional neural network.

The second improvement targets the computational cost for resolving boundary layers by integrating an ODE-based wall model with the SF, producing accurate wall fluxes with 10 to 50 times coarser grids. A coupling procedure is proposed to maintain stability and ensure correct sub-grid fluctuation profiles. Simulations of a supersonic channel agree well with direct numerical simulations, showing significant improvement over LES without a wall model.

Finally, the wall-modelled SF is applied to simulate a dual-mode ramjet engine. The method shows good agreement with experimental results in terms of shock train length, pressure profile, and flame position, in two fundamentally different conditions. This demonstrates the model's wide applicability, allowing for confident use in the design and optimisation of ramjet and scramjet engines.

This study represents the first application of VSPDF in simulating ramjet engines, as well as the first solver to integrate SF, AMR, and wall modelling.

# Statement of originality

I declare that this thesis and all works presented therein are originated, conducted, and written by myself. References are provided whenever external materials are used. I acknowledge the use of Grammarly (`https://app.grammarly.com`) and its generative AI to improve the language of the text. I confirm that I reviewed all generated content to ensure that the ideas remain unchanged and reflect my own work.

# Copyright declaration

The copyright of this thesis rests with the author. Unless otherwise indicated, its contents are licensed under a Creative Commons Attribution-Non Commercial 4.0 International Licence (CC BY-NC).

Under this licence, you may copy and redistribute the material in any medium or format. You may also create and distribute modified versions of the work. This is on the condition that: you credit the author and do not use it, or any derivative works, for a commercial purpose.

When reusing or sharing this work, ensure you make the licence terms clear to others by naming the licence and linking to the licence text. Where a work has been adapted, you should indicate that the work has been changed and describe those changes.

Please seek permission from the copyright holder for uses of this work that are not included in this licence or permitted under UK Copyright Law.

# Acknowledgements

I would like to express my deepest gratitude to my supervisor, Dr Salvador Navarro-Martinez, for his continuous support and guidance throughout my PhD journey. He taught me what research truly is—doing something that you don't know will work or not, and most importantly, with patience and a cheerful heart.

Next, I would like to extend my thanks to the seniors of my group, Kieran, Omer, and Monal, for their assistance when I first started.

I am also grateful to my officemates, Pietro, Jiaye, Yanji, and Weiyue, for sharing jokes, complaints, knowledge, and (of course) snacks in the office, making it the best place to work in.

Thank you to Kazuki and Jake for teaching me how to operate the supersonic wind tunnel, sharing fun facts, and showing me many cool stuffs.

I would like to especially thank my Mum, Dad, and younger brother for their love throughout my life. Thank you for the unconditional support that allowed me to study in the UK. You have given me the confidence to take on whatever challenges lie ahead.

Lastly, I want to thank Cindy for her care and encouragement, which have been incredibly helpful for me during difficult times. I feel so lucky to have met you.

"On ne voit bien qu'avec le cœur. L'essentiel est invisible pour les yeux."

— *Antoine de Saint-Exupéry 1943, Le Petit Prince*

# Contents

**Abstract** 1

**Statement of originality** 2

**Copyright declaration** 3

**Acknowledgements** 4

**List of figures** 10

**List of tables** 14

**Nomenclature** 15

**1 Introduction** 22

1.1 Ramjets and supersonic combustion ramjets (scramjets) . . . . . 22

1.2 Previous works . . . . . 25

1.2.1 Experimental campaigns . . . . . 25

1.2.2 Computational simulations . . . . . 27

1.3 Thesis objectives . . . . . 30

1.4 Thesis outline . . . . . 30

**2 Theoretical background** 32

2.1 Governing equations . . . . . 32

2.1.1 Assumptions . . . . . 32

2.1.2 Navier-Stokes equations . . . . . 33

2.2 Large eddy simulation . . . . . 35

2.2.1 Eddy-viscosity models . . . 38
2.2.2 Turbulent combustion models . . . 40
2.3 Numerical methods . . . 42
2.3.1 High-order shock-capturing schemes . . . 42
2.3.2 Central difference for diffusive fluxes . . . 49
2.3.3 Time integration . . . 50
2.3.4 Adaptive mesh refinement . . . 51
2.4 Solver verification and validation . . . 55
2.4.1 Method of manufactured solutions . . . 55
2.4.2 Isentropic vortex convection . . . 56
2.4.3 Laminar boundary layer . . . 57
2.4.4 Reactive shock tube . . . 59
2.4.5 Performance scaling . . . 60
2.5 Summary . . . 61

**3 Joint-velocity-scalar Eulerian stochastic fields** **62**
3.1 Probability density function method . . . 62
3.1.1 PDF transport equation . . . 64
3.1.2 Closure models . . . 64
3.2 Eulerian stochastic fields . . . 66
3.2.1 Conservation and thermodynamic consistency . . . 68
3.3 Implementation . . . 70
3.3.1 Modifications to the existing solver . . . 70
3.3.2 Discretising the stochastic model . . . 71
3.3.3 Treatment with AMR . . . 71
3.3.4 Performance scaling with stochastic fields . . . 72
3.4 Results . . . 73
3.4.1 Ornstein-Uhlenbeck process . . . 73
3.4.2 Taylor-Green vortex . . . 75
3.4.3 Autoignition in homogeneous-isotropic turbulence . . . 78
3.4.4 Supersonic jet flame . . . 80
3.5 Summary . . . 84

**4 Data-driven generalised Langevin model** **87**

4.1 Introduction . . . 87

4.1.1 Simplified Langevin model . . . 87

4.1.2 Machine learning in CFD . . . 89

4.2 Tensor function regression . . . 90

4.3 Summary . . . 94

**5 Wall-modelled stochastic fields** **96**

5.1 Introduction . . . 96

5.2 Wall fluxes model . . . 97

5.2.1 Numerical solution . . . 99

5.2.2 Coordinate system . . . 101

5.3 Near-wall treatments for stochastic fields . . . 101

5.3.1 Coupling with the wall fluxes model . . . 101

5.3.2 Sub-grid model treatments . . . 102

5.4 Supersonic turbulent channel flow . . . 104

5.4.1 Comparison with DNS . . . 104

5.4.2 Effect of the $C_0$ limiter . . . 106

5.4.3 Stochastic fields and sub-grid quantities . . . 106

5.5 Summary . . . 107

**6 Simulation of a cavity-stabilised ramjet** **108**

6.1 Case specifications . . . 108

6.1.1 Experimental setup . . . 108

6.1.2 Computational setup . . . 109

6.1.3 Previous WMLES study . . . 110

6.2 Results . . . 111

6.2.1 Steady-state flow field . . . 111

6.2.2 Flame structure . . . 115

6.2.3 Sub-grid scale interactions . . . 118

6.3 Shock train initiation and propagation . . . 120

6.4 Summary . . . 123

**7 Conclusions** **125**

7.1 Summary of the thesis . . . . . 125

7.2 Key findings . . . . . 126

7.3 Scientific contributions . . . . . 127

7.4 Future outlooks . . . . . 128

**Bibliography** **130**

**A Eigen-system of the Euler equations** **146**

**B Scripts for proving the order of the central difference schemes** **148**

**C Derivation of the PDF transport equation** **150**

**D An alternative VSPDF system** **154**

# List of figures


1.1 Specific impulse versus operating Mach number of different propulsion systems (Fry 2004). Efficiency is quantified by specific impulse ($I_{sp}$), defined as the unit thrust generated per unit mass flow rate of propellant. . . . . 22

1.2 Schematics of a ramjet/scramjet engine. It is a ramjet engine if the flow in the combustor is subsonic, and a scramjet engine if the flow in the combustor is supersonic. ER stands for equivalence ratio, which is the ratio of the mass of fuel injected to that required to consume all the oxidiser. (Modified from U.S. Government Accountability Office 2019; Baccarella *et al.* 2021) . . . . 23

1.3 Air-breathing hypersonic vehicle flight trajectory and operational limits (Andreadis 2004). Unit conversions: 1 ft $\approx$ 0.305 m, 1 R $\approx$ 0.56 K, 1 lbf/ft$^2$ $\approx$ 47.88 Pa. . . . . 25

1.4 Previous scramjet experimental configurations (not to scale) (Urzay 2018). . 26

2.1 Stencils of a fifth-order WENO/TENO scheme. . . . . 46

2.2 Wave system of the HLLC approximate Riemann solver. This figure shows the case where $\mathbf{F}_{i+\frac{1}{2}} = \mathbf{F}^*_L$. . . . . 47

2.3 An example block-structured AMR mesh and ghost cells. . . . . 51

2.4 Coupling procedure during a time step between two AMR levels. . . . . 52

2.5 Illustrations of (a) fluxes in a EB cut cell, (b) neighbourhoods in the redistribution algorithm, and (c) stencil for EB wall-normal derivative. . . . . 53

2.6 MMS error convergence. Left to right: Euler equations with M = 1; Navier-Stokes equations with M = 1, Re = 1, Pr = 0.72; Navier-Stokes equations with two AMR levels and with second- and fourth-order interpolation. . . . 56

2.7 Vortex velocity profiles after five pass-through. The number of grid points is next to the scheme name. . . . . 57

2.8 Velocity magnitude over a flat plate: (a, d) regular wall, (b, e) EB wall, and (c, f) inclined EB wall. . . . . 58

2.9 Boundary layer velocity and temperature profiles compared to self-similar solution. . . . 58

2.10 Reactive shock tube solution at $t = 190$ $\mu$s and $t = 230$ $\mu$s, compared with the reference solution (Fedkiw *et al.* 1997). . . . 59

2.11 Strong and weak scaling on CPUs. . . . 60

3.1 Algorithm of generating independent and consistent Wiener process increments across AMR levels, illustrated for three levels. . . . 72

3.2 Weak scaling of the stochastic fields on CPU. Four fields per node are used. 73

3.3 Sub-grid scalar variance at different times and the static mesh used. . . . 74

3.4 Time evolution of sub-grid scalar variance averaged over space (identical for both scalars) and error convergence. . . . 74

3.5 Comparison of TGV using different turbulence models and $128^3$ mesh. Ref: DNS (TENO6) from Lusher and Sandham 2021. All quantities are normalised by their initial values. . . . 75

3.6 Enlarged view of Figure 3.5 for clearer interpretation of the differences between ILES, Smagorinsky LES, and SF in the vortex stretching phase. . . . 76

3.7 Comparison of TGV using different numerical schemes and $128^3$ mesh. Ref: DNS (TENO6) from Lusher and Sandham 2021. All quantities are normalised by their initial values. . . . 77

3.8 Comparison of TGV using 16 SF and different random number generation methods or $\Delta W$ and $128^3$ mesh. Ref: DNS (TENO6) from Lusher and Sandham 2021. All quantities are normalised by their initial values. . . . 78

3.9 Illustration of the initial velocity field before and after filtering, the sub-grid temperature variance, and the kinetic energy spectra. . . . 79

3.10 Time evolution of temperature. The solid line indicates the spatial average and the shaded region represents the range. $t_{\text{ign}}$ denotes the ignition time in the DNS. . . . 80

3.11 Instantaneous temperature field of implicit LES (ILES) and stochastic fields (SF). The shaded region represents the buffer layer. . . . 82

3.12 Instantaneous mass fractions of OH and $HO_2$ of implicit LES (ILES) and stochastic fields (SF). The shaded region represents the buffer layer. . . . 83

3.13 Mean temperature compared with previous LES studies and experiment. The number of cells used in the LES is included in brackets ("M" means millions, $10^6$). Green square: Boivin *et al.* 2012; Blue triangle: Moule *et al.* 2014; Red star: Bouheraoua *et al.* 2017; Black circle: Cheng, Wehrmeyer, and Pitz 1991. . . . 84

3.14 Radial profiles of mean (solid line) and RMS (dashed line) quantities. Blue: implicit LES; Orange: stochastic fields; Black circle and cross: experimental measurement of mean and RMS (Cheng, Wehrmeyer, and Pitz 1991). . . . . 85

4.1 Example trajectory of sub-grid stress in the turbulence triangle using SLM and a complex model (Haworth and Pope 1986). The three vertices correspond to three states of turbulence (1C: one-component, rod-like; 2C: axisymmetric two-component, pancake-like; 3C: isotropic) and the three edges represent different physical behaviours (Emory and Iaccarino 2014). . . . . 88

4.2 Architecture of the tensor-based neural network. . . . . 91

4.3 NN predictions of $\epsilon_{\text{sgs}}$. Left: Training and testing curves; Middle: ground truth-prediction correlation; Right: predictions with unrotated verses rotated inputs. . . . . 92

4.4 NN predictions of the $\mathbf{N}$ tensor. . . . . 94

5.1 Illustrations of (a) the one-dimensional domain used in the wall model and (b) the wall-parallel coordinate system in three dimensions. . . . . 98

5.2 Changes in the wall model outputs in response to the changes in inputs. Isocontours of the outputs are overlaid on the graphic. . . . . 102

5.3 Left: Production ($\mathcal{P}$) and dissipation ($\epsilon$) of turbulent kinetic energy ($k$) in RANS, along with (5.21); Middle: Production-like $\hat{\mathcal{P}}_{\text{sgs}}$ and dissipation ($\epsilon_{\text{sgs}}$) of sub-grid kinetic energy ($k_{\text{sgs}}$) in LES (box filter, $\Delta^+ \approx 50$), along with (3.10) and (5.21); Right: Reynolds stress (dash line) and sub-grid stress (solid line) normalised by $u_\tau$, in descending order of the peak value, $u'u'$, $v'v'$, $w'w'$, $u'v'$, respectively. . . . . 103

5.4 Mean and RMS profiles. Labels are "DNS": DNS from Modesti and Pirozzoli 2016; "SF": SF without wall model; "SF-WM": SF with wall model; "WALE": WALE without wall model; "WALE-WM": WALE with wall model. Quantities with the superscript + are non-dimensionalised with $u_\tau$ from the DNS. 105

5.5 $Q$-criterion contours of a fine-grid ILES ($\Delta x^+ = \Delta y^+ = \Delta z^+ = 7$) and the wall-modelled SF ($\Delta x^+ = \Delta y^+ = \Delta z^+ = 31.7$). . . . . 105

5.6 Pressure of individual fields with and without near-wall $C_0$ modification (5.22). Each line represents one field. . . . . 106

5.7 Comparison between solutions with 8 and 16 stochastic fields. Quantities with the superscript + are non-dimensionalised with $u_\tau$ from the DNS. . . . 107

6.1 Experimental setup with the computational domain marked in red. All sections are rectangular and have a constant width of 38.1 mm. Modified from Micka 2010. . . . . 108

6.2 Instantaneous flow field, from top to bottom: temperature, pressure, $H_2$ mass fraction (in logarithmic scale), and density gradient magnitude. Quantities from both inflow cases share the same colourmap for comparison. . . . 111

6.3 Mean and RMS values of bottom wall pressure. The dashed lines mark the cavity location. "Ref." is the WMLES by Fureby and Nilsson 2023 and "Exp." is the experimental measurements by Micka 2010. $x = 0$ at the fuel injector. . . . . 112

6.4 Mean streamwise velocity field overlaid with mean streamwise velocity (solid line) and RMS velocity (dashed line) profiles at different sections. . . . . 113

6.5 Mean temperature field with adiabatic and isothermal walls. . . . . 115

6.6 Top two rows: Line-of-sight $T^4$ in the WMSF (top) and combustion luminosity in the experiment (bottom); Bottom three rows: Line-of-sight mean heat release rate in the present WMSF (top) and CFD++ (middle) compared to $OH^*$ chemiluminescence in the experiment (bottom). Note that all colourmaps are relative rather than quantitative. The white dashed lines indicate a slope of 29.7°. All axis lengths are in mm. . . . . 116

6.7 Flame index at the centre plane masked by the heat release rate greater than $10^8$ J m$^{-3}$ s$^{-1}$. Negative indicates a non-premixed flame and positive indicates a premixed flame. . . . . 117

6.8 Sub-grid kinetic energy ratio and sub-grid Mach number at the centre plane computed from SF directly (3.26) and using Yoshizawa 1986's model (2.26). Cells with a value greater than 0.2 are coloured black. Note that the colour scale is logarithmic. . . . . 118

6.9 Sub-grid Damköhler number at the centre plane masked by $\tau_{\text{chem}} < 0.1$ s. Note that the simulation time step is $O(10^{-8})$ s. . . . . 120

6.10 Time sequence of the flame and shock train formation. All axis lengths are in mm. . . . . 121

6.11 Centreline pressure over time. $t = 0$ is chosen to be the time where the leading shock passes through $x = 0$. On the right-hand-side plot, "fitted $p_1$" and "2.35 $p_1$" (grey dashed lines) refer to $p_1$ and $p_2$ in (6.3), while "background $p$" (black dotted line) is the pressure computed using (6.4)–(6.5). 122

# List of tables


1.1 A list of previous LES studies of ramjet/scramjet combustor. See the text and the references in the citation for details. . . . . 28

2.1 Length and time scales in turbulent flows, where $\nu = \mu/\rho$ is kinematic viscosity, and $\epsilon$ is the turbulent kinetic energy dissipation rate. The domain size $L$ is assumed to have the same order of magnitude as the integral length $\ell$, hence can be used interchangeably. . . . . 36

2.2 Expressions and relative magnitudes of the unclosed terms in (2.19), modified from Vreman *et al.* 1995 based on DNS of compressible mixing layers. . 38

2.3 MMS problem parameters . . . . . 56

3.1 Supersonic jet flame conditions (Cheng, Wehrmeyer, Pitz, *et al.* 1994) . . . 81

4.1 Performance metrics of different models in predicting $\epsilon_{\text{sgs}}$. The best and the worst models in each metric are coloured. . . . . 93

4.2 Performance metrics of different models in predicting $\mathbf{N}$. All entries are summed. The best and the worst models in each metric are coloured. . . . . 93

5.1 Summary of simulation parameters (Modesti and Pirozzoli 2016). . . . . 104

6.1 Inflow and fuel conditions in the simulations. . . . . 109

# Nomenclature

### Greek letters

| | |
|---|---|
| $\chi_\alpha$ | Chemical species symbol |
| $\Delta e_{f,\alpha}$ | Species energy of formation |
| $\Delta h_{f,\alpha}$ | Species enthalpy of formation ($= \Delta e_{f,\alpha} + R_u T_f / W_\alpha$) |
| $\Delta t$ | Time step size |
| $\Delta x$ | Grid size |
| $\Delta$ | LES filter width |
| $\delta(\phi)$ | Dirac delta ($= \infty$ if $\phi = 0$, $= 0$ otherwise) |
| $\delta_F$ | Flame thickness |
| $\delta_{ij}$ | Kronecker delta ($= 1$ if $i = j$, $= 0$ otherwise) |
| $\ell$ | Integral length scale |
| $\epsilon, \epsilon_{ij}$ | Turbulent dissipation rate ($\epsilon = \epsilon_{kk}$) |
| $\eta$ | Kolmogorov length scale ($\eta/\ell \propto \mathrm{Re}^{-3/4}$) |
| $\gamma$ | Heat capacity ratio ($= c_p/c_v$) |
| $\kappa$ | Thermal conductivity |
| $\lambda$ | Taylor microscale ($\lambda/\ell \propto \mathrm{Re}^{-1/2}$) |
| $\mu$ | Dynamic viscosity |
| $\mu_b$ | Bulk viscosity |
| $\nu$ | Kinematic viscosity ($= \mu/\rho$) |
| $\Omega_{ij}$ | Rotation rate tensor ($= (\partial u_i/\partial x_j - \partial u_j/\partial x_i)/2$) |
| $\phi, \phi_i$ | Arbitrary variables |

$\rho$ Density

$\sigma, \sigma(\phi)$ Variance (of a random variable $\phi$)

$\tau_{ij}^{\text{sgs}}$ SGS stress tensor

$\tau_{\text{sgs}}$ Sub-grid mixing timescale

$\tau_w$ Wall shear stress

$\tau_{ij}$ Viscous stress tensor

$\upsilon'_{\alpha,i}, \upsilon''_{\alpha,i}$ Stoichiometric coefficient

$\varkappa$ von Kármán constant

$\varphi, \varphi_i$ Variable in PDF sample space corresponding to $\phi_i$

$q_w$ Wall heat flux

**Roman letters**

$A$ Area

$A$ Drift term in SDE

$B$ Diffusion term in SDE

$b_{ij}$ Normalised SGS stress anisotropy tensor ($= \tau_{ij}^{\text{sgs}}/\tau_{kk}^{\text{sgs}} - \delta_{ij}/3$)

$c$ Speed of sound

$C_0, C_\epsilon, C_u, C_e, C_Y$ PDF sub-grid model coefficients

$C_\alpha$ Molar concentration

$C_f$ Skin friction coefficient ($= \tau_w/(\rho_\infty u_\infty/2)$

$C_I$ Yoshizawa model coefficient

$C_s$ Smagorinsky model coefficient

$c_v, c_p$ Specific heat capacity at constant volume and pressure

$D_\alpha$ Mixture-averaged diffusivity

$D_H$ Hydrodynamic diameter

$D_{\alpha\beta}$ Differential diffusivity matrix

$E$ Mass-specific total energy

$e$ Mass-specific internal energy

$E^{act}$ Activation energy in chemical reaction

$f$ PDF

$f^*$ Fine-grained PDF

$fn, Q$ Arbitrary functions

$G$ LES spatial filter function

$G_{ij}$ Langevin model tensor

$h_\alpha$ Species internal enthalpy

$J_{\alpha,i}$ Species diffusion flux ($= -\rho Y_\alpha V_{\alpha,i}$)

$k$ Turbulent kinetic energy ($= R_{kk}/2$)

$k^f, k^r, k^e$ Forward and reverse rates, and equilibrium constant

$k_{\text{sgs}}$ Sub-grid kinetic energy ($= \tau_{kk}^{\text{sgs}}/2$)

$N_f$ Number of stochastic particles/fields

$N_r$ Number of reactions

$N_s$ Number of species

$N_v$ Number of variables in PDF sample space

$p$ Static pressure

$q_i$ Heat diffusion flux

$R$ Refinement ratio in AMR

$R_u$ Universal gas constant in mole unit ($= 8.31446$ J/K·mol)

$R_{ij}$ Reynolds stress tensor ($= \{u_i'' u_j''\}$)

$S_\alpha$ Chemical reaction source term

$S_{ij}$ Strain rate tensor ($= (\partial u_i/\partial x_j + \partial u_j/\partial x_i)/2$)

$T$ Temperature

$t, t'$ Time

$T_f$ Reference temperature for species formation energy/enthalpy (usually 298.15 K)

$u, v, w, u_i$ Velocities

$u_\tau$ Friction velocity ($= \sqrt{\tau_w/\rho_w}$)

$V$ Volume

$V_\alpha$ Species diffusion velocity

$W$ Mixture molecular weight

$W, W_i$ Wiener process

$W_\alpha$ Species molecular weight

$x, y, z, x_i$ Positions

$X_\alpha$ Species mole fraction

$y^+$ Non-dimensional wall distance ($= yu_\tau/\nu_w$)

$Y_\alpha$ Species mass fraction

$\mathbf{F}_i$ Flux vector in the Navier-Stokes equations

**RHS** Right-hand side of the non-reacting Navier-Stokes equations ($= -\partial \mathbf{F}_j/\partial x_j$)

**S** Source term vector in the Navier-Stokes equations

**U** Conservative variable vector in the Navier-Stokes equations

$FI$ Flame index

Da Damköhler number ($= \tau_{\text{turb}}/\tau_{\text{chem}}$)

Ka Karlovitz number ($= \delta_F^2/\eta^2 = 1/\text{Da}$)

Kn Knudsen number ($= \sqrt{\gamma\pi/2}\ \text{M}/\text{Re}$)

$\text{Le}_\alpha$ Lewis number ($= \text{Sc}_\alpha/\text{Pr}$)

Pr Prandtl number ($= c_p\mu/\kappa$)

Re Reynolds number

$\text{Sc}_\alpha$ Schmidt number ($= \nu/D_\alpha$)

**Operators**

$\breve{\phi}$ Quantity evaluated using the filtered flow states ($= \phi(\overline{\mathbf{U}})$)

$\langle\phi\rangle$ Ensemble average

$\mathrm{d}\phi$ An infinitesimal change in $\phi$

$\overline{\phi}$ LES spatial filtering

$\phi \mid \varphi$ $\phi$ conditioned on $\varphi$

$\widetilde{\phi}, \widetilde{\phi \ldots}$ Density-weighted (Favre) filtering ($= \overline{\rho\phi}/\overline{\rho}$)

$\{\phi\}$ Density-weighted (Favre) average ($= \langle\rho\phi\rangle/\langle\rho\rangle$)

**Superscripts**

$^{+}$ In dimensionless wall unit

$^{,}$ Fluctuation about ensemble averaged value

$^{\prime}$ Fluctuation about filtered value

$^{\top}$ Matrix transpose

$^{(n)}$ Quantity of the stochastic particle/field

$^{,,}$ Fluctuation about Favre averaged value

$^{\prime\prime}$ Fluctuation about Favre-filtered value

$^{t}$ Quantity at time $t$

**Subscripts**

$_{0}$ Stagnation quantities

$_{\alpha,\ \beta}$ Quantity of the chemical species (no summation implied)

$_{\infty}$ Freestream condition

$_{\mathrm{sgs}}$ Sub-grid scale quantity

$_{i,\ j,\ k}$ Components of a Cartesian vector or tensor (Einstein summation implied)

$_{t}$ Turbulent (time) quantity

$_{w}$ Quantity at a wall

**Acronyms**

AMR Adaptive mesh refinement

CD Central difference

CFD Computational fluid dynamics

CFL Courant-Friedrichs-Lewy (condition/number)

CMC Conditional moment closure

DNN Deep neural network

DNS Direct numerical simulation

DRP Dispersion-relation-preserving (scheme)

EB Embedded boundary

EBU Eddy break up (model)

EDC Eddy dissipation concept

EDM Eddy dissipation model

ENO Essentially non-oscillatory (scheme)

FD Finite difference

FPV Flamelet-progress variable

FV Finite volume

GLM Generalised Langevin model

HPC High-performance computing

IEM Interaction-by-exchange-with-the-mean (model)

ILES Implicit LES

LDKM Localised dynamic kinetic-energy model

LEM Linear eddy model

LES Large eddy simulation

MDF Mass density function

MMS Method of manufactured solutions

PaSR Partially-stirred reactor

PDF Probability density function

RANS Reynolds-averaged Navier-Stokes

RBCC Rocket-based combined cycle

RK Runge-Kutta (time integration scheme)

SBLI Shock-boundary layer interaction

SF Stochastic fields

SGS Sub-grid scale

SLM Simplified Langevin model

SPDF (Joint-) scalar PDF

TBCC Turbine-based combined cycle

TBNN Tensor-based neural network

TCI Turbulence-chemistry interaction

TENO Targeted essentially non-oscillatory (scheme)

TGV Taylor-Green vortex

TVD Total variation diminishing

VSPDF Joint-velocity-scalar PDF

WALE Wall-adapting local eddy-viscosity (model)

WENO Weighted essentially non-oscillatory (scheme)

WM- Wall-modelled (*e.g.* WMLES, WMSF)

# Chapter 1

# Introduction

## 1.1 Ramjets and supersonic combustion ramjets (scramjets)

Ramjet engines, first proposed by French inventor René Lorin in 1913, serve as an efficient propulsion system for high-supersonic and hypersonic[1] flights. By removing the compressor and turbine and instead using shock waves to achieve sufficient compression, ramjet engines can operate at significantly higher speeds, where conventional turbojet and turbofan engines become inefficient due to mechanical losses and turbine temperature limits (Segal 2009). They combine the efficiency of air-breathing engines with the capability to operate at high Mach numbers like rockets, as illustrated in Figure 1.1.

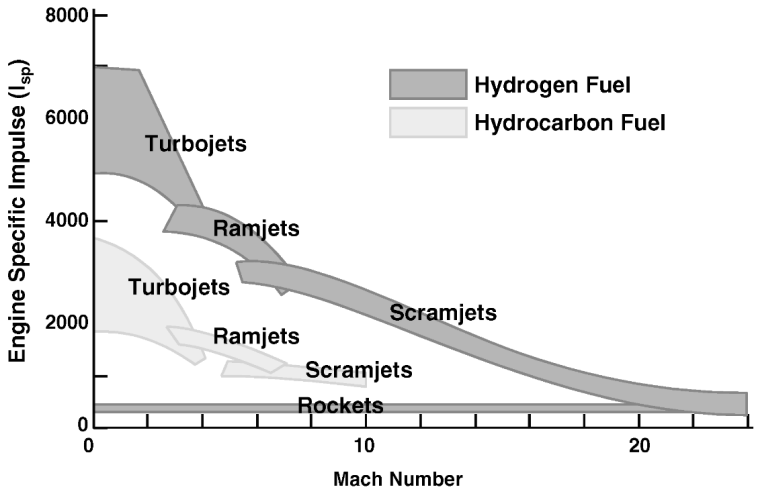



Figure 1.1: Specific impulse versus operating Mach number of different propulsion systems (Fry 2004). Efficiency is quantified by specific impulse ($I_{sp}$), defined as the unit thrust generated per unit mass flow rate of propellant.

[1]Hypersonic flows are characterised by the high stagnation temperature, where molecular processes of vibration, rotation, translation, and dissociation become important behind shock waves. A generally accepted threshold for hypersonic speed is Mach number greater than five, or stagnation enthalpy reaching the order of MJ/kg (Leyva 2017).

This technology opens up a range of exciting applications, such as accelerating air travel and enabling the rapid transportation of time-critical goods and personnel, creating new opportunities for business, government, and humanitarian operations. For military applications, ramjet technology unlocks the possibility of long-range hypersonic cruise missiles. Their high speed and ability to fly below the radar horizon make them difficult to detect and intercept, while being powered throughout the flight enhances flexibility and allows guided precision strikes (Urzay 2018). Moreover, ramjets could replace the mid-stages of traditional rockets. Since the oxidiser constitutes 30–60% of a rocket's weight at launch, switching to an air-breathing system can significantly increase payload capacity and reduce the cost per launch weight, paving a more economical way of accessing space (Falempin 2007; Smart and Tetlow 2009), and potentially leading to the emergence of a new space tourism industry (Leyva 2017).

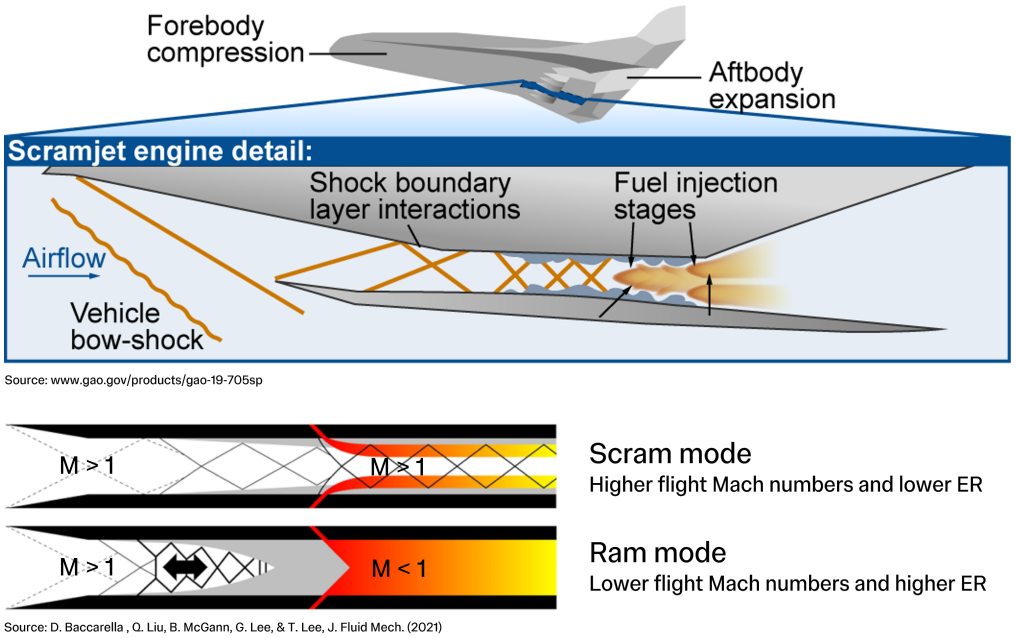



Figure 1.2: Schematics of a ramjet/scramjet engine. It is a ramjet engine if the flow in the combustor is subsonic, and a scramjet engine if the flow in the combustor is supersonic. ER stands for equivalence ratio, which is the ratio of the mass of fuel injected to that required to consume all the oxidiser. (Modified from U.S. Government Accountability Office 2019; Baccarella *et al.* 2021)

The ramjet engines operate with the same Brayton cycle as turbojet engines. The flow path within the engine, as shown in Figure 1.2, follows:

1. **Compression**: To reduce the weight and length of the vehicle, compression usually starts externally, via shock waves generated by the airframe. The design of the forebody is a trade-off between pressure losses from strong shocks, friction losses from a long body, thermal loading, and off-design performance. Therefore, the airframe design is highly coupled with the engine design in hypersonic vehicles.
2. **Isolator**: It is a long passage connecting the inlet and the combustor. The com-

bustion pressure rise can lead to the formation of a shock wave that may exit the inlet, leading to a catastrophic loss of mass flow and thrust—a phenomenon known as "unstart" (Im *et al.* 2016). The isolator helps retain the shock within it, creating a shock train that gradually increases the pressure to match that in the combustor.

3. **Fuel injection**: Given the short residence time in the engine, effective mixing is crucial. This is typically done using fuel jets. The main goal is to generate large-scale streamwise vortices that enhance mixing through both entrainment of air and small-scale turbulence (Ben-Yakar 2000). The jets can be oriented normal or inclined to the flow. Normal jets offer better penetration but also induce greater losses. Multiple jets can be used, arranged in the spanwise or streamwise direction. Although circular orifices are most commonly used, research suggests that other shapes may be more effective in enhancing mass and heat transfer (Tyliszczak *et al.* 2022).

4. **Combustor**: In addition to effective mixing, flame stabilisation is also important. Typical stabilisation devices include struts, steps, cavities, vortex generators, and jets. They can be used in combination to create low-speed zones that increase residence time and trap hot air and reactive radicals. In ramjets, the flow is slowed down to subsonic speeds before entering the combustor. However, if the flight Mach number is too high, bringing the flow to subsonic may generate a large pressure loss. It will also heat up the flow substantially, limiting the amount of fuel that can burn before reaching the temperature limits of the material or even the adiabatic flame temperature. Dissociation and recombination of air molecules could also increase losses. Therefore, scramjets, in which the flow remains supersonic through the combustor, become relevant when the flight Mach number exceeds approximately seven (Weber and Mackay 1958). A dual-mode ramjet which can operate in both conditions is favourable, as it extends the operating envelope.

5. **Nozzle**: Located downstream of the combustor, the nozzle is responsible for accelerating the flow to the required pressure and speed. Its diverging geometry helps prevent thermal choking due to heat release, as some portion of combustion takes place here since the residence time in the combustor is often too short (Segal 2009).

The flight envelope of ramjet/scramjet engines is illustrated in Figure 1.3. The low-speed limit is determined by an insufficient compression ratio, with which the engine cannot produce thrust. Therefore, another type of engine, usually turbojet or rocket, is needed to bring the aircraft from takeoff to operating speed. The high-speed limit is bounded by dynamic pressure at lower altitudes, where air density is higher, and by thermal loads at higher altitudes. As an air-breathing engine, the maximum operational altitude of ramjets is limited by oxygen starvation, although this altitude is significantly higher than that of turbojet engines due to the greater flight speed. Rocket or oxygen augmentation is required for orbital launch missions. The use of different types of engines in different flight segments is known as a combined cycle, including the turbine-based combined cycle

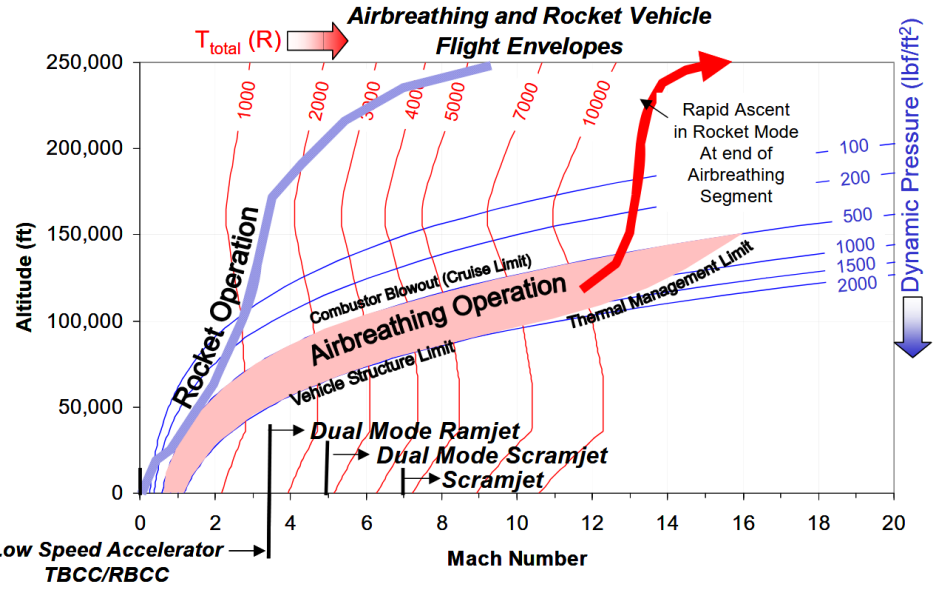



Figure 1.3: Air-breathing hypersonic vehicle flight trajectory and operational limits (Andreadis 2004). Unit conversions: 1 ft $\approx$ 0.305 m, 1 R $\approx$ 0.56 K, 1 lbf/ft$^2$ $\approx$ 47.88 Pa.

(TBCC) when combined with a turbojet or turbofan, and the rocket-based combined cycle (RBCC) when integrated with rockets. Due to the operational envelope of ramjet/scramjet engines, vehicle trajectory optimisation and mission planning are critical to successful operations. See, *e.g.*, Forbes-Spyratos 2020 for more information regarding trajectory optimisation in hypersonic vehicles.

## 1.2 Previous works

### 1.2.1 Experimental campaigns

The development of ramjet engines began in the mid-twentieth century in countries such as France, the USSR, the UK, the USA, and later in Germany and Japan. Curran 2001 and Segal 2009 provide an overview of the development timeline until the early 2000s.

Earlier prototypes of ramjets were predominantly axisymmetrical, with initial development focusing on fuel mixing and flame holding. In the 1990s, the research interests gradually shifted toward cavity-based flame holding and rectangular designs for easier integration into airframes. While fuel mixing and flame-holding remain major concerns, modern research also emphasises on combustor-isolator coupling and dual-mode capabilities. Plasma-assisted ignition and combustion (Starikovskiy and Aleksandrov 2011) and aero-thermo-structural interaction (Horing *et al.* 2024) are also active research directions.

Most recent test programmes include initiatives from the German Aerospace Centre (DLR) (Waidmann *et al.* 1996), HyShot I–IV conducted by the University of Queensland and the British defence company QinetiQ (Gardner *et al.* 2004; Smart, Hass, *et al.* 2006),

and the HIFiRE 0–8 supported by the US and Australian governments[2] (Jackson *et al.* 2013). Other contributors include the US Air Force Research Laboratory (AFRL) (Gruber *et al.* 2011), the University of Virginia (UVa) configurations A and C (Cutler *et al.* 2012, 2013), the University of Michigan (Micka 2010; Fotia and Driscoll 2013), a joint effort between the French Aerospace Laboratory (ONERA) and the Japanese Aerospace Exploration Agency (JAXA) (Collin *et al.* 1997; Sunami *et al.* 2002), and the National University of Defence Technology (NUDT) in the People's Republic of China (Sun *et al.* 2009; Zhong *et al.* 2016). All of these studies use hydrogen as fuel, except the AFRL which uses ethylene. A selection of the experimental configurations illustrated in Figure 1.4.

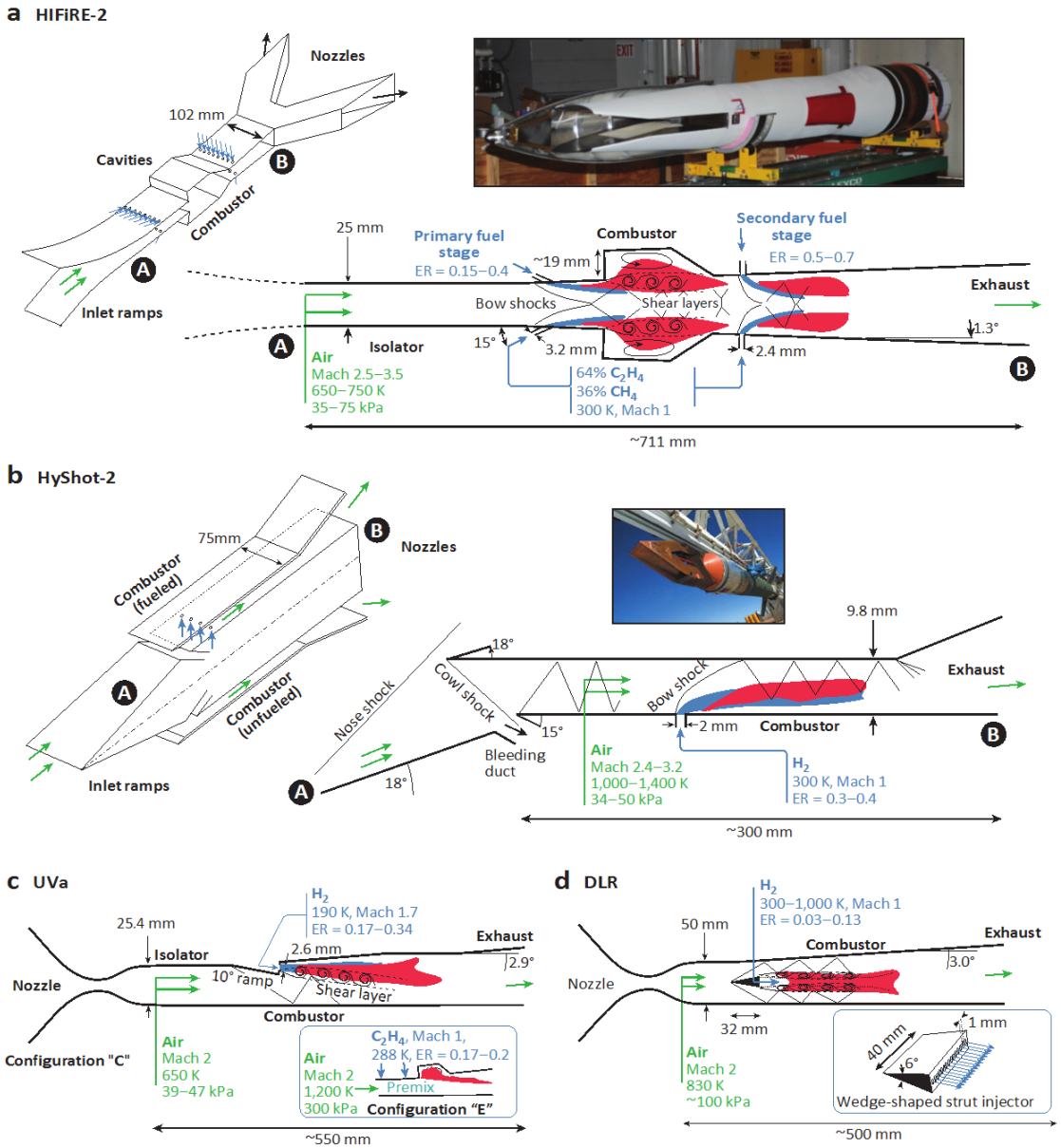



Figure 1.4: Previous scramjet experimental configurations (not to scale) (Urzay 2018).

[2]These tests are not in numerical order but instead focus on testing different components and designs.

### 1.2.2 Computational simulations

While flight tests and ground-based experiments have sparked many interesting ideas and validated numerous new concepts, they are expensive to operate and have lengthy timeframes. Additionally, the measurements taken during flight tests are often limited to basic parameters, such as pressure and temperature, and the inflow conditions are usually not accurately known. In ground testing facilities, emulating high-enthalpy conditions often requires pre-combustion, which may alter the inflow composition. Furthermore, the size of the models used in these tests is also limited. If high-enthalpy shock or expansion tunnels are used, the test duration is limited to milliseconds, making it challenging to observe relatively long-timescale phenomena such as recirculation flows in wakes or cavities and isolator unstart (Veeraragavan 2025).

With the rapid advancement of computing hardware over the past few decades, computational fluid dynamics (CFD) has become an increasingly important tool for engineering design. There is no reason this should not be the case for hypersonic research. In fact, the extreme flow conditions make an even stronger case for its use.

The three main approaches in CFD are Reynolds-averaged Navier-Stokes (RANS), large eddy simulation (LES), and direct numerical simulation (DNS). RANS solves the ensemble-averaged flow field (or time-averaged in statistically stationary flows), while any fluctuations are modelled. It is the most computationally inexpensive among the three approaches because the averaged flow field is relatively smooth and can be resolved using coarse grids. LES, as its name suggests, resolves large fluid motions and models smaller sub-grid scales. It requires more refined computational grids than RANS and needs to compute the time evolution of the flow. DNS takes this a step further by resolving all flow scales without the need for any modelling. However, it is computationally expensive and is still limited to laboratory-scale flows with low Reynolds numbers, even with the latest high-performance computing (HPC) facility.

While RANS is widely used in engineering thanks to its fast simulation time, there is a growing trend advocating a shift toward LES, such as in NASA's CFD Vision 2030 (Slotnick *et al.* 2014) and CbA 2040 (Mauery *et al.* 2021) initiatives. The scale-resolving capability of LES has proven to be more beneficial than RANS in capturing complex phenomena such as flow transition, separation, dynamic response, turbulent mixing, and local ignition and extinction in flames. All of these phenomena are relevant to ramjet/scramjet flows, therefore, this work will focus on LES. More details regarding the LES methodology will be discussed in section 2.2.

Table 1.1 presents various LES codes that have been validated against experimental data in ramjet/scramjet configurations, serving as a reference point for this study. See Gonzalez-Juez *et al.* 2017 for additional examples of LES and RANS studies related to high-speed combustion.

Table 1.1: A list of previous LES studies of ramjet/scramjet combustor. See the text and the references in the citation for details.

| **Investigators** | **Numerical schemes** | | | **Chemical** | **Turbulence models** | | | **Validation** |
|---|---|---|---|---|---|---|---|---|
| | **Time** | **Space** | **Grid (cell)** | **mechanism** | **LES SGS** | **TCI** | **Near-wall** | **case** |
| Génin, Chernyavsky, *et al.* 2003; Génin and Menon 2010 | RK2 | TVD + CD | Mapped (0.7–2.5M) | Génin and Menon 2010 | LDKM | LEM | / | DLR |
| Larsson, Vicquelin, *et al.* 2011 | RK4 | ENO2 + CD | Mapped (0.04 mm, 14M) | Hong *et al.* 2011 | Vreman | FPV | ODE WM | HyShot-II |
| Donde *et al.* 2012; Koo *et al.* 2013 | RK2 | WENO5/ BQUICK3 | Mapped (4M) | Yetter *et al.* 1991 | Dynamic Smagorinsky | SPDF-QMOM | / | Michigan |
| Edwards *et al.* 2012 | Crank-Nicholson | TVD + CD4 | Mapped (28M) | Jachimowski 1992; Conaire *et al.* 2004 | Lenormand | Quadrature-reconstruction | $k$–$\omega$ BSL | DLR, UVa-A |
| Bermejo-Moreno, Larsson, *et al.* 2013 | RK3 | ENO2 + CD2 | Mapped (12-250M) | CEFRC v0.9 | Vreman | FPV | ODE WM | HIFiRE-2 |
| Chan and Ihme 2014 | Backward Euler | TVD + CD | Unstructured (40M) | Burke *et al.* 2012 | Verman | C-FPV | / | UVa-A |
| Fulton *et al.* 2014 | Crank-Nicholson | TVD/PPM + CD4 | Mapped (0.005–0.35 mm, 50M) | Burke *et al.* 2012; Jachimowski 1992 | Lenormand | / | $k$–$\omega$ BSL | UVa-A |
| Wang *et al.* 2014 | LU-Gauss-Seidel | WENO-JS5 | Mapped (0.3 mm, 8.5M) | Jachimowski 1992 | $k$-equation | Presumed beta-PDF | S-A RANS | NUDT |
| Fureby, Nordin-Bates, *et al.* 2015 | RK2 | Monotonicity-preserving | Unstructured (22M) | Davidenko *et al.* 2003 | Mixed model | PaSR | Algebric WM | ONERA/ JAXA |
| Nordin-Bates *et al.* 2017 | RK2 | TVD | Mapped (0.03–0.5 mm, 100M) | Jachimowski 1992 | Mixed model | PaSR | / | HyShot-II |
| Gong *et al.* 2017 | Backward Euler | Kurganov2 | 0.1–0.5 mm | Jachimowski 1992 | $k$-equation | SPDF-SF | / | DLR |
| Zettervall and Fureby 2018; Fureby and Nilsson 2023 | RK2 | Kurganov2 | Unstructured (25M) | Zettervall and Fureby 2018 | LDKM | PaSR | Algebric WM | Michigan |
| Almeida 2019 | RK3 | TVD + DRP4 | Uniform (0.35 mm, 4M) | Yetter *et al.* 1991 | Smagorinsky | SPDF-SF | / | UVa-A |
| Ribeiro *et al.* 2020 | RK3 | WENO7 | Mapped (0.015–0.27 mm, 42M) | Conaire *et al.* 2004 | WALE | / | / | Michigan (no isolator) |
| Jain *et al.* 2025; Sharma *et al.* 2025 | RK2 | TVD | AMR (0.25 mm, 200M) | Smith *et al.* 2016 | / | / | / | AFRL |

A few observations can be drawn from Table 1.1:

1. **Low-dissipation shock-capturing scheme is essential**
   All the LES listed in the table employ shock-capturing schemes to discretise the inviscid fluxes, necessary for maintaining numerical stability in the presence of discontinuities. However, the numerical dissipation introduced by such schemes risks damping small-scale turbulent structures and can even mask out the LES SGS model (Larsson 2010). Two common remedies are used to address this issue: 1) use of high-order schemes, such as fifth- and seventh-order Weighted Essentially Non-Oscillatory (WENO) methods; and 2) hybrid schemes which use a sensor (*e.g.* Ducros *et al.* 1999) to selectively activate shock-capturing near discontinuities while applying a low-dissipation scheme elsewhere.

2. **Adaptive mesh refinement (AMR) is favourable but rarely used**
   Due to the relatively simple geometry of ramjet combustors, structured grids are commonly used, with grid sizes ranging from $O(0.01)$ to $O(0.1)$ mm. However, few studies have explored the use of AMR until very recently (Jain *et al.* 2025; Sharma *et al.* 2025). AMR is particularly suited for ramjet simulations since the position of the flame and the shock train is difficult to know *a priori*. By dynamically refining the mesh in regions of interest, AMR enables more efficient use of computational resources without compromising accuracy.

3. **Realistic chemical and transport properties are important**
   All reviewed LES studies use detailed chemical kinetics mechanisms for combustion, suggesting that finite-rate effects may be important given the short flow residence times. Realistic transport properties, including differential diffusion, may also be important, especially for hydrogen-fuelled systems (Han *et al.* 2016; Zhu *et al.* 2024).

4. **Various turbulence and TCI models are employed, but a unified and general model is lacking**
   Various sub-grid scale (SGS) models are used in the LES, ranging from classical Smagorinsky and wall-adaptive large eddy (WALE) models to more advanced dynamic and one-equation models, such as the $k$-equation and the localised dynamic kinetic-energy model (LDKM). A similar variety exists for turbulence-chemistry interaction (TCI) models. These include flamelet progress variable (FPV) and presumed probability density function (PDF) models commonly used for low-speed flows, as well as more sophisticated models like the transport scalar PDF (SPDF) and the linear eddy model (LEM). These SGS and TCI models will be introduced in greater detail in section 2.2. Moreover, in all current LES, the SGS model for velocity and the TCI model are treated separately, hence transport and reaction are decoupled. Also, most TCI models, apart from the SPDF model, rely on assumptions about the flame mode (premixed or non-premixed) and combustion regime (*e.g.*, flamelet, distributed reaction), which are, again, difficult to know *a priori*.

5. **Wall-modelling offers potential for order-of-magnitude cost savings**
   Accurate prediction of the boundary layer behaviour is critical in internal flows, such as the isolator, particularly if shear stress and heat transfer are major concerns or when the flow field is driven by shock-boundary layer interaction (SBLI). While a wall-resolving grid can be used, having very fine grids near walls is often prohibitively expensive. Some LES approaches utilise wall modelling techniques to reduce the resolution requirements, such as hybrid RANS/LES methods where RANS is applied near walls, and wall flux models that use the outer LES solution in combination with some algebraic relationships or ODEs to model the wall fluxes (see chapter 5).

## 1.3 Thesis objectives

This thesis aims to contribute towards a high-fidelity LES approach that can aid in the research and development of dual-mode ramjet engine combustors and ultimately for whole-vehicle simulation. Such an LES approach must meet several criteria:

1. It should have an accurate LES SGS model;
2. It must be capable of modelling TCI across different flame modes and combustion regimes;
3. It needs to be robust in complex flow fields that include shock waves, vortices, and boundary layers, while maintaining high accuracy and low numerical dissipation to effectively capture multi-scale turbulent phenomena;
4. It should be efficient and scalable, allowing it to leverage modern computing hardware, making simulations feasible and affordable for practical-scale problems.

To achieve these goals, and based on the observations and discussions from the previous section, this thesis develops a joint-velocity-scalar PDF model, solved by the Eulerian stochastic fields approach that includes high-order numerics, AMR, and wall-modelling capabilities. The solver will use detailed chemical mechanisms and realistic transport properties, including differential diffusion.

## 1.4 Thesis outline

The remainder of this thesis is organised as follows:

**Chapter 2** provides the preliminaries for simulating compressible reacting flows. It covers the governing equations used in DNS and LES, as well as the high-order finite difference method used to discretise these equations and the AMR technique. The implementation is verified and validated through a series of test cases.

**Chapter 3** introduces the joint-velocity-scalar probability density function (VSPDF) as a unified framework for closing all turbulent interactions. It also presents the Eulerian stochastic fields (SF) approach for solving the PDF transport equation, with attention paid to ensuring thermodynamic consistency for each field, which is crucial for numerical stability. The performance of the SF-AMR methodology is validated with a number of non-reacting and reacting cases, marking it as the first such study reported in the literature.

Chapters 4 and 5 focus on two approaches for improving the PDF method: enhancing the accuracy of the SGS model and reducing the computational cost, respectively.

**Chapter 4** presents a tensor-based neural network approach that significantly improves the SGS model in the PDF framework. The network's architecture is designed to automatically enforce Galilean invariance, rotational equivariance, and dimensional consistency.

**Chapter 5** introduces a wall modelled stochastic fields (WMSF) approach that couples the stochastic fields with a state-of-the-art wall model, allowing for accurate prediction of wall fluxes at reasonable cost, without needing to resolve near-wall flows.

**Chapter 6** applies the WMSF strategy developed to the Michigan dual-mode ramjet experiment. Two cases are analysed, demonstrating that the WMSF approach can accurately predict the flame structure and isolator shock train in two fundamentally different stabilisation mechanisms.

**Chapter 7** concludes the work and provides suggestions for future research directions. Supplementary materials are included in the appendices.

# Chapter 2

# Theoretical background

This chapter introduces the preliminary theoretical background in compressible reacting flow modelling, large eddy simulation, and high-order finite difference numerical methods. The resulting solver is verified and validated to be accurate and suitable for further investigation and model development.

## 2.1 Governing equations

### 2.1.1 Assumptions

The scope of this thesis is restricted to compressible multi-species reacting and non-reacting gases where the following assumptions hold:

1. Continuum hypothesis — the molecular mean free path is much smaller than the flow length scale, *i.e.*, Knudsen number $\lesssim 0.03$ (Anderson Jr. 2019).
2. Newtonian fluid — the shear stress is proportional to local strain rate.
3. Local thermodynamic equilibrium — a single internal energy[1] is sufficient to characterise the local thermodynamic system. This assumption holds for altitudes below 40 km and velocities below 4 km/s, or approximately Mach 12 (Bottin *et al.* 2006). These conditions are true for most ramjet and scramjet applications.
4. Mixture of ideal gases — the pressure, density, and temperature are related by the ideal gas equation of state, and the specific heat capacities are functions of temperature and composition only. Note that the solver introduced later in this chapter can handle non-ideal equation of states as well, but this capability is outside the scope of this thesis.

[1] The internal energy of a gas is stored in translational, rotational, vibrational, and electronic modes. At elevated temperatures, these modes may be excited independently and have different characteristic temperatures. Typically, translational and rotational modes relax to equilibrium very fast and are assumed to be in equilibrium. Vibrational relaxation is slower, which depends on temperature and pressure (Millikan and White 1963). The electronic mode has the longest relaxation time, but at moderate Mach numbers, electronic excitation is minimal (Candler 2019).

### 2.1.2 Navier-Stokes equations

The Navier-Stokes equations express the conservation of mass, momentum, and energy (Ern and Giovangigli 1994; Chen, Choudhary, *et al.* 2009; Poinsot and Veynante 2012). They can be written in conservative form as

$$\frac{\partial \mathbf{U}}{\partial t} + \underbrace{\frac{\partial \mathbf{F}_j(\mathbf{U})}{\partial x_j}}_{-\mathbf{RHS}(\mathbf{U})} = \mathbf{S}(\mathbf{U}, t)\,, \tag{2.1}$$

where $\mathbf{U}(\mathbf{x}, t) \in \mathbb{R}^{N_s+4}$ is the conservative variable vector, $\mathbf{F}_j$ is the flux vector in $j$ direction, and $\mathbf{S}$ is the source term vector. The divergence of $\mathbf{F}$ is also referred to as the right-hand side (**RHS**) when written in a more compact form.

$$\mathbf{U} = \begin{bmatrix} \rho Y_\alpha \\ \rho u_i \\ \rho E \end{bmatrix}, \quad \mathbf{F}_j = \underbrace{\begin{bmatrix} \rho Y_\alpha u_j \\ \rho u_i u_j + p\delta_{ij} \\ (\rho E + p) u_j \end{bmatrix}}_{\text{hyperbolic}} + \underbrace{\begin{bmatrix} -J_{\alpha,j} \\ -\tau_{ij} \\ q_j - \tau_{ij} u_i \end{bmatrix}}_{\text{diffusive}}, \quad \mathbf{S} = \begin{bmatrix} \rho S_\alpha \\ 0 \\ 0 \end{bmatrix}.$$

The symbol $\rho$ is density, $Y_\alpha$ is the mass fraction of species $\alpha$, $u_i$ is the velocity in direction $i$, and $E$ is the mass-specific total energy. Throughout this document, unless otherwise specified, Roman indices denote spatial directions and imply summation when repeated, while Greek indices denote species and do not imply summation.

#### Thermochemical relationships

The mass-specific total energy of a mixture of $N_s$ gases is the sum of the kinetic, sensible, and chemical energies

$$E = \frac{u_i u_i}{2} + \underbrace{\sum_{\alpha=1}^{N_s} Y_\alpha \left( \int_{T_f}^{T} c_{v,\alpha}\, \mathrm{d}T + \Delta e_{f,\alpha} \right)}_{e}, \tag{2.2}$$

where $c_{v,\alpha}$ is the specific heat capacity at constant volume, and $\Delta e_{f,\alpha}$ is the energy of formation of a unit mass of species $\alpha$ at the reference temperature $T_f$. The sum of the sensible and chemical energies is known as the internal energy ($e$), which can also be written in terms of enthalpy,

$$e = \sum_{\alpha=1}^{N_s} Y_\alpha h_\alpha - \frac{p}{\rho} = \sum_{\alpha=1}^{N_s} Y_\alpha \left( \int_{T_f}^{T} c_{p,\alpha}\, \mathrm{d}T + \Delta h_{f,\alpha} \right) - \frac{p}{\rho}\,, \tag{2.3}$$

where $h_\alpha$ is the species enthalpy, $c_{p,\alpha}$ is the specific heat capacity at constant pressure, and $\Delta h_{f,\alpha} = \Delta e_{f,\alpha} + R_u T_f / W_\alpha$ is the enthalpy of formation.

The static pressure follows the ideal gas law

$$p = \frac{\rho R_u T}{W}\,, \tag{2.4}$$

where $R_u$ is the universal gas constant and $W$ is the mixture molecular weight. The species' mass fraction ($Y_\alpha$), mole fraction ($X_\alpha$), and molecular weight ($W_\alpha$) are related by

$$\frac{Y_\alpha}{X_\alpha} = \frac{W_\alpha}{W}\,, \tag{2.5}$$

noting that $\sum_\alpha Y_\alpha = \sum_\alpha X_\alpha = 1$, and $1/W = \sum_\alpha Y_\alpha / W_\alpha$.

### Diffusive fluxes

The viscous stress tensor is

$$\tau_{ij} = 2\mu S_{ij} + \left(\mu_b - \frac{2}{3}\mu\right) S_{kk}\delta_{ij}\,, \tag{2.6}$$

where $\mu$ is the dynamic viscosity and $\mu_b$ is the bulk viscosity[2]. The strain rate tensor is

$$S_{ij} = \frac{1}{2}\left(\frac{\partial u_i}{\partial x_j} + \frac{\partial u_j}{\partial x_i}\right)\,. \tag{2.7}$$

Neglecting the Dufour and Soret effects (thermal diffusion), the heat flux vector is

$$q_i = -\kappa\frac{\partial T}{\partial x_i} + \rho\sum_{\alpha=1}^{N_s} h_\alpha V_{\alpha,i} Y_\alpha\,, \tag{2.8}$$

where $\kappa$ is the thermal conductivity, and the species mass diffusion velocity is (Coffee and Heimerl 1981; Ern and Giovangigli 1994)

$$V_{\alpha,i} = -\frac{D_\alpha}{X_\alpha}\left(\frac{\partial X_\alpha}{\partial x_i} + (X_\alpha - Y_\alpha)\frac{\partial \ln p}{\partial x_i}\right)\,, \tag{2.9}$$

where $D_\alpha$ is the mixture-averaged diffusivity[3] (Curtiss and Hirschfelder 1949)

$$D_\alpha = \frac{1 - Y_\alpha}{\sum_{\beta\neq\alpha} X_\beta / D_{\alpha\beta}}\,. \tag{2.10}$$

[2]The Stokes' hypothesis states that $\tau_{ij}$ is traceless, implying that $\mu_b = 0$. It is true for monoatomic gases, but not for polyatomic gases. For generality, this work retains $\mu_b$ as a function of temperature and composition, modelled using the NASA polynomial form.

[3]In multi-component diffusion, each species $\alpha$ diffuses into every other species $\beta$ with a binary diffusivity $D_{\alpha\beta}$ for $\beta = 1, ..., N_s$. Determining $V_\alpha$ requires solving an $N_s \times N_s$ linear system, which can be computationally expensive for large mixtures. Alternatively, the species $\alpha$ can be approximated to diffuse into a mixture of all other species, characterised by a mixture-averaged diffusivity $D_\alpha$. This approximation is exact if all $D_{\alpha\beta}$ are the same. Furthermore, if $W_\alpha$ are the same across all species, $V_\alpha$ simplifies to Fick's law, $\mathbf{V}_\alpha = -D\nabla Y_\alpha / Y_\alpha$.

For conservation of mass, a correction velocity $\mathbf{V}_c = -\sum_\alpha \mathbf{V}_\alpha Y_\alpha$ is added to $\mathbf{V}_\alpha$. The species diffusion flux is

$$J_{\alpha,j} = -\rho Y_\alpha (V_{\alpha,j} + V_{c,j})\,. \tag{2.11}$$

Realistic transport properties ($\mu$, $\mu_b$, $\kappa$, $D_{\alpha\beta}$) are modelled as functions of temperature and composition, using the NASA polynomials (Mcbride *et al.* 1993; Ern and Giovangigli 1995).

### Chemical reaction

A chemical mechanism can be written as a set of $N_r$ reversible reactions,

$$\sum_{\alpha=1}^{N_s} \nu'_{\alpha,m}\,\chi_\alpha \rightleftharpoons \sum_{\alpha=1}^{N_s} \nu''_{\alpha,m}\,\chi_\alpha \qquad \text{for } m = 1, ..., N_r\,, \tag{2.12}$$

with $\nu'_{\alpha,m}, \nu''_{\alpha,m}$ being the molar stoichiometric coefficients for species $\alpha$ in reaction $m$, and $\chi_\alpha$ the chemical symbol of species $\alpha$. The chemical source term is expressed by

$$\rho S_\alpha = W_\alpha \sum_{m=1}^{N_r} (\nu''_{\alpha,m} - \nu'_{\alpha,m}) \left[ k_m^f \prod_{\beta=1}^{N_s} C_\beta^{\nu'_{\beta,m}} - k_m^r \prod_{\beta=1}^{N_s} C_\beta^{\nu''_{\beta,m}} \right]\,, \tag{2.13}$$

where $C_\alpha = \rho Y_\alpha / W_\alpha$ is the molar concentration, and $k_m^f$ and $k_m^r$ are the forward and reverse rates of reaction $m$, respectively. For mass conservation, $\sum_\alpha (\nu''_{\alpha,m} - \nu'_{\alpha,m}) W_\alpha = 0$ and $\sum_\alpha S_\alpha = 0$. The forward rate constants are modelled by the Arrhenius law

$$k_m^f = A_m T^{b_m} \exp\left(-\frac{E_m^{act}}{R_u T}\right)\,, \tag{2.14}$$

where $A_m$ and $b_m$ are model constants and $E_m^{act}$ is the activation energy. They are defined in the chemical mechanisms. The reverse rate constants are linked to the forward rate constants through the equilibrium constants $k_m^e$,

$$k_m^r = k_m^f / k_m^e\,. \tag{2.15}$$

This work focuses on hydrogen combustion and uses detailed mechanisms exclusively.

## 2.2 Large eddy simulation

A distinctive feature of turbulent flows is the presence of motions across a wide range of spatial and temporal scales. Direct numerical simulation (DNS), which solves the Navier-Stokes equations directly, requires a computational mesh and time step size sufficiently fine to resolve all these scales. According to the theory of Kolmogorov 1962, the ratio

between the largest and smallest turbulent eddies grows with the Reynolds number (Re), see Table 2.1. In three spatial dimensions and one temporal dimension, the computational cost of DNS scales with $\mathrm{Re}^{11/4}$.[4]

In addition, DNS of reacting flows also need to resolve the inner flame structure. Poinsot and Veynante 2012 estimated that the flame thickness $\delta_F$ decreases with increasing Reynolds number and Damköhler number (Da), as $L/\delta_F \propto (\mathrm{Re}\,\mathrm{Da})^{1/2}$, where $\mathrm{Da} = \tau_{\mathrm{turb}}/\tau_{\mathrm{chem}}$ is the ratio between the turbulent and chemical timescales. In practice, tens of grid points are placed across the flame front, which is $\approx 0.1$ mm for a hydrogen-air flame at atmospheric conditions. The high computational cost makes DNS infeasible for engineering applications with high Reynolds numbers.

Table 2.1: Length and time scales in turbulent flows, where $\nu = \mu/\rho$ is kinematic viscosity, and $\epsilon$ is the turbulent kinetic energy dissipation rate. The domain size $L$ is assumed to have the same order of magnitude as the integral length $\ell$, hence can be used interchangeably.

| | Largest | Smallest | Ratio |
|---|---|---|---|
| Length scale | $L$ | $\eta = (\nu^3/\epsilon)^{1/4}$ | $L/\eta \propto \mathrm{Re}^{3/4}$ |
| Timescale | $\tau = L/U$ | $\tau_\eta = \sqrt{\nu/\epsilon}$ | $\tau/\tau_\eta \propto \mathrm{Re}^{1/2}$ |

Large eddy simulation (LES) introduces a low-pass spatial filter $G$ which removes scales smaller than a certain filter width $\Delta$ (Smagorinsky 1963). The filtered field, defined as

$$\overline{\phi}(\mathbf{x}, t) = \int_{-\infty}^{\infty} \phi(\mathbf{x} + \mathbf{r}, t) G(\mathbf{r}; \Delta)\, \mathrm{d}^3\mathbf{r}\,, \tag{2.16}$$

is resolved on the LES grid, while the sub-grid scale (SGS), $\phi' = \phi - \overline{\phi}$, is modelled. The filter function must satisfy $\int_{-\infty}^{\infty} G(\mathbf{r}; \Delta)\, \mathrm{d}^3\mathbf{r} = 1$ and is positive everywhere[5]. It can be chosen explicitly or, as in this work, implicitly linked to the computational grid (known as the box filter or top-hat filter)

$$G(\mathbf{r}; \Delta) = \begin{cases} 1/\Delta & \text{if } |r_i| < \Delta_i/2\,, \\ 0 & \text{otherwise.} \end{cases} \tag{2.17}$$

The symbol $\Delta_i$ denotes the grid size in direction $i$ and $\Delta$ is taken as $(\Delta_1\Delta_2\Delta_3)^{1/3}$. In the limit of $\Delta \to \eta$, LES should return to DNS.

The filtering operation is linear, and hence, commutative with spatial derivatives if $\Delta$ is constant in space. However, this condition does not hold generally in CFD. For instance, in adaptive mesh refinement, $\Delta$ can change abruptly at the coarse-fine level interface.

[4] This estimate assumes that the time step size is limited by resolving $\tau_\eta$ rather than being bounded by the CFL condition. If the time step size is instead limited by the CFL condition, the cost of DNS scales with a higher $\mathrm{Re}^3$.

[5] The spectral cut-off filter, which is the box filter in wavenumber space, can be negative in physical space. However, since the positivity condition is important for defining a probability density function later, this work excludes all non-positive filters.

Arguably, the solution is usually smooth at the level boundaries, so given a sensible choice of refinement criteria, the commutation error may be small. The role of $\Delta$ in the probability density function methods is slightly different and will be discussed in subsection 3.1.2.

The cost of LES is proportional to $(L/\Delta)^4$, as the mesh only needs to capture scales as small as $\Delta$.[6] Pope 2000, 2004 suggest that an adequate LES should resolve at least 80% of the total kinetic energy. At large Re, the smallest scales carry a progressively smaller portion of the total energy as the energy spectrum decays rapidly. As a result, the $\Delta$ required to meet this criterion becomes almost independent of Re,[7] making LES a cost-effective method for studying high-Re flows.

For variable-density flows, it is convenient to use the density-weighted Favre filtering as it reduces the number of unclosed terms (Favre 1965)

$$\overline{\rho}\tilde{\phi} = \overline{\rho\phi}\,, \qquad \phi'' = \phi - \tilde{\phi}\,, \qquad \tilde{\phi} = \bar{\phi} + \frac{\overline{\rho'\phi'}}{\bar{\rho}}\,. \tag{2.18}$$

Applying the filter to (2.1) yields the LES equations. Following Vreman *et al.* 1995,

$$\frac{\partial \overline{\mathbf{U}}}{\partial t} + \frac{\partial \breve{\mathbf{F}}_j(\overline{\mathbf{U}})}{\partial x_j} = \overline{\mathbf{S}(\mathbf{U})} + \mathbf{R}\,, \tag{2.19}$$

where $\mathbf{R}$ is the unclosed residual that arose due to the non-linearity of $\mathbf{F}$

$$\overline{\mathbf{U}} = \begin{bmatrix} \overline{\rho}\tilde{Y}_\alpha \\ \overline{\rho}\tilde{u}_i \\ \overline{\rho}\breve{E} \end{bmatrix}, \quad \mathbf{R} = \frac{\partial[\breve{\mathbf{F}}_j(\overline{\mathbf{U}}) - \overline{\mathbf{F}_j(\mathbf{U})}]}{\partial x_j} = \begin{bmatrix} -a_1 + a_2 \\ -b_1 - b_2 + b_3 \\ -c_1 - c_2 - c_3 + c_4 + c_5 + c_6 - c_7 - c_8 \end{bmatrix}.$$

The breve $\breve{\cdot}$ denotes variables which are functions of $\overline{\mathbf{U}}$. The unclosed terms are given in Table 2.2, where $\partial_j = \partial/\partial x_j$, and the SGS stress tensor is

$$\tau_{ij}^{\mathrm{sgs}} = \bar{\rho}(\widetilde{u_i u_j} - \tilde{u}_i\tilde{u}_j)\,. \tag{2.20}$$

In LES, only the terms with "medium" influence are relevant for modelling as they have dominating orders. A thorough overview of compressibility effects in turbulence is given by Génin 2009, section 1.1. Note that the filtered source terms $\bar{\rho}\tilde{S}_\alpha$ are also unclosed. Models for the turbulence-chemistry interaction will be introduced in subsection 2.2.2.

[6] It is worth noting that the filtering operation is reversible as long as the Fourier transform of $G$ has an inverse. The loss of information from DNS to LES occurs when truncating the grid's space-time resolution, not at filtering.

[7] Using the model energy spectrum in Pope 2000, p. 231 and a spectral cut-off filter, it is estimated that 80% of the total kinetic energy is resolved with $\ell/\Delta \approx 40$ when $\mathrm{Re} \gtrsim 10^5$.

[8] Vreman *et al.* 1995 found that $c_2$ magnitude is comparable to the diffusive fluxes (medium importance). However, Moin *et al.* 1991; Martín, Piomelli, *et al.* 2000 argued that it is negligible, citing the incompressibility of small scales, similar to Morkovin 1962's hypothesis for compressible turbulent boundary layers. In practice, $c_2$ is always modelled collectively with $c_1$.

Table 2.2: Expressions and relative magnitudes of the unclosed terms in (2.19), modified from Vreman *et al.* 1995 based on DNS of compressible mixing layers.

| | Term | Expression | Magnitude |
|---|---|---|---|
| Species equation | $a_1$ | $\partial_j(\bar{\rho}(\widetilde{Y_\alpha u_j} - \tilde{Y}_\alpha \tilde{u}_j))$ | Medium |
| | $a_2$ | $\partial_j(\bar{J}_{\alpha,j} - \breve{J}_{\alpha,j})$ | Negligible |
| Momentum equation | $b_1$ | $\partial_j \tau_{ij}^{\mathrm{sgs}}$ | Medium |
| | $b_2$ | $\partial_j(\bar{p} - \breve{p})$ | Negligible |
| | $b_3$ | $\partial_j(\bar{\tau}_{ij} - \breve{\tau}_{ij})$ | Negligible |
| Energy equation | $c_1$ | $\partial_j \bar{\rho}(\widetilde{Eu_j} - \tilde{E}\tilde{u}_j)$ | Medium |
| | $c_2$ | $\overline{p\partial_j u_j} - \bar{p}\partial_j \tilde{u}_j$ | Medium[8] |
| | $c_3$ | $\partial_j(\tau_{ij}^{\mathrm{sgs}} \tilde{u}_i)$ | Medium |
| | $c_4$ | $\tau_{ij}^{\mathrm{sgs}} \partial_j \tilde{u}_i$ | Small |
| | $c_5$ | $\overline{\tau_{ij}\partial_j u_i} - \bar{\tau}_{ij}\partial_j \tilde{u}_i$ | Small |
| | $c_6$ | $\partial_j(\bar{\tau}_{ij}\tilde{u}_i - \breve{\tau}_{ij}\tilde{u}_i)$ | Negligible |
| | $c_7$ | $\partial_j(\bar{q}_j - \breve{q}_j)$ | Negligible |
| | $c_8$ | $\partial_j(\bar{p}\tilde{u}_j - \breve{p}\tilde{u}_j)$ | Negligible |

### 2.2.1 Eddy-viscosity models

The Boussinesq hypothesis states that SGS velocity behaves like random motion[9], and consequently, can be described by an eddy viscosity analogous to the molecular viscosity. From an energy point of view, turbulent fluctuations lead to an additional viscosity that dissipates the mean flow. The SGS stress tensor is written as

$$\tau_{ij}^{\mathrm{sgs}} = -2\,\bar{\rho}\nu_{\mathrm{sgs}}\left(\tilde{S}_{ij} - \frac{\delta_{ij}}{3}\tilde{S}_{kk}\right) - \frac{2}{3}\,\bar{\rho}k_{\mathrm{sgs}}\delta_{ij}\,, \tag{2.21}$$

where $\nu_{\mathrm{sgs}}$ is the eddy viscosity[10], $\tilde{S}_{ij}$ is the strain rate tensor of the resolved velocity, and $k_{\mathrm{sgs}} = \tau_{ii}^{\mathrm{sgs}}/2$ is the SGS kinetic energy. Past research efforts have been devoted to determining $\nu_{\mathrm{sgs}}$ and $k_{\mathrm{sgs}}$.

#### Smagorinsky model

The most commonly used model is undoubtedly the one by Smagorinsky 1963, largely thanks to its simplicity.

$$\nu_{\mathrm{sgs}} = (C_s\Delta)^2|\tilde{S}|\,, \tag{2.22}$$

$$|\tilde{S}| = (2\,\tilde{S}_{ij}\tilde{S}_{ij})^{1/2}\,, \tag{2.23}$$

[9] More precisely, Brownian motion or Wiener process as in the kinetic gas theory.

[10] By dimensional analysis, $\nu_{\mathrm{sgs}} \propto \ell_{\mathrm{sgs}}^2/\tau_{\mathrm{sgs}}$ represents an eddy length scale $\ell_{\mathrm{sgs}}$ and an eddy timescale $\tau_{\mathrm{sgs}}$. This is analogous to Prandtl's mixing-length hypothesis, in which the timescale is related to the mean velocity gradient.

where $C_s$ is the Smagorinsky constant, usually taken between 0.1 and 0.2 (Germano *et al.* 1991; Moin *et al.* 1991; Martín, Piomelli, *et al.* 2000).

### WALE model

The wall-adapting local eddy-viscosity (WALE) model by Nicoud and Ducros 1999 is designed to yield the correct asymptotic scaling of $\nu_{\text{sgs}} \propto y^3$ near walls, where $y$ is wall normal distance.

$$\nu_{\text{sgs}} = (C_w \Delta)^2 \frac{(S^d_{ij} S^d_{ij})^{3/2}}{(\tilde{S}_{ij}\tilde{S}_{ij})^{3/2} + (S^d_{ij} S^d_{ij})^{5/2}} \,, \tag{2.24}$$

$$S^d_{ij} = \frac{1}{2}\left(\frac{\partial \tilde{u}_i}{\partial x_k}\frac{\partial \tilde{u}_k}{\partial x_j} + \frac{\partial \tilde{u}_j}{\partial x_k}\frac{\partial \tilde{u}_k}{\partial x_i}\right) + \frac{1}{3}\frac{\partial \tilde{u}_l}{\partial x_k}\frac{\partial \tilde{u}_k}{\partial x_l}\delta_{ij} \,, \tag{2.25}$$

with $C_w \approx 0.5$. Compared to the Smagorinsky model, the WALE model ensures correct wall shear stress prediction and produces zero $\nu_{\text{sgs}}$ in pure two-dimensional shear flows.

### SGS kinetic energy model

Yoshizawa 1986 proposed a model for $k_{\text{sgs}}$ based on the direct-interaction approximation[11],

$$k_{\text{sgs}} = C_I \Delta^2 |\tilde{S}|^2 \,. \tag{2.26}$$

A wide range of $C_I$ is reported in the literature, from 0.0066 to 0.1. Martín, Piomelli, *et al.* 2000 use $C_I = 0.09$ for compressible turbulence simulations.

### SGS species and heat fluxes

The eddy viscosity approach is extended to SGS species and heat fluxes using the sub-grid Schmidt number ($\text{Sc}_{\text{sgs}}$) and sub-grid Prandtl number ($\text{Pr}_{\text{sgs}}$), both around 0.4 to 0.7 (Moin *et al.* 1991). They are taken as 0.7 in this work. $\text{Sc}_{\text{sgs}}$ is the same for all species because SGS diffusion is driven by small turbulent motions, which act on all species equally.

$$a_1 = \frac{\partial J^{\text{sgs}}_{\alpha,j}}{\partial x_j} = \frac{\partial}{\partial x_j}\left(-\bar{\rho}\frac{\nu_{\text{sgs}}}{\text{Sc}_{\text{sgs}}}\frac{\partial \tilde{Y}_\alpha}{\partial x_j}\right) \,, \tag{2.27}$$

$$c_1 + c_2 = \frac{\partial q^{\text{sgs}}_j}{\partial x_j} = \frac{\partial}{\partial x_j}\left(-\bar{\rho}\breve{c}_p\frac{\nu_{\text{sgs}}}{\text{Pr}_{\text{sgs}}}\frac{\partial \breve{T}}{\partial x_j}\right) \,. \tag{2.28}$$

[11] The direct-interaction approximation proposed by Kraichnan 1959 models the energy transfer in wave-number space by solving the triad interactions (three points in spectral domain). Perturbation method is used to close the higher-order statistical moments in terms of second-order moments. It is related to other spectral closure models such as the eddy-damped quasinormal Markovian model (Xia *et al.* 2010).

#### Other SGS models

Sagaut 2001 divides the SGS modelling strategies into two families: *functional modelling*, which reproduces the effects of the SGS term without necessarily having the same structure; and *structural modelling*, in which the model is constructed by approximating the SGS term, usually through formal series expansions.

The eddy viscosity models introduced above belong to the functional modelling approach. Other improvements have been proposed, such as the dynamic procedure which determines the Smagorinsky constant using a test filter (Germano *et al.* 1991; Moin *et al.* 1991), and the $\sigma$-model of Nicoud, Toda, *et al.* 2011 which expresses the timescale using singular values of the velocity gradient tensor.

A non-exhaustive list of structural models includes the gradient models (also known as tensor diffusivity models) derived from Taylor expansion of the SGS tensor (Clark *et al.* 1979; Vreman *et al.* 1995), as well as scale-similarity models and approximate deconvolution models which are based on deconvolution of the filtered field (Stolz and Adams 1999). Further description and discussion regarding SGS models can be found in Sagaut 2001; Moser *et al.* 2021 for incompressible and Garnier *et al.* 2009 for compressible LES.

### 2.2.2 Turbulent combustion models

Unlike turbulence stresses, the filtered chemical source term cannot be expressed as a finite series of sub-grid moments due to its non-polynomial non-linearity (Poinsot and Veynante 2012, chapter 4.5). Therefore, turbulence-chemistry interaction (TCI) models are typically developed based on other physical or functional foundations. These models can be categorised by combustion mode (Poinsot and Veynante 2012), the role of chemistry mechanism (Giusti and Mastorakos 2019), or the assumptions made (Veynante and Vervisch 2002). Here, common TCI models are grouped according to the physical arguments on which they are based:

1. **Timescale-based models** relate the reaction rate to the sub-grid Damköhler number ($\mathrm{Da}_{\mathrm{sgs}}$). The quasi-laminar approximation assumes that the chemical reaction is much slower than turbulence ($\mathrm{Da}_{\mathrm{sgs}} \ll 1$), allowing the sub-grid to be well-stirred before reaction takes place (Bouheraoua *et al.* 2017). In contrast, turbulent mixing models such as the EBU (Spalding 1971) and EDM (Magnussen and Hjertager 1977) assume infinitely fast chemistry ($\mathrm{Da}_{\mathrm{sgs}} \gg 1$), meaning that the fuel and oxidiser react immediately upon mixing, and the reaction rate is controlled by turbulent mixing. For intermediate $\mathrm{Da}_{\mathrm{sgs}}$ values, the partially-stirred reactor (PaSR) model conjectures that reaction occurs only in a small region within the LES cell, akin to the fine structure in eddy dissipation concept (EDC) of Magnussen 1981. The volume fraction of the reacting region is $1/(1 + \mathrm{Da}_{\mathrm{sgs}})$ (Sabelnikov and Fureby 2013), such that the

PaSR model recovers the quasi-laminar and turbulent mixing behaviours for both limits of small and large $Da_{sgs}$.

2. **Geometry-based models** assume that the flame is a thin continuous surface. Flamelet-type models treat the flame surface as a locally one-dimensional laminar flamelet, linking the reaction rate or flame speed to a tracker variable, such as progress variable for premixed flames or mixture fraction for non-premixed flames (Williams 2000). The chemical source terms are usually pre-computed and stored in a lookup table to avoid costly runtime evaluation. The thickened flame model does not use tabulated chemistry, instead, it increases flame thickness through increasing the diffusion coefficient, such that the flame can be resolved on LES grids (Colin *et al.* 2000). The increased flame speed is compensated for by scaling down the reaction rate, and an efficiency function is required to model the effects of SGS wrinkling (Rathore and Navarro-Martinez 2023).

3. **Reduced manifold-based models** build on the idea that the flamelet model can be viewed as a projection of the chemical system onto a one-dimensional space of a "tracker" variable. These models allow for projection onto a manifold with higher, yet still reduced, dimensions. The reaction source term can thus account for more complex phenomena by incorporating additional quantities, such as both mixture fraction and progress variable, heat loss, and pressure, into the manifold (van Oijen *et al.* 2001; Pierce and Moin 2004; Nguyen, Vervisch, *et al.* 2010).

4. **PDF-based methods** relax the assumptions on combustion mode and flame structure by closing the filtered reaction rate using a one-point PDF. The transport PDF methods advance the PDF in time, often using Monte Carlo-type approaches (both Lagrangian: Pope 1985, and Eulerian: Valiño 1998; Soulard and Sabel'nikov 2006) or moment methods (Donde *et al.* 2012; Koo *et al.* 2013). Presumed PDF methods reduce computational cost by assuming a certain PDF shape, typically independent beta or Gaussian distributions, and transport a number of parameters related to the PDF (Gerlinger *et al.* 2001). Another class of methods is the conditional moment closure (CMC), which solves the reaction source term conditioned on the progress variable or mixture fraction (Bilger 1993; Navarro-Martinez, Kronenburg, *et al.* 2005).

5. **Resolution-based methods** tackle the TCI problem by approximating DNS resolution from filtered information. These include the linear eddy model (LEM), which partitions a cell in one spatial dimension and performs one-dimensional DNS on it (Menon and Kerstein 2011), polynomial reconstruction or high-order quadrature approaches (Edwards *et al.* 2012), and, more recently, super-resolution using deep neural networks (Chung, Akoush, *et al.* 2023; Nista *et al.* 2023).

Each TCI model has its strengths and weaknesses, and no single "best" model has been agreed upon. This work focuses on the transport PDF method, which will be discussed in

further detail in the next chapter. Although being more computationally demanding, it carries the fewest assumptions and is valid across all combustion modes and regimes. This is particularly important for high-speed combustion, where large variations in conditions can occur within the flow field. For more details on TCI models, readers are directed to the references cited above and the books of Veynante and Vervisch 2002; Poinsot and Veynante 2012; Domingo and Vervisch 2025.

## 2.3 Numerical methods

### 2.3.1 High-order shock-capturing schemes

This section describes the numerical procedure for obtaining the flux derivative in one dimension. Extension to multiple dimensions is done in a dimension-by-dimension manner. The discussion is limited to a Cartesian grid with uniform spacing of $\Delta x$ between $x_{lo}$ and $x_{hi}$. For brevity, the subscript will change to represent the location on the grid, *e.g.*, $\mathbf{F}(x_{lo} + i\Delta x) = \mathbf{F}_i$.

To solve the governing equations (2.1), we seek a numerical approximation of the interfacial fluxes that is $q$-order accurate:

$$\frac{\partial \mathbf{F}_i}{\partial x} = \frac{\mathbf{F}^{\text{num}}_{i+\frac{1}{2}} - \mathbf{F}^{\text{num}}_{i-\frac{1}{2}}}{\Delta x} + O(\Delta x^q)\,, \tag{2.29}$$

To achieve high-order accuracy, one can interpolate the flux $\mathbf{F}$ or the flow variables $\mathbf{U}$ with a high-order polynomial. However, this approach fails near discontinuities, as the interpolation polynomial becomes oscillatory due to the Gibbs phenomenon[12]. The oscillations are $O(1)$, meaning that they do not vanish with mesh refinement. This problem is associated with the hyperbolic part of the Navier-Stokes equations, while the diffusive part is naturally smoothing and does not lead to discontinuities.

The essentially non-oscillatory (ENO) scheme of Harten, Engquist, *et al.* 1987 is one of the first attempts to construct a high-order essentially non-oscillatory interpolation[13]. The idea is to divide the interpolation stencil into a number of smaller candidate stencils, and then perform interpolation on the smoothest one. Jiang and Shu 1996 extended the idea to using a convex combination of the candidate stencils instead of just one as in ENO, resulting in the weighted essentially non-oscillatory (WENO) scheme. Over the years, numerous improvements to the original WENO have been made, most notably the WENO-Z that improves on the accuracy around critical points (points with zero derivatives) through a novel smoothness indicator (Castro *et al.* 2011), and the targeted essentially non-oscillatory (TENO) which returns to the ideal linear interpolation when the solution is smooth up to a

[12] Formally, the Gibbs phenomenon (Bocher 1906) refers to the persistent undershoot and overshoot of $\approx 8\%$ on each side when approximating a discontinuous function using a finite Fourier series. It is often extended to describe similar behaviour in polynomial interpolation (*e.g.* Jiang and Shu 1996).

[13] "Essentially" means that the magnitude of the oscillations decreases with $O(\Delta x^q)$.

certain threshold (Fu, Hu, *et al.* 2016). These improvements contributed to reduced numerical dissipation, which is crucial for simulating shocked turbulent flows. A comprehensive review of the numerical methods for high-speed flows is given by Pirozzoli 2011.

### Discussions

Before introducing the implementation, this section aims to clarify a few concepts.

*Difference between finite difference (FD) and finite volume (FV) methods*

FD and FV methods differ in the quantity being solved. The FD method solves for the point value of the conservative variable. The flux divergence is calculated in a dimension-by-dimension manner, with the flux derivatives computed by a weighted sum of the solution in a stencil around the position of interest. To obtain high-order accuracy, the weights are determined using the Taylor series, such that the numerical derivative converges to the exact derivative at a rate of $\Delta x^q$. While not all FD schemes are conservative, all conservative FD schemes can be written in the form of (2.29), as the difference between the mid-point fluxes. High-order FD requires the numerical derivative to converge to the exact derivative. This means that the numerical fluxes at the midpoints do not necessarily converge to the exact mid-point fluxes, and that a high-order interpolation of the fluxes to the midpoints does not guarantee a high-order approximation of the flux derivative. This can be illustrated by using the Taylor series. Let $\mathbf{F}^{\text{num}}_{i\pm\frac{1}{2}}$ be the high-order interpolation of the flux function at the midpoints.

$$\mathbf{F}^{\text{num}}_{i\pm\frac{1}{2}} = \mathbf{F}_i \pm \frac{\partial \mathbf{F}_i}{\partial x}\frac{\Delta x}{2} + \frac{\partial^2 \mathbf{F}_i}{\partial x^2}\frac{\Delta x^2}{8} \pm \ldots + \frac{\partial^q \mathbf{F}_i}{\partial x^q}\frac{\Delta x^q}{2^q q!} \tag{2.30}$$

$$\frac{\mathbf{F}^{\text{num}}_{i+\frac{1}{2}} - \mathbf{F}^{\text{num}}_{i-\frac{1}{2}}}{\Delta x} = \frac{\partial \mathbf{F}_i}{\partial x} + O(\Delta x^2)\,. \tag{2.31}$$

This shows that high-order accurate interpolation of the flux function cannot achieve high-order FD, even in one dimension. To attain high-order FD, there are two methods: the first is by reconstructing the flux function as if it were a cell-averaged quantity (Jiang and Shu 1996), and the second involves interpolating the fluxes followed by applying a correction term (Balsara *et al.* 2024). This thesis will focus on the latter method, which will be introduced in the next section.

In contrast to FD, the FV method solves for the volume-averaged quantities. Using Gauss's theorem, the volume-averaged flux divergence can be converted into the surface integral over the cell boundary:

$$\frac{\partial}{\partial t}\int_V \mathbf{U}\,\mathrm{d}V + \int_A \mathbf{F}\cdot\hat{\mathbf{n}}\,\mathrm{d}A = \int_V \mathbf{S}\,\mathrm{d}V\,, \tag{2.32}$$

where $V$ and $A$ are the volume and surface of the control volume, respectively, and $\hat{\mathbf{n}}$ is the outward normal vector of the surface of the control volume. A high-order FV seeks

a numerical approximation of the face-averaged fluxes ($\int_A \mathbf{F} \cdot \hat{\mathbf{n}} \, \mathrm{d}A$) that converges to its exact value, unlike in FD, where the derivative is approximated. Therefore, FV requires first calculating high-order numerical fluxes at points on the interface, and then performing a high-order numerical quadrature to obtain the face average. Omitting the numerical quadrature will limit the FV to second order, regardless of the reconstruction scheme used, because evaluating the flux at the face centre is equivalent to using a second-order Gauss quadrature.

As a result, high-order FV are more computationally expensive than FD of the same order because of the need to perform multiple reconstructions for numerical quadrature, as opposed to only one in FD. However, FV offers the flexibility to use unstructured meshes. It is worth noting that up to second-order accuracy, FV and FD methods are identical, because the cell average and the midpoint value are the same if the function is linear and the second-order Gauss quadrature uses only the face centre value. In this work, a conservative FD approach is used.

*Is a high-order scheme always better than a low-order one?*

When developing a numerical algorithm, the primary focus should be on minimising the error. Therefore, having a scheme with the highest possible order of accuracy while remaining stable is ideal. However, the pioneering work of Lele 1992 reveals that simply optimising for order of accuracy is insufficient for simulating turbulent flows in practice. Factors such as dissipation and dispersion are important, as the scheme must preserve vortical structures correctly. As a result, a new class of "optimised" numerical schemes has emerged, which sacrifice some order of accuracy in exchange for improved dissipation and dispersion properties (*e.g.* Tam and Shen 1993; Martín, Taylor, *et al.* 2006; Tan and Ooi 2022). However, this does not mean that developing or using high-order schemes is obsolete or without merit. For example, comparing a fifth-order WENO scheme that uses a five-point stencil to a third-order WENO scheme with a three-point stencil shows significantly better results, as higher-order schemes naturally have better dissipation and dispersion properties due to their ability to capture more terms in the Taylor series. When comparing a fifth-order WENO to a lower-order optimised WENO scheme that uses the same stencil, some improvement can be observed, but it is less pronounced.

### Alternative finite-difference WENO procedure

There are two approaches for implementing a high-order finite-difference WENO scheme. The first approach, given in Jiang and Shu 1996, centres around splitting the flux vector into left- and right-running components. Each component is then treated as a scalar advection problem, with WENO applied to reconstruct the fluxes to the cell interface. However, Balsara *et al.* 2024 highlighted the limitations of this approach. Most concerning for this work is that it requires a smooth flux splitting, which precludes the use of many Riemann

solvers that are important for preserving interfaces, particularly material interfaces. The fifth-order scheme in this work follows the procedure of Balsara *et al.* 2024:

1. For a stencil $\{\mathbf{U}_{i-2}, \mathbf{U}_{i-1}, \mathbf{U}_i, \mathbf{U}_{i+1}, \mathbf{U}_{i+2}, \mathbf{U}_{i+3}\}$, project the states into characteristic space

$$\mathbf{W}_j = \mathbf{P}(\mathbf{U}_j; \hat{\mathbf{U}}_{i+\frac{1}{2}}) \,, \tag{2.33}$$

   where $\mathbf{P}$ is the projection operator (see Appendix A), using the interfacial average states $\hat{\mathbf{U}}_{i+\frac{1}{2}}$ which is the same for the entire stencil.

2. Interpolate[14] the characteristic variables to the left and right side of the cell interface

$$\mathbf{W}_{R,i+\frac{1}{2}} = \mathit{Interp}(\mathbf{W}_{i-1}, ..., \mathbf{W}_{i+3}) \,, \tag{2.34}$$

$$\mathbf{W}_{L,i+\frac{1}{2}} = \mathit{Interp}(\mathbf{W}_{i+2}, ..., \mathbf{W}_{i-2}) \,. \tag{2.35}$$

3. Transform the interpolated values back to physical space and compute the flux using a Riemann solver, similar to finite volume methods

$$\mathbf{U}_{K,i+\frac{1}{2}} = \mathbf{P}^{-1}(\mathbf{W}_{K,i+\frac{1}{2}}; \hat{\mathbf{U}}_{i+\frac{1}{2}}) \quad \text{for } K = L, R \,, \tag{2.36}$$

$$\mathbf{F}^*_{i+\frac{1}{2}} = \mathbf{F}(\mathbf{U}_{L,i+\frac{1}{2}}, \mathbf{U}_{R,i+\frac{1}{2}}) \,. \tag{2.37}$$

4. The flux computed in the previous step is high-order accurate, but, as noted in (2.31), applying it directly to the derivative in (2.29) is only second-order accurate. A correction term is needed to cancel out the higher-order errors explicitly

$$\mathbf{F}^{\text{num}}_{i+\frac{1}{2}} = \mathbf{F}^*_{i+\frac{1}{2}} - \frac{\Delta x^2}{24} \left.\frac{\partial^2 \mathbf{F}}{\partial x^2}\right|_{i+\frac{1}{2}} + \frac{7\Delta x^4}{5760} \left.\frac{\partial^4 \mathbf{F}}{\partial x^4}\right|_{i+\frac{1}{2}} \,. \tag{2.38}$$

   The above expression leads to a sixth-order accurate flux derivative. The overall scheme is fifth-order, limited by the interpolation. In practice, this correction is added only when the solution is smooth across the entire stencil. Hence, a simple central difference is used to compute the second and fourth derivatives.

### WENO-Z5

The fifth-order WENO-Z scheme uses a five-point stencil $\{s_0, s_1, s_2, s_3, s_4\}$, as illustrated in Figure 2.1. It is formed of three candidate stencils, whose smoothness indicators are

$$\beta_0 = \frac{13}{12}(s_0 - 2s_1 + s_2)^2 + \frac{1}{4}(s_0 - 4s_1 + s_2)^2 \,, \tag{2.39}$$

$$\beta_1 = \frac{13}{12}(s_1 - 2s_2 + s_3)^2 + \frac{1}{4}(s_1 - s_3)^2 \,, \tag{2.40}$$

[14] There is a subtle difference between reconstruction and interpolation in the context of WENO: the former computes the interface point value from *cell averages*, while the latter uses *point values*. In implementation, the two differ only in $d_j$ in (2.44) and $f_j$ in (2.45).

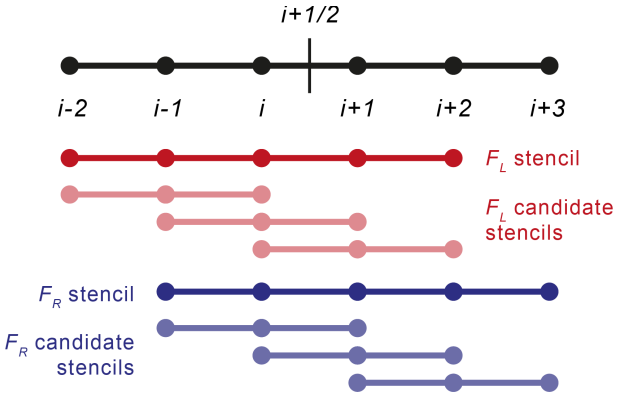



Figure 2.1: Stencils of a fifth-order WENO/TENO scheme.

$$\beta_2 = \frac{13}{12}(s_2 - 2s_3 + s_4)^2 + \frac{1}{4}(s_2 - 4s_3 + s_4)^2 \,. \tag{2.41}$$

The weight of each stencil is calculated by

$$w_j = \frac{\alpha_j}{\sum_{k=0}^{2} \alpha_k} \qquad \text{for } j = 0, 1, 2 \,, \tag{2.42}$$

where

$$\tau_5 = |\beta_0 - \beta_2| \,, \tag{2.43}$$

$$\alpha_j = d_j \left(1 + \frac{\tau_5}{\beta_j + \epsilon}\right) \,. \tag{2.44}$$

The optimal weights of the linear reconstruction are $d_0 = 5$, $d_1 = 10$, $d_2 = 1$, and $\epsilon = 10^{-20}$ is a small number to prevent division by zero.

The reconstructed value is a weighted combination of the individual reconstructed values of the candidate stencils

$$f = \sum_{j=0}^{2} w_j f_j \,, \tag{2.45}$$

where

$$f_0 = \frac{3}{8}s_0 - \frac{5}{4}s_1 + \frac{15}{8}s_2 \,, \quad f_1 = -\frac{1}{8}s_1 + \frac{3}{4}s_2 + \frac{3}{8}s_3 \,, \quad f_2 = \frac{3}{8}s_2 + \frac{3}{4}s_3 - \frac{1}{8}s_4 \,. \tag{2.46}$$

**TENO-5**

The TENO scheme identifies a weakness of the WENO scheme that even if a candidate stencil contains a shock, it is still assigned a small but non-zero weight. This prevents other smooth candidate stencils from using their optimal weights. The idea is to introduce a cut-off value for the smoothness indicator, where a candidate stencil is discarded (weight set to zero) if its smoothness indicator is below such threshold.

The $\alpha_j$ in (2.44) are modified as

$$\gamma_j = \left(1 + \frac{\tau_5}{\beta_j + \epsilon}\right)^6, \qquad \chi_j = \frac{\gamma_j}{\sum_{k=0}^{2} \gamma_k}, \qquad \alpha_j = \begin{cases} 0 & \text{if } \chi_j < C_T\,, \\ d_j & \text{otherwise.} \end{cases} \tag{2.47}$$

The cut-off parameter $C_T$ is taken as $10^{-4}$ in this work. It can also be determined using an adaptive procedure (Fu, Hu, *et al.* 2019). Other parts of the scheme are identical to the WENO-Z5.

### HLLC approximate Riemann solver

The HLLC Riemann solver (Toro *et al.* 1994) used in (2.37) is an extension to the earlier HLL solver (Harten, Lax, *et al.* 1983) by restoring the contact waves in the Riemann problem—hence "C" in its name. This modification improves the resolution for vortices, material interfaces, and entropy waves, which are important in turbulent reacting flows.

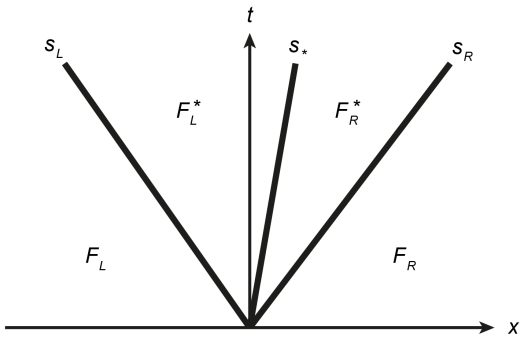



Figure 2.2: Wave system of the HLLC approximate Riemann solver. This figure shows the case where $\mathbf{F}_{i+\frac{1}{2}} = \mathbf{F}_L^*$.

The three waves[15] divide the domain into four parts, as illustrated in Figure 2.2. The flux at the centre ($x = 0$) is given by

$$\mathbf{F}_{i+\frac{1}{2}} = \begin{cases} \mathbf{F}(\mathbf{U}_{L,i+\frac{1}{2}})\,, & \text{if } 0 \le s_L\,, \\ \mathbf{F}_{*L}\,, & \text{if } s_L < 0 \le s_*\,, \\ \mathbf{F}_{*R}\,, & \text{if } s_* < 0 \le s_R\,, \\ \mathbf{F}(\mathbf{U}_{R,i+\frac{1}{2}})\,, & \text{if } s_R < 0\,, \end{cases} \tag{2.48}$$

where $s_L$, $s_*$, $s_R$ are the speeds of the three waves from left to right, estimated by

$$s_L = \min(u_L - c_L, u_R - c_R, \hat{u} - \hat{c})\,, \tag{2.49}$$

[15] In fact, the number of waves equals the number of variables ($N_s + 4$), but the centre waves all travel at the same speed, thus they can be treated collectively as one wave. Also note that the leftmost and rightmost waves can be shock waves or expansion fans, and the centre waves are contact surfaces.

$$s_R = \max(u_L + c_L, u_R + c_R, \hat{u} + \hat{c})\,, \tag{2.50}$$

$$s_* = \frac{p_R - p_L + \rho_L u_L(s_L - u_L) - \rho_R u_R(s_R - u_R)}{\rho_L(s_L - u_L) - \rho_R(s_R - u_R)}\,, \tag{2.51}$$

where $\hat{u}$ and $\hat{c}$ are the Roe-averaged normal velocity and speed of sound (see Appendix A). Note that the current wave speed estimates are slightly more dissipative but more robust than the originally proposed method.

The fluxes in the centre (star) regions are

$$\mathbf{F}_{*K} = \mathbf{F}(\mathbf{U}_{K,i+\frac{1}{2}}) + s_K(\mathbf{U}_{*K} - \mathbf{U}_{K,i+\frac{1}{2}}) \qquad \text{for } K = L, R\,, \tag{2.52}$$

$$\mathbf{U}_{*K} = \rho_K \frac{s_K - u_K}{s_K - s_*} \begin{bmatrix} Y_1 \\ \vdots \\ Y_{N_s} \\ s_* \\ v_K \\ w_K \\ e_K + (s_* - u_K)\left(s_* + \frac{p_K}{\rho_K(s_K - u_K)}\right) \end{bmatrix}, \tag{2.53}$$

where $v$ and $w$ are velocities in the transverse directions.

### Approximate characteristic projection

A major source of computation in the finite difference WENO/TENO scheme is transforming the variables between physical and characteristic spaces

$$\mathbf{W}_j = \mathbf{P}(\mathbf{U}_j; \theta_{i+\frac{1}{2}})\,, \qquad \mathbf{U}_j = \mathbf{P}^{-1}(\mathbf{W}_j; \theta_{i+\frac{1}{2}})\,, \tag{2.54}$$

where $\mathbf{U}_j$ and $\mathbf{W}_j$ are the physical and characteristic variables at point $j$; $\theta_{i+\frac{1}{2}} = \theta(\hat{\mathbf{U}}_{i+\frac{1}{2}})$ is the thermodynamic variable (speed of sound or specific heat ratio) evaluated using some interfacial averaged state $\hat{\mathbf{U}}_{i+\frac{1}{2}}$, constant across the stencil for all $j$; and $\mathbf{P}$ and $\mathbf{P}^{-1}$ are the forward (from physical to characteristic) and backward (from characteristic to physical) projection operators, respectively. This projection procedure decouples the Euler equations (inviscid part of the Navier-Stokes equations) into independent one-dimensional advection equations, and is crucial for numerical stability (see Appendix A).

At least eight projections (six forwards and two backwards) are needed per flux $\mathbf{F}_{i+\frac{1}{2}}$. A new approximation is proposed where the state variables are projected to their *local* characteristic space, before transforming back to physical space with an *interpolated* thermodynamic variable.

$$\mathbf{W}_j = \mathbf{P}(\mathbf{U}_j; \theta_j)\,, \tag{2.55}$$

$$\mathbf{U}_{K,i+\frac{1}{2}} = \mathbf{P}^{-1}\left(\mathbf{W}_{K,i+\frac{1}{2}}, \theta_{K,i+\frac{1}{2}}\right) \qquad \text{for } K = L, R\,. \tag{2.56}$$

Note that in the forward step, the interfacial $\theta_{i+\frac{1}{2}}$ is replaced by the local $\theta_j$, while the interfacial $\theta_{K,i+\frac{1}{2}}$ in the backward step is interpolated the same way as the characteristic variables in (2.34)–(2.35):

$$\theta_{L,i+\frac{1}{2}} = Interp(\theta_{i+2}, ..., \theta_{i-2}) \,, \qquad \theta_{R,i+\frac{1}{2}} = Interp(\theta_{i-1}, ..., \theta_{i+3}) \,. \tag{2.57}$$

As a result, only three characteristic projections (one forwards and two backwards) are performed per flux evaluation, significantly reducing computational cost. The method of manufactured solutions (subsection 2.4.1) confirms that this approximation preserves the order of accuracy of the original scheme in smooth regions.

### 2.3.2 Central difference for diffusive fluxes

Central difference schemes are used to discretise the diffusive fluxes at the cell interface. Two types of derivative operators are required: normal derivatives, taken perpendicular to the cell face on which they are evaluated, and transverse derivatives, taken tangent to the cell face. In this subsection, the schemes will be described in two dimensions, $x$ and $y$, with two subscripts denoting the indices of the grid point in the two directions.

#### Second order

Second-order normal derivative of $\phi$ is computed by

$$\left.\frac{\partial \phi}{\partial x}\right|_{i+\frac{1}{2},j} = \frac{\phi_{i+1,j} - \phi_{i,j}}{\Delta x} \,. \tag{2.58}$$

And the transverse derivative is computed by

$$\left.\frac{\partial \phi}{\partial y}\right|_{i+\frac{1}{2},j} = \frac{\phi_{i,j+1} - \phi_{i,j-1} + \phi_{i+1,j+1} - \phi_{i+1,j-1}}{4\Delta y} \,. \tag{2.59}$$

#### Fourth order

As discussed in (2.31), since the flux derivative is only second-order accurate, care must be taken to ensure that applying (2.29) to the fluxes yields a fourth-order approximation of the second derivatives at the cell centre,

$$\frac{1}{\Delta x}\left( \left.\frac{\partial \phi}{\partial x}\right|_{i+\frac{1}{2},j} - \left.\frac{\partial \phi}{\partial x}\right|_{i-\frac{1}{2},j} \right) = \left.\frac{\partial^2 \phi}{\partial x^2}\right|_{i,j} + O(\Delta x^4) \,. \tag{2.60}$$

This implies that even though the local fluxes may not be a good (high-order) approximation to the interfacial first derivatives, the overall scheme is fourth-order accurate.

For instance, the first derivative at the cell interface

$$\left.\frac{\partial\phi}{\partial x}\right|_{i+\frac{1}{2},j} = \frac{-\phi_{i+2,j} + 15\phi_{i+1,j} - 15\phi_{i,j} + \phi_{i-1,j}}{12\Delta x} \tag{2.61}$$

will yield an overall fourth-order second derivative at the cell centre

$$\begin{aligned}\frac{1}{\Delta x}\left( \left.\frac{\partial\phi}{\partial x}\right|_{i+\frac{1}{2},j} - \left.\frac{\partial\phi}{\partial x}\right|_{i-\frac{1}{2},j} \right) &= \frac{-\phi_{i+2,j} + 16\phi_{i+1,j} - 30\phi_{i,j} + 16\phi_{i-1,j} - \phi_{i-2,j}}{12\Delta x^2} \\ &= \left.\frac{\partial^2\phi}{\partial x^2}\right|_{i,j} + O(\Delta x^4)\,.\end{aligned} \tag{2.62}$$

Similarly, the transverse derivative is constructed by

$$\left.\frac{\partial\phi}{\partial y}\right|_{i+\frac{1}{2},j} = \frac{-\phi_y|_{i+2,j} + 7\phi_y|_{i+1,j} + 7\phi_y|_{i,j} - \phi_y|_{i-1,j}}{12}\,, \tag{2.63}$$

where

$$\phi_y|_{i+k,j} = \left.\frac{\partial\phi}{\partial y}\right|_{i+k,j} = \frac{-\phi_{i+k,j+2} + 8\phi_{i+k,j+1} - 8\phi_{i+k,j-1} + \phi_{i+kj-2}}{12\Delta y}\,. \tag{2.64}$$

With some algebra, using the Python script provided in Appendix B, it can be shown that the above schemes deliver the promised order of accuracy:

$$\frac{\phi_x|_{i+\frac{1}{2},j} - \phi_x|_{i-\frac{1}{2},j}}{\Delta x} = \left.\frac{\partial^2\phi}{\partial x^2}\right|_{i,j} - \frac{\Delta x^4}{90}\left.\frac{\partial^6\phi}{\partial x^6}\right|_{i,j} + ... \tag{2.65}$$

$$\frac{\phi_y|_{i+\frac{1}{2},j} - \phi_y|_{i-\frac{1}{2},j}}{\Delta x} = \left.\frac{\partial^2\phi}{\partial x\partial y}\right|_{i,j} - \frac{\Delta x^4}{30}\left.\frac{\partial^6\phi}{\partial x^5\partial y}\right|_{i,j} - \frac{\Delta y^4}{30}\left.\frac{\partial^6\phi}{\partial x\partial y^5}\right|_{i,j} + ... \tag{2.66}$$

### 2.3.3 Time integration

Time integration is performed in an operator-splitting manner. The hydrodynamic and viscous terms are integrated using a second-order Runge-Kutta (predictor-corrector) scheme, and the chemical source term is integrated implicitly using the CVODE (Hindmarsh *et al.* 2005):

$$\mathbf{U}^* = \mathbf{U}^t + \left(\mathbf{RHS}(\mathbf{U}^t) + \mathbf{S}(\mathbf{U}^t)\right)\Delta t\,, \tag{2.67}$$

$$\mathbf{U}^{**} = \mathbf{U}^t + \left(\mathbf{RHS}(\mathbf{U}^t) + \mathbf{RHS}(\mathbf{U}^*)\right)\frac{\Delta t}{2}\,, \tag{2.68}$$

$$\mathbf{U}^{t+1} = \mathbf{U}^{**} + \mathbf{S}(\mathbf{U}^{t+1})\Delta t\,. \tag{2.69}$$

Note that $\mathbf{S}(\mathbf{U}^{t+1})$ can be stored and reused as $\mathbf{S}(\mathbf{U}^t)$ of the "next" time step. Therefore, the computationally expensive evaluation of $\mathbf{S}$ is carried out only once per time step.

The explicit integration scheme is stable subject to the Courant-Friedrichs-Lewy (CFL) condition for convection

$$\Delta t \leq \min \left[ \frac{C \Delta x_i}{|u_i| + c} \right] , \tag{2.70}$$

and the Fourier condition for diffusion

$$\Delta t \leq \min \left[ \frac{\rho \Delta x_i^2}{2 \max(\mu, \kappa / c_v)} \right] . \tag{2.71}$$

The minimum is taken in all spatial directions and across the entire domain. A CFL number of $C = 0.3$ is typically used. Note that due to the implicit chemical integration, the time step size of the simulation is not limited by the chemical timescale which can be extremely small for stiff reaction mechanisms.

### 2.3.4 Adaptive mesh refinement

The solver developed in this work, Cerisse (Navarro-Martinez, Un, *et al.* 2025), is built upon the block-structured adaptive mesh refinement (AMR) framework AMReX (Zhang *et al.* 2019). Following the algorithm of Berger and Oliger 1984, the computational mesh consists of a hierarchy of nested levels, where the finer levels are subsets of the coarser ones. Each level is formed by a union of rectangular boxes. The coarsest level (level 0) covers the entire computational domain, and each subsequent level is refined by an integer refinement factor $R$ in each direction, typically set to 2. A typical block-structured AMR mesh is illustrated in Figure 2.3.

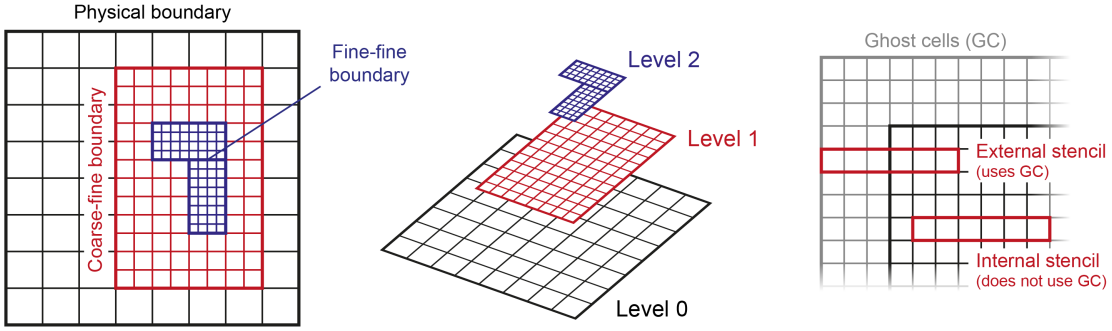



Figure 2.3: An example block-structured AMR mesh and ghost cells.

#### Boundary conditions

Boundary conditions at the box edge are imposed using a set of ghost cells located outside of the box, such that the numerical schemes maintain a full stencil support. Three ghost points are required for the fifth-order scheme used in this work.

There are three possible types of boundaries at a box's edges:

- Physical boundaries, which are the boundaries of the computational domain: ghost cells are filled according to user-defined boundary conditions.
- Fine-fine boundaries, which separate adjacent boxes of the same level: ghost cells are simply taken from the adjacent box.
- Coarse-fine boundaries, which are the boundaries of the current level: (fine) ghost cells are interpolated from the data of the coarser level. A total variation diminishing (TVD) limiter can be used to ensure that the interpolation process does not create new extrema. The limiter can be applied to each conservative variable separately, or by using the most restrictive one across all variables. The latter approach is preferred as it is more robust, despite more dissipative.

**Subcycling and refluxing**

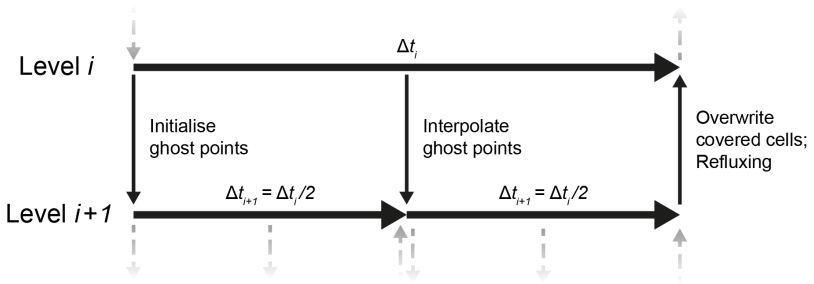



Figure 2.4: Coupling procedure during a time step between two AMR levels.

After filling in the ghost cells, each level can be advanced independently. However, since the finer level has a cell size $R$-times smaller than the coarser level, the time step size is also $R$-times smaller (the problems investigated in this work are mostly restricted by the inviscid CFL condition). A V-cycle update is performed:

1. Advance level $i$ for $\Delta t_i$, where $\Delta t_i$ denotes the time step size of level $i$;
2. Advance level $i+1$ for $\Delta t_{i+1} = \Delta t_i / R$;
3. Fill level $i+1$ coarse-fine boundaries by spatial-temporal interpolation of level $i$ data;
4. Advance level $i+1$ for another $\Delta t_{i+1}$;
5. Overwrite level $i$ cells which are covered by the finer level with the averaged solution at level $i+1$ ("average down") and correct level $i$ solution based on the fluxes of both levels ("refluxing").

It is important to note that the flux across the coarse-fine boundaries differs when calculated on the coarse or the fine level. A flux correction step, known as "refluxing" is needed at the end of each coarse time step to restore conservation.

### Geometry handling

The cut-cell embedded boundary (EB) method is used to represent complex geometries on the Cartesian mesh. Flux divergence is computed with the cell faces scaled by their area—essentially a finite volume method, thus, conservation is guaranteed. A two-dimensional case is illustrated in Figure 2.5, whose semi-discrete form is

$$\frac{\partial \mathbf{U}_{i,j}}{\partial t} = -\frac{\mathbf{F}_{i+\frac{1}{2},j}A_{i+\frac{1}{2},j} - \mathbf{F}_{i-\frac{1}{2},j}A_{i-\frac{1}{2},j} + \mathbf{F}_{i,j+\frac{1}{2}}A_{i,j+\frac{1}{2}} - \mathbf{F}_{i,j-\frac{1}{2}}A_{i,j-\frac{1}{2}} + \mathbf{F}_w A_w}{V_{i,j}}, \quad (2.72)$$

where $A$ is the area of the face and $V$ is the volume of the cell. The subscript $w$ denotes quantities of the EB wall.

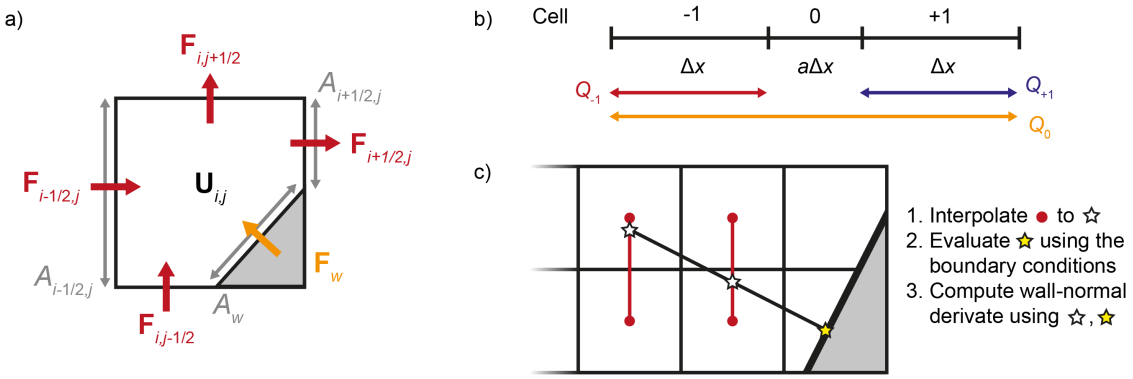



Figure 2.5: Illustrations of (a) fluxes in a EB cut cell, (b) neighbourhoods in the redistribution algorithm, and (c) stencil for EB wall-normal derivative.

A problem arises as the cut-cell volume appears in the denominator of the RHS. To remain stable, explicit time-stepping schemes require a time step size inversely proportional to the minimum cut-cell volume, which can be arbitrarily small. A redistribution procedure is carried out to distribute the excess update to neighbouring cells (Berger and Giuliani 2021).

For a simplified one-dimensional example, consider three cells $-1$, 0, $+1$ with volume fractions 1, $a$, 1, where the small cell $a < 1$ is in the middle. The updated states before redistribution are $\mathbf{U}_i^{\text{before}} = \mathbf{U}_i^t + \mathbf{RHS}_i^t \Delta t$. The redistribution process starts by constructing three "neighbourhoods", all of which have a volume fraction $\geq 1$ to avoid the small cell problem. They may overlap, which will be reflected in the coefficients later. The weighted average of the update in the merged neighbourhood 0 is

$$Q_0 = \frac{1}{\frac{\Delta x}{2} + a\Delta x + \frac{\Delta x}{2}} \left( \frac{\Delta x}{2}\mathbf{U}_{-1}^{\text{before}} + a\Delta x \mathbf{U}_0^{\text{before}} + \frac{\Delta x}{2}\mathbf{U}_{+1}^{\text{before}} \right). \quad (2.73)$$

The weights of $\mathbf{U}_{\pm 1}^{\text{before}}$ are divided by two because there are two neighbourhoods covering cells $\pm 1$. And the update in the unmerged neighbourhoods is unmodified, $Q_{\pm 1} = \mathbf{U}_{\pm 1}^{\text{before}}$.

Finally, the stabilised solutions are averaged across all neighbourhoods that cover the cell.

$$\mathbf{U}_0^{\text{redis}} = Q_0\,, \qquad \mathbf{U}_{\pm1}^{\text{redis}} = \frac{1}{2}(Q_{\pm1} + Q_0)\,, \tag{2.74}$$

because only one neighbourhood (0) covers cell 0, and two neighbourhoods ($\pm1$ and 0) cover cells $\pm1$.

It can be verified that this redistribution algorithm is conservative as the total states remain unchanged, *i.e.*,

$$\sum_{k=-1}^{1} V_k \mathbf{U}_k^{\text{redis}} = \sum_{k=-1}^{1} V_k \mathbf{U}_k^{\text{before}}\,. \tag{2.75}$$

Extensions to higher dimensions exist, although defining the neighbourhoods becomes complicated, see Berger and Giuliani 2021.

Wall-normal derivatives needed for obtaining $\mathbf{F}_w$ are computed using a stencil as depicted in Figure 2.5. The procedures follow Henry de Frahan, Rood, *et al.* 2023:

0. Consider the vertical and horizontal grid lines that connect all grid points and intersect at those points. Draw a normal line from the centroid of the EB surface. The first point where this line intersects a grid line is the first interpolation point, and the second intersection with another grid line is the second interpolation point.
1. Interpolate the variable for which the derivative is needed to these two interpolation points, using the two nearest grid points along the grid line.
2. Calculate the flow states at the wall centroid using the appropriate boundary conditions.
3. With the three points obtained from the previous steps, construct a quadratic function and compute its derivative at the wall. This will be second-order accurate.

This method can be extended to three dimensions by replacing grid lines with grid surfaces and using more neighbouring points for interpolation rather than two.

### Computational costs

The computational cost of an AMR simulation with $N_L + 1$ levels is estimated by the number of time steps multiplied by the number of grid points,

$$N_0 \sum_{n=0}^{N_L} \left(\frac{v}{\zeta} R^4\right)^n = N_0 \frac{1 - ((v/\zeta)R^4)^{N_L+1}}{1 - (v/\zeta)R^4}\,, \tag{2.76}$$

where $N_0$ is the number of grid points in level 0, $v$ is the volume fraction of a fine level in the coarser level, and $0 < \zeta < 1$ is the efficiency of the AMR algorithm. $v$ is assumed to be constant for all levels to simplify the analysis. To attain the same effective resolution

(grid size of the finest level), the computational cost of a single-level simulation is

$$N_0 R^{4N_L} \,. \tag{2.77}$$

For $R = 2$ and $N_L = 2$, the cost of an AMR simulation will be lower than a single-level simulation of the same effective resolution if $v/\zeta < 0.97$.

## 2.4 Solver verification and validation

Verification and validation are essential processes to ensure that the numerical solver is implemented correctly and is fit for further investigation and model development. This section presents four test cases, each designed to evaluate specific capabilities of the solver. All test cases are run with the TENO and HLLC for inviscid fluxes, and the fourth-order central difference for diffusive fluxes, unless otherwise specified.

### 2.4.1 Method of manufactured solutions

The method of manufactured solutions (MMS) is used to verify the order of accuracy of the solver. In MMS, a manufactured solution is first prescribed, and then a source term is constructed such that the solution satisfies the PDE in the numerical solver. Therefore, numerical error can be calculated as the difference between the manufactured solution and the numerical solution. Based on experience, MMS is particularly good at identifying implementation or algorithmic errors because the overall convergence rate is limited by the least accurate component—the shortest plank of the bucket.

In this case, the manufactured solution takes a periodic form of

$$\phi(x, y, z) = \phi_0 + \phi_x \sin(a_{\phi,x}\pi x/L) + \phi_y \cos(a_{\phi,y}\pi y/L) + \phi_z \sin(a_{\phi,z}\pi z/L)\,, \tag{2.78}$$

for $\phi = [\rho, u, v, w, p]$, where the parameters are given in Table 2.3. Constant diffusivities and specific heat are used to simplify the calculation. The MMS source term is computed as the residual after substituting the manufactured solution into the Navier-Stokes equations:

$$\mathbf{S}_{\text{MMS}} = \frac{\partial \mathbf{F}_j(\mathbf{U}_{\text{MMS}})}{\partial x_j} \,. \tag{2.79}$$

All simulations are run for 100 steps with a CFL number of 0.1, to prevent the error from being dominated by that of the time-stepping scheme (which is second order).

Figure 2.6 shows four settings: the left panel assesses the inviscid part of the solver. It achieves a fifth-order accuracy, the same as the underlying numerical scheme. The approximate characteristic transform (p. 48) is proven to maintain accuracy while reducing computational costs. The centre-left panel shows the full Navier-Stokes equations including

Table 2.3: MMS problem parameters

| Variable ($\phi$) | $\phi_0$ | $\phi_x/\phi_0$ | $\phi_y/\phi_0$ | $\phi_z/\phi_0$ | $a_{\phi,x}$ | $a_{\phi,y}$ | $a_{\phi,z}$ |
|---|---|---|---|---|---|---|---|
| $\rho$ | 1.161 | 0.1 | 0.15 | 0 | 2 | 4 | 0 |
| $u$ | 347.2 | 0.06 | -0.17 | 0 | 2 | 4 | 0 |
| $v$ | 451.4 | 0.06 | 0 | 0 | 4 | 2 | 0 |
| $w$ | 0 | 0 | 0 | 0 | 0 | 0 | 0 |
| $p$ | $1\times10^5$ | -0.3 | 0.2 | 0 | 2 | 4 | 0 |

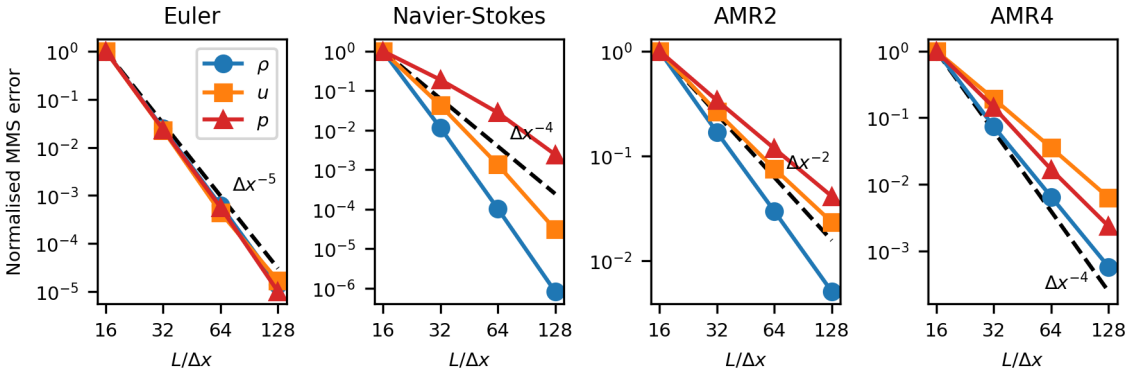



Figure 2.6: MMS error convergence. Left to right: Euler equations with M = 1; Navier-Stokes equations with M = 1, Re = 1, Pr = 0.72; Navier-Stokes equations with two AMR levels and with second- and fourth-order interpolation.

the viscous fluxes, with a Reynolds number set to 1 such that viscous and inviscid effects are equally important. It achieves approximately fourth-order accuracy as the grid refines. The right panels show an AMR solution with two coarse-fine boundary interpolation schemes, both of which are conservative but only the second-order one is TVD. In practice, the second-order scheme is used more often because of its robustness.

### 2.4.2 Isentropic vortex convection

This test case assesses the numerical dissipation of the scheme. An isentropic vortex is convected to the right by a mean flow. Since the problem is inviscid, the vortex magnitude and shape should stay constant, and hence, any discrepancy is caused by numerical dissipation. The initial conditions follow

$$\rho(x,y) = \rho_0\,, \tag{2.80}$$

$$u(x,y) = u_0\left(1 - \beta\frac{y}{R}\exp\left(\frac{-r^2}{2R^2}\right)\right)\,, \tag{2.81}$$

$$v(x,y) = u_0\beta\frac{x}{R}\exp\left(\frac{-r^2}{2R^2}\right)\,, \tag{2.82}$$

$$p(x,y) = p_0 - \frac{\rho_0 u_0^2\beta^2}{2}\exp\left(\frac{-r^2}{R^2}\right)\,, \tag{2.83}$$

where $\beta = 0.02$ is the vortex strength and $R = 0.5$ is its radius. $\rho_0 = 1.161\ \mathrm{kg\,m^{-3}}$, $u_0 = 17.36\ \mathrm{m\,s^{-1}}$, and $p_0 = 1 \times 10^5$ Pa correspond to a Mach number of 0.05.

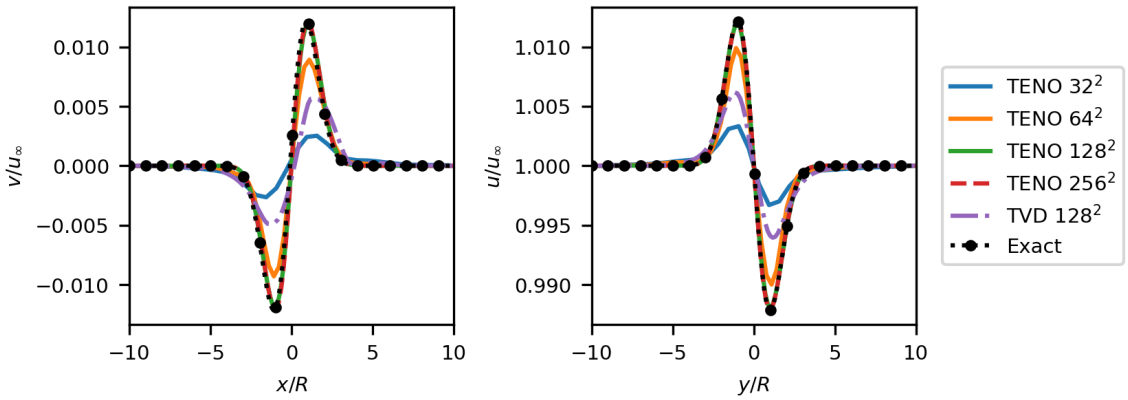



Figure 2.7: Vortex velocity profiles after five pass-through. The number of grid points is next to the scheme name.

Figure 2.7 shows that after five pass-throughs, the TENO scheme is still able to maintain the vortex shape, showing minimal numerical dissipation. In contrast, the second-order TVD scheme, which is widely used in compressible LES solvers, introduces excessive dissipation that its results on a $128^2$ grid are worse than TENO's on a $64^2$ grid. This will not only adversely affect the prediction of vortex dynamics, but may also mask out the effects of the turbulence model.

### 2.4.3 Laminar boundary layer

This test case is used to validate the diffusion fluxes and boundary conditions. A boundary layer develops on a flat no-slip plate, in a hypersonic free-stream of $M_\infty = 6.85$ and $Re_{\infty,L} = 5 \times 10^5$, where $L = 0.205$ m is the length of the plate. Viscosity is modelled using the Sutherland's law,

$$\mu = \mu_{\mathrm{ref}} \left( \frac{T}{T_{\mathrm{ref}}} \right)^{3/2} \frac{T_{\mathrm{ref}} - S}{T - S}, \tag{2.84}$$

where $T_{\mathrm{ref}} = T_\infty$ and $\mu_{\mathrm{ref}}$ is calculated from the free-stream Reynolds number. The Prandtl number is taken as 0.72.

An analytical solution can be obtained following Chapman and Rubesin 1949's extension of the Blasius boundary layer equation. The velocity and temperature profiles are self-similar about the transformation

$$\eta = \frac{u_e}{\sqrt{2\xi}} \int_0^y \frac{\rho(y')}{\rho_e} dy', \tag{2.85}$$

where $\xi = \mu_e \rho_e u_e x$, and the subscripts $e$ denote the conditions at the boundary layer edge.

Figure 2.8 shows the computational domains for the regular wall with anisotropic mesh ($\Delta x : \Delta y = 2 : 1$), the EB wall with isotropic mesh (EB does not support anisotropic

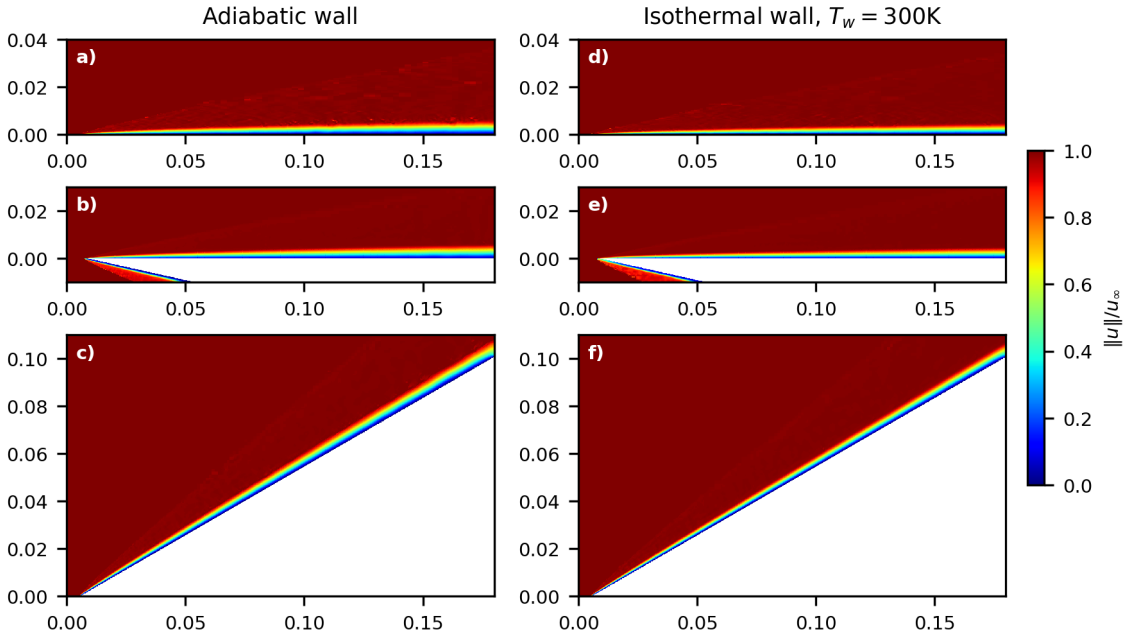



Figure 2.8: Velocity magnitude over a flat plate: (a, d) regular wall, (b, e) EB wall, and (c, f) inclined EB wall.

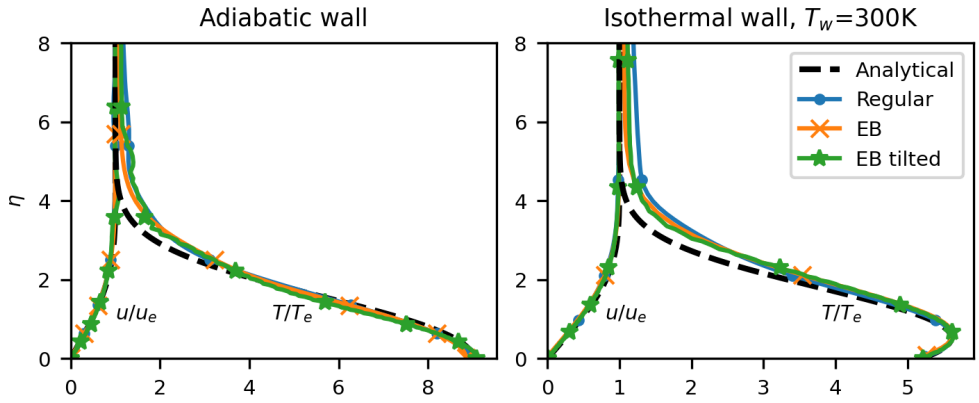



Figure 2.9: Boundary layer velocity and temperature profiles compared to self-similar solution.

mesh currently), and the EB wall inclined by 30°. Wall-parallel velocity and temperature profiles are taken 0.14 m downstream of the leading edge of the plate, and are plotted in Figure 2.9. All three setups show good agreement with each other and with the analytical solution. The recovery temperature is predicted correctly, despite some mismatch in the temperature profile away from the wall, possibly due to the weak shock wave formed on the leading edge of the plate.

### 2.4.4 Reactive shock tube

The test case of Fedkiw *et al.* 1997 is used to validate the reaction routine and to test the solver's stability near discontinuities.

A shock tube of length $L = 0.12$ m is filled with a homogeneous mixture of $X_{\mathrm{H_2}} : X_{\mathrm{O_2}} : X_{\mathrm{Ar}} = 2 : 1 : 7$ and is initialised with

$$(\rho, u, p) = \begin{cases} 0.072\ \mathrm{kg\,m^{-3}}, 0\ \mathrm{m\,s^{-1}}, 7173\ \mathrm{Pa} & \text{if } x < L/2\,, \\ 0.18075\ \mathrm{kg\,m^{-3}}, -48.734\ \mathrm{m\,s^{-1}}, 35594\ \mathrm{Pa} & \text{otherwise}\,. \end{cases} \tag{2.86}$$

The left boundary is a solid wall, and the right is an inflow. The 9-species 37-reaction chemical mechanism of Fedkiw *et al.* 1997 is used, apart from the third-body collision efficiency of $\mathrm{H_2}$, which is modified to a more reasonable value of 2 from 100, similar to that in Yetter *et al.* 1991; Ó Conaire *et al.* 2004; Zettervall and Fureby 2018.

The left-running shock, with a post-shock temperature of 686 K, is initially unable to ignite the mixture. However, as it reflects off the left wall, both the temperature and pressure rise rapidly, leading to successful ignition. The flame then propagates to the right until it catches up with the shock, forming a detonation wave.

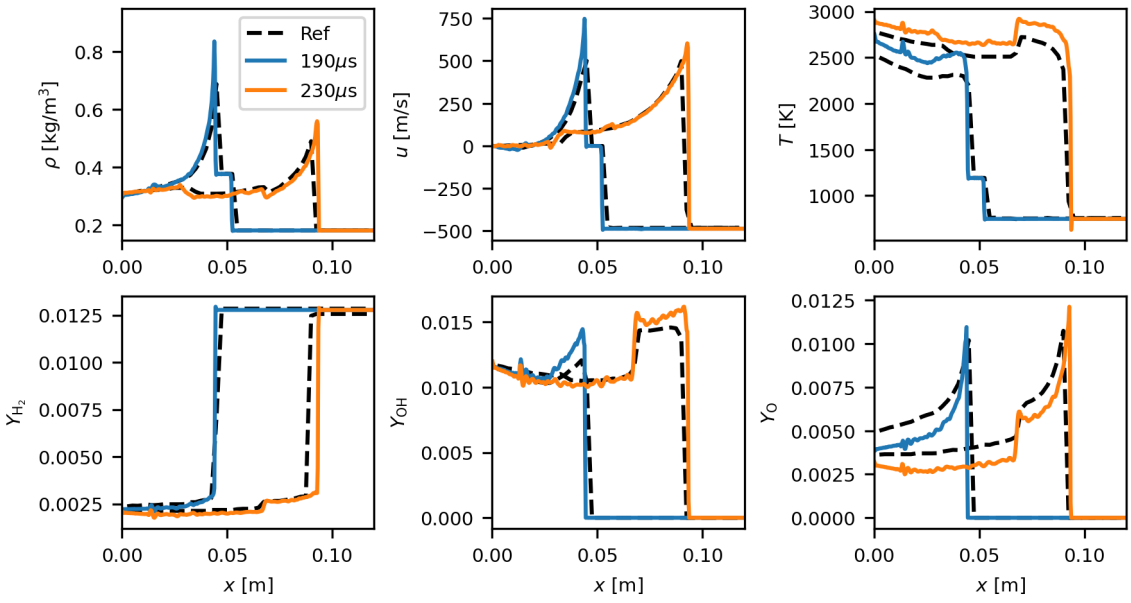



Figure 2.10: Reactive shock tube solution at $t = 190$ $\mu$s and $t = 230$ $\mu$s, compared with the reference solution (Fedkiw *et al.* 1997).

Solution at two time snapshots are plotted in Figure 2.10, both showing good alignment with the reference solution. The wave speeds are accurately predicted, and the mass fractions (which infer reaction rates) are correct even for minor species such as OH. However, some small discrepancies are observed in the post-shock temperature and $Y_{\mathrm{O}}$, possibly due to the less dissipative numerical schemes used in this work. The solver is able to capture

discontinuities, including the shock wave, reaction wave, and contact surface, with great sharpness, and the solution is free from excessive oscillations. AMR also contributes to the improved resolution of discontinuities, with three levels added around regions of high density gradient ($\|\nabla\rho\| > 10$ kg m$^{-4}$ for the first two levels, and $\|\nabla\rho\| > 100$ kg m$^{-4}$ for the third level).

### 2.4.5 Performance scaling

The parallel efficiency of the solver is checked using the Taylor-Green vortex case with M = 1.25 and Re = 1600 (see subsection 3.4.2 for the problem description). The numerical schemes used are the same as previous subsections, with no AMR applied.

The strong scaling test is performed on a single node of Imperial's CX3 (Phase 1) HPC. Each node is equipped with two AMD EPYC 7742 CPUs (128 cores in total) and up to 1TB of RAM. The solver is compiled with the GCC compiler and Intel MPI. Simulations are run on a $128^3$ grid with a CFL number of 0.3.

The weak scaling test uses up to eight nodes on the ARCHER2 HPC, which features the same CPU as CX3. In this case, the solver is compiled with the GCC compiler and MPICH. The initial grid size is $256^3$, and a constant $\Delta t$ of $1.5\times10^8$ is used. Each time the number of nodes is doubled, the number of grid points along one axis is also doubled to keep the number of grid points per node constant.

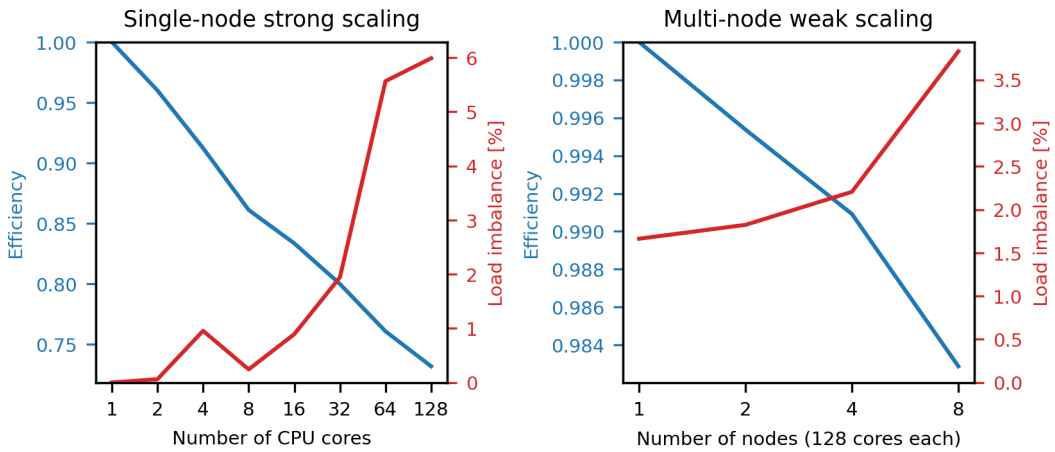



Figure 2.11: Strong and weak scaling on CPUs.

Figure 2.11 shows that the strong-scaling efficiency reduces as the number of CPUs increases. This is mainly due to an increase in load imbalance, measured by the difference in runtime between the fastest and slowest CPUs, normalised by the average. To maintain an efficiency of above 80%, each CPU should ideally manage approximately 60,000 grid points. For multi-node weak scaling, the solver is able to maintain an impressive 98% efficiency with 8 nodes (1,024 cores), and the load imbalance is low. This shows that the solver is efficient in performing large-scale simulations on modern HPC systems.

Note that the current scaling study excludes reaction and AMR, as they may potentially affect load balancing, making it difficult to obtain a fair comparison between problem sizes. Nevertheless, these results provide a useful indication of the parallel efficiency of the solver, as convection-diffusion constitutes the majority of the runtime. In practice, the time spent on each part of the solver is problem- and settings-dependent. For example, in the ramjet case presented in chapter 6, approximately 50% of the time is used for convection-diffusion, 30% for reaction, and 20% for AMR, MPI, and other operations.

The current code is also portable to GPU systems without modification, though this is outside of the scope of this thesis. Interested readers can refer to the documentation in the code repository (Navarro-Martinez, Un, *et al.* 2025) for further information.

## 2.5 Summary

This chapter presented the preliminaries of the project. It introduced the Navier-Stokes equations as the mathematical framework for simulating compressible reacting flows. The challenges posed by the computational costs of performing direct numerical simulation (DNS) were discussed, and large eddy simulation (LES) was presented as a practical approach for studying high-Re engineering applications. The closure problem associated with LES and various modelling efforts were explained.

Next, the numerical methods were presented, which include a high-order TENO scheme and the HLLC Riemann solver that preserve sharp contact interfaces. A novel approximate characteristic transformation procedure was also proposed that significantly reduces computational costs without sacrificing the order of accuracy. The diffusive fluxes were discretised using a fourth-order central difference scheme, which is formulated in flux form for the adaptive mesh refinement (AMR) refluxing procedure. The computational mesh is automatically refined around regions of interest, reducing the costs while preserving accuracy and conservation properties. Complex geometries are represented using the cut-cell embedded boundary (EB) method.

The governing equations and numerical schemes were verified and validated through five benchmark test cases. The method of manufactured solutions (MMS) confirmed the expected order of accuracy, the isentropic vortex demonstrated low numerical dissipation, while the laminar boundary layer validated the viscous fluxes and the EB wall derivatives, and the reacting shock tube validated both the reaction calculations and the robustness of the numerical schemes in the presence of discontinuities. Finally, the strong and weak scaling tests highlighted the parallel performance of the solver, suitable for performing large-scale simulations on modern HPC systems.

# Chapter 3

# Joint-velocity-scalar Eulerian stochastic fields

This chapter introduces the joint-velocity-scalar probability density function (VSPDF) and the Eulerian stochastic fields (SF) approach for closing the sub-grid turbulence interactions in large eddy simulations (LES). Coupling with adaptive mesh refinement (AMR), the resultant SF-AMR strategy represents the first such implementation in the literature and serves as an effective tool for simulating high-speed reacting flows.

## 3.1 Probability density function method

The probability density function (PDF) method, also known as the filtered density function (FDF) method in LES, was first applied to turbulence modelling in the mid-twentieth century (Hawthorne *et al.* 1948; Corrsin 1958). Lundgren 1967, 1969 and Monin 1967 derived the transport equation for velocity PDFs. Later, Dopazo and O'Brien 1974; Dopazo 1975, 1976 developed a joint-scalar PDF for reacting flows. At this stage, the PDF transport equation is solved either by assuming a specific distribution shape or using the finite difference method (Janicka *et al.* 1978). The seminal works of Pope 1976, 1985 shaped the PDF method in its modern form by using the Monte Carlo method to solve the PDF transport equation. This allows the PDF method to be applied to more complex flow fields and detailed chemical mechanisms. A comprehensive review of the subsequent developments is provided by Haworth 2010. Interesting discussions can be found in O'Brien 1980; Pope 2000; Heinz 2003.

Recall that in LES, a spatial filter $G$ is used to remove scales smaller than a filter width $\Delta$. The filtered field is defined in (2.16), as

$$\overline{\phi}(\mathbf{x},t) = \int_{-\infty}^{\infty} \phi(\mathbf{x}',t) G(\mathbf{x}'-\mathbf{x};\Delta)\,\mathrm{d}^3\mathbf{x}' \,. \tag{3.1}$$

The sub-grid one-point PDF $f(\boldsymbol{\varphi}; \mathbf{x}, t)$ is defined by filtering the Dirac delta function:

$$f(\boldsymbol{\varphi}; \mathbf{x}, t) = \overline{\prod_{m=1}^{N_V} \delta(\phi_m(\mathbf{x}, t) - \varphi_m)}\,. \tag{3.2}$$

It provides the likelihood of finding a point $\mathbf{x}'$, which flow state is $\boldsymbol{\phi}(\mathbf{x}', t) = \boldsymbol{\varphi}$, within $\Delta$ around the point $\mathbf{x}$ at time $t$. The set of $N_V$ variables $\boldsymbol{\varphi}$ is said to be in the sample space of the flow state vector $\boldsymbol{\phi}$. To ensure that $f$ behaves like a PDF, the LES filter function must be positive and normalises to one, as discussed in section 2.2. If the box filter (2.17) is used, the PDF can be viewed as a joint histogram of the DNS flow states within a LES cell. When the histogram's bin width approaches zero, it transforms into a continuous probability distribution.

The filtering operation can be rewritten as the expected value

$$\overline{Q(\boldsymbol{\phi}(\mathbf{x}, t))} = \int_{-\infty}^{\infty} Q(\boldsymbol{\varphi}) f(\boldsymbol{\varphi}; \mathbf{x}, t)\, \mathrm{d}\boldsymbol{\varphi}\,, \tag{3.3}$$

where $Q$ is an arbitrary function. The above expression is closed if $f$ is known and if $Q$ can be fully described by the variables within the sample space of the PDF. For example, the highly non-linear chemical source term $\overline{\rho S_\alpha(\mathbf{Y}, T)}$ is closed if we know a joint PDF whose sample space covers $\rho$, $\mathbf{Y}$, and $T$.[1] If the PDF extends to cover velocities $\mathbf{u}$ as well, all filtered transport terms, $\widetilde{u_i u_j}$, $\widetilde{u_i Y_\alpha}$, $\widetilde{u_i E}$, source terms, and potentially non-ideal equation of state effects, can be closed without approximation, leading to a unified modelling framework for all turbulence interactions. This motivates the use of the VSPDF.

For variable density flows, the mass density function (MDF) is defined as

$$F(\boldsymbol{\varphi}; \mathbf{x}, t) = \overline{\rho(\mathbf{x}, t) \prod_{m=1}^{N_V} \delta(\phi_m(\mathbf{x}, t) - \varphi_m)}\,. \tag{3.4}$$

whose expectation gives the Favre-filtered quantity

$$\overline{\rho(\mathbf{x}, t)}\,\widetilde{Q(\boldsymbol{\phi}(\mathbf{x}, t))} = \int_{-\infty}^{\infty} Q(\boldsymbol{\varphi}) F(\boldsymbol{\varphi}; \mathbf{x}, t)\, \mathrm{d}\boldsymbol{\varphi}\,, \tag{3.5}$$

Hereafter, the dependencies on space and time will be omitted for brevity.

[1] Any internal thermodynamic quantities, such as $T$, $p$, $e$, or $h$, could serve the purpose, as they are connected by the equation of state.

### 3.1.1 PDF transport equation

For a MDF with sample space $\boldsymbol{\phi} = [\rho, \mathbf{Y}, \mathbf{u}, E]$ and $\boldsymbol{\varphi} = [r, \boldsymbol{\Upsilon}, \mathbf{v}, \mathcal{E}]$, the transport equation is derived in Appendix C as

$$\begin{aligned}\frac{\partial F}{\partial t} + \frac{\partial v_j F}{\partial x_j} = &-\frac{\partial}{\partial r}\left[\left(-\overline{\rho\frac{\partial u_j}{\partial x_j}\middle|\boldsymbol{\phi}}\right)F\right] - \frac{\partial}{\partial \Upsilon_\alpha}\left[\left(-\overline{\frac{1}{\rho}\frac{\partial J_{\alpha,j}}{\partial x_j}\middle|\boldsymbol{\phi}} + S_\alpha(\boldsymbol{\varphi})\right)F\right] \\ &-\frac{\partial}{\partial v_i}\left[\left(-\overline{\frac{1}{\rho}\frac{\partial p}{\partial x_i}\middle|\boldsymbol{\phi}} + \overline{\frac{1}{\rho}\frac{\partial \tau_{ij}}{\partial x_j}\middle|\boldsymbol{\phi}}\right)F\right] \\ &-\frac{\partial}{\partial \mathcal{E}}\left[\left(-\overline{\frac{1}{\rho}\frac{\partial q_j}{\partial x_j}\middle|\boldsymbol{\phi}} - \overline{\frac{1}{\rho}\frac{\partial p u_j}{\partial x_j}\middle|\boldsymbol{\phi}} + \overline{\frac{1}{\rho}\frac{\partial \tau_{ij} u_i}{\partial x_j}\middle|\boldsymbol{\phi}}\right)F\right].\end{aligned} \tag{3.6}$$

Note that the chemical source term $S_\alpha$ appears in closed form, without requiring knowledge about the combustion regime, flame structure, or the level of turbulence and compressibility. This makes the PDF method more general and widely applicable than other TCI models. The turbulent transport terms are also closed as they do not appear in the transport equation.

### 3.1.2 Closure models

However, the conditional filtered terms $\overline{Q\,|\,\boldsymbol{\phi}}$ are unclosed and require modelling. This is because they involve spatial derivatives that require two-point correlations that are not present in the one-point PDF. Note that spatial derivatives of statistical moments, such as mean and variance, are available. For example, although the conditional filtered velocity gradient is not closed, the filtered velocity gradient (which is the same as the gradient of the filtered velocity) is closed when using a one-point PDF.

In the literature (*e.g.* Pope 1985; Fox 2003; Heinz 2003; Haworth 2010), the unclosed conditional filtered terms are decomposed into a mean (filtered) component which is deterministic, and a fluctuating component which is stochastic and is modelled:

$$\overline{Q\,|\,\boldsymbol{\phi}} = \widetilde{Q} + \overline{Q''\,|\,\boldsymbol{\phi}} = \widetilde{Q} + \mathcal{M}\,. \tag{3.7}$$

For instance, the generalised Langevin model (GLM) by Haworth and Pope 1986 approximates the velocity-related terms as

$$\begin{aligned}-\frac{\partial}{\partial v_i}\left[\left(-\overline{\frac{1}{\rho}\frac{\partial p}{\partial x_i}\middle|\boldsymbol{\phi}} + \overline{\frac{1}{\rho}\frac{\partial \tau_{ij}}{\partial x_j}\middle|\boldsymbol{\phi}}\right)F\right] = &-\frac{\partial}{\partial v_i}\left[\left(-\overline{\frac{1}{\rho}\frac{\partial p}{\partial x_i}} + \overline{\frac{1}{\rho}\frac{\partial \tau_{ij}}{\partial x_j}}\right)F\right] \\ &-\frac{\partial}{\partial v_i}\left(G_{ij}(v_j - \tilde{u}_j)F\right) + \frac{\partial^2}{\partial v_i \partial v_i}\left(\frac{1}{2}C_0\epsilon_{\mathrm{sgs}}F\right).\end{aligned} \tag{3.8}$$

The second term on the right-hand side is the drift term, which reduces sub-grid variance and represents the effect of sub-grid mixing. The following term is diffusion in the PDF space, which increases sub-grid variance and drives the PDF towards a Gaussian distribution. It corresponds to two effects: sub-grid turbulent diffusion at the resolved scale, analogous to how random walk of microscopic particles leads to diffusion in macroscopic scale (Einstein 1905), and returning to normality as a consequence of the central limit theorem.

If we assume small-scale isotropy[2], the GLM reduces to the simplified Langevin model (SLM),

$$G_{ij} = -\frac{1}{\tau_{\text{sgs}}}\left(\frac{1}{2} + \frac{3}{4}C_0\right)\delta_{ij}\,, \tag{3.9}$$

where the sub-grid time scale $\tau_{\text{sgs}} = k_{\text{sgs}}/\epsilon_{\text{sgs}}$ is the ratio between sub-grid kinetic energy ($k_{\text{sgs}}$) and its dissipation rate ($\epsilon_{\text{sgs}}$). $\delta_{ij}$ is the Kronecker delta, $= 1$ if $i = j$ and $= 0$ otherwise. The parameter $C_0$ controls the rate of return to isotropy (see Equation 4.5), which is set to 2.1 following Haworth and Pope 1986, despite Pope and Chen 1990 suggesting that $C_0$ may be Re-dependent. While $k_{\text{sgs}}$ is readily available from the PDF, the sub-grid dissipation requires modelling:

$$k_{\text{sgs}} = \frac{1}{2}\widetilde{u_i'' u_i''}\,, \qquad \epsilon_{\text{sgs}} = C_\epsilon\left(1 + \mathrm{M}_{\text{sgs}}^2\right)\frac{k_{\text{sgs}}^{3/2}}{\Delta}\,. \tag{3.10}$$

The model for $\epsilon_{\text{sgs}}$ is based on the well-known result from dimensional analysis that $\epsilon_{\text{sgs}} \propto U^3/\ell$, independent of $\nu$ at high Re (Vassilicos 2015). Here, $U^2$ is the turbulent kinetic energy, $\ell$ is the integral length scale, and $\nu = \mu/\rho$ is the kinematic viscosity. The model's dependence on the sub-grid Mach number $\mathrm{M}_{\text{sgs}} = \sqrt{2k_{\text{sgs}}}/\overline{c}$ accounts for the dilatational dissipation effect in compressible turbulence (Zeman 1991; Delarue and Pope 1997), where $c$ is the local speed of sound. Note that other Mach number scalings of dilatational dissipation have been proposed, for instance, Ristorcelli 1997 argues that the correction should $\propto \mathrm{M}_{\text{sgs}}^4/\mathrm{Re}$. In practice, $\mathrm{M}_{\text{sgs}}$ is usually small ($< 0.3$) even if the mean flow is supersonic, see subsection 6.2.3 for an example, and all dissipation models give similar values of $\epsilon_{\text{sgs}}$. The model coefficient is taken as $C_\epsilon = 1.05$ following Almeida 2019, which is also close to the value of $C_\epsilon = 1$ used by Gicquel *et al.* 2002; Sheikhi *et al.* 2007. Note that the filter-width $\Delta$ enters the PDF model indirectly through $\epsilon_{\text{sgs}}$, unlike conventional SGS models where $\Delta$ enters the filtered scale directly through the sub-grid turbulent viscosity.

The scalar-related conditional filtered terms are modelled similarly, using the interaction-

[2]When the PDF method was originally developed for RANS (Reynolds-averaged Navier-Stokes), much effort has been devoted to developing complex models that account for the anisotropy of the Reynolds stress. However, in LES, it is argued that the resolved large eddies capture most of the flow anisotropy, and the sub-grid scales are closer to the isotropy assumption. This will be discussed further in chapter 5 concerning near-wall models.

by-exchange-with-the-mean (IEM) model[3] (Dopazo 1975):

$$-\frac{\partial}{\partial \Upsilon_\alpha}\left[-\overline{\frac{1}{\rho}\frac{\partial J_{\alpha,j}}{\partial x_j}\middle|\boldsymbol{\phi}}\,F\right] = -\frac{\partial}{\partial \Upsilon_\alpha}\left[-\overline{\frac{1}{\rho}\frac{\partial J_{\alpha,j}}{\partial x_j}}\,F\right] - \frac{\partial}{\partial \Upsilon_\alpha}\left(\frac{C_Y}{\tau_{\text{sgs}}}(\tilde{Y}_\alpha - \Upsilon_\alpha)F\right), \quad (3.11)$$

$$-\frac{\partial}{\partial \mathcal{E}}\left[\left(-\overline{\frac{1}{\rho}\frac{\partial q_j}{\partial x_j}\middle|\boldsymbol{\phi}} - \overline{\frac{1}{\rho}\frac{\partial p u_j}{\partial x_j}\middle|\boldsymbol{\phi}} + \overline{\frac{1}{\rho}\frac{\partial \tau_{ij}u_i}{\partial x_j}\middle|\boldsymbol{\phi}}\right)F\right]$$
$$= -\frac{\partial}{\partial \mathcal{E}}\left[\left(-\overline{\frac{1}{\rho}\frac{\partial q_j}{\partial x_j}} - \overline{\frac{1}{\rho}\frac{\partial p u_j}{\partial x_j}} + \overline{\frac{1}{\rho}\frac{\partial \tau_{ij}u_i}{\partial x_j}}\right)F\right] - \frac{\partial}{\partial \mathcal{E}}\left(\frac{C_E}{\tau_{\text{sgs}}}(\tilde{E} - \mathcal{E})F\right). \quad (3.12)$$

It is assumed that mixing at sub-grid level is dominated by small eddies (equivalent to assuming $\text{Re} \gg 1$), the mixing time scales for all scalars are therefore all the same, equal to the turbulence timescale, $C_Y = C_E = 1$. Note that the diffusion term is not added to species mass fractions and energy.

## 3.2 Eulerian stochastic fields

Due to the high dimensionality of the PDF sample space (1 density + 3 velocities + 1 energy + $N_s$ species), the transport equation is computationally expensive to solve with mesh-based numerical methods, such as finite difference, finite volume, or finite element.

Two classes of solutions are typically used. Deterministic approaches such as the quadrature method of moments solves the transport equations of a truncated set of moments (Tang *et al.* 2007; Donde *et al.* 2012; Koo *et al.* 2013). The deterministic nature makes this approach free from stochastic sampling errors, but it still suffers from the curse of dimensionality unless assumptions are made about the independence of certain PDF variables, which is common. Also, special treatment is often required to prevent the problem from becoming singular.

On the other hand, the Monte Carlo approach approximates the PDF by an ensemble of $N_f$ realisations, such that statistical moments are captured. It is more robust and the approximation converges with $N_f^{-1/2}$, independent of the problem dimension (Kloeden and Platen 1992). Early literature (*e.g.* Pope 1985; Haworth and Pope 1986; Delarue and Pope 1997) uses an ensemble of Lagrangian particles, each having a position, velocity, and the PDF states, and follows a set of stochastic differential equations (SDEs). However, implementing the Lagrangian formulation requires coupling between Lagrangian and Eulerian solvers, as most codes in combustion are grid-based. Several challenges arise, including the need to ensure consistency between the Lagrangian and Eulerian representations, the

[3]The IEM model can be alternatively understood as assuming that the unclosed terms and the PDF variable are joint-normally distributed, with the covariance modelled through the sub-grid timescale.

mass of the particles must match the density in the finite-volume cell, and velocity divergence must also be consistent. Moreover, since the spatial gradients of the particles are usually noisy, smoothing is necessary, making it difficult to use high spatial-order and low dissipation numerical methods. Load balancing of both the spatial domain and particles simultaneously, while keeping the data local to the processors, is also challenging. Special algorithms have been developed over the years to address these challenges, see Haworth 2010, section 7 for more details regarding the hybrid Lagrangian/Eulerian method.

Alternatively, Valiño 1998 and Soulard and Sabel'nikov 2006 proposed a statistically equivalent Eulerian system where the PDF is approximated by $N_f$ stochastic fields (SF), such that

$$F(\mathbf{x}, t; \boldsymbol{\varphi}) \approx \frac{1}{N_f} \sum_{n=1}^{N_f} \rho^{(n)}(\mathbf{x}, t) \prod_{m=1}^{N_V} \delta\left(\phi_m^{(n)}(\mathbf{x}, t) - \varphi_m\right) , \tag{3.13}$$

$$\bar{\phi}_m(\mathbf{x}, t) \approx \frac{1}{N_f} \sum_{n=1}^{N_f} \phi_m^{(n)}(\mathbf{x}, t) . \tag{3.14}$$

The superscript $(n)$ denotes the solution of the $n^{\text{th}}$ SF. Compared to the Lagrangian approach, the SF can be easily implemented in any grid-based solvers, taking advantage of existing capabilities such as high-order numerical schemes, AMR, efficient parallelisation, and portability across CPU and GPU platforms.

The system of stochastic partial differential equations (SPDEs) equivalent to the PDF transport equation (3.6) is

$$\frac{\mathrm{d}\rho^{(n)}}{\mathrm{d}t} + u_j^{(n)} \frac{\partial \rho^{(n)}}{\partial x_j} = -\overbrace{\rho \frac{\partial u_j}{\partial x_j}\bigg| \boldsymbol{\phi}} , \tag{3.15}$$

$$\frac{\mathrm{d}Y_\alpha^{(n)}}{\mathrm{d}t} + u_j^{(n)} \frac{\partial Y_\alpha^{(n)}}{\partial x_j} = -\frac{1}{\bar{\rho}} \frac{\partial \bar{J}_{\alpha,j}}{\partial x_j} + S_\alpha^{(n)} + \frac{1}{\tau_{\text{sgs}}} \left(\tilde{Y}_\alpha - Y_\alpha^{(n)}\right) , \tag{3.16}$$

$$\frac{\mathrm{d}u_i^{(n)}}{\mathrm{d}t} + u_j^{(n)} \frac{\partial u_i^{(n)}}{\partial x_j} = -\frac{1}{\bar{\rho}} \frac{\partial \bar{p}}{\partial x_i} + \frac{1}{\bar{\rho}} \frac{\partial \bar{\tau}_{ij}}{\partial x_j} + \frac{1}{\tau_{\text{sgs}}} \left(\frac{1}{2} + \frac{3}{4} C_0\right) \left(\tilde{u}_i - u_i^{(n)}\right) + \sqrt{C_0 \epsilon_{\text{sgs}}} \frac{\mathrm{d}W_i^{(n)}}{\mathrm{d}t} , \tag{3.17}$$

$$\frac{\mathrm{d}E^{(n)}}{\mathrm{d}t} + u_j^{(n)} \frac{\partial E^{(n)}}{\partial x_j} = -\frac{1}{\bar{\rho}} \frac{\partial \bar{q}_j}{\partial x_j} - \frac{1}{\bar{\rho}} \frac{\partial \overline{p u_j}}{\partial x_j} + \frac{1}{\bar{\rho}} \frac{\partial \overline{\tau_{ij} u_i}}{\partial x_j} + \frac{1}{\tau_{\text{sgs}}} \left(\tilde{E} - E^{(n)}\right) . \tag{3.18}$$

The Wiener process increment $\mathrm{d}\mathbf{W}$ has a mean of $\sum_n \mathrm{d}\mathbf{W}^{(n)} = \mathbf{0}$, a time average of $\langle \mathrm{d}\mathbf{W}^{(n)} \rangle = \mathbf{0}$, and a time covariance of $\langle \mathrm{d}W_i^{(m)} \mathrm{d}W_j^{(n)} \rangle = \mathrm{d}t \delta_{ij} \delta_{mn}$. The covariance property implies that the solutions of the SPDEs are continuous but not differentiable with respect to time. Therefore, temporal derivatives can only be interpreted as a finite change in the variable $\mathrm{d}\boldsymbol{\phi}$ over a finite time step $\mathrm{d}t$ and an increment $\mathrm{d}\mathbf{W}$. However, conventional partial derivatives exist in space as $\mathrm{d}\mathbf{W}$ is constant in space.

### 3.2.1 Conservation and thermodynamic consistency

Conservation and thermodynamic consistency (density, pressure, and temperature follow the equation of state) are important for numerical stability, especially at high Re and M, in the presence of shock waves, and when high-order numerical schemes are employed.

#### Density-dilatation term

In order to cast the SPDEs (3.15)–(3.18) into conservative form, the conditional density dilatation is decomposed into a conservative part and a non-conservative part which accounts for the interaction between SFs:

$$-\overbrace{\rho\frac{\partial u_j}{\partial x_j}\middle|\boldsymbol{\phi}} \approx -\rho^{(n)}\frac{\partial u_j^{(n)}}{\partial x_j} + \frac{C_\rho}{\tau_{\text{sgs}}}\left(\bar{\rho}-\rho^{(n)}\right) . \tag{3.19}$$

The sub-grid mixing-like term carries some physical interpretation, as there are three thermodynamic quantities need to equilibrate in a gas: mechanical equilibrium ($\rho \to \bar{\rho}$ or $p \to \bar{p}$), thermal equilibrium ($T \to \tilde{T}$), and chemical equilibrium ($Y_\alpha \to \tilde{Y}_\alpha$), but there are only two sub-grid mixing terms (on $E$ and $Y_\alpha$) in the SPDEs. This suggests that there ought to be a third sub-grid mixing term.

This novel density mixing term opens up new opportunities for modelling sub-grid mixing and interactions in compressible turbulence. However, considering that $\text{M}_{\text{sgs}}$ is typically small in the case of interest (see *e.g.* subsection 6.2.3), the fluctuations in sub-grid density are small compared to fluctuations in temperature and velocity. Therefore, this work neglects $C_\rho$. Nevertheless, its significance may be worth exploring in the future, potentially through highly compressible DNS.

#### Stochastic pressure gradient

For thermodynamic consistency, the mean pressure in the momentum equation is replaced with a stochastic pressure calculated from the field's states using the equation of state, similar to Azarnykh *et al.* 2016; Almeida 2019. This substitution does not alter the mean of the pressure gradient term, as differentiation is linear. It does, however, add higher-order statistical moments. For example, the variance can be calculated by first principle, as

$$\begin{aligned}\operatorname{var}\left(\frac{\partial p}{\partial x}\right) = \overline{\left(\frac{\partial p}{\partial x}\right)^2} - \left(\frac{\partial \bar{p}}{\partial x}\right)^2 = \lim_{\Delta x\to 0}\frac{1}{\Delta x^2}\Big(&\underbrace{\overline{p(x+\Delta x)^2} - \overline{p(x+\Delta x)}^2}_{\sigma_p^2(x+\Delta x)} \\ &+ \underbrace{\overline{p(x)^2} - \overline{p(x)}^2}_{\sigma_p^2(x)} - 2\underbrace{\left(\overline{p(x+\Delta x)p(x)} - \bar{p}(x+\Delta x)\bar{p}(x)\right)}_{\rho_p(x+\Delta x,x)\sigma_p(x+\Delta x)\sigma_p(x)}\Big),\end{aligned} \tag{3.20}$$

where $\sigma_p$ is the standard derivation of $p$, and $\rho_p$ is its Pearson correlation coefficient. Substituting in the Taylor expansions of $\sigma_p$ and $\rho_p$ and taking the limit, the variance of the stochastic pressure gradient is

$$\mathrm{var}\left(\frac{\partial p}{\partial x}\right) = \left(\frac{\partial \sigma_p}{\partial x}\right)^2 - \frac{\partial^2 \rho_p}{\partial x^2}\sigma_p^2 \,. \tag{3.21}$$

The second derivative of $\rho_p$ resembles the definition of the Taylor micro-scale $\lambda$,

$$-\frac{\partial^2 \rho_p}{\partial x^2} = \frac{1}{\lambda^2} \,. \tag{3.22}$$

It is important to clarify that this is *not* the physical Taylor scale, but a measure of the smoothness of the SF. Additionally, all terms in (3.21) are associated with the statistical moments, so their derivatives are meaningful and can be evaluated from the SF. If $p$ is a Gaussian random field—meaning that $p$ from a set of arbitrary points follows a joint normal distribution—then the mean pressure gradient together with the above variance can uniquely describe all moments of $\partial p/\partial x$.

This novel analysis establishes a connection between the formulation that uses the mean pressure gradient and that uses the stochastic pressure gradient. Future development could aim at introducing a term in the Langevin model to make these two formulations equivalent. This will require determining the joint distribution or correlation of pressure and velocity.

### Final stochastic PDE system

The final SPDE system is

$$\frac{\mathrm{d}\rho Y_\alpha^{(n)}}{\mathrm{d}t} + \frac{\partial \rho Y_\alpha^{(n)} u_j^{(n)}}{\partial x_j} = -\frac{\rho^{(n)}}{\bar{\rho}}\frac{\partial \bar{J}_{\alpha,j}}{\partial x_j} + \rho^{(n)} S_\alpha^{(n)} + \frac{\rho^{(n)}}{\tau_{\mathrm{sgs}}}\left(\tilde{Y}_\alpha - Y_\alpha^{(n)}\right) , \tag{3.23}$$

$$\begin{aligned}\frac{\mathrm{d}\rho u_i^{(n)}}{\mathrm{d}t} + \frac{\partial \rho u_i^{(n)} u_j^{(n)}}{\partial x_j} = &-\frac{\partial p^{(n)}}{\partial x_i} + \frac{\rho^{(n)}}{\bar{\rho}}\frac{\partial \bar{\tau}_{ij}}{\partial x_j} + \frac{\rho^{(n)}}{\tau_{\mathrm{sgs}}}\left(\frac{1}{2} + \frac{3}{4}C_0\right)\left(\tilde{u}_i - u_i^{(n)}\right) \\ &+ \rho^{(n)}\sqrt{C_0 \epsilon_{\mathrm{sgs}}}\frac{\mathrm{d}W_i^{(n)}}{\mathrm{d}t} \,,\end{aligned} \tag{3.24}$$

$$\frac{\mathrm{d}\rho E^{(n)}}{\mathrm{d}t} + \frac{\partial\left(\rho E^{(n)} + p^{(n)}\right) u_j^{(n)}}{\partial x_j} = -\frac{\rho^{(n)}}{\bar{\rho}}\frac{\partial \bar{q}_j}{\partial x_j} + \frac{\rho^{(n)}}{\bar{\rho}}\frac{\partial \overline{\tau_{ij} u_i}}{\partial x_j} + \frac{\rho^{(n)}}{\tau_{\mathrm{sgs}}}\left(\tilde{E} - E^{(n)}\right) . \tag{3.25}$$

with

$$k_{\mathrm{sgs}} = \frac{\sum_{n=1}^{N_f} \rho^{(n)}\left(u_i^{(n)} - \tilde{u}_i\right)^2}{\sum_{n=1}^{N_f} \rho^{(n)}} \,, \tag{3.26}$$

and $\tau_{\mathrm{sgs}}$ and $\epsilon_{\mathrm{sgs}}$ are computed using (3.10).

Using the notation of the Navier-Stokes equations in (2.1),

$$\mathrm{d}\mathbf{U}^{(n)} = \Bigg( \underbrace{-\frac{\partial \mathbf{F}_j^{\mathrm{hyp}}(\mathbf{U}^{(n)})}{\partial x_j} - \frac{\rho^{(n)}}{\bar{\rho}} \frac{1}{N_f} \sum_{m=1}^{N_f} \frac{\partial \mathbf{F}_j^{\mathrm{diff}}(\mathbf{U}^{(m)})}{\partial x_j}}_{\mathbf{RHS}^{\mathrm{SF}}} + \mathbf{S}(\mathbf{U}^{(n)}) + \mathbf{A}(\mathbf{U}^{(n)}, \overline{\mathbf{U}}) \Bigg) \mathrm{d}t + \mathbf{B}(\mathbf{U}^{(n)}, \overline{\mathbf{U}})\, \mathrm{d}\mathbf{W}^{(n)}\,, \quad (3.27)$$

where the superscripts on the flux vector denote the hyperbolic (inviscid) and diffusive parts, and

$$\mathbf{A}(\mathbf{U}^{(n)}, \overline{\mathbf{U}}) = \frac{\rho^{(n)}}{\tau_{\mathrm{sgs}}} \begin{bmatrix} \tilde{Y}_\alpha - Y_\alpha^{(n)} \\ \left(\frac{1}{2} + \frac{3}{4} C_0\right)\left(\tilde{u}_i - u_i^{(n)}\right) \\ \tilde{E} - E^{(n)} \end{bmatrix}, \qquad \mathbf{B}(\mathbf{U}^{(n)}, \overline{\mathbf{U}}) = \begin{bmatrix} 0 \\ \rho^{(n)} \sqrt{C_0 \epsilon_{\mathrm{sgs}}} \\ 0 \end{bmatrix}. \quad (3.28)$$

Note that only Eulerian systems can be written in conservative form, while Lagrangian systems cannot.

## 3.3 Implementation

### 3.3.1 Modifications to the existing solver

The main advantage of the SF approach is that it can be easily implemented in any existing grid-based solver. The state variable vector is extended to be $\mathbf{U} = [\overline{\mathbf{U}}, \mathbf{U}^{(1)}, ..., \mathbf{U}^{(N_f)}]$. The mean $\overline{\mathbf{U}}$ is redundant and is included only to avoid repeated calculation of the average. When computing the RHS update, the inviscid fluxes are computed as normal, while the viscous fluxes, because need to be averaged, are stored in a temporary variable for taking the mean before adding back to all fields.

The SF sub-grid model, $\mathbf{A}$ and $\mathbf{B}$, is added after the RHS evaluations, following the Euler-Maruyama scheme which has a time accuracy of strong order $\sqrt{\Delta t}$ and weak order $\Delta t$ (Kloeden and Platen 1992)[4]. The Runge-Kutta integrator in (2.67)–(2.69) is modified by adding an extra sub-step before the reaction step, such that the advantage of computing the reaction term only once per time step is retained.

$$\mathbf{U}^{*} = \mathbf{U}^{t} + \left(\mathbf{RHS}^{\mathrm{SF}}(\mathbf{U}^{t}) + \mathbf{S}(\mathbf{U}^{t})\right) \Delta t\,, \quad (3.29)$$

$$\mathbf{U}^{**} = \mathbf{U}^{t} + \left(\mathbf{RHS}^{\mathrm{SF}}(\mathbf{U}^{t}) + \mathbf{RHS}^{\mathrm{SF}}(\mathbf{U}^{*})\right) \frac{\Delta t}{2}\,, \quad (3.30)$$

$$\mathbf{U}^{***} = \mathbf{U}^{**} + \mathbf{A}(\mathbf{U}^{**})\Delta t + \mathbf{B}(\mathbf{U}^{**})\Delta \mathbf{W}\,, \quad (3.31)$$

$$\mathbf{U}^{t+1} = \mathbf{U}^{***} + \mathbf{S}(\mathbf{U}^{t+1})\Delta t\,. \quad (3.32)$$

[4]Strong and weak order refer to the convergence rate to a particular path of a stochastic process and its statistical moments, respectively.

### 3.3.2 Discretising the stochastic model

Special care is needed when discretising **A** and **B**. When the sub-grid time scale is too small, the sub-grid mixing term places a stringent requirement on the time step size, analogous to the CFL condition. It can be circumvented using a new two-step integration procedure by first applying the random walk, and then performing sub-grid mixing. The sub-grid time scale is also rewritten in a semi-implicit way, such that it is unconditionally stable (Prasad 2011), even if $\tau_{\text{sgs}} \to 0$ approaches zero, and the states correctly converge to the mean solution of the Runge-Kutta predictor $\mathbf{U}^{**}$. For example, the momentum equation in step (3.31) is discretised as $(\rho u_i)^{***} = (\rho u_i)^{**} + \Delta u_i$, and the change in velocity $\Delta u_i$ is obtained through the following procedure:

$$\Delta u_i^W = B \Delta W_i \,, \tag{3.33}$$

$$\Delta u_i = \int_t^{t+\Delta t} A_{u_i} dt + B dW \approx \Delta u_i^W + \frac{\left(\widetilde{u}_i - u_i^{(n)} - \Delta u_i^W\right)\Delta t}{\Delta t + 1/G_{ij}} \,. \tag{3.34}$$

Here, $A_{u_i} = G_{ij}\left(\tilde{u}_i - u_i^{(n)}\right)$ and $B = \sqrt{C_0 \epsilon_{\text{sgs}}}$. For the species and energy equations, $B = 0$ and (3.34) is applied directly with $1/\tau_{\text{sgs}}$ in place of $G_{ij}$.

It is also important to ensure that the discretised Wiener process sums to zero, $\sum_n \Delta W^{(n)} = 0$, such that conservation is respected (the mean remains unchanged). This can be done in several ways:

1. Shift and scale a random normal number to have zero mean and $\Delta t$ variance;
2. Mirror half a set of random normal numbers about zero (antithetic sampling);
3. Use a set of random numbers with half valued $-\sqrt{\Delta t}$ and the other half $\sqrt{\Delta t}$ (dichotomic vector).

The second and third approaches are found to perform better (Jones and Navarro-Martinez 2007). The present work uses the dichotomic vector because of its another advantage that the Wiener term is always bounded, whereas drawing from a normal distribution may result in extreme events. These extreme events, although having a low probability, will almost certainly occur over the large number of time steps, and will adversely affect the statistical error, especially when $N_f$ is small.

### 3.3.3 Treatment with AMR

To maintain consistency between the AMR hierarchy while preserving time independence, the Wiener term is initialised at the finest level and then summed up accordingly to the coarse levels, as illustrated in Figure 3.1.

The coarse-level Wiener process increments $\Delta W$ are independent, as the sum of independent fine-level $\Delta W$ is also independent. It is also consistent because for each field, the

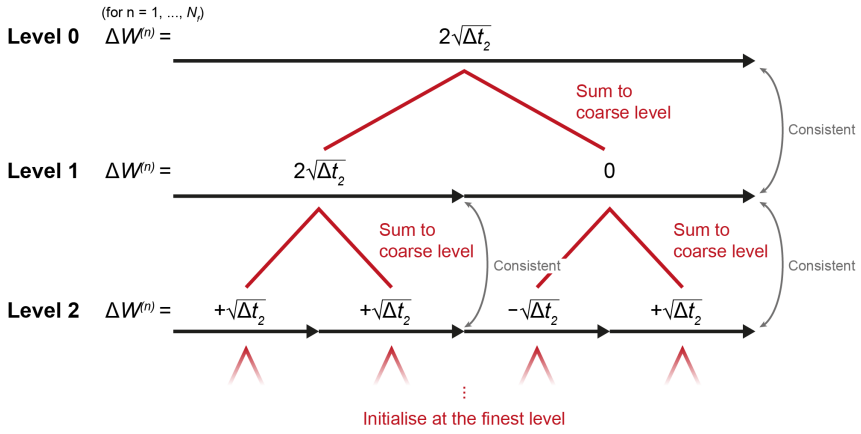



Figure 3.1: Algorithm of generating independent and consistent Wiener process increments across AMR levels, illustrated for three levels.

coarse and fine Wiener processes over the coarse time step have the same value. The only inconsistency occurs at half the coarse time step, when spatial-temporal interpolation is performed at coarse-fine level boundaries. For instance, at the end of the first step of level 1 in Figure 3.1, the solution from level 0 is interpolated to half of its time step, therefore, $\Delta W$ is effectively halved to $\sqrt{\Delta t_2}$. While in level 1, $\Delta W$ equals $2\sqrt{\Delta t_2}$ is different from the value in the coarse level.

The inconsistency can be resolved by instead initialising $\Delta W$ in the coarsest level and then dividing it to the finer levels. However, the aforementioned method (Figure 3.1) still yields a better statistical accuracy. This is because although the second method avoids inconsistency, it substantially increases the effective time step size of the SPDE, especially when multiple AMR levels are used, and as previously mentioned, the statistical error is proportional to the time step size.

### 3.3.4 Performance scaling with stochastic fields

The implementation of SF is mostly similar to adding a loop around the time advance loop, hence, it is expected that the computational cost will scale linearly with the number of fields $O(N_f)$. However, additional operations are required, including computing the mean, applying the stochastic model, and generating and syncing the random number, although the computational cost for these operations is expected to be insignificant compared to evaluating the RHS. A weak scaling test is carried out on ARCHER2, using the same settings as in subsection 2.4.5 except that the problem size is reduced to $128^3$. Figure 3.2 shows that the parallel efficiency of the SF solver reduces with increasing number of nodes. However, it is able to maintain approximately 84% efficiency with 32 fields and 8 nodes (1,024 CPU cores). The load imbalance also increases with the number of nodes, indicating that the decline in efficiency is partly due to communication rather than the SF implementation. In practice, the number of fields used is a compromise between accuracy

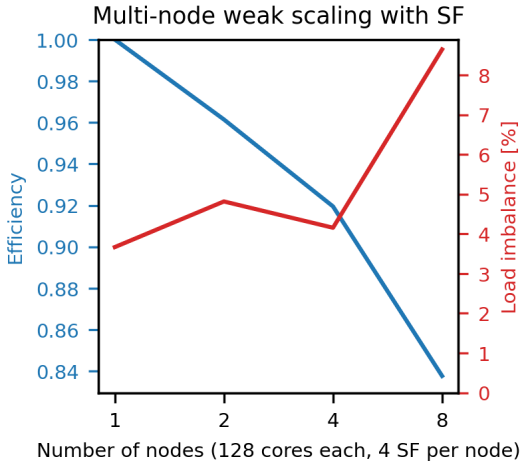



Figure 3.2: Weak scaling of the stochastic fields on CPU. Four fields per node are used.

and cost. In the literature, 8 fields is a common choice (*e.g.* Mustata *et al.* 2006; Gong *et al.* 2017; Almeida and Navarro-Martinez 2021; Liu and Jones 2025).

## 3.4 Results

### 3.4.1 Ornstein-Uhlenbeck process

A simplified test case is used to verify the implementation of the stochastic solver. The computational domain is filled with two passive scalars of equal mass fractions, $Y_1 = Y_2 = 0.5$. At the centre, SGS scalar variance is imposed by offsetting the scalar mass fractions in different fields, *e.g.*, field 1 has $(Y_1^{(1)}, Y_2^{(1)}) = (0.4, 0.6)$ and field 2 has $(Y_1^{(2)}, Y_2^{(2)}) = (0.6, 0.4)$, and so on. This process keeps the filtered (mean) values unchanged. The scalars advect with a base flow and follow the Ornstein-Uhlenbeck process (Särkkä and Solin 2019),

$$\frac{\mathrm{d}\rho Y_\alpha^{(n)}}{\mathrm{d}t} + \frac{\partial \rho Y_\alpha^{(n)} \widetilde{u}_j}{\partial x_j} = -\rho^{(n)} A (Y_\alpha - 0.5) + \rho^{(n)} B \frac{\mathrm{d}W^{(n)}}{\mathrm{d}t}. \tag{3.35}$$

With constant coefficients $A = 500$ and $B = \sqrt{2}$, the Ornstein-Uhlenbeck process can be understood as a linear version of the SGS model employed in SF where $\tau_{\mathrm{sgs}}$ and $\epsilon_{\mathrm{sgs}}$ are constant. The time evolution of SGS scalar variance can be derived analytically and is used to assess the stochastic error convergence:

$$\mathrm{var}(Y)(t) = \mathrm{var}(Y)(0) e^{-2At} + \frac{B^2}{2A}\left(1 - e^{-2At}\right). \tag{3.36}$$

The $L_2$ error in sub-grid variance is defined as

$$\varepsilon_{L2} = \sqrt{\frac{1}{t_{\mathrm{end}}} \int_0^{t_{\mathrm{end}}} \left(\mathrm{var}(Y)_{\mathrm{SF}} - \mathrm{var}(Y)_{\mathrm{Analytical}}\right)^2}. \tag{3.37}$$

The simulation duration $t_{\text{end}}$ is chosen to be four flow-through times ($t_{\text{ref}}$), approximately two times the time needed for the SGS scalar variance to reach equilibrium. In this way, the error reflects both the transient and equilibrium behaviour of the sub-grid variance.

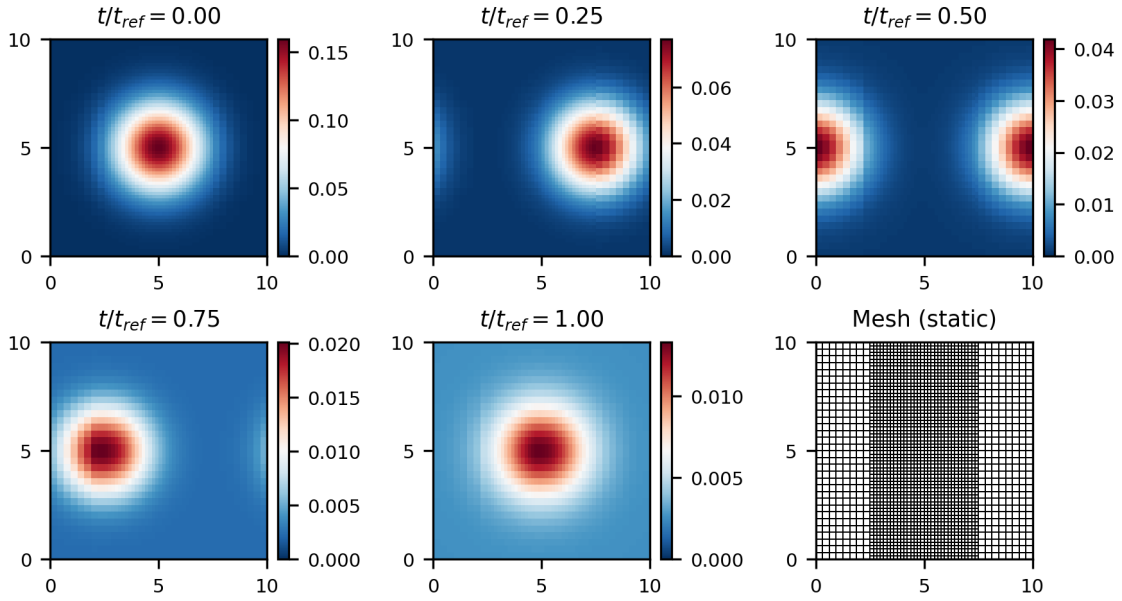



Figure 3.3: Sub-grid scalar variance at different times and the static mesh used.

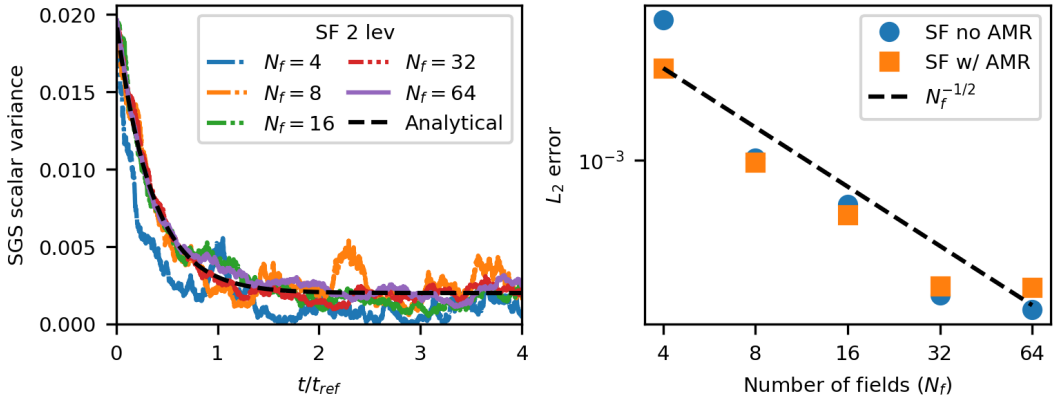



Figure 3.4: Time evolution of sub-grid scalar variance averaged over space (identical for both scalars) and error convergence.

Figure 3.3 displays snapshots of $\sigma_{\text{SF}}$ with 8 fields and 2 levels. It is seen that the sub-grid variance is advected to the right and decays as time passes. The shape of the sub-grid variance is free from any noticeable distortion or noise when passing through the AMR level boundaries. A quantitative view is provided in Figure 3.4, showing that the scalar variance decay matches the analytical solution ($t/t_{\text{ref}} < 2$) and maintains a correct equilibrium level afterwards. With an increasing $N_f$, the curve becomes smoother with less fluctuation. The stochastic error converges with $N_f^{-1/2}$, consistent with the Monte Carlo method used. The AMR implementation is proven to be consistent and does not affect convergence.

### 3.4.2 Taylor-Green vortex

Next, the performance of the velocity PDF as a turbulence model is assessed through the Taylor-Green vortex (TGV) problem. The case setup follows Lusher and Sandham 2021, with an initial Reynolds number of 1600 and a constant Prandtl number of 0.7. Four modelling configurations are examined, implicit LES (ILES, or no model) where numerical diffusion acts as SGS model to provide turbulent diffusion, Smagorinsky model (Martín, Piomelli, *et al.* 2000) with a constant of $C_s = 0.1$, and the SF with 8 and 16 fields. A uniform $128^3$ mesh is used for all configurations.

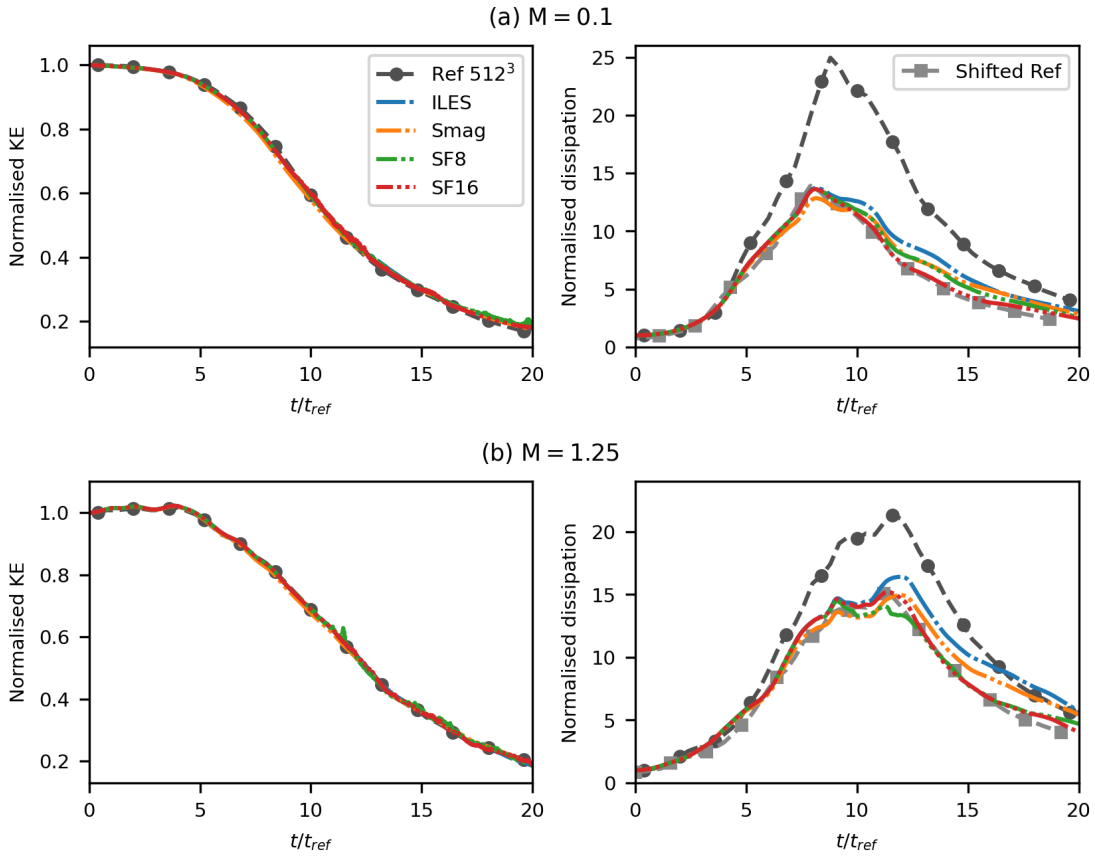



Figure 3.5: Comparison of TGV using different turbulence models and $128^3$ mesh. Ref: DNS (TENO6) from Lusher and Sandham 2021. All quantities are normalised by their initial values.

The case is conducted at two Mach numbers, M = 0.1 within the incompressible limit, and M = 1.25 where shocklets are present. For both Mach numbers, Figure 3.5 shows that the time evolutions of kinetic energy for all configurations agree well with DNS data. More information about the vortical structure is revealed by the (normalised) total dissipation,

$$\epsilon = \int \|\nabla \times \mathbf{u}\|^2 + \frac{4}{3}(\nabla \cdot \mathbf{u})^2 \, \mathrm{d}\mathbf{x} \,. \tag{3.38}$$

The first term in the integral is enstrophy (solenoidal dissipation), and the second term

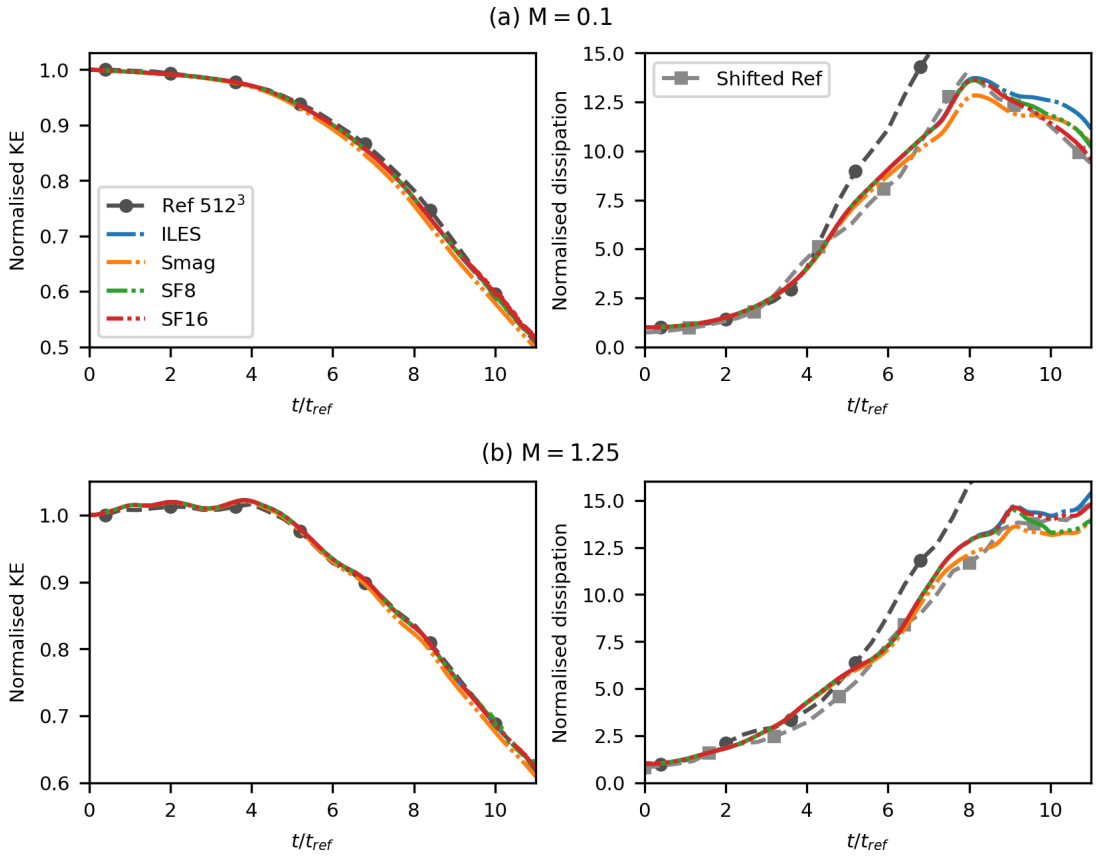



Figure 3.6: Enlarged view of Figure 3.5 for clearer interpretation of the differences between ILES, Smagorinsky LES, and SF in the vortex stretching phase.

is dilatational dissipation, which is zero in incompressible flows and is still much smaller than the solenoidal term in the M = 1.25 case.

Compared to DNS results, all LES suffered from considerable numerical diffusion, as seen by the difference between the total dissipation curves. However, when the DNS data is scaled down and shifted in time such that the peak dissipation matches that of the LES results, the inclusion of an LES SGS model is seen to provide significant improvement in terms of matching the decay of the vortical structures, where the ILES failed to model the decay of dissipation. In Figure 3.6, it is also interesting to note that in the vortex stretching phase (before peak dissipation, $t/t_{\text{ref}} < 8$), the SF solution is the same as that of no model, indicating that no turbulent dissipation has been added at the time. This shows that the SF model introduces turbulent dissipation only when necessary, unlike eddy viscosity-type models, such as the Smagorinsky model, which add dissipation from the start of the simulation. The SF model appears to be able to distinguish between laminar shear and turbulence. A few small peaks are observed in the kinetic energy curves for SF, possibly due to the stochastic nature of the method, but overall the simulations remain stable.

The difference between 8 and 16 fields is small in the high Mach number case, suggesting

that 8 fields are sufficient to handle the stochastic error in turbulent flows of this problem. However, the difference is visible in the low Mach number case, where 16 fields yield better predictions closer to the shifted DNS results, confirming the convergent property of the stochastic model.

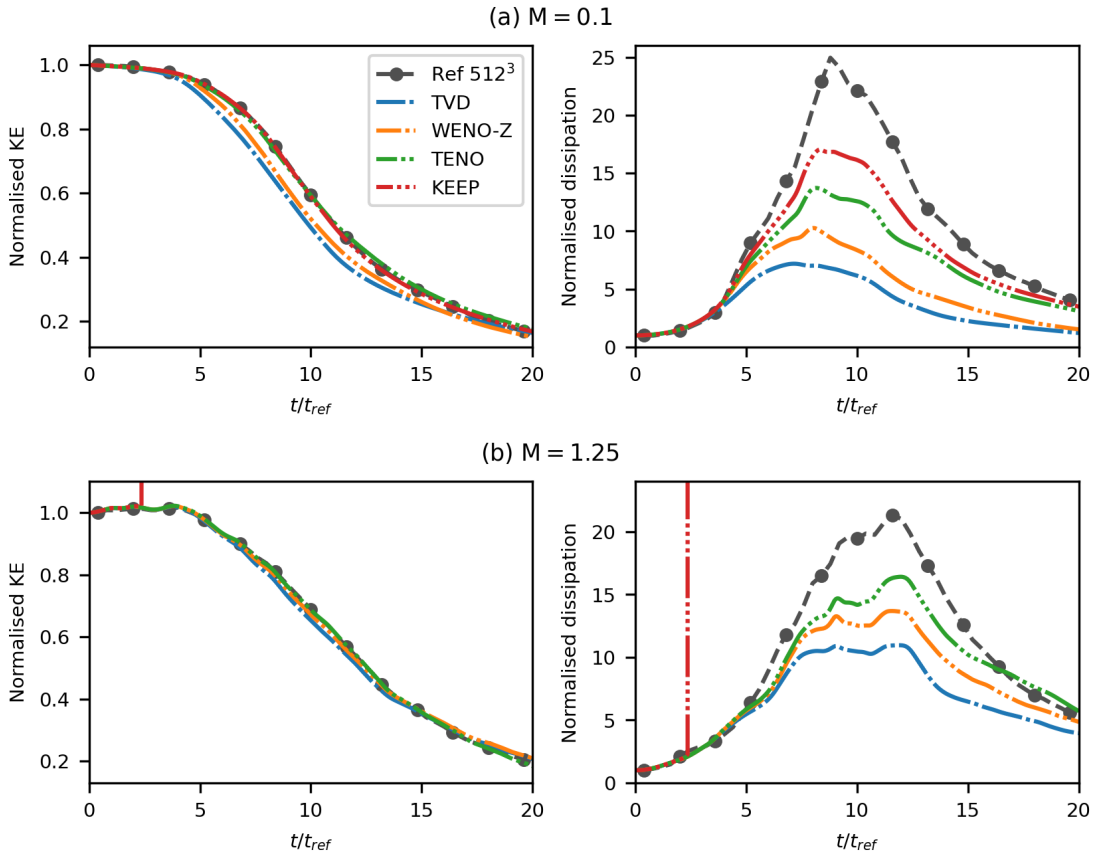



Figure 3.7: Comparison of TGV using different numerical schemes and $128^3$ mesh. Ref: DNS (TENO6) from Lusher and Sandham 2021. All quantities are normalised by their initial values.

Figure 3.7 shows the difference between numerical schemes. A low dissipation scheme has a dramatic effect on turbulence as excessive numerical dissipation will mask out the SGS model. The TVD scheme, which is commonly used in compressible CFD solvers, is too dissipative for LES purposes. The difference is more pronounced in smooth flows. In shocked flows, numerical dissipation is inevitable, in which case AMR will be effective. The fourth-order central KEEP (kinetic energy and entropy-preserving) scheme of Fujiwara *et al.* 2023 shows some advantages due to the spectral properties, but it requires very smooth (well-resolved) flows and is unstable without artificial dissipation in shocked flows. A hybrid strategy may be useful by combining the best of both schemes, but it is beyond the scope of this work.

The difference in the choice of discretisation for the Wiener process $\Delta W$ is examined in Figure 3.8. The use of a random normal number, which produces a non-zero mean,

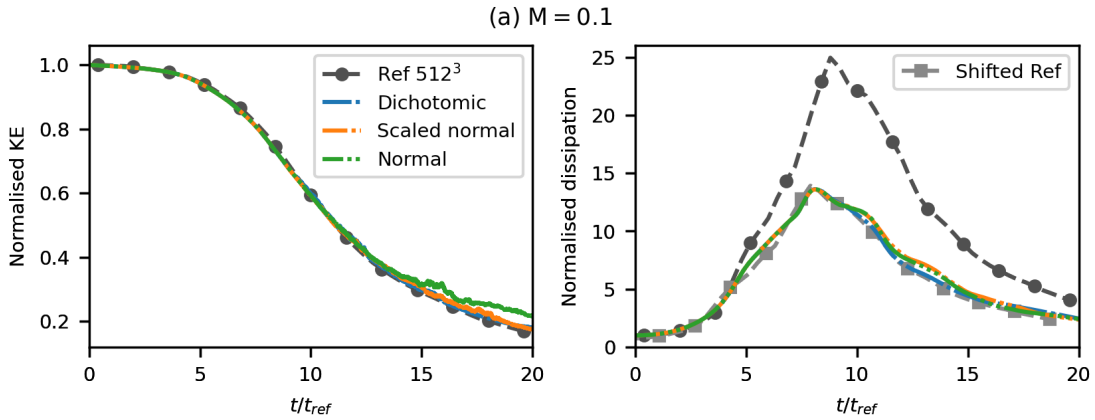



Figure 3.8: Comparison of TGV using 16 SF and different random number generation methods or $\Delta W$ and $128^3$ mesh. Ref: DNS (TENO6) from Lusher and Sandham 2021. All quantities are normalised by their initial values.

contaminates the solution, leading to a significant deviation in kinetic energy from $t/t_{\text{ref}} > 15$. While scaling and shifting the random normal number to zero mean and $\Delta t$ variance results in some improvement, the current approach of using a dichotomic random number is shown to be the most effective.

### 3.4.3 Autoignition in homogeneous-isotropic turbulence

The following case demonstrates the behaviour of the SF model in situations involving turbulence and autoignition. The case is set up with a decaying homogeneous-isotropic turbulence of Re $\approx$ 11,000 and M = 0.1. The initial velocity field is generated on a DNS mesh using the von Kármán-Pao spectrum (Bailly and Juve 1999)

$$E(k) = \frac{3.07\ (12/5)^2}{\sqrt{\pi}} \times \frac{(k/k_\ell)^4}{\left(1 + \left(k/k_\ell\sqrt{12/5}\right)^2\right)^{17/6}} \times \exp\left(-2(k/k_\eta)^2\right)\ , \tag{3.39}$$

where the first part is a normalising constant, and the second and third parts are the spectra controlling the large and small scales, respectively; $k$ is the wavenumber, and $k_\ell = 2$ and $k_\eta = 45$ are the wavenumbers corresponding to the most energetic scale and the smallest (Kolmogorov) scales. The velocity field is then filtered to create the initial conditions for the LES, as shown in Figure 3.9. The mesh sizes for the DNS and LES are $128^3$ and $32^3$, respectively. Sub-grid temperature fluctuations follow the strong Reynolds analogy (assuming constant total energy, $c_v T'' = 3/2u''^2$) while density remains constant.

A fictitious one-step irreversible mechanism is used with a forward rate given by

$$k = ATe^{-T_a/T}s(T - T_{\text{ref}})\,, \tag{3.40}$$

with $A = 2 \times 10^7$ K s$^{-1}$, $T_a = 15096.5$ K, $T_{\text{ref}} = 806.3$ K, and $s(\phi) = 1/(1 + e^{-\phi})$ is the standard logistic function. These parameters are selected such that the turbulence

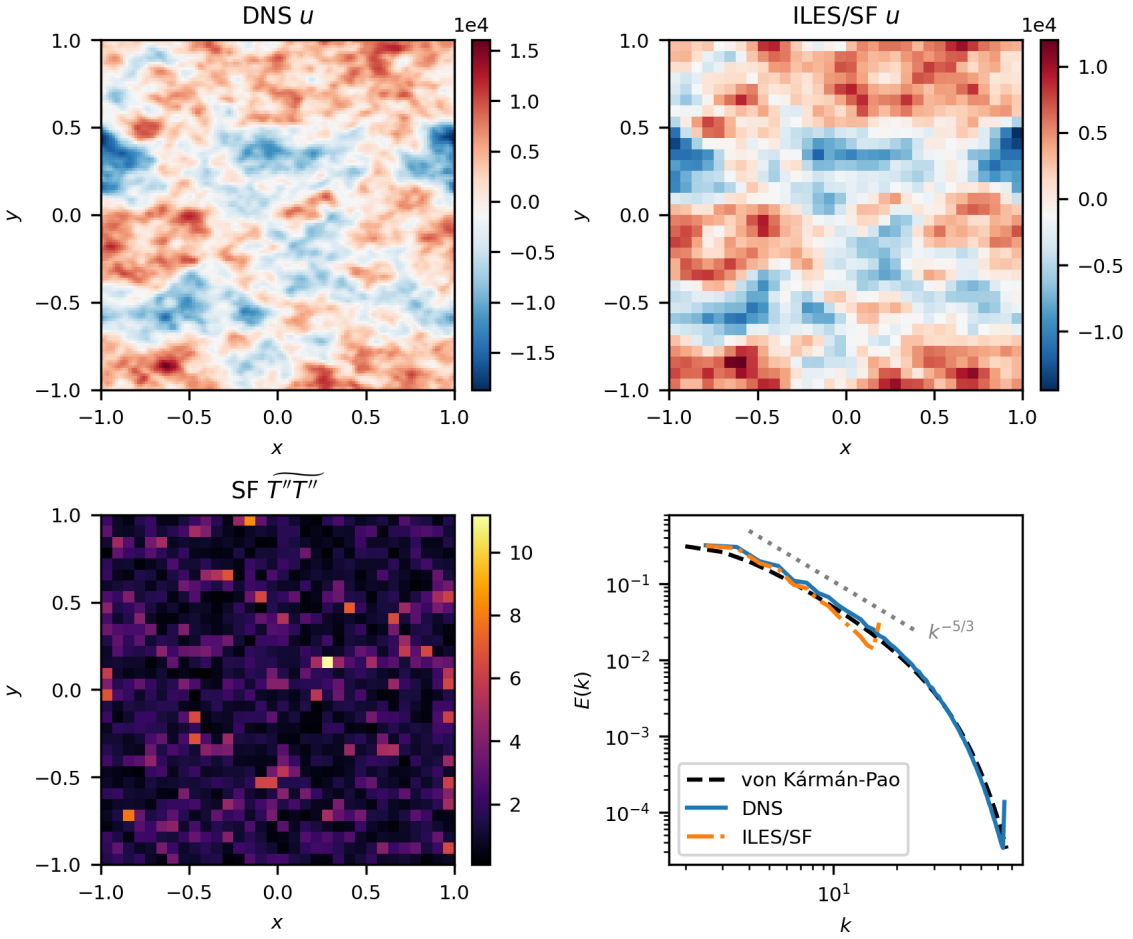



Figure 3.9: Illustration of the initial velocity field before and after filtering, the sub-grid temperature variance, and the kinetic energy spectra.

timescale and the ignition delay $t_{\text{turb}} \sim t_{\text{ign}}$ are comparable. This simplified case aims to show the general behaviour of the SF with a strongly non-linear source term in the presence of sub-grid variance.

Three simulations are run, including one ILES, two SF, and a DNS. All simulations start with an identical temperature distribution. From Figure 3.10, the temperature rises as the decaying kinetic energy converts into heat. However, the SF simulation starts to ignite shortly after 0.8 $t_{\text{ign}}$, as indicated by a sharp rise in temperature, while the no model simulation is not ignited throughout the simulated time. Compared to DNS, the SF predicts an earlier autoignition. Initially, it was suspected to be due to the added dissipation from a coarser grid, meaning that kinetic energy is transferred into heat more quickly. However, the left panel of Figure 3.10 suggests that the kinetic energy dissipation is mainly due to sub-grid scales. It may also be due to the initial condition being slightly different, as positional information is lost with the one-point PDF. Nevertheless, the SF successfully predicts the ignition event whereas the ILES approach fails[5]. The simulations

[5]The ILES is stopped at $t/t_{\text{ign}} \approx 1.35$ because it already represents a 35% error compared to the DNS and $> 50\%$ difference from the SF which uses the same mesh.

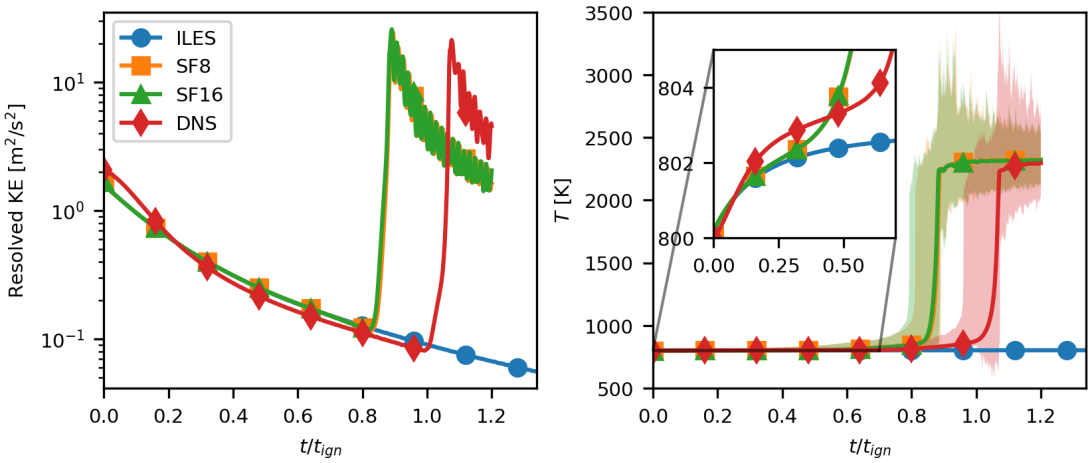



Figure 3.10: Time evolution of temperature. The solid line indicates the spatial average and the shaded region represents the range. $t_{\text{ign}}$ denotes the ignition time in the DNS.

with 8 and 16 SF show the same behaviour with ignition at $t = 0.8\ t_{\text{ign}}$, suggesting that ignition is correctly predicted even with a low number of fields. This is because ignition is sensitive to extreme values but not the mean.

The case showcases a feature of the SF model, when there are considerable SGS temperature and species fluctuations, points within an LES cell can get ignited much sooner than the filtered states due to the non-linear nature of the chemical process. SF can capture this behaviour as it permits some fields to have states more favourable for ignition. The "ignited" fields will generate radicals and heat, which in turn will propagate to the other fields through the sub-grid mixing mechanism.

### 3.4.4 Supersonic jet flame

Finally, the supersonic jet flame experimentally studied by Cheng, Wehrmeyer, and Pitz 1991; Cheng, Wehrmeyer, Pitz, *et al.* 1994 is used to validate the ability of the SF to simulate realistic high-speed turbulent combustion problems. The case has documented experimental data as well as LES studies by Möbus *et al.* 2003; Boivin *et al.* 2012; Moule *et al.* 2014; Bouheraoua *et al.* 2017.

The burner comprises a sonic circular hydrogen jet surrounded by a Mach-2 coflow of hot combusted gas. Detailed inflow conditions are listed in Table 3.1. The computation domain is $(75D \times 37.5D \times 37.5D)$, with a base grid of $(160 \times 80 \times 80)$ and up to 3 levels of refinement, resulting in around 14 million cells. The minimum cell size is 0.138 mm, mainly around the fuel injector at $x/D < 10$. Most of the jet is covered by the second finest level, with a cell size of 0.277 mm, roughly 10 times the Kolmogorov length scale and 0.05 times the integral length scale estimated in the experiment (Cheng, Wehrmeyer, Pitz, *et al.* 1994). The refinement region is adaptively generated based on the density gradient, pressure gradient, and vorticity magnitude. If SF is used, $k_{\text{sgs}}$ is also available and can be

Table 3.1: Supersonic jet flame conditions (Cheng, Wehrmeyer, Pitz, *et al.* 1994)

| Geometrical parameters | |
|---|---|
| Fuel injector inner diameter ($D$) | 2.36 mm |
| Fuel injector outer diameter | 3.81 mm |
| Coflow inner diameter | 17.78 mm |

| | Fuel jet | Coflow jet | Atmospheric |
|---|---|---|---|
| Pressure [kPa] | 112 | 107 | 101 |
| Temperature [K] | 545 | 1350 | 296 |
| Mach number | 1.0 | 2.0 | 0.0 |
| $O_2$ mole fraction | 0.0 | 0.201 | 0.23 |
| $N_2$ mole fraction | 0.0 | 0.544 | 0.77 |
| $H_2$ mole fraction | 1.0 | 0.0 | 0.0 |
| $H_2O$ mole fraction | 0.0 | 0.255 | 0.0 |

used as a refinement criterion, although in this case, the tagged region is almost identical to using the aforementioned criteria. A buffer layer is placed at the outflow to prevent spurious pressure waves from reflecting back into the domain. The 9-species 21-reaction mechanism by Li, Zhao, *et al.* 2004 is used, different from most previous LES studies where reduced chemistry is used (Möbus *et al.* 2003; Boivin *et al.* 2012; Bouheraoua *et al.* 2017).

Previous studies show that velocity fluctuations at the inlet are crucial to the break-up distance of the jet. An artificial perturbation by Danaila and Boersma 1998 is used, which has been shown to work well in jet flames (Pitsch and Steiner 2000):

$$u(\theta,t) = \langle u \rangle + \frac{u_{\text{rms}}}{2}\left[\sum_{m=1}^{6} \sin\left(\frac{a_m\langle u\rangle}{D} m\pi t + m\theta + b_m\right) + \sum_{m=7}^{8} \sin\left(\frac{a_m\langle u\rangle}{D} m\pi t + b_m\right)\right], \quad (3.41)$$

where $\theta$ is the azimuthal angle, $\langle u \rangle$ is the time-averaged velocity, $a_m$ and $b_m$ are random numbers drawn between 0 and 1. $a_m$ carries the physical meaning as the Strouhal number and $b_m$ is a phase shift. The root mean square (RMS) velocity $u_{\text{rms}}$ is 18% and 22% $\langle u \rangle$ for the fuel jet and coflow, respectively, following Bouheraoua *et al.* 2017.

The burner is simulated with two configurations, an ILES and an SF with 8 fields. Figure 3.11 shows the instantaneous temperature slices, revealing a highly dynamic flow field characterised by strong gradients and the presence of a wide range of scales. Autoignition of partially premixed pockets occurs at $x/D \approx 30$, similar for both configurations. The SF approach exhibits a stronger and more sustained flame compared to the no model, which shows a more broken flame structure. The same trend is observed by OH and $HO_2$ radicals depicted in Figure 3.12. The SF model predicts slightly earlier production of $HO_2$, and a

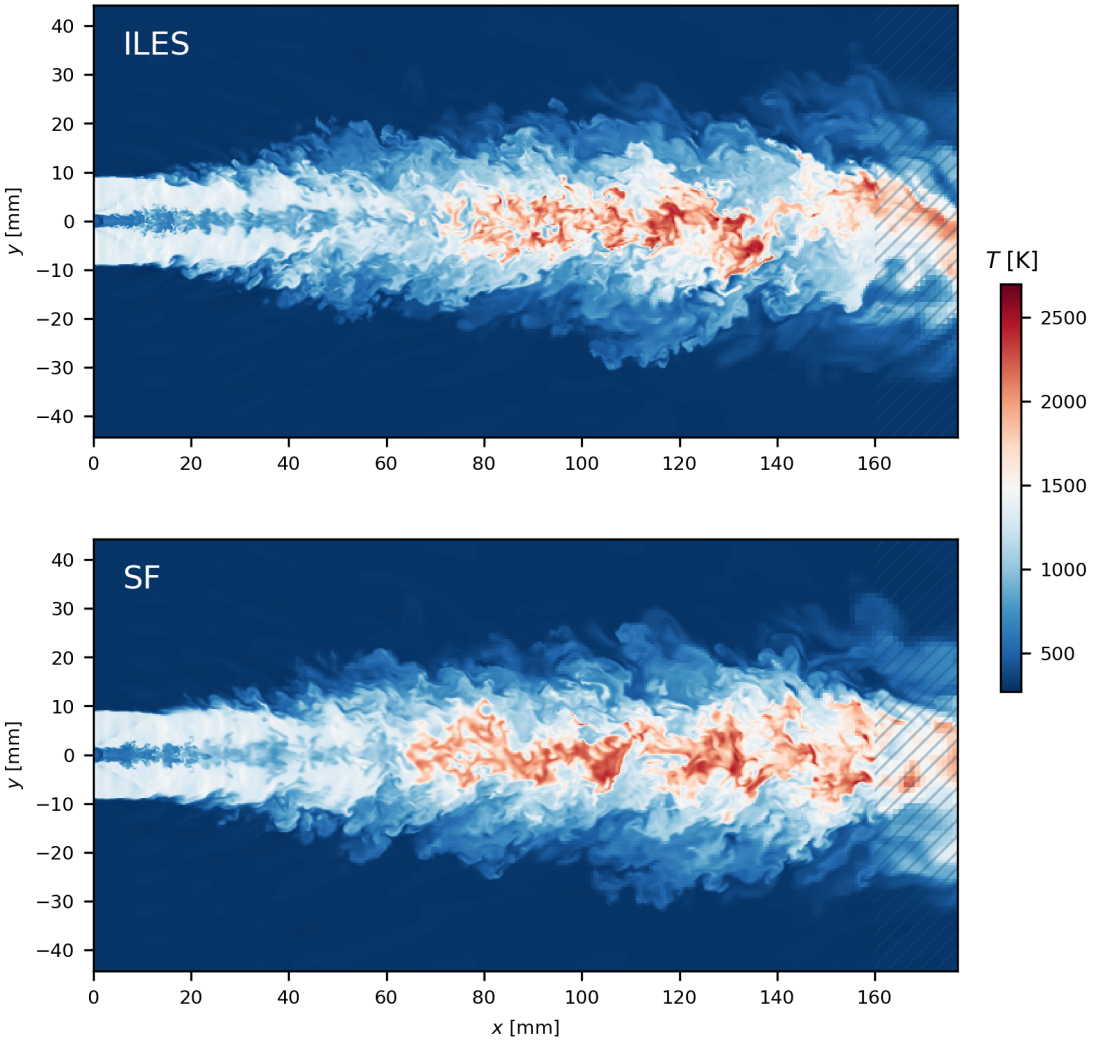



Figure 3.11: Instantaneous temperature field of implicit LES (ILES) and stochastic fields (SF). The shaded region represents the buffer layer.

higher OH mass fraction downstream. These observations are consistent with the previous test case, where the SF approach "ignites" before the ILES.

Figure 3.13 compares the mean temperature of the present solver with previous LES studies. The present results agree well with the well-resolved LES by Bouheraoua *et al.* 2017 using up to 268 million cells[6] and outperform other previous LES studies. The final plot suggests that the ignition position is further downstream compared to the other LES. However, caution must be exercised in interpreting these results, as the chemical mechanism used is slightly different and may have an impact on the autoignition location.

Figure 3.14 compares the radial profiles of time statistics with experimental measure-

[6]In their study, the authors tested three grids of 4, 32, and 268 million cells. They showed that grid convergence is achieved with the 4-million-cell grid, while the 268-million quasi-DNS resolution is employed for a more detailed analysis to the flame stabilisation mechanism.

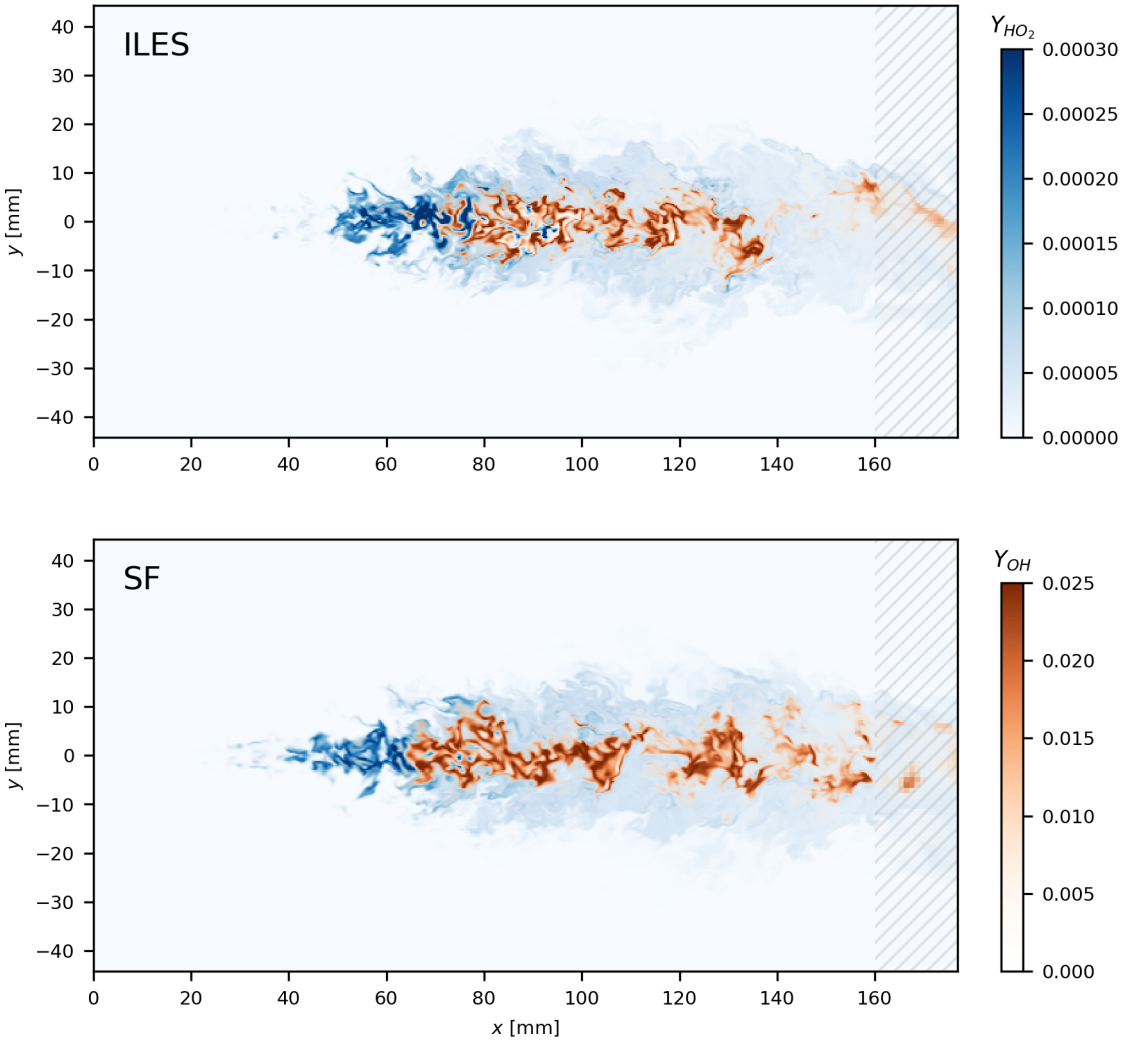



Figure 3.12: Instantaneous mass fractions of OH and $HO_2$ of implicit LES (ILES) and stochastic fields (SF). The shaded region represents the buffer layer.

ments. At $x/D = 10.8$, the jet has not ignited thus the maximum temperature is reached at the coflow, and the plot shows the mixing of the hot coflow and cold $H_2$ streams. The double peaks around the inner jet in RMS suggest that it has not broken up. Both models produce similar results and agree with the experiment, with some over-prediction seen in $H_2O$ and $H_2$ RMS. This may be caused by the small values and experimental uncertainty.

At $x/D = 32.3$, the peak temperature level shows that ignition has occurred, and the inner jet is no longer distinctly visible. All time averages and RMS results match well with the experiment. The SF and no model show similar trends. However, differences in predicted $H_2$ are starting to be observed, with the SF showing slightly faster fuel consumption.

At $x/D = 43.1$, the differences between the two models begin to grow, as a higher $H_2O$ and a lower $H_2$ level suggest a stronger flame in SF. Overall, both configurations show

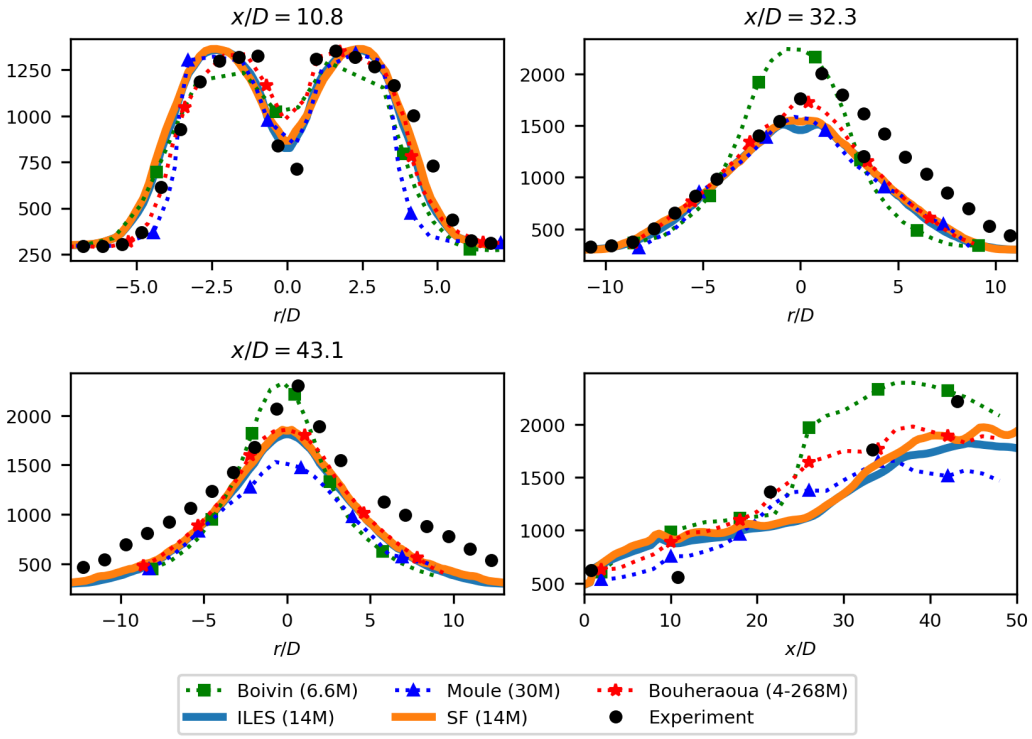



Figure 3.13: Mean temperature compared with previous LES studies and experiment. The number of cells used in the LES is included in brackets ("M" means millions, $10^6$). Green square: Boivin *et al.* 2012; Blue triangle: Moule *et al.* 2014; Red star: Bouheraoua *et al.* 2017; Black circle: Cheng, Wehrmeyer, and Pitz 1991.

reasonable agreement with the experiment.

At the last station, $x/D = 64.7$, the SF predicts that the $H_2$ is nearly all consumed, consistent with that measured in the experiment. Stronger discrepancies between approaches occur in $O_2$ and $N_2$ RMS concentrations, which suggest larger fluctuations in the experiment than in the numerical flames. The OH mean and RMS values of the ILES agree better with the experiment, although these may be due to an erroneously delayed flame.

Finally, it is worth noting that the SF without the conservation and thermodynamic consistency treatment introduced in subsection 3.2.1 crashes in this case.

## 3.5 Summary

This chapter presented the development and validation of the joint-velocity-scalar probability density function (VSPDF) formulation in large eddy simulations (LES), which closes all turbulent transport and non-linear chemical source terms without approximation. The PDF transport equation is solved using the Eulerian stochastic fields (SF) approach, making it straightforward to implement in grid-based compressible solvers. It allows integration of AMReX's adaptive mesh refinement (AMR) capabilities, enabling efficient computation

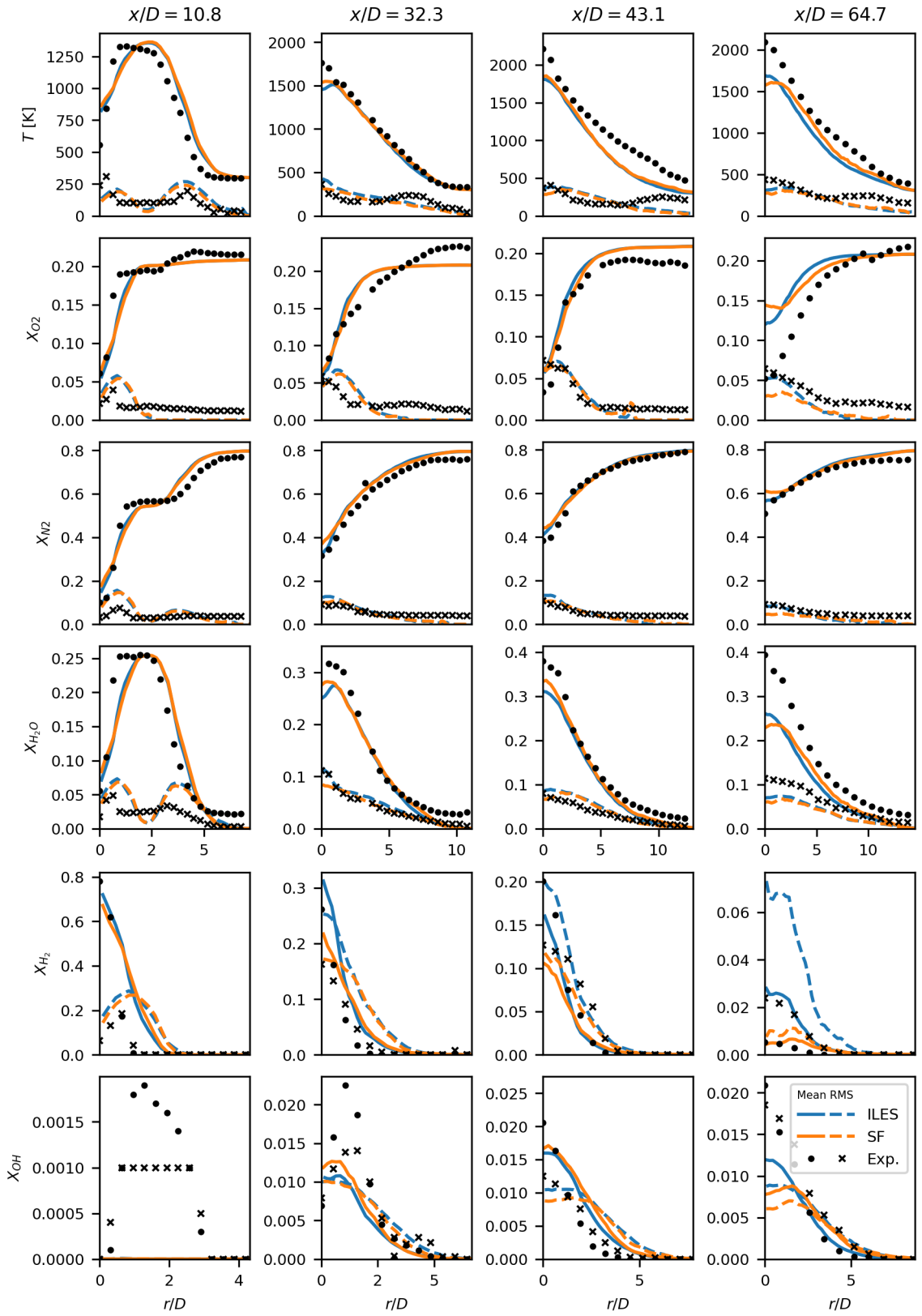



Figure 3.14: Radial profiles of mean (solid line) and RMS (dashed line) quantities. Blue: implicit LES; Orange: stochastic fields; Black circle and cross: experimental measurement of mean and RMS (Cheng, Wehrmeyer, and Pitz 1991).

while maintaining accuracy. To the author's knowledge, this is the first SF-AMR study added to the literature.

The sub-grid closure models were carefully formulated to preserve conservation and thermodynamic consistency, crucial for numerical stability in compressible flows. The implications of using a conservative system and a stochastic pressure gradient were analysed. Attention was paid when discretising the sub-grid closure terms to ensure conservation, stability, and accuracy, especially across AMR boundaries.

Four validation cases were considered to assess the performance of the SF model:

1. The Ornstein-Uhlenbeck process verified the stochastic solver, achieving the theoretical convergence rate of $N_f^{-1/2}$ and demonstrating that the AMR implementation maintains consistency and convergence across refinement boundaries.
2. The Taylor-Green vortex demonstrated the effectiveness of the velocity PDF as an LES turbulence model, outperforming the conventional Smagorinsky model in both low and high Mach number regimes. The unique advantage of the SF model, which adds turbulent dissipation only when necessary, is highlighted. In addition, it was shown that using 8–16 fields yields a decent approximation of the sub-grid PDF.
3. The turbulence autoignition case revealed the model's characteristics in predicting autoignition in an under-resolved flow field, showcasing its ability to predict extreme non-linear events more effectively compared to implicit LES approaches.
4. The supersonic burner of Cheng, Wehrmeyer, and Pitz 1991; Cheng, Wehrmeyer, Pitz, *et al.* 1994 validated the model's overall performance in supersonic combustion scenarios. The solver was proven robust in highly dynamic flow fields, yielding good agreement with experimental data and LES results from the literature. Compared to implicit LES, the SF model predicted a stronger flame and greater fuel consumption, aligning closely with experimental observations.

In conclusion, the VSPDF-SF-AMR strategy presented in this chapter serves as a robust, accurate, and computationally efficient framework for LES of compressible turbulent reactive flows. It provides a unified closure for all turbulent interactions, valid across all combustion regimes, with particular strengths in applications where sub-grid mixing and non-linear extreme events may be important.

# Chapter 4

# Data-driven generalised Langevin model

Having introduced the joint-velocity-scalar PDF framework, the following two chapters consider two directions for improving it, through increasing the accuracy of the sub-grid model and reducing computational costs. This chapter explores the use of a data-driven approach to better understand and to enhance the Langevin model in the velocity PDF.

## 4.1 Introduction

### 4.1.1 Simplified Langevin model

To understand the effect of the Langevin model, consider an incompressible flow with zero mean gradients. The Reynolds stress equation in a reference frame that moves with the mean flow[1] can be simplified as an ODE (Haworth and Pope 1986)

$$\frac{\mathrm{d}\overline{u_i'u_j'}}{\mathrm{d}t} = -\frac{1}{\rho}\overline{u_i'\frac{\partial p'}{\partial x_j} + u_j'\frac{\partial p'}{\partial x_i}} + \overline{\nu u_i'\frac{\partial^2 u_j'}{\partial x_k x_k} + u_j'\frac{\partial^2 u_i'}{\partial x_k x_k}} = N_{ij}\,. \tag{4.1}$$

Compared to the second moment equation of the velocity PDF

$$\frac{\mathrm{d}\overline{u_i'u_j'}}{\mathrm{d}t} = G_{ik}\overline{u_j'u_k'} + G_{jk}\overline{u_i'u_k'} + C_0\epsilon\delta_{ij}\,, \tag{4.2}$$

it is clear that the SF sub-grid model represents the unclosed pressure-scrambling and dissipation terms, collectively labelled as $\mathbf{N}$.

The Reynolds stress tensor $\boldsymbol{\tau}^{\mathrm{sgs}} = \overline{u_i'u_j'}$ can be decomposed into an isotropic part and a traceless anisotropic part: $\boldsymbol{\tau}^{\mathrm{sgs}} = 2k_{\mathrm{sgs}}(\mathbf{I}/3 + \mathbf{b})$, where $\mathbf{I}$ is the identity matrix, and the

[1] The assumption of zero mean gradients and the choice of reference frame are not necessary because all turbulent transport terms and mean diffusion terms are closed with the PDF method. They are made here solely to simplify the equations.

sub-grid kinetic energy $k_{\text{sgs}}$ and sub-grid stress anisotropy tensor $\mathbf{b}$ are

$$k_{\text{sgs}} = \frac{\tau_{ii}^{\text{sgs}}}{2}\,, \qquad b_{ij} = \frac{\tau_{ij}^{\text{sgs}}}{\tau_{ii}^{\text{sgs}}} - \frac{1}{3}\delta_{ij}\,. \tag{4.3}$$

If the simplified Langevin model (SLM) in (3.9) is applied, (4.2) becomes

$$\frac{\mathrm{d}\tau_{ij}^{\text{sgs}}}{\mathrm{d}t} = -\frac{\epsilon_{\text{sgs}}}{k_{\text{sgs}}}\left(1 + \frac{3C_0}{2}\right)\tau_{ij}^{\text{sgs}} + C_0\epsilon_{\text{sgs}}\delta_{ij}\,. \tag{4.4}$$

This represents a dissipation of $k_{\text{sgs}}$ and a linear return to isotropy:

$$\frac{\mathrm{d}k_{\text{sgs}}}{\mathrm{d}t} = -\epsilon_{\text{sgs}}\,, \qquad \frac{\mathrm{d}b_{ij}}{\mathrm{d}t} = -\frac{3C_0\epsilon_{\text{sgs}}}{2k_{\text{sgs}}}b_{ij}\,. \tag{4.5}$$

As illustrated by Figure 4.1, the trajectory of an initial state forms a straight line towards the origin on the turbulence triangle $(\sqrt[3]{III/2},\ \sqrt{II/3})$, where $II = b_{ij}b_{ji}/2$ and $III = b_{ij}b_{jk}b_{ki}/3$ are the second and third principal components of $\mathbf{b}$.

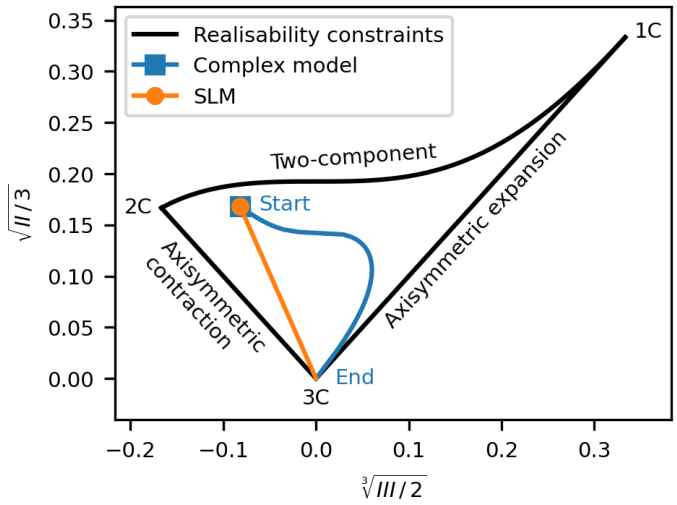



Figure 4.1: Example trajectory of sub-grid stress in the turbulence triangle using SLM and a complex model (Haworth and Pope 1986). The three vertices correspond to three states of turbulence (1C: one-component, rod-like; 2C: axisymmetric two-component, pancake-like; 3C: isotropic) and the three edges represent different physical behaviours (Emory and Iaccarino 2014).

The SLM is simple, computationally inexpensive, and extensively tested. Yet, like many other simple turbulence models, such as the Smagorinsky model, it assumes isotropic flow and correlates poorly with the term it aims to model. The SLM relies on parameters that are calibrated in the RANS context. Although a more theoretically complete generalised Langevin model (GLM) has been proposed, it is rarely used, and no general closure has been presented in the literature. The turbulence dissipation rate $\epsilon$, central to many mixing models, depends on a dimensional argument (3.10) that is strictly valid in the limit of Re $\to \infty$.

In addition, approximating $G_{ij}$ with a scalar essentially sacrifices eight degrees of freedom. While assuming a dependence on $k$ only makes the model unaware of flow anisotropy, and cannot model the relativistic trajectory of returning to isotropy. With these considerations, this chapter sets out to develop a new SGS modelling workflow for LES-PDF approaches based on machine learning techniques.

### 4.1.2 Machine learning in CFD

Machine learning (ML) techniques and deep neural networks (DNN) have been widely applied in fluid dynamics, gaining significant traction over the past decade. This subsection aims to provide a brief overview of the area, more detailed reviews of ML work in CFD and combustion modelling can be found in Zhou *et al.* 2022; Ihme and Chung 2024.

#### Reynolds stress

In non-reacting flows, ML methods are primarily used for predicting the Reynolds stress tensor in both RANS and LES frameworks. These methods can either predict the Reynolds stress tensor directly (King *et al.* 2016; Prat *et al.* 2020), or augment existing turbulence models (Singh *et al.* 2017). DNN is the most popular approach largely thanks to its flexibility. However, its "black box" nature means that the results from a DNN are difficult to interpret, and it can sometimes violate physical constants, such as realisability (the Reynolds stress tensor must be positive semi-definite) and rotational and Galilean invariance. To address these issues, various physics-informed neural networks (PINN) (Ling *et al.* 2016) or symbolic regression approaches (Weatheritt and Sandberg 2016; Chung, Mishra, *et al.* 2021) have been employed. More recently, super-resolution based on sophisticated models (*e.g.* Chung, Akoush, *et al.* 2023; Nista *et al.* 2023) has gained popularity, advancing towards predicting the resolved flow field directly from LES solutions.

The training dataset plays a crucial role in model accuracy, as models tend to deteriorate when extrapolating to high Re, possibly due to the high Re data covering a larger input space. Additionally, Wu *et al.* 2019 point out that data-driven models, acting as an explicit source term, yield an ill-conditioned system, making the simulation sensitive to small perturbations. Beck *et al.* 2019 also show that direct closure models trained on DNS data will replace the LES operator with a DNS operator, leading to numerical instability.

#### Combustion

In combustion modelling, a major use case of ML models is to speed up the evaluation of the chemical source term, especially when dealing with large detailed mechanisms. These models can compute the chemical source term to avoid costly direct integration (Ding *et al.* 2021; Readshaw *et al.* 2021; Nguyen, Barnaud, *et al.* 2023), or can replace traditional flamelet tabulation to reduce memory usage (Ihme, Schmitt, *et al.* 2009; Nikolaou

*et al.* 2022). Another common application is to provide closure for the filtered chemical source term, often using information from nearby cells or even flow field from the entire domain, such as using the convolutional neural network (CNN) or the aforementioned super-resolution models (Lapeyre *et al.* 2019; Seltz, Domingo, Vervisch, and Nikolaou 2019). Other usages of ML techniques in combustion include chemical kinetics reduction, data extraction and analysis, and reduced-order models.

#### PDF methods

All examples discussed above are based on conventional LES methods. ML modelling in the PDF method is a relatively less-explored area. Henry de Frahan, Yellapantula, *et al.* 2019 compare different ML methods, including random forest, DNN, and conditional variational autoencoder, in predicting the joint PDF of mixture fraction and progress variable in a presumed-PDF method. They conclude that DNN provides fast and accurate prediction, though noting that using the finite moment of the PDF limits the model's generalisability. Yao *et al.* 2020 employ a DNN to model the conditional scalar dissipation rate from mean mixture fraction and strain rate. The model takes in the mixture fraction of one realisation and outputs the scalar dissipation rate conditioned on the mixture fraction of that realisation. They report good agreement of the marginal PDF with DNS data in an *a priori* study. Seltz, Domingo, and Vervisch 2021 combine DNN, CNN, and long short-term memory to predict the PDF of particle size for the next time step given the current PDF. This, in the population balance equation framework, is essentially a one-dimensional PDF. Liu and Wang 2022 compare the RF, boosted decision tree, and DNN in predicting the mixing timescale in a power-law IEM. Using a DNS of a high-Karlovitz number (Ka) jet flame as training data, their results indicate that all three ML methods yield similar performances. They suggest that the mixing timescale can be well modelled with four non-dimensional inputs: Ka, Re, progress variable or local equivalence ratio, and the Lewis number (Le).

## 4.2 Tensor function regression

In this study, the GLM is formulated as a tensor function regression problem of $(\epsilon_{\text{sgs}}, \mathbf{G}, C_0) = fn(\boldsymbol{\tau}^{\text{sgs}}, \mathbf{D}, \Delta, \nu)$ such that

$$\epsilon_{\text{sgs}} = \nu \overline{\frac{\partial u_i'}{\partial x_k} \frac{\partial u_i'}{\partial x_k}}, \qquad \mathbf{G}\boldsymbol{\tau}_{\text{sgs}} + (\mathbf{G}\boldsymbol{\tau}_{\text{sgs}})^\top + C_0 \epsilon_{\text{sgs}} \mathbf{I} = \mathbf{N}, \tag{4.6}$$

where the input tensors are

$$\tau_{ij}^{\text{sgs}} = \overline{u_i' u_j'}, \qquad D_{ij} = \frac{\partial \bar{u}_i}{\partial x_j}. \tag{4.7}$$

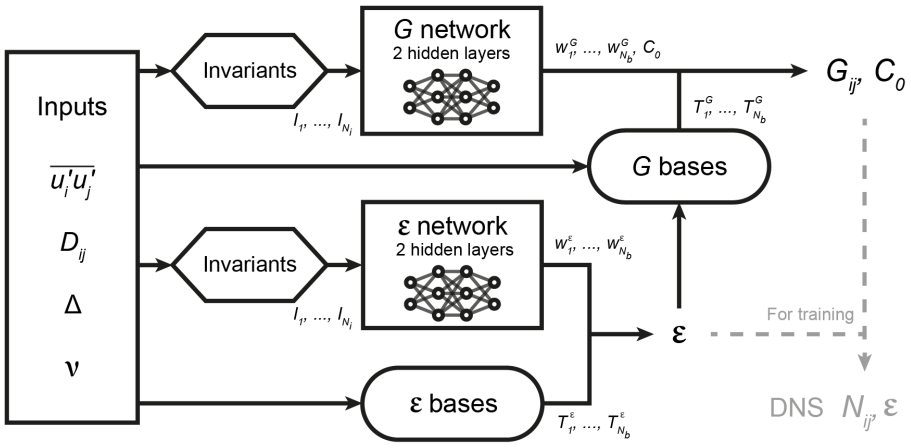



Figure 4.2: Architecture of the tensor-based neural network.

However, the output entries are not entirely "free", as they must preserve the symmetries of the Navier-Stokes equation. In particular, the current work focuses on equivariance under rotation, constant speed translation, and time shift, meaning that any transformed inputs must result in an equally transformed output (Pope 2000, section 2.9).

While the translation and time shift constraints (Galilean invariance) can be easily satisfied by choosing the appropriate inputs, the rotational symmetry is less straightforward. Ling *et al.* 2016 suggests a tensor-based neural network (TBNN) framework, in which a tensor function is written as a weighted combination of $N_b$ bases,

$$\mathbf{G}(\boldsymbol{\phi}) = \sum_{n=1}^{N_b} w_n(I_1(\boldsymbol{\phi}), ..., I_{N_i}(\boldsymbol{\phi}))\mathbf{T}_n(\boldsymbol{\phi})\,. \tag{4.8}$$

For any three-dimensional rotational matrix $\mathbf{R} \in \mathrm{SO}(3)$, $\mathbf{R}\mathbf{T}_n(\boldsymbol{\phi})\mathbf{R}^\top = \mathbf{T}_n(\mathbf{R}\boldsymbol{\phi}\mathbf{R}^\top)$ are the equivariant tensor bases. The scalar weights ($w_n$) are learnt by a DNN, which takes in the $N_i$ invariants $I_m(\boldsymbol{\phi}) = I_m(\mathbf{R}\boldsymbol{\phi}\mathbf{R}^\top)$ such that $w_n$ are invariant under rotation. The Cayley-Hamilton theorem implies that for any matrix function, the set of independent tensor bases is finite.

In addition, these bases are chosen such that the units match those of the output, and the invariants are normalised to be dimensionless. Therefore, the overall output of the model not only respects the symmetries of the Navier-Stokes equations, but is also dimensionally consistent.

Training and testing data for the DNN are extracted from DNS of homogeneous isotropic turbulence and channel flows at the Johns Hopkins Turbulence Database (Li, Perlman, *et al.* 2008). Snapshots of DNS are filtered with various $\Delta$ to compute the inputs and targets. In total, more than 15,000 LES cells are included, which span the entire turbulence triangle and a broad range of $\mathrm{Re}_\Delta = \sqrt{k_{\mathrm{sgs}}}\Delta/\nu$. The TBNN architecture is illustrated in Figure 4.2, where the $\epsilon$ network consists of two hidden layers of 64 and 32

neurons, and the $G$ network has two hidden layers with 128 and 64 neurons due to its larger output size. Both networks use ReLU as activation function, and are trained using the Adam optimiser on a mean squared error (MSE) loss function. The element-wise MSE is equivalent to the Frobenius norm for tensor functions.

First, the SGS dissipation rate is predicted. Although $\epsilon_{\text{sgs}}$ is a scalar, the TBNN architecture is still useful for ensuring invariance and dimensional consistency. Two bases were explored, the first based on the usual sub-grid time scale, while the second one represents some large-scale time scale as used in the Smagorinsky model:

$$T_1 = \frac{k_{\text{sgs}}^{3/2}}{\Delta}, \qquad T_2 = k_{\text{sgs}}|\tilde{S}|\,. \tag{4.9}$$

Six invariants are used:

$$I_1 = \text{Re}_\Delta\,,\ I_2 = \text{tr}(\mathbf{b}^2)\,,\ I_3 = \det(\mathbf{b})\,,\ I_4 = \text{tr}(\hat{\mathbf{S}}^2)\,,\ I_5 = \det(\hat{\mathbf{S}})\,,\ I_6 = \text{tr}(\hat{\mathbf{\Omega}}^2)\,, \tag{4.10}$$

which are normalised to be dimensionless using

$$\hat{\mathbf{S}} = \frac{1}{2}(\mathbf{D} + \mathbf{D}^\top)\frac{\Delta}{\sqrt{k_{\text{sgs}}}}, \quad \hat{\mathbf{\Omega}} = \frac{1}{2}(\mathbf{D} - \mathbf{D}^\top)\frac{\Delta}{\sqrt{k_{\text{sgs}}}}\,. \tag{4.11}$$

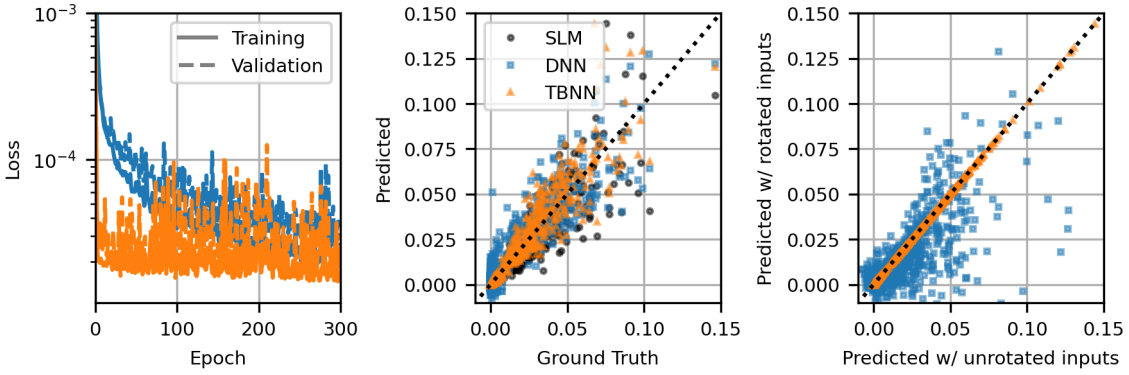



Figure 4.3: NN predictions of $\epsilon_{\text{sgs}}$. Left: Training and testing curves; Middle: ground truth-prediction correlation; Right: predictions with unrotated verses rotated inputs.

Results of the TBNN are compared to the SLM and the outputs from a naive DNN approach which flattens all tensor inputs directly. Figure 4.3 shows that the TBNN yields reasonable agreement with the targets, achieving a Pearson correlation coefficient and $R^2$ coefficient both above 0.9. When comparing the predictions of a set of inputs with those of the same set of inputs after a random rotation (rightmost plot in Figure 4.3), the TBNN approach shows that both predictions are the same, meaning that the TBNN is exactly rotational equivariant (invariant in this case of scalar output). In contrast, the naive DNN approach, trained on randomly rotated input data, does not achieve rotational invariance, which undermines its performance. Some results from the DNN even predict negative $\epsilon_{\text{sgs}}$, which are unphysical.

Table 4.1: Performance metrics of different models in predicting $\epsilon_{\text{sgs}}$. The best and the worst models in each metric are coloured.

| | $R^2$ | Pearson | RMSE | MAE | MAPE (%) |
|---|---|---|---|---|---|
| DNN | 0.84 | 0.92 | 6.07E-03 | 2.62E-03 | 7.05 |
| DNN (rotated inputs) | 0.45 | 0.69 | 1.13E-02 | 4.05E-03 | 8.01 |
| TBNN w/ 1 basis | 0.92 | 0.96 | 4.44E-03 | 1.11E-03 | 2.66 |
| TBNN w/ 2 bases | 0.91 | 0.96 | 4.56E-03 | 1.25E-03 | 3.44 |
| SLM | 0.91 | 0.95 | 4.70E-03 | 1.15E-03 | 2.34 |

The second timescale in (4.9) does not improve the accuracy, as shown by the performance metrics[2] in Table 4.1. In fact, it is found that the weight of the second basis is much smaller, which supports Lumley 1970's findings that the dissipation rate is independent of large-scale shear. Finally, and surprisingly, the SLM performs quite well overall, showing competitive accuracy compared to the data-driven models.

Table 4.2: Performance metrics of different models in predicting $\mathbf{N}$. All entries are summed. The best and the worst models in each metric are coloured.

| | $R^2$ | Pearson | RMSE | MAE | MAPE (%) |
|---|---|---|---|---|---|
| DNN w/ $\mathbf{D}$ | 0.28 | 0.58 | 1.99E-03 | 3.00E-04 | 3.63 |
| DNN w/ $\mathbf{D}$ (rotated inputs) | -38.96 | 0.26 | 1.47E-02 | 1.85E-03 | 10.13 |
| TBNN w/o $\mathbf{D}$ | 0.17 | 0.41 | 2.13E-03 | 3.39E-04 | 14.29 |
| TBNN w/ $\mathbf{D}$ | 0.37 | 0.70 | 1.86E-03 | 2.47E-04 | 0.38 |
| SLM | -44.49 | 0.38 | 1.57E-02 | 1.62E-03 | 84.89 |

For the $\mathbf{G}$ tensor, 11 tensor bases inspired by Haworth and Pope 1986 are used alongside the six invariants as before:

$$\begin{aligned}&\mathbf{T}_1 = \frac{\epsilon_{\text{sgs}}}{k_{\text{sgs}}}\mathbf{I}\,,\ \mathbf{T}_2 = \frac{\epsilon_{\text{sgs}}}{k_{\text{sgs}}}\mathbf{b}\,,\ \mathbf{T}_3 = \frac{\epsilon_{\text{sgs}}}{k_{\text{sgs}}}\mathbf{b}^2\,,\ \mathbf{T}_4 = \text{tr}(\mathbf{D})\mathbf{I}\,,\ \mathbf{T}_5 = \mathbf{D}\,,\\ &\mathbf{T}_6 = \mathbf{D}^\top\,,\ \mathbf{T}_7 = \mathbf{b}\mathbf{D}\,,\ \mathbf{T}_8 = \mathbf{b}\mathbf{D}^\top\,,\ \mathbf{T}_9 = \mathbf{b}^\top\mathbf{D}\,,\ \mathbf{T}_{10} = \mathbf{D}\mathbf{b}\,,\ \mathbf{T}_{11} = \text{tr}(\mathbf{b}\mathbf{D})\mathbf{I}\,.\end{aligned} \tag{4.12}$$

The results are assessed by the prediction of $\mathbf{N}$, as shown in Table 4.2 and Figure 4.4. The TBNN yields a significant improvement over DNN and SLM in all metrics. When tested with rotated input tensors, the DNN sees a severe performance reduction, whereas the TBNN does not, thanks to its built-in symmetries. Analysing the model inputs and outputs suggests that the resolved velocity gradients $\mathbf{D}$ are important for predicting $\mathbf{G}$, which is currently not taken into account by the SLM. It is important to note that a weak correlation, such as the one observed with SLM, does not necessarily indicate poor

[2] $R^2$: Coefficient of determination, explains variance of prediction (-$\infty$, 1];
Pearson: Pearson coefficient, measures correlation with ground truth [-1, 1];
RMSE: Root mean squared error, same as $L_2$ error [0, $\infty$);
MAE: Mean absolute error, same as $L_1$ error [0, $\infty$);
MAPE: Percentage error [0, $\infty$)%

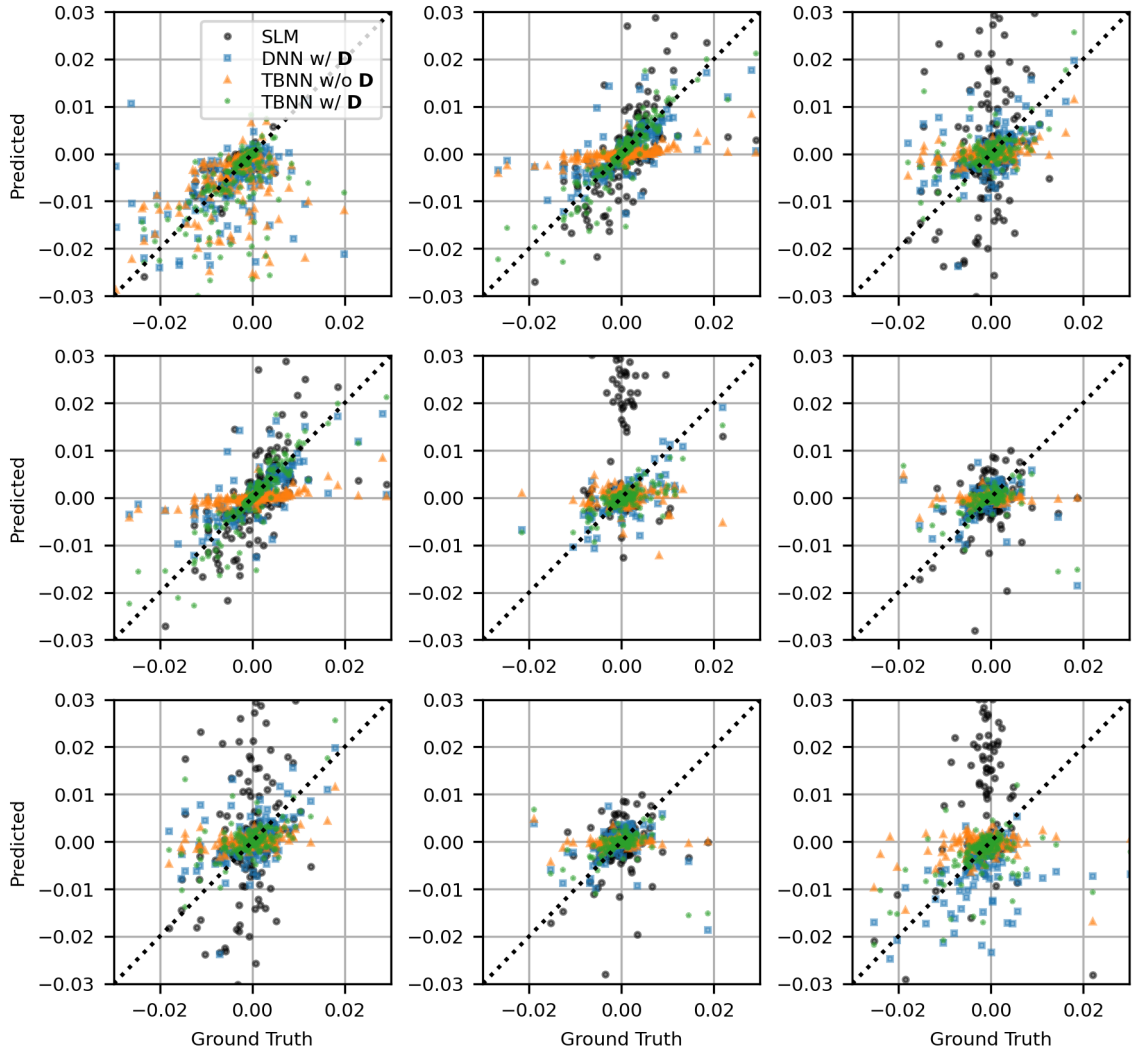



Figure 4.4: NN predictions of the $\mathbf{N}$ tensor.

model performance, as the effects of SGS interactions, such as dissipation and return to isotropy, can still be captured even if the structural representation differs markedly (see the discussion regarding functional and structural modelling in subsection 2.2.1). Nevertheless, this *a priori* test demonstrates the effectiveness of the TBNN approach in tensor function regression problems, which are common in turbulence modelling.

## 4.3 Summary

This chapter developed a tensor-based neural network (TBNN) to replace the simplified Langevin model (SLM) in the velocity PDF. The TBNN architecture demonstrated considerable potential for preserving physical symmetries, including Galilean invariance, rotational equivalence, and dimensional consistency, making it attractive for tensor regression problems in turbulence modelling. *A priori* validation using DNS data showed promising

improvement over the SLM, reducing $L_1$ and $L_2$ errors by up to an order of magnitude. The TBNN also consistently outperformed traditional DNN across all performance metrics. Another interesting finding is that resolved velocity gradients are important for predicting $\mathbf{G}$, which should be included in the model inputs.

To apply this model to SF simulation, several challenges need to be overcome. For instance, how to ensure that the predicted $\mathbf{G}$ results in a physically realisable stress tensor; how to optimise the model architecture and implementation such that it can integrate efficiently with the CFD solver; and whether the added cost of evaluating the model translates to meaningful accuracy improvement in *a posteriori* test cases. These questions will be explored in future research. The remainder of this thesis will focus on another direction to enhance the LES-PDF approach, namely, by reducing the computational cost through AMR and wall modelling.

# Chapter 5

# Wall-modelled stochastic fields

This chapter extends the joint-velocity-scalar stochastic fields (SF) to near-wall flows. The high computational costs associated with resolving viscous length scales are circumvented by coupling the SF with a state-of-the-art wall model. The necessary modifications to the model will be discussed, and the solver will be evaluated in a canonical channel flow case.

## 5.1 Introduction

The preceding chapters demonstrated that the joint-velocity-scalar probability density function (VSPDF) can be used as a unified framework for modelling turbulent reacting flows. It provides closure for all sub-grid turbulent transports, turbulence-chemistry interactions, and potentially non-ideal equations of state, without relying on assumptions of specific combustion regimes or flame structures. This model can effectively capture the production and decay of turbulence in a large eddy simulation (LES) context and can accurately predict autoignition in a supersonic jet flame.

Since most combustion applications occur in confined geometries, accurate prediction of wall-bounded turbulent flow can be of extreme importance to the quantities of interest. However, applying a velocity PDF model near walls is not trivial, as turbulent stresses become highly anisotropic and must follow certain asymptotic scalings close to the wall (Dreeben and Pope 1998; Wacławczyk *et al.* 2004). In high-speed flows, the challenge becomes even more complex due to significant variations in temperature and density within the boundary layer (Yang, Urzay, *et al.* 2018).

Most attempts to adapt the PDF model near walls focus on modelling the turbulent kinetic energy dissipation rate $\epsilon$ in the proximity of solid walls. Early works by Dreeben and Pope 1997a,b employed a joint PDF of velocity and turbulent frequency ($\omega = 1/\tau$). They suggest that $\epsilon \propto u_\tau^3/\kappa y$ and the turbulent length scale $\ell \propto y$ near the wall, where $y$ is the distance to the wall. A tensor dissipation term $\wp_{ij} \propto 1/y$ is proposed to account for the non-local effect of fluctuating pressure. The approach was later revised in Dreeben

and Pope 1998 to include an additional dissipation in the wall-normal velocity component. Their method was extended by Wacławczyk *et al.* 2004, who proposed a blending function $\propto y$ to switch between the near-wall dissipation model and the standard homogeneous isotropic model away from walls.

It is important to note that the above literature considers turbulent stress in the Reynolds-averaged Navier-Stokes (RANS, ensemble average) context. In LES (spatial filter), resolved large eddies capture most anisotropic and non-local effects, and the sub-grid stress is expected to return to isotropy much quicker than the RANS stress. Hence, in this work, it is assumed that the tensor $\wp_{ij}$ is unnecessary and the simpler simplified Langevin model (SLM) of Haworth and Pope 1986 would suffice in an LES framework. Nevertheless, the model needs to be modified near the wall to ensure that the modelled sub-grid kinetic energy behaves correctly.

For clarity in notation, we denote turbulent quantities in the RANS and LES using

| | | | | |
|---|---|---|---|---|
| RANS: | $k\,,$ | $\epsilon\,,$ | $\phi = \langle\phi\rangle + \phi' = \{\phi\} + \phi''\,,$ | $\langle\rho\phi\rangle = \langle\rho\rangle\{\phi\}\,,$ |
| LES: | $k_{\text{sgs}}\,,$ | $\epsilon_{\text{sgs}}\,,$ | $\phi = \overline{\phi} + \phi' = \tilde{\phi} + \phi''\,,$ | $\overline{\rho\phi} = \bar{\rho}\tilde{\phi}\,.$ |

Another major challenge is that previous studies require wall-resolving grids, whose cost is estimated to scale with Reynolds number $\mathrm{Re}^{1.8}$ in LES (Piomelli 2008; Choi and Moin 2012), rendering them impractical for many engineering applications. This requirement can be alleviated using hybrid RANS/LES approaches, *e.g.* detached-eddy simulation (DES) of Spalart 2009, or LES wall models, where the near-wall region is modelled instead of resolved, see reviews of Larsson, Kawai, *et al.* 2016; Bose and Park 2018.

The Eulerian nature of the SF formulation allows the direct application of these near-wall modelling strategies. This simplifies the effort to apply the PDF method close to walls and allows straightforward extension to high-speed flows, *e.g.*, by incorporating the energy equation into an ODE-based wall model (Kawai and Larsson 2012).

## 5.2 Wall fluxes model

The boundary layer is a thin region near a wall where a steep velocity gradient exists as a result of the no-slip condition. Its profile is self-similar with respect to the non-dimensional distance and velocity[1],

$$y^+ = \frac{y u_\tau \rho_w}{\mu_w}\,, \qquad u^+ = \frac{u}{u_\tau}\,, \tag{5.1}$$

where $u_\tau = \sqrt{\tau_w/\rho_w}$ is the friction velocity, and $\rho_w$, $\mu_w$, $\tau_w$, are density, dynamic viscosity, and shear stress at the wall ($y = 0$), respectively. A wall-resolved LES (WRLES) requires

[1]Strictly speaking, this scaling rule is only valid for incompressible flows. Extensions to compressible flows are typically done by considering a compressibility transformation that maps the compressible profiles onto the incompressible ones. See *e.g.* Modesti and Pirozzoli 2016 for a summary.

the first grid point to be positioned at $y^+ \approx 1$. As $u_\tau$ increases with Re, the number of grid points required to maintain this condition grows quickly. Alternatively, wall-modelled LES (WMLES) strategies leverage some universality of the boundary layer to model, instead of resolve, the near-wall region. Therefore, the grid-point requirement is only bounded by the outer turbulence scales. The cost savings can be up to several orders of magnitude, especially when Re is high (Choi and Moin 2012; Yang and Griffin 2021).

Although LES wall modelling has been widely used in subsonic flows, extensions and applications to high-speed flows are relatively limited. This work uses the equilibrium wall stress model by Kawai and Larsson 2012, designed for compressible boundary layers. This wall model has been applied to study supersonic non-reacting (Bermejo-Moreno, Campo, *et al.* 2014; Chen, Lv, *et al.* 2022; van Noordt *et al.* 2022) and reacting (Larsson, Laurence, *et al.* 2015) flows, and hypersonic flows (Fu, Karp, *et al.* 2021).

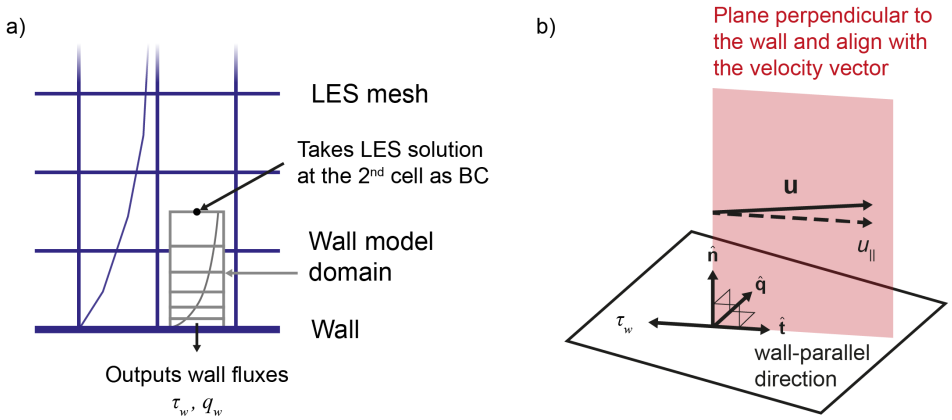



Figure 5.1: Illustrations of (a) the one-dimensional domain used in the wall model and (b) the wall-parallel coordinate system in three dimensions.

Two coupled ODEs are solved on a one-dimensional virtual domain normal to the wall. The virtual domain is embedded in the LES grid, which takes the LES solution as boundary conditions at the far end, and no-slip adiabatic or isothermal wall conditions on the wall end (see Figure 5.1). The output wall shear stress $\tau_w$ and heat flux $q_w$, are, in turn, used to update the LES flow field.

$$\frac{d}{dy}\left[(\mu+\mu_t)\frac{du_\parallel}{dy}\right] = 0\,, \tag{5.2}$$

$$\frac{d}{dy}\left[(\mu+\mu_t)u_\parallel\frac{du_\parallel}{dy} + (\kappa+\kappa_t)\frac{dT}{dy}\right] = 0\,, \tag{5.3}$$

where $d/dy$ denotes wall-normal derivative, and $u_\parallel$ is the wall-parallel velocity. Turbulent viscosity and conductivity are modelled following Kawai and Larsson 2012,

$$\mu_t = \varkappa\rho u_\tau y\left[1-\exp\left(-\frac{y^+}{A^+}\right)\right]^2, \qquad \kappa_t = \frac{c_p\mu_t}{\mathrm{Pr}_t}\,, \tag{5.4}$$

where the von Kármán constant is $\varkappa = 0.41$, and the model parameters are $\mathrm{Pr}_t = 0.9$, $A^+ = 17$ (Kawai and Larsson 2012).

This two-ODE wall model can be seen as an extension of the classical logarithmic law. Approaching the limit of constant density and temperature, the two ODEs reduce to only one for velocity, which can be solved to yield a logarithmic law profile.

Note that the current model assumes equilibrium (self-similar) boundary layers with zero pressure gradient. However, previous studies have shown that the equilibrium wall model performs effectively even in flows with non-negligible pressure gradients, such as in shock-boundary layer interactions (Bermejo-Moreno, Campo, *et al.* 2014; Larsson, Laurence, *et al.* 2015). Bose and Park 2018 suggest that the validity of equilibrium wall models depends on the near-wall resolution relative to the local boundary layer thickness, as pressure gradient effects are resolved by the outer LES. A higher near-wall resolution may be required in the presence of strong pressure gradients. Non-equilibrium wall models *e.g.,* Kawai and Larsson 2013; Park and Moin 2014 could potentially offer more accurate results by retaining temporal derivatives, pressure gradient, and convective terms in the wall model equations, albeit at higher computational costs.

### 5.2.1 Numerical solution

The ODEs (5.2)–(5.3) are solved numerically using an iterative solver. The one-dimensional virtual grid is defined as

$$y_i = h_{\mathrm{wm}} \frac{r^{i-1} + r^i - 2}{r^{N_g-1} + r^{N_g} - 2} \quad \text{for } i = 1, ..., N_g \,, \tag{5.5}$$

where $y_i$ is the location of the $i^{\mathrm{th}}$ grid point, $h_{\mathrm{wm}}$ is the height of the wall model domain, also known as the matching point. $h_{\mathrm{wm}}$ is chosen to be the second LES cell from the wall, as suggested by Kawai and Larsson 2012. $r$ and $N_g$ are the stretch factor and the number of grid points, which are set to 1.1 and 30, respectively. This choice of $r$ and $N_g$ is tested to be robust and effectively balances computational cost and accuracy. The above formula ensures that $y_{N_g} = h_{\mathrm{wm}}$ and the grid points cluster towards the wall where large gradients of velocity and temperature are observed.

The velocity equation is discretised using central difference:

$$\mu^{\mathrm{eff}}_{i+\frac{1}{2}} \frac{u_{i+1} - u_i}{y_{i+1} - y_i} - \mu^{\mathrm{eff}}_{i-\frac{1}{2}} \frac{u_i - u_{i-1}}{y_i - y_{i-1}} = 0 \quad \text{for } i = 2, ..., N_g - 1 \,, \tag{5.6}$$

with the effective viscosity being the sum of the molecular and turbulent viscosities

$$\mu^{\mathrm{eff}}_{i+\frac{1}{2}} = \frac{1}{2}(\mu^{\mathrm{eff}}_{i+1} + \mu^{\mathrm{eff}}_i) = \frac{1}{2}(\mu_{i+1} + \mu_{t,i+1} + \mu_i + \mu_{t,i}) \,. \tag{5.7}$$

Dirichlet boundary conditions are applied at both ends of the domain. At the wall, $y_0 = 0$

and $u_0 = 0$, hence

$$\mu^{\text{eff}}_{\frac{3}{2}} \frac{u_2 - u_1}{y_2 - y_1} - \mu^{\text{eff}}_{\frac{1}{2}} \frac{u_1}{y_1} = 0\,. \tag{5.8}$$

At the far end, the velocity is set to the velocity in the LES: $u_{N_g} = u_{||,\text{LES}}$.

The temperature equation is discretised similarly. For $i = 2, ..., N_g - 1$:

$$\kappa^{\text{eff}}_{i+\frac{1}{2}} \frac{T_{i+1} - T_i}{y_{i+1} - y_i} - \kappa^{\text{eff}}_{i-\frac{1}{2}} \frac{T_i - T_{i-1}}{y_i - y_{i-1}} = \mu^{\text{eff}}_{i-\frac{1}{2}} u_{i-\frac{1}{2}} \frac{u_i - u_{i-1}}{y_i - y_{i-1}} - \mu^{\text{eff}}_{i+\frac{1}{2}} u_{i+\frac{1}{2}} \frac{u_{i+1} - u_i}{y_{i+1} - y_i}\,, \tag{5.9}$$

where

$$\kappa^{\text{eff}}_{i+\frac{1}{2}} = \frac{1}{2}(\kappa^{\text{eff}}_{i+1} + \kappa^{\text{eff}}_i) = \frac{1}{2}(\kappa_{i+1} + \kappa_{t,i+1} + \kappa_i + \kappa_{t,i})\,, \tag{5.10}$$

$$u_{i-\frac{1}{2}} = \frac{u_i + u_{i-1}}{2}\,. \tag{5.11}$$

For isothermal walls with a wall temperature of $T_w$, the boundary condition at the wall is

$$\kappa^{\text{eff}}_{\frac{3}{2}} \frac{T_2 - T_1}{y_2 - y_1} - \kappa^{\text{eff}}_{\frac{1}{2}} \frac{T_1 - T_w}{y_1} = \mu^{\text{eff}}_{\frac{1}{2}} \frac{u_1^2}{2y_1} - \mu^{\text{eff}}_{\frac{3}{2}} \frac{u_2 + u_1}{2} \frac{u_2 - u_1}{y_2 - y_1}\,. \tag{5.12}$$

For adiabatic walls, $T_0 \approx T_1$,

$$\kappa^{\text{eff}}_{\frac{3}{2}} \frac{T_2 - T_1}{y_2 - y_1} = \mu^{\text{eff}}_1 \frac{u_1^2}{2y_1} - \mu^{\text{eff}}_{\frac{3}{2}} \frac{u_2 + u_1}{2} \frac{u_2 - u_1}{y_2 - y_1}\,. \tag{5.13}$$

The temperature at the far end is set to the LES solution: $T_{N_g} = T_{\text{LES}}$.

Wall shear stress and heat flux are computed by

$$\tau_w = \mu_0 \frac{u_1}{y_1}\,, \qquad q_w = \kappa_0 \frac{T_1 - T_w}{y_1}\,. \tag{5.14}$$

The above discretised equations can be written as tridiagonal matrix equations, which are solved using an LU solver. The solution procedure is

1. Initial guesses: $u = u_{||,\text{LES}}\, y/h_{\text{wm}}$, $T = T_{\text{LES}}$;
2. Update $u$ based on $u$ and $T$ from the previous iteration;
3. Update $T$ based on the newly computed $u$ and $T$ from the previous iteration;
4. Compute error as the difference between the solutions in the two iterations. Repeat step 2 until the error in $u$ or $T$ converge to below 0.1%.

To the LES solver, the wall model acts like a black box function which takes $(\rho, u_{||}, T)$ at $h_{\text{wm}}$ from the LES solution, and outputs $\tau_w$ and $q_w$ which are incorporated into the EB wall fluxes:

$$\tau_w,\, q_w = WM(h_{\text{wm}}, \rho_{\text{LES}}, u_{||,\text{LES}}, T_{\text{LES}}, T_w)\,. \tag{5.15}$$

### 5.2.2 Coordinate system

Note that the ODE coordinate system is normal to the wall. Trigonometric operations are needed to extract the wall-parallel velocity from the LES. In three dimensions, we define the wall-normal and wall-parallel directions on a plane which is normal to the wall and tangent to the velocity vector. The output $\tau_w$ also aligns with the wall-parallel direction, see Figure 5.1.

Mathematically, the wall-normal unit vector $\hat{\mathbf{n}}$ and the two wall-parallel unit vectors $\hat{\mathbf{t}}$, $\hat{\mathbf{q}}$ are perpendicular to each other, so their dot products are zero:

$$\hat{\mathbf{n}} \cdot \hat{\mathbf{t}} = 0\,, \qquad \hat{\mathbf{n}} \cdot \hat{\mathbf{q}} = 0\,, \qquad \hat{\mathbf{t}} \cdot \hat{\mathbf{q}} = 0\,. \tag{5.16}$$

The LES velocity vector $\mathbf{u}$ can be projected to this orthonormal basis by

$$\mathbf{u} = (\mathbf{u} \cdot \hat{\mathbf{n}})\hat{\mathbf{n}} + (\mathbf{u} \cdot \hat{\mathbf{t}})\hat{\mathbf{t}} + (\mathbf{u} \cdot \hat{\mathbf{q}})\hat{\mathbf{q}}\,. \tag{5.17}$$

This projection is not unique unless we define $\mathbf{u} \cdot \hat{\mathbf{q}} = 0$, *i.e.*, $\mathbf{u}$ is on the plane of $\hat{\mathbf{n}}$ and $\hat{\mathbf{t}}$. Hence,

$$(\mathbf{u} \cdot \hat{\mathbf{t}})\hat{\mathbf{t}} = \mathbf{u} - (\mathbf{u} \cdot \hat{\mathbf{n}})\hat{\mathbf{n}}\,, \tag{5.18}$$

and since $\hat{\mathbf{t}}$ is a unit vector, the wall-parallel unit vector is computed by

$$\hat{\mathbf{t}} = \frac{\mathbf{u} - (\mathbf{u} \cdot \hat{\mathbf{n}})\hat{\mathbf{n}}}{\|\mathbf{u} - (\mathbf{u} \cdot \hat{\mathbf{n}})\hat{\mathbf{n}}\|}\,, \qquad u_{||} = \mathbf{u} \cdot \hat{\mathbf{t}}\,. \tag{5.19}$$

## 5.3 Near-wall treatments for stochastic fields

### 5.3.1 Coupling with the wall fluxes model

The wall model is applied to the mean/filtered flow quantities, and all SF share the same $\bar{\tau}_w$ and $\bar{q}_w$. This allows the formulation to stay consistent with the filtered diffusive fluxes in (3.23)–(3.25) in the limit of the wall[2]. This implicitly assumes that the wall model is linear, such that the wall fluxes computed using the filtered flow states are the filtered wall fluxes. The assumption is verified by checking the sensitivity of the wall model.

Centring around the set of input states representative of the scramjet isolator in chapter 6, $(h_{\text{wm}}, \rho_{\text{LES}}, u_{||,\text{LES}}, T_{\text{LES}}, T_w) = (3{\times}10^{-3}\text{ m}, 0.1\text{ kg/m}^3, 500\text{ m/s}, 600\text{ K}, 300\text{ K})$, $u_{||,\text{LES}}$ and $T_{\text{LES}}$ are perturbed by 20% on each side, and the relative change in the output $\tau_w$ and $q_w$ are recorded. Density variation is not considered here because it is usually small,

[2]Recall the definition of the PDF (3.2) that the location where that flow state is observed is unknown—it can be up to $\Delta$ around the grid point. As a result, the distance from the wall to the matching point, $h_{\text{wm}}$, is not properly defined. This may be a consequence of the wall model, similar to the diffusion terms, requiring positional information that is not included in the one-point PDF. This prevents the use of SF flow states as inputs to the wall model.

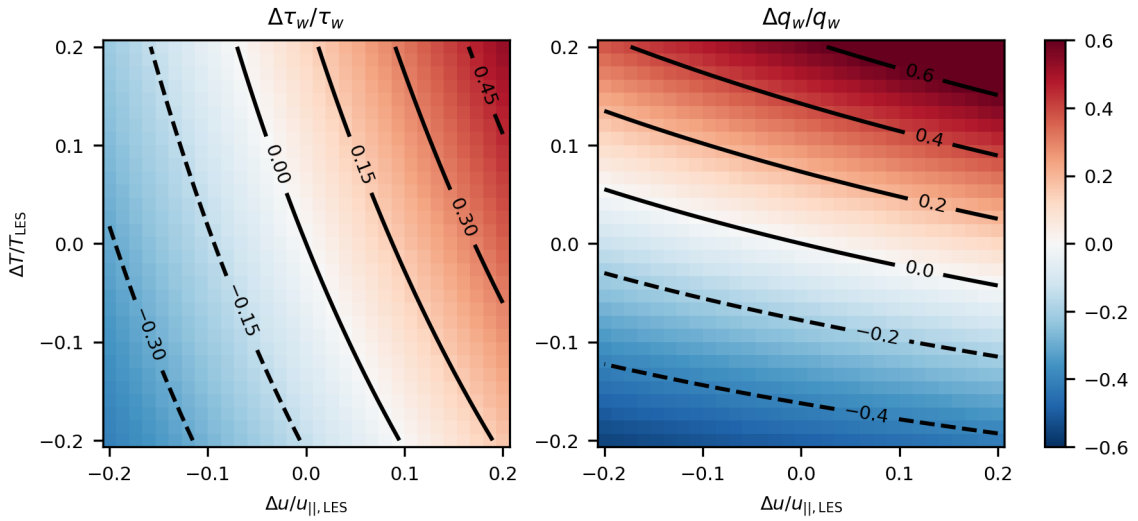



Figure 5.2: Changes in the wall model outputs in response to the changes in inputs. Isocontours of the outputs are overlaid on the graphic.

as discussed in section 2.2. Figure 5.2 shows that even with 20% variation in the inputs, which is large considering sub-grid levels, the outputs of the wall model change linearly, as evidenced by the isocontours being close to straight lines. The difference between the averaged $\overline{\tau_w(\cdots)}$ and the $\tau_w(\overline{\cdots})$ computed using the mean input states is less than 0.6%, and that of $|\overline{q_w(\cdots)} - q_w(\overline{\cdots})|$ is less than 1.5%. The coupling procedure using the filtered flow quantities is therefore appropriate.

### 5.3.2 Sub-grid model treatments

While the wall stress model accurately captures the mean flow, additional measures are required to ensure the proper behaviour of sub-grid quantities near walls. If we follow Dreeben and Pope 1997b, in the logarithmic layer,

$$k \propto -\langle u'v' \rangle \propto u_\tau^2 \,, \tag{5.20}$$

$$\epsilon = \mathcal{P} = -\langle u'v' \rangle \frac{u_\tau}{\kappa y} \propto \frac{k^{3/2}}{\kappa y} \,, \tag{5.21}$$

where $u$ and $v$ denote the wall-parallel and wall-normal velocity components, respectively. These relationships were originally discussed in RANS context. *A priori* analysis by filtering the DNS turbulent channel flows by Lee and Moser 2015 reveals that although (5.20) is true for LES, (5.21) is not. Therefore, even though $k_{\mathrm{sgs}}^{3/2}/(\kappa y)$ follows accurately the production-like term $\hat{\mathcal{P}}_{\mathrm{sgs}} = \overline{u'v'}u_\tau/(\kappa y)$, it fails to model $\epsilon_{\mathrm{sgs}}$ as intended. This is a consequence of the fact that turbulence production and dissipation do not equate at the same location—equilibrium is only observed in a statistically averaged sense.

Surprisingly, Figure 5.3 shows that the $\epsilon_{\mathrm{sgs}}$ model in (3.10), assuming isotropic flow, agrees well with DNS across the whole range of $y^+$ at both $\mathrm{Re}_\tau$ tested. This can be

explained physically by the fact that even though $\ell$ decreases with $y$, $C_\epsilon$ also changes, possibly due to a change in the dissipation mechanism or breakdown of the equilibrium hypothesis on which the dissipation model is based, leading to the two effects cancelling each other out.

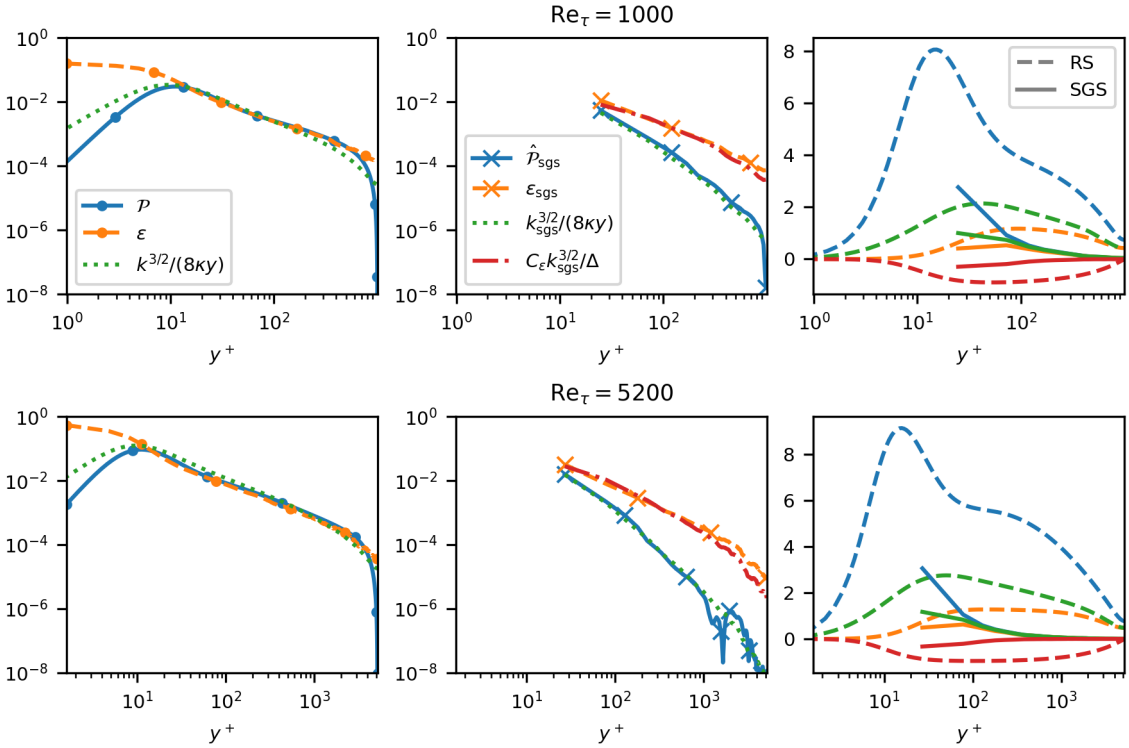



Figure 5.3: Left: Production ($\mathcal{P}$) and dissipation ($\epsilon$) of turbulent kinetic energy ($k$) in RANS, along with (5.21); Middle: Production-like $\hat{\mathcal{P}}_{\text{sgs}}$ and dissipation ($\epsilon_{\text{sgs}}$) of sub-grid kinetic energy ($k_{\text{sgs}}$) in LES (box filter, $\Delta^+ \approx 50$), along with (3.10) and (5.21); Right: Reynolds stress (dash line) and sub-grid stress (solid line) normalised by $u_\tau$, in descending order of the peak value, $u'u'$, $v'v'$, $w'w'$, $u'v'$, respectively.

Another key observation is that LES sub-grid stresses are significantly smaller than RANS stresses and return to isotropy much more rapidly. This suggests that in LES, the resolved large eddies primarily capture the flow anisotropy, while the sub-grid scales align more closely with Kolmogorov 1962's hypothesis. As a result, the applicability of the simple model is substantially extended.

Another requirement for the model is that $C_0 \to 0$ as $y \to 0$ (Dreeben and Pope 1997b). This represents the reliability constraint of the Reynolds stress tensor. More importantly, the stochastic forcing $\sqrt{C_0\epsilon}\,\mathrm{d}\mathbf{W}$ normal to the wall must vanish as it approaches the wall to satisfy the non-permissible condition. If this is not done, spurious pressure waves will form, as shown in section 5.4. In this work, $C_0$ is to decay linearly with $y$,

$$C_0 = \min(C_{0,\text{LM}}, y^+/a^+)\,, \tag{5.22}$$

where $C_{0,\text{LM}}$ is the $C_0$ from the Langevin model (subsection 3.1.2) or potentially from

the neural network approach (section 4.2), and $a^+$ is a constant to be determined in subsection 5.4.2. Additionally, for numerical stability, $C_0 = 0$ is applied to the two cells closest to the wall. This is consistent with the region where the wall stress model is applied.

## 5.4 Supersonic turbulent channel flow

The supersonic turbulent channel flow of Modesti and Pirozzoli 2016 is used to test the wall-modelled SF strategy. The case parameters are listed in Table 5.1. The computational domain $12h \times 2h \times 4h$ is discretised into a uniform mesh of $192 \times 32 \times 64$, where $h$ is the channel's half height. This results in $y^+ = 31.7$ for the first grid point and $h^+_{\mathrm{wm}} = 95.2$ for the wall model matching point. Top and bottom boundaries are isothermal non-slip walls of 500 K, and cyclic (periodic) conditions are applied on the other boundaries for homogeneity in the streamwise and spanwise directions. To maintain a statistically stationary flow, a (mass-specific) body force is applied in the flow direction, using the friction velocity $u_\tau$ from the DNS:

$$f_x = \frac{\rho_w u_\tau^2}{\rho_b h} \,. \tag{5.23}$$

LES with the WALE model of Nicoud and Ducros 1999 (p. 39) are used for a comparative assessment with SF. All simulations share the same mesh and numerical schemes (TENO5-HLLC for inviscid fluxes and $4^{\mathrm{th}}$-order central difference for diffusive fluxes).

Table 5.1: Summary of simulation parameters (Modesti and Pirozzoli 2016).

| Parameter [unit] | Value |
|---|---|
| Bulk Reynolds number $\mathrm{Re}_b = \rho_b u_b h/\mu_w$ [-] | 17000 |
| Bulk Mach number $\mathrm{M}_b = u_b/c_w$ [-] | 1.5 |
| Friction velocity $u_\tau$ [m/s] | 29.1343 |
| Wall temperature $T_w$ [K] | 500 |
| Wall dynamic viscosity $\mu_w$ [kg/m-s] | $2.67\times10^{-5}$ |
| Channel half height $h$ [m] | 0.006845 |
| Domain size $L_x, L_y, L_z$ [m] | $12h$, $2h$, $4h$ |
| Mesh size $N_x, N_y, N_z$ [-] | 192, 32, 64 |

### 5.4.1 Comparison with DNS

Due to the coarse near-wall resolution, LES without a wall model underpredicts both $\bar{\tau}_w$ and $\bar{q}_w$, leading to an overestimated bulk velocity $\langle u \rangle$ and temperature $\langle T \rangle$, as shown in Figure 5.4. Applying the wall model significantly improves the results. The SF predicts a lower $\langle T \rangle$ both with and without wall model, by approximately 5% compared to WALE. The exact reason behind this phenomenon remains unclear, but possibly due to the lower density near the walls as compared to the WALE model. Furthermore, SF without the

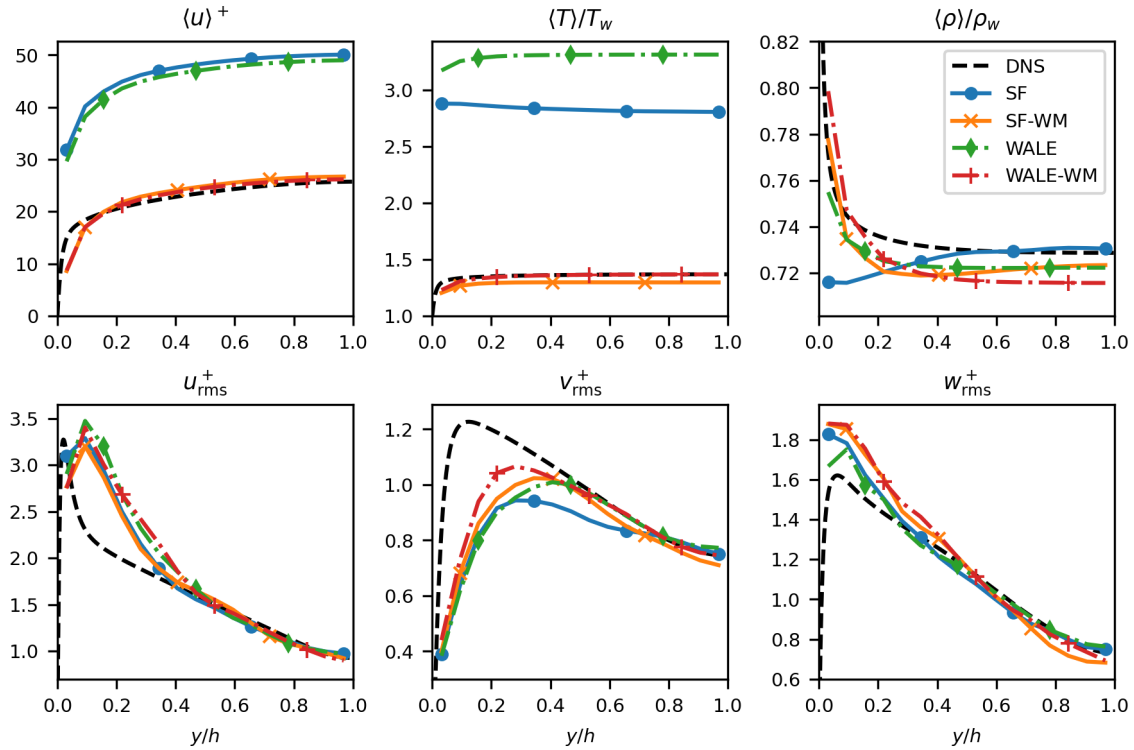



Figure 5.4: Mean and RMS profiles. Labels are "DNS": DNS from Modesti and Pirozzoli 2016; "SF": SF without wall model; "SF-WM": SF with wall model; "WALE": WALE without wall model; "WALE-WM": WALE with wall model. Quantities with the superscript + are non-dimensionalised with $u_\tau$ from the DNS.

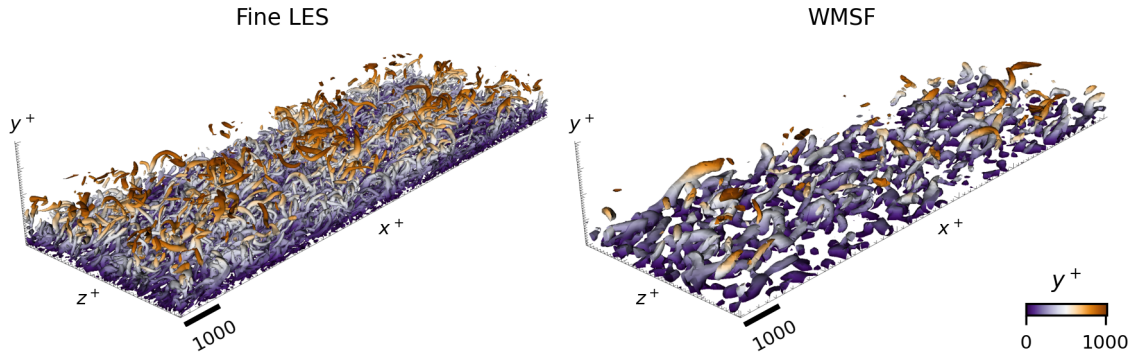



Figure 5.5: $Q$-criterion contours of a fine-grid ILES ($\Delta x^+ = \Delta y^+ = \Delta z^+ = 7$) and the wall-modelled SF ($\Delta x^+ = \Delta y^+ = \Delta z^+ = 31.7$).

wall model and the $C_0$ modification performs worse than other approaches and deviates further from DNS, especially in density, showcasing the importance of modifying $C_0$.

The root-mean-square (RMS) velocities for all simulations agree well with DNS results, even in the absence of a wall model. This suggests that the RMS values are less sensitive to wall stress than the mean values. However, discrepancies are observed within a few grid points from the wall. This is somewhat expected because, even if $\bar{\tau}_w$ is predicted correctly,

the grid is too coarse to capture the small eddies in the boundary layer. This is evident by the $Q$-criterion contours plotted in Figure 5.5. While the wall-modelled SF can resolve larger hairpin vortices and quasi-streamwise streak structures in the outer layer, whose size is $O(1000)$ wall units, it struggles to capture the smaller streamwise streaks located closer to the wall (in the logarithmic layer and below) due to the coarse near-wall resolution. This limitation may have some impact on predicting phenomena that are sensitive to the near-wall fluctuations, such as shock-boundary layer interaction. However, since the small vortices also have a short timescale, their influence on larger-scale motion may be limited.

### 5.4.2 Effect of the $C_0$ limiter

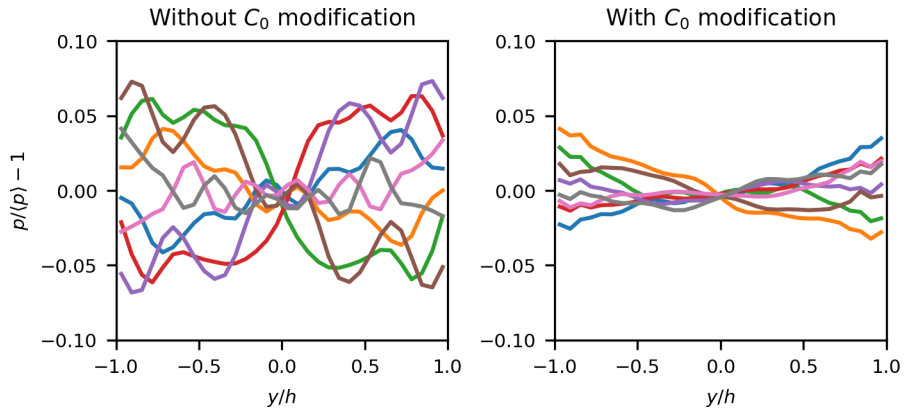



Figure 5.6: Pressure of individual fields with and without near-wall $C_0$ modification (5.22). Each line represents one field.

The direct effect of $C_0$ can be seen in Figure 5.6. Without the modification in (5.22), non-zero $C_0$ in the stochastic term creates a forcing in the wall-normal direction, generating spurious pressure waves that contaminate the SF solution. After applying the $C_0$ modification, the pressure fields are smoother and exhibit less fluctuations.

The limiter constant $a^+$ is empirically calibrated to be 250. It is chosen to be the smallest value that can effectively suppress the pressure fluctuations.

### 5.4.3 Stochastic fields and sub-grid quantities

The effect of the number of fields is examined in Figure 5.7. The prediction of $\langle u \rangle$ is unchanged, while that of $\langle T \rangle$ improves with more fields, but the overall difference remains small. Similarly, the shape and magnitude of the sub-grid kinetic energy $k_{\text{sgs}}$ vary slightly. It is difficult to assess the predictions of $k_{\text{sgs}}$, as they are not available in the literature and are mesh (or filter) dependent. Nevertheless, SFs with the wall model produced $k_{\text{sgs}}$ that follow the general trend, similar to that observed in Figure 5.3, whereas the SF without the wall model fails to replicate it.

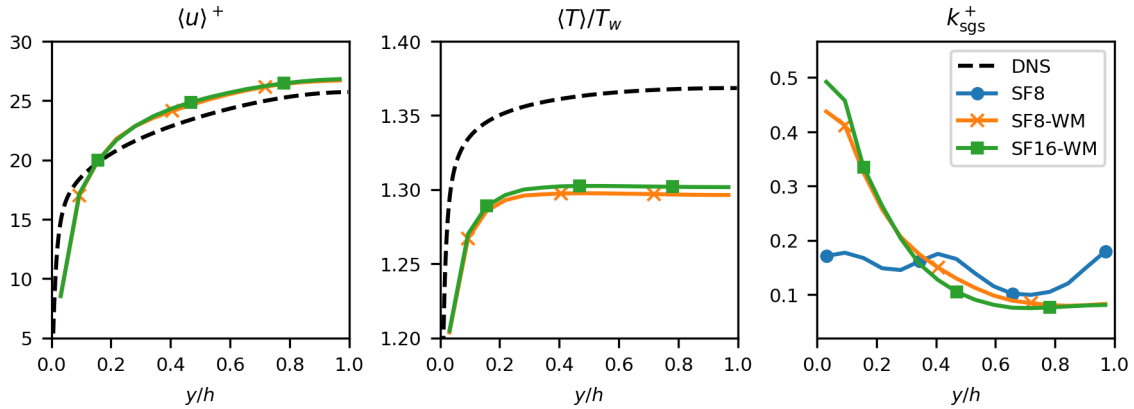



Figure 5.7: Comparison between solutions with 8 and 16 stochastic fields. Quantities with the superscript + are non-dimensionalised with $u_\tau$ from the DNS.

## 5.5 Summary

This chapter proposed a wall-modelled stochastic fields (WMSF) strategy as a straightforward extension for applying the joint-velocity-scalar PDF to wall-bounded flows. The primary objective of this approach was to reduce the high computational costs associated with resolving viscous length scales close to solid walls. This was achieved by coupling the SF with a state-of-the-art wall stress model of Kawai and Larsson 2012 that can accurately predict wall shear stress and heat flux. The Eulerian SF approach simplified the implementation of most existing wall models, with the potential of applying more advanced wall models with PDF methods in the future.

Key results include:

1. Analysis of DNS data demonstrated that the sub-grid dissipation model, originally designed for isotropic flow, is valid in LES across a wide range of $y^+$ values.
2. Modification to the stochastic term ($C_0$) in the SF momentum equation is necessary to ensure it vanishes near the wall, preventing spurious pressure generation.
3. The resultant WMSF framework was tested in a supersonic turbulent channel flow. Its performance was comparable to its WMLES counterpart, showing good agreement with DNS results. The $C_0$ limiter proved effective, and the WMSF produced a realistic profile of sub-grid kinetic energy $k_{\text{sgs}}$, insensitive to the number of fields used.

This novel approach represents a significant improvement over the SF without wall modelling, thereby enabling accurate simulations of wall-bounded turbulent reacting flows, particularly in propulsion applications, while maintaining a reasonable computational cost.

# Chapter 6

# Simulation of a cavity-stabilised ramjet

This chapter applies the wall-modelled stochastic fields (WMSF) developed in the previous chapters to an experimental rig at the University of Michigan (Micka and Driscoll 2008; Micka, Torrez, *et al.* 2009; Micka and Driscoll 2009; Micka 2010). The aims of this study are twofold: the first is to validate the predictive capability of the WMSF framework in simulating the complex flow field and multi-physics phenomena in high-speed propulsion systems; the second is to understand the coupling between the isolator shock train and the combustor.

## 6.1 Case specifications

### 6.1.1 Experimental setup

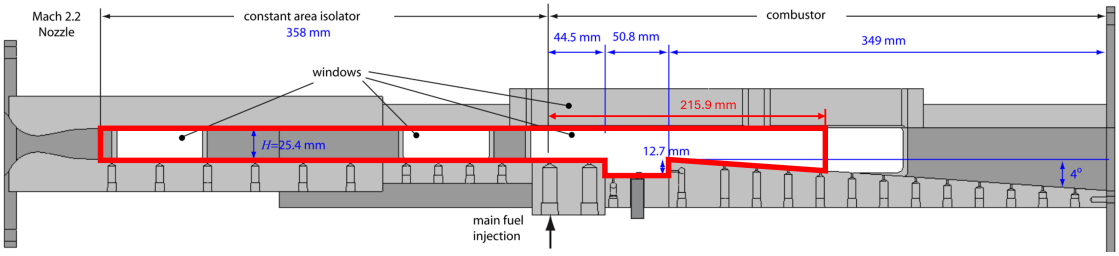



Figure 6.1: Experimental setup with the computational domain marked in red. All sections are rectangular and have a constant width of 38.1 mm. Modified from Micka 2010.

LES are performed on the dual-mode ramjet at the University of Michigan supersonic combustion facility (Micka and Driscoll 2008; Micka, Torrez, *et al.* 2009; Micka and Driscoll 2009; Micka 2010). The complex flow patterns in this configuration are characterised by: 1) the shock-boundary layer interactions (SBLI) and the shock train induced by combustor

back pressure, 2) high-speed fuel injection into a crossflow, and 3) multi-modal flame stabilised by the jet wake and cavity.

The experimental setup is illustrated in Figure 6.1. The Mach 2.2 inflow gas is first heated using an electric heater followed by a pre-burner to raise the stagnation temperature ($T_{0,\text{in}}$) to between 1050 K and 1400 K, while the stagnation pressure is held constant at 590 kPa. Due to the pre-combustion, the inflow gas composition varies with $T_{0,\text{in}}$.

Pure hydrogen fuel is injected sonically[1] through a jet of 2.49 mm diameter, at a stagnation temperature of 288 K (room temperature). The injection pressure is adjusted based on the desired equivalence ratio.

Micka and Driscoll 2008 found that this setup exhibits two distinct flame stabilisation modes: at low $T_{0,\text{in}}$, the flame anchors at the cavity leading edge and the cavity shear layer, while at high $T_{0,\text{in}}$, the flame is stabilised by the jet wake. This study focuses on two cases, one at the highest and the other at the lowest $T_{0,\text{in}}$, to examine whether the SF model can accurately predict the flame position and pressure rise in both cases. The inflow and fuel conditions are detailed in Table 6.1. Based on the inflow conditions and isolator height, the Reynolds number is approximately $10^7$. Given the high stagnation temperature and global equivalence ratio, the engine operates in ram mode, where combustion occurs subsonically.

Table 6.1: Inflow and fuel conditions in the simulations.

| | Hot inflow case | | Cold inflow case | |
|---|---|---|---|---|
| Parameters [unit] | Inflow | Fuel | Inflow | Fuel |
| Mach number $M$ [-] | 2.2 | 1.0 | 2.2 | 1.0 |
| Stagnation temperature $T_0$ [K] | 1400 | 288 | 1100 | 288 |
| Stagnation pressure $p_0$ [kPa] | 590 | 755 | 590 | 845 |
| $H_2O$ mass fraction [-] | 0.145 | 0.0 | 0.085 | 0.0 |
| $O_2$ mass fraction [-] | 0.228 | 0.0 | 0.244 | 0.0 |
| $N_2$ mass fraction [-] | 0.627 | 0.0 | 0.671 | 0.0 |
| $H_2$ mass fraction [-] | 0.0 | 1.0 | 0.0 | 1.0 |
| Global equivalence ratio [-] | 0.27 | | 0.27 | |

### 6.1.2 Computational setup

Since velocity and turbulence measurements are not available from the experiment, the computational domain covers the entire isolator, starting from the exit of the converging-diverging nozzle where a uniform velocity is imposed (see Figure 6.1). An adiabatic no-slip boundary condition is applied to all walls, as suggested by Micka 2010. A comparison with isothermal walls in Figure 6.5 shows that the wall temperature does not affect the shock

[1] Sonic injection is the most common way of injecting gaseous fuel because its injection hole is much easier to manufacture than supersonic injectors (Micka 2010).

and flame structures. The wall model developed in chapter 5 is applied to all solid walls, apart from the fuel injector, because of its small diameter.

For each $T_{0,\text{in}}$, three cases are studied, including a WMILES, a WMSF, and a fine-mesh WMILES. All cases share the same base isotropic mesh, which is adaptively refined around areas of high pressure gradient and vorticity to capture shocks and mixing. Eight SF are employed as a compromise between accuracy and computational cost, which is also in line with usual practice (*e.g.* Mustata *et al.* 2006; Gong *et al.* 2017; Almeida and Navarro-Martinez 2021; Liu and Jones 2025). In the standard mesh cases, two levels are applied, with a refinement ratio of two in all directions. The finest mesh size is 0.3 mm, and the average $y^+$ of the first grid point is approximately 140, resulting in a total cell count of 8.6 million, including the cells covered by the geometry. In the refined case, three levels are used, leading to a finest mesh size of 0.15 mm and a total cell count of 30 million.

The same numerical schemes and chemical kinetic mechanism used in the supersonic jet flame in subsection 3.4.4 are employed.

### 6.1.3 Previous WMLES study

The same case is studied numerically by Fureby and Nilsson 2023, which is used as a reference for comparison in the following section. They performed WMLES using a code based on OpenFOAM, which features a second-order reconstruction scheme, a second-order multistep time integration scheme, and an algebraic wall model. SGS stresses are modelled using the LDKM, and the filtered chemical source terms are closed with the PaSR model and a detailed reaction mechanism by Zettervall and Fureby 2018. Their paper showcases results using 24.6 million cells, although the authors claim that a coarser mesh of 7.3 million cells is sufficient to yield similar time-averaged and RMS quantities.

There are three differences in the setup that may affect the comparison between this reference case and the present study:

1. The wall model is applied only to the top and bottom walls in the reference case, whereas in the present study, it is applied to all walls.
2. The computational domain in their study includes the converging-diverging nozzle at the inflow, while the domain in this study starts from the exit of the converging-diverging nozzle. This is because the boundary layer is expected to be thin under the strong favourable pressure gradient in the diverging nozzle. This may lead to a difference in the boundary layer at the isolator inlet.
3. The cold inflow case $T_{0,\text{in}}$ is 20 K hotter in the present study compared to both the reference case and the experiment. While the $T_{0,\text{in}}$ in this study is the same as the RANS case used by Micka 2010 for comparison with the experiment, this may affect the results.

## 6.2 Results

### 6.2.1 Steady-state flow field

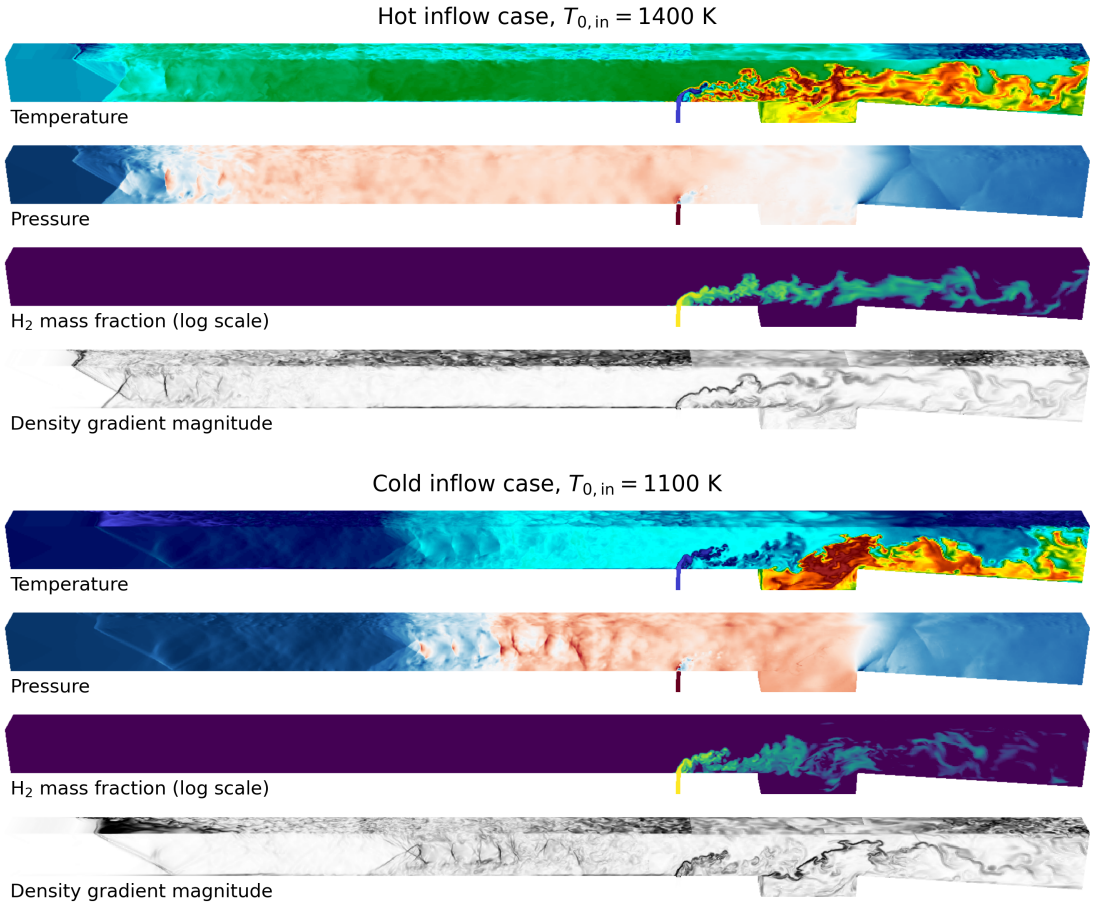



Figure 6.2: Instantaneous flow field, from top to bottom: temperature, pressure, $H_2$ mass fraction (in logarithmic scale), and density gradient magnitude. Quantities from both inflow cases share the same colourmap for comparison.

The flow field is analysed using instantaneous plots (Figure 6.2), wall pressure (Figure 6.3), and time-averaged velocity (Figure 6.4). All results presented are from the WMSF case unless otherwise specified.

In the hot inflow case, both WMILES and WMSF predict an X-type shock train, where the leading shock is an oblique shock formed by flow deflection around the separation bubble, as seen in the instantaneous plots and the velocity plots. There are four to five shocks in the shock train, which become weaker and less stable further downstream, as seen by the more smeared shape in the time-averaged velocity. The separation bubble generates velocity fluctuations and injects vortices into the flow, even though the position and structure of the shock train remain relatively steady. The large eddies dissipate, and the flow unsteadiness is evenly distributed along the entire cross-section ahead of fuel injection. The fuel jet creates a strong shear layer on the windward side and a large

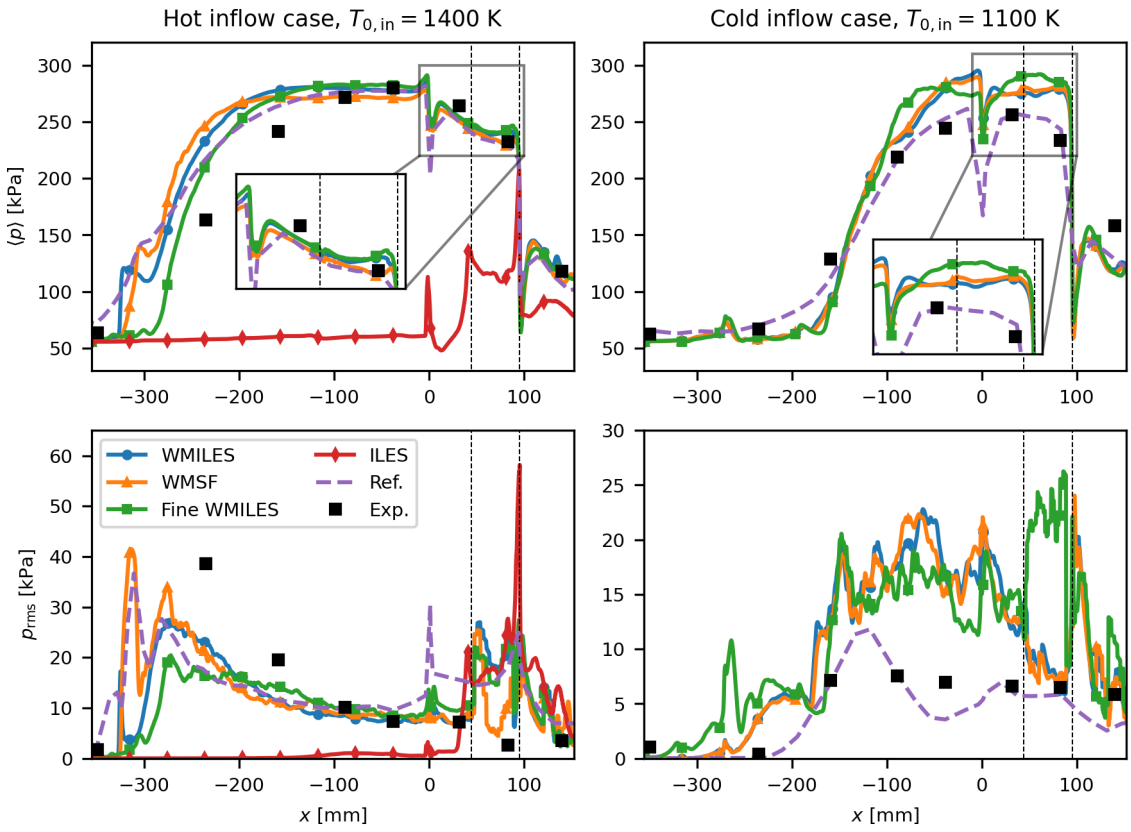



Figure 6.3: Mean and RMS values of bottom wall pressure. The dashed lines mark the cavity location. "Ref." is the WMLES by Fureby and Nilsson 2023 and "Exp." is the experimental measurements by Micka 2010. $x = 0$ at the fuel injector.

recirculation on the leeward side, which promotes mixing and stabilises the flame. The low-speed zone in the cavity increases residence time and serves as a reservoir for reactive radicals, which is important in the engine start-up phase. However, as the flame transitions from the cavity shear layer to the jet wake, the primary stabilisation mechanism becomes the jet wake recirculation. This process will be further discussed in section 6.3.

The mean and RMS pressure results align with the experiment and the reference WMLES. The pressure in the combustor and nozzle is accurately predicted, indicating a good representation of combustion intensity. However, the isolator shock train is predicted to be slightly more upstream than in the experiment. A comparison across WMILES, WMSF, and fine-WMILES (Figure 6.4) reveals different shock structures: the fine mesh case predicts a $\lambda$ shock train, where the leading shock is close to a normal shock, which corresponds to a single pressure rise at $x \approx$ -270 mm. In the coarser mesh cases, a two-step pressure rise is observed, initially due to the leading shock in the X-type shock train, followed by a slight pressure drop due to the expansion fan at the top of the separation bubble, and then a further pressure rise in the shock train. The fine-WMILES matches the experimental mean pressure more accurately. This difference in shock structure can be attributed to the finer mesh being able to resolve the turbulent boundary layer better, resulting in a

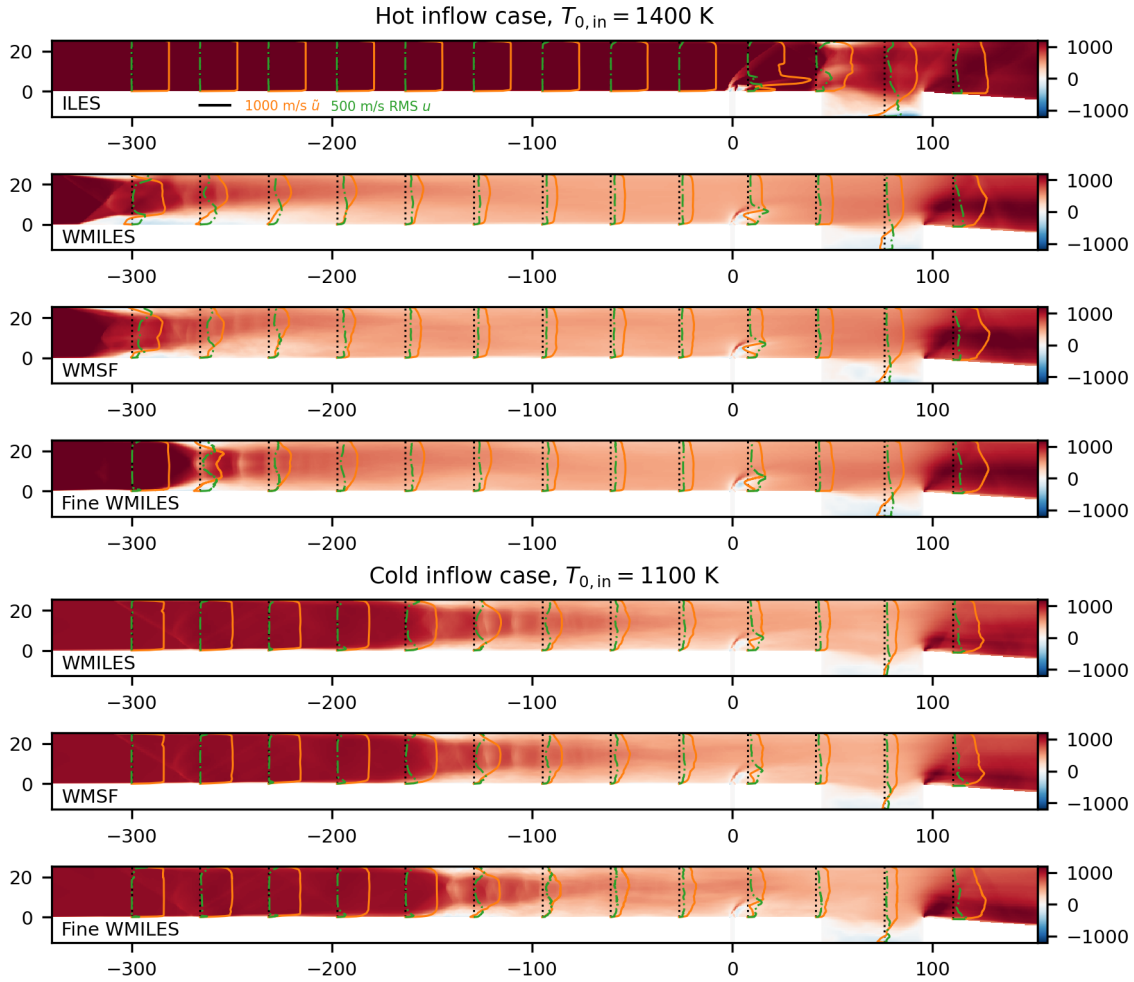



Figure 6.4: Mean streamwise velocity field overlaid with mean streamwise velocity (solid line) and RMS velocity (dashed line) profiles at different sections.

faster flow near the wall which is less susceptible to separation. This may also suggest that the wall model is inaccurate in challenging conditions such as separation and SBLI, particularly when the boundary layer is thin, thus the matching point $y^+ \approx 200$ is too large and could be outside the logarithmic layer. Nevertheless, similar pressure profiles indicate that mixing and combustion processes are insensitive to the shock train structure located more than 10 channel heights upstream, as the velocity and turbulence intensity at the combustor inlet are indistinguishable.

Moreover, the RMS values of pressure suggest that all mesh configurations transition at approximately the same position $x \approx -325$ mm, where pressure fluctuations begin to appear. In the standard mesh cases, the flow separates almost immediately after transition, indicated by the location of the first RMS pressure peak. Among the standard mesh cases, WMSF predicts a smaller separation zone, and its RMS pressure results agree very well with the reference WMLES, especially in the two peaks pattern, whereas the WMILES has a larger separation bubble, evident by the bigger and longer pressure drop. These observations align with previous studies (*e.g.* Kotov *et al.* 2016; Roy *et al.* 2025) that

boundary layer separation positions are highly sensitive to mesh and numerical scheme. Capturing such behaviour in a wall model is an active research topic. Note that this conclusion has to be drawn with caution, as there is no experimental image in the isolator to verify which shock structure is the "correct" one.

The necessity of a wall model is immediately clear in this case, as the ILES without a wall model fails to predict the shock train structure. This is because when shear stress is underpredicted, the boundary layer grows much more slowly and cannot provide sufficient room for the back pressure to transmit upstream, hence preventing the formation of the shock train. As a result, the flow remains supersonic throughout the isolator, and a bow shock is formed at the fuel jet and a weak flame is stabilised in the cavity.

In the cold inflow case, all simulations predict a $\lambda$-type shock train further downstream compared to the hot inflow case, with around six to seven consecutive shocks. The jet penetration and recirculation are similar in both cases. Due to the lower inflow temperature, the fuel does not ignite immediately upon injection, allowing for a short distance of premixing before reaching the flame stabilised above the cavity. The mean pressure profile confirms that the shock train position agrees well with the experiment and the reference WMLES, but the combustor pressure and RMS pressure are overpredicted. The difference may be caused by the fact that the experimental data and reference cases have a slightly lower stagnation temperature of 1080 K. A similar two-peak shape in RMS pressure is observed; the first, flatter peak is attributed to the transition shock, and the second peak is due to the shock train. The reference WMLES, however, only observes the second peak associated with the shock train. The experimental measurements are placed too far apart to confirm which is the correct behaviour.

In this case, the differences between WMILES, WMSF, and fine-WMILES are in the combustor rather than the shock train. The fine-WMILES sees a higher mean pressure in the combustor, accompanied by 2.5 times higher RMS pressure. This could be due to the finer mesh better promoting mixing and increasing combustion heat release. Conversely, the standard mesh cases appear to match closer to the experimental data and the reference WMLES. A similar pattern is observed in the hot inflow case, where the fine-WMILES prediction of RMS pressure is the furthest from the experiment. Further studies are needed to clarify whether this trend arises from non-monotonic grid convergence or from the cancellation of errors in the standard mesh.

The effect of wall temperature is examined for the hot inflow case only because the temperature difference is the largest. A simulation with isothermal walls at 300 K is compared to that with adiabatic walls. Figure 6.5 shows that both results are very similar, with the isothermal case having a slightly colder temperature less than 1 mm around the wall. The shock train and the flame appear insensitive to wall temperature.

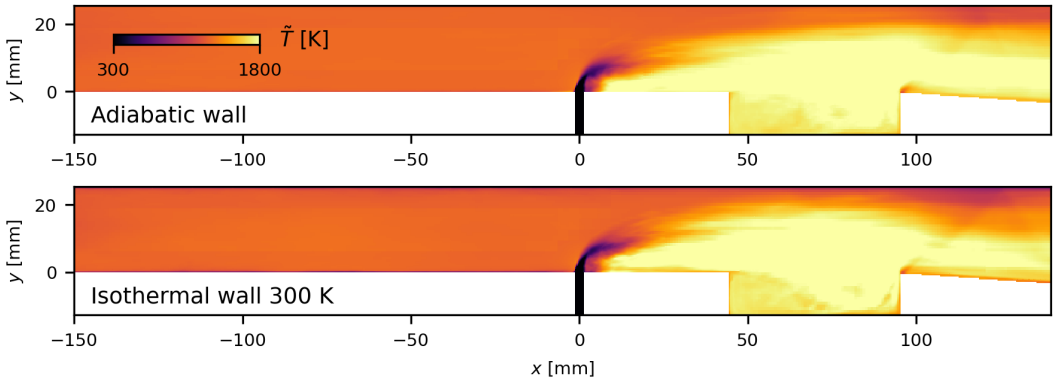



Figure 6.5: Mean temperature field with adiabatic and isothermal walls.

### 6.2.2 Flame structure

#### OH* chemiluminescence and combustion luminosity

The flame is visualised using two techniques. The OH* chemiluminescence imaging measures the UV light emitted when the excited OH* radicals return to their ground state. It infers the OH* concentration and, hence, the heat release rate (HRR). Flame luminosity measures light from the entire visible spectrum. It is proportional to the fourth power of temperature $T^4$ according to the Stefan-Boltzmann law.

Figure 6.6 shows that a jet wake stabilised flame is present in the hot inflow case, whereas a cavity stabilised flame is observed in the cold inflow case, both consistent with experimental observations. In the hot inflow case, the average HRR shows that the flame is anchored at the fuel injector, but the experimental OH* chemiluminescence image observes a flame slightly downstream in the recirculation zone. This may be due to the sharp discontinuity at the fuel-air interface, causing excessive numerical diffusion that mixes the fuel and air more rapidly and increases HRR. Additionally, it could also be a result of the slightly stronger shock train, which raises the temperature higher than that in the experiment, ultimately accelerating ignition. In the cold inflow case, a triangular-shaped flame attaches to the cavity shear layer. The angle of the flame front is approximately 29.7°, which aligns well with the angle measured in the experiment, and is close to the angle of an oblique laminar flame using the local velocity (Micka 2010). This resembles the classical Bunsen flame, suggesting that the flame may be premixed.

In both cases, a shock is formed near the inlet of the expansion section, as seen in the combustion luminosity images. This is a reattachment shock created by a small separation bubble due to the sharp cavity rear edge. This flow structure is also visible in the experimental luminosity images.

Note that the colourmaps used in Figure 6.6 only indicate the relative intensity. Caution should be exercised when interpreting or comparing exact magnitudes, as the relationships may not be linear. Moreover, the combustion luminosity is currently compared to $T^4$ from

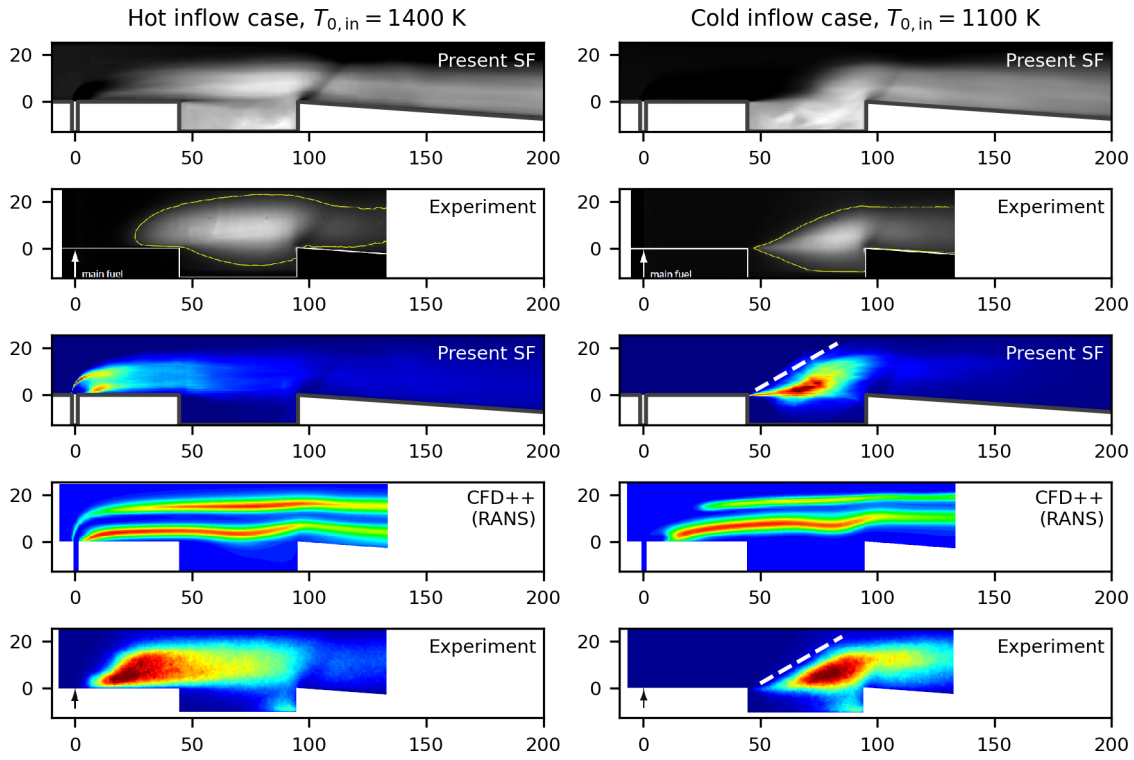



Figure 6.6: Top two rows: Line-of-sight $T^4$ in the WMSF (top) and combustion luminosity in the experiment (bottom); Bottom three rows: Line-of-sight mean heat release rate in the present WMSF (top) and CFD++ (middle) compared to OH* chemiluminescence in the experiment (bottom). Note that all colourmaps are relative rather than quantitative. The white dashed lines indicate a slope of 29.7°. All axis lengths are in mm.

the simulation. This is an approximation as the Stefan-Boltzmann law is strictly valid for black body radiation. The presence of multiple species with very different radiation properties may also affect the luminosity results. That could explain why the cavity appears brighter in the simulation, with another possible explanation being heat loss to the side walls.

The numerical results are compared to a commercial solver, CFD++, as included in Micka 2010. It uses a $k - \epsilon$ turbulence model for RANS and a 9-species 18-reactions detailed chemistry by Drummond *et al.* 1987, but without TCI modelling. Only half of a smaller domain is simulated, accounting for approximately 0.4 million cells. It shows that finite-rate chemistry is essential for predicting the flame in the hot inflow case, which is mixing-limited autoignition-based. However, the fuel jet core in RANS remains visible even downstream of the cavity, meaning that it underpredicts the turbulent mixing and breaking down of the jet. In the cold inflow case, the RANS also fails to predict the premixed flame. This could be due to the lower resolution and more dissipative numerical scheme artificially thickening the flame, causing the flame speed to be overestimated. It could also be attributed to the small turbulence structures that could locally quench the flame not being captured, because of the lack of TCI modelling.

### Flame index

Yamashita *et al.* 1996's flame index is used to analyse the combustion mode of the flame. It is defined as

$$FI = \frac{\nabla \tilde{Y}_{H_2} \cdot \nabla \tilde{Y}_{O_2}}{\|\nabla \tilde{Y}_{H_2}\| \|\nabla \tilde{Y}_{O_2}\| + \varepsilon}, \tag{6.1}$$

where $\varepsilon$ is a small number to prevent division by zero, and the normalisation allows $FI$ to stay within [-1, 1]. It is also clipped to reacting cells with HRR greater than $10^8$ J m$^{-3}$ s$^{-1}$. A positive $FI$ means that the fuel and oxidiser gradients are aligned, which corresponds to a premixed flame. Conversely, a negative $FI$ indicates a non-premixed flame.

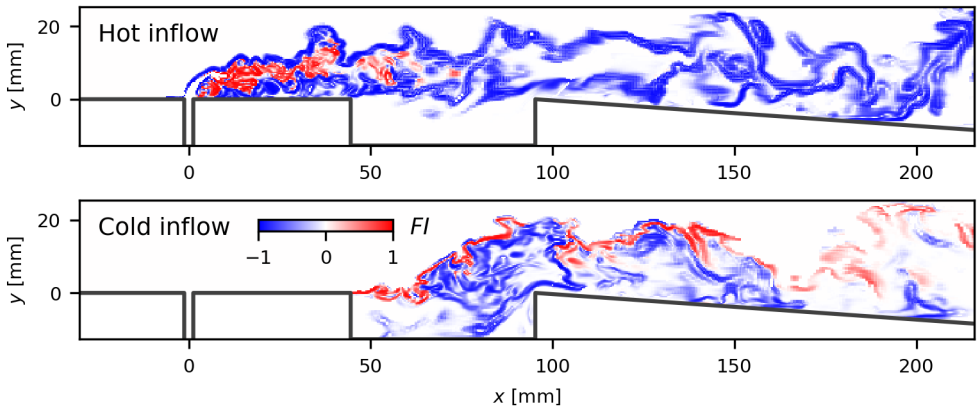



Figure 6.7: Flame index at the centre plane masked by the heat release rate greater than $10^8$ J m$^{-3}$ s$^{-1}$. Negative indicates a non-premixed flame and positive indicates a premixed flame.

Figure 6.7 shows that in the hot inflow case, the flame is primarily non-premixed, as the incoming air is sufficiently hot to initiate reaction with the fuel upon mixing. A small premixed zone exists in the jet wake, where strong vortices enhance mixing with the surrounding hot air. The cavity appears to have little effect on flame stabilisation in this case.

In the cold inflow case, the surrounding air is not hot enough to ignite the fuel, resulting in a longer distance for premixing, leading to a fuel-rich premixed flame downstream. The flame anchors at the cavity leading edge, showing that the hot air and reactive radicals within the cavity have a stabilising effect on the flame in this case. The flame angle is significantly greater than that of a supersonic mixing layer (Slessor *et al.* 2000), suggesting that the effect of the cavity contributes more than merely providing a shear layer as a source of instability, but also supports the flame. A broken partially premixed flame develops downstream of the initial, strong premixed flame because the fuel is not fully consumed as the initial premixed flame is fuel-rich. The fuel mixes and reacts with the surrounding gases, which consist of inflow air and combustion products. The flame appears more disconnected than in the hot inflow case, with pockets of fuel observed close to the main flame front.

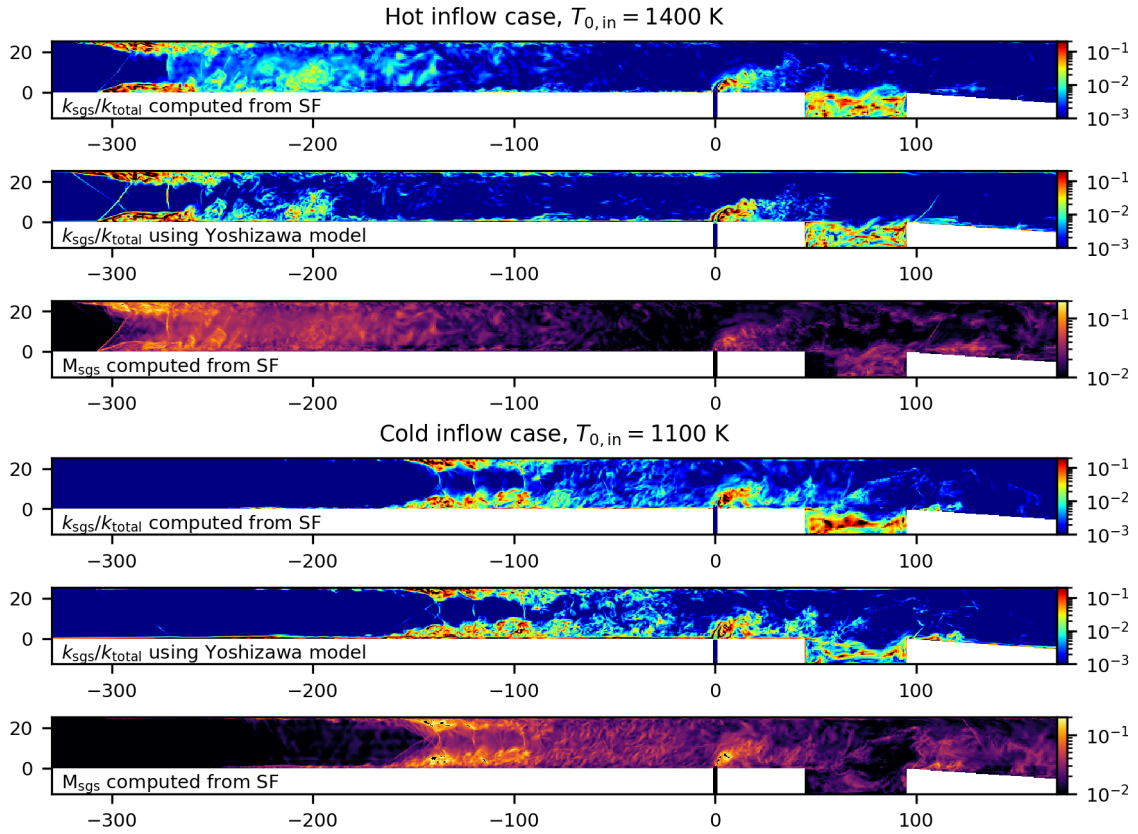



Figure 6.8: Sub-grid kinetic energy ratio and sub-grid Mach number at the centre plane computed from SF directly (3.26) and using Yoshizawa 1986's model (2.26). Cells with a value greater than 0.2 are coloured black. Note that the colour scale is logarithmic.

Note that the current flame index is based on resolved gradients. At smaller scales, there may be sub-grid scale flame wrinkling, fuel pockets, or local ignition or extinction that could complicate the picture.

### 6.2.3 Sub-grid scale interactions

#### Sub-grid kinetic energy

Sub-grid kinetic energy can be directly calculated from the SF using (3.26). It is compared with Yoshizawa 1986's model in (2.26) with $C_I = 0.09$. This $C_I$ value is used by Martín, Piomelli, *et al.* 2000 for compressible turbulence simulations. Figure 6.8 shows that the two methods agree qualitatively, highlighting regions of strong turbulence interactions, including the first few shocks in the shock train, the jet wake recirculation zone, and the cavity. The model using velocity gradients tends to estimate a higher $k_{\mathrm{sgs}}$ near walls. These areas of high turbulence intensity are nearly identical to the AMR refinement region, which tags high vorticity and pressure gradients.

When compared to the total kinetic energy (resolved plus sub-grid), Pope's criterion (Pope 2000, 2004), which suggests that a good LES resolution should resolve 80% of the

total kinetic energy, is generally satisfied, except for small regions within the shock train separation bubble, and a few vortices in the cavity where the kinetic energy is small. Note that although a similar analysis has been performed for supersonic jet flame (Bouheraoua *et al.* 2017), it is unclear whether Pope's criterion and the 80% threshold hold for compressible LES. Also note that the Pope's criterion could be used as an AMR refinement criterion.

### Sub-grid Mach number

Sub-grid Mach number is computed using the local filtered speed of sound, defined as $\mathrm{M}_{\mathrm{sgs}} = \sqrt{k_{\mathrm{sgs}}}/\bar{c}$. As depicted in Figure 6.8, although the mean flow Mach number is high, $\mathrm{M}_{\mathrm{sgs}}$ is relatively low throughout. In the hot inflow case, the maximum $\mathrm{M}_{\mathrm{sgs}}$ is 0.25, with the 99$^{\mathrm{th}}$ percentile at 0.085. For the cold inflow case, the maximum $\mathrm{M}_{\mathrm{sgs}}$ is 0.38, and the 99$^{\mathrm{th}}$ percentile is 0.109. This supports the assumptions of small-scale incompressibility and the Morkovin hypothesis used in the sub-grid model.

### Sub-grid Damköhler number

The sub-grid Damköhler number is defined as the ratio between the sub-grid timescale and the chemical timescale, where the chemical timescale is calculated based on the production rate of $H_2O$, following Bouheraoua *et al.* 2017:

$$\mathrm{Da}_{\mathrm{sgs}} = \frac{\tau_{\mathrm{sgs}}}{\tau_{\mathrm{chem}}} = \frac{\Delta/\sqrt{2k_{\mathrm{sgs}}/3}}{1/|\tilde{S}_{\mathrm{H_2O}}|}\,. \tag{6.2}$$

If $\mathrm{Da}_{\mathrm{sgs}} \ll 1$, it means that the sub-grid mixing is much faster than chemical reaction, and hence, the fuel and oxidiser within the cell are well-mixed before reaction occurs, and $\widetilde{S(\boldsymbol{\phi})} \approx S(\tilde{\boldsymbol{\phi}})$. This can be used to assess the validity of the quasi-laminar assumption in the filtered chemical source term, and can potentially predict how much different the simulation is with and without a TCI model (Cordier *et al.* 2022). Only reacting cells are considered, masked by $\tau_{\mathrm{chem}} < 0.1$ s. It is shown that in the hot inflow case, $\mathrm{Da}_{\mathrm{sgs}}$ is small everywhere, except for a few points in the windward face of the jet, which may be experiencing nearly laminar conditions, peaking at approximately 2.3. The 99$^{\mathrm{th}}$ percentile of $\mathrm{Da}_{\mathrm{sgs}}$ is 0.15, which may explain why a quasi-laminar or no TCI modelling approach works well in this case.

In the cold inflow case, cells on the flame front have higher $\mathrm{Da}_{\mathrm{sgs}}$, peaking at approximately 1.5, while 99% of the cells have a $\mathrm{Da}_{\mathrm{sgs}} < 0.20$. Modelling may be more relevant in this case than in the hot inflow case. However, the difference between WMSF and WMILES is still not significant. Note that the $\mathrm{Da}_{\mathrm{sgs}}$ values presented are approximations, as both $\tau_{\mathrm{sgs}}$ and $\tau_{\mathrm{chem}}$ are models only, although the filtered production rate $\tilde{S}_{\mathrm{H_2O}}$ is closed in SF.

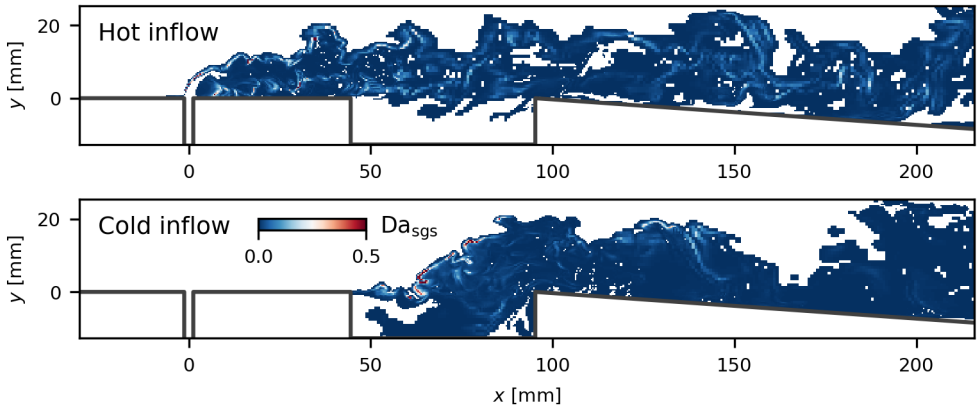



Figure 6.9: Sub-grid Damköhler number at the centre plane masked by $\tau_{\text{chem}} < 0.1$ s. Note that the simulation time step is $O(10^{-8})$ s.

## 6.3 Shock train initiation and propagation

This section focuses on the shock train in the hot inflow case. Figure 6.10 depicts the initiation sequence of the shock train. Initially, the crossflow at the fuel injection is supersonic, indicated by the presence of a bow shock at the jet. Combustion starts at the back of the cavity, caused by the strong shock wave generated when the supersonic air impinges on the cavity rear wall, raising the temperature locally. As the cavity accumulates hot gases and reactive radicals, the flame intensifies, accompanied by a rise in static pressure. When static pressure becomes too high, a normal shock begins to form above the cavity. This shock then moves upstream and merges with the jet bow shock. Eventually, multiple trailing shocks form because of the boundary layer reattaching and re-accelerating the flow, leading to the formation of a shock train.

As shown in Figure 6.11, the shock moves upstream quickly in the initial stage. This is because as it advances, it increases the boundary layer thickness, promoting stronger combustion and a further rise in pressure. Later, combustion reaches a peak level, limited by the fuel available, and the pressure at the combustor plateaus. The shock train continues to propagate at a nearly constant speed of approximately 45 m/s before slowing down as it approaches the isolator inlet.

To explain the observed propagation speed of the shock train, two methods are tried. The first follows the model by Li, Chang, *et al.* 2021:

$$u_s = u_1 - c_1 \left[ \frac{2}{\gamma F \sqrt{2C_f}} \left( \frac{p_2}{p_1} - 1 \right) \right]^{2/3}, \tag{6.3}$$

where $u_s$ is the speed of the leading shock, $c$ is the speed of sound, and $C_f = 3.5 \times 10^{-3}$ is the friction coefficient approximated from the LES solutions. The subscripts 1 and 2 correspond to conditions immediately upstream and downstream of the leading shock, respectively. They are different from the inflow and combustor conditions. The model

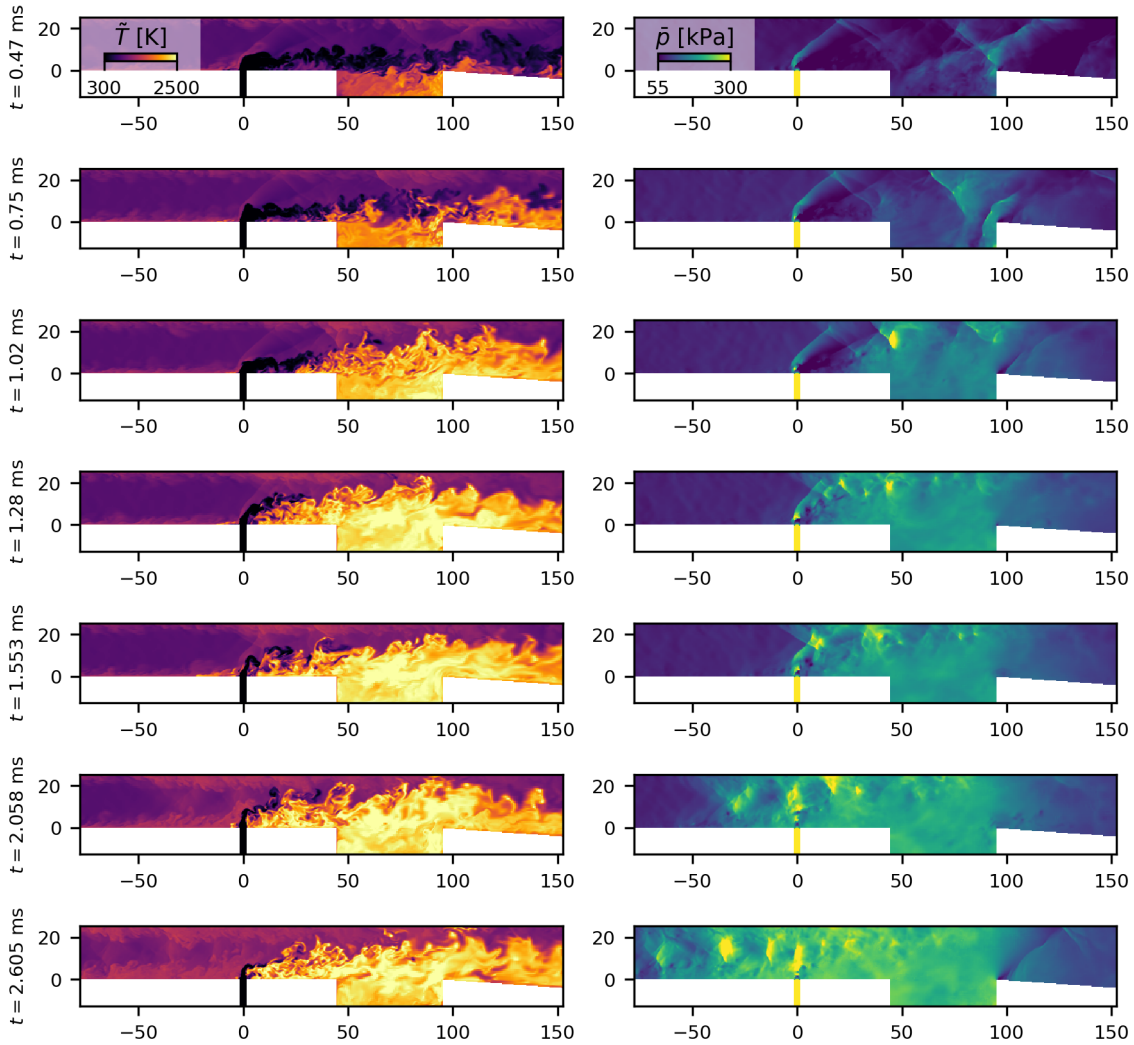



Figure 6.10: Time sequence of the flame and shock train formation. All axis lengths are in mm.

constant $F$ is reported to be 7.5 (Li, Chang, *et al.* 2021). However, it is difficult to estimate $p_2$, as the pressure oscillates between shocks. In 6.11, it is found that $p_2/p_1 \approx 2.35$ gives a reasonable estimate of the leading shock at multiple times. This results in a $u_s$ of 45.4 m/s, agreeing well with the observation. However, this method has two limitations: 1) it is extremely sensitive to the value of $p_2/p_1$, as a 5 % change in $p_2/p_1$ results in a 50 % change in the estimated $u_s$; and 2) it only explains the nearly-constant speed region, but cannot explain the initial acceleration and the final deceleration of the shock train.

A new method is proposed to better explain the observed propagation speed of the shock train. Based on the Fanno flow model, the background Mach number without the shock train and combustor back pressure is given by

$$\frac{\mathrm{d}M^2}{\mathrm{d}x} = \frac{\gamma M^4}{1-M^2}\left(1+\frac{\gamma-1}{2}M^2\right)\frac{4C_f}{D_H}\,, \tag{6.4}$$

where $D_H$ is the hydrodynamic diameter. For a rectangular tube with width $W$ and height $H$, $D_H = 2WD/(W+D)$.

Integrating from the inflow conditions (denoted by the subscript $\infty$), the local Mach number $M$ can be computed as a function of $x$, and the local pressure $p$, temperature $T$, and streamwise velocity $u$ can be calculated from $M$ using adiabatic and constant mass flow rate conditions:

$$\frac{T}{T_\infty} = \frac{1+\frac{\gamma-1}{2}M_\infty^2}{1+\frac{\gamma-1}{2}M^2}, \qquad \frac{p}{p_\infty} = \sqrt{\frac{M_\infty^2}{M^2}\frac{T}{T_\infty}}, \qquad \frac{u}{u_\infty} = \frac{M_\infty^2}{M^2}\sqrt{\frac{T}{T_\infty}}. \tag{6.5}$$

Next, a normal shock is introduced to satisfy the overall back pressure ratio $p_b/p_\infty$, approximately 5.3 in the present LES. The normal shock Mach number $M_s$ can be determined from the pressure ratios

$$\frac{p_b}{p} = \frac{p_b}{p_\infty}\frac{p_\infty}{p} = \frac{2\gamma M_s^2 - (\gamma-1)}{\gamma+1}. \tag{6.6}$$

Finally, with these information, the shock speed in an inertial reference frame is

$$u_s = (M - M_s)c = (M - M_s)c_\infty\sqrt{T/T_\infty}. \tag{6.7}$$

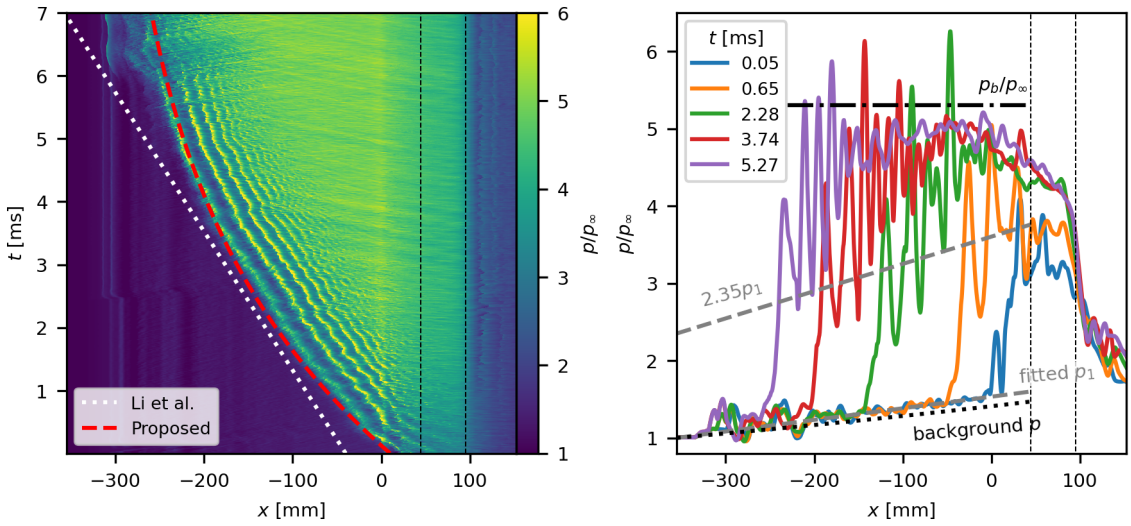



Figure 6.11: Centreline pressure over time. $t = 0$ is chosen to be the time where the leading shock passes through $x = 0$. On the right-hand-side plot, "fitted $p_1$" and "2.35 $p_1$" (grey dashed lines) refer to $p_1$ and $p_2$ in (6.3), while "background $p$" (black dotted line) is the pressure computed using (6.4)–(6.5).

The result, as plotted in Figure 6.11, aligns closely with the LES throughout the entire isolator, except at the very upstream location where boundary layer transition and separation occur, or where the shock becomes too diffused that it can no longer be treated as a normal shock. This simple analytical model can effectively capture the overall propagation

of the shock train without any empirical constants and is not very sensitive to $p_b/p_\infty$. This model bears some similarities to the one developed by Vanstone *et al.* 2018, but it identifies the variation of Mach number using wall friction instead of boundary layer growth and area ratio. Also note that the current method only estimates the position of the first shock. It could be combined with other models, such as Smart 2015, to obtain the overall pressure profile in the isolator.

The key implication of this new model is that the propagation of the shock train is primarily driven by the wall shear stress and the back pressure ratio. Factors such as the boundary layer profile and the blockage ratio appear to have little impact on the results, although it is worth noting that the dependency on $C_f$ might already account for boundary layer effects. These findings offer new insights for understanding the shock train dynamics and the development of reduced-order models.

## 6.4 Summary

This chapter applied the wall-modelled joint-velocity-scalar stochastic fields (WMSF), developed in previous chapters, to simulate a cavity-stabilised ramjet at two inflow temperatures.

Comparisons with the experimental wall pressure and different imaging techniques confirmed that the WMSF approach accurately predicts the flame and shock train structures at both inflow temperatures. The flame index analysis revealed that the two flames are fundamentally different: a non-premixed flame in the hot inflow case and a more broken premixed flame in the cold inflow case. This distinction underscored the effectiveness of the WMSF in modelling combustion in both modes. The wall model was proven important for flows in a ramjet engine, as the simulation without a wall model failed to predict the shock train.

A few findings emerged from the results:

1. The shock train structure is sensitive to boundary layer resolution. In the hot inflow case, the shock train is situated upstream, where the boundary layer is thin; thus, a fine mesh predicts a normal shock train, whereas the coarser mesh predicts an oblique shock train. In contrast, when the shock train is further downstream in the cold inflow case, the boundary layer is thicker and better resolved, and the two mesh resolutions show fewer differences.
2. Although the filtered flow field is supersonic and highly turbulent, both sub-grid kinetic energy and Mach number remain relatively small. This supports the small-scale incompressibility and the Morkovin hypothesis. Moreover, the Yoshizawa model was shown to yield a similar estimate of sub-grid kinetic energy to that computed directly from SF, depicting a consistency between the two very different models.

3. The small sub-grid Damköhler number suggests that a quasi-laminar approach may be sufficient in modelling the turbulence-chemistry interactions in this case. This is mainly due to the sub-grid kinetic energy, which, despite being small compared to the filtered kinetic energy, is large enough such that the turbulent timescale is small. Additional studies are needed to confirm if this is true for other ramjet or scramjet configurations.
4. An analytical model was derived to describe the shock train propagation. Based on the Fanno flow, this model accurately predicted the shock train movement across the entire isolator. Its dependency on the wall stresses and back pressure only suggests that the shock train motion is primarily driven by these two factors. This finding has the potential for developing reduced-order models for rapid conceptual design.

In conclusion, this study demonstrated that the WMSF is a reliable tool for simulating supersonic combustion problems, especially in cases where the flame structure is not known in advance, or it is uncertain whether the sub-grid Damköhler number will be small. It can be useful in the design and optimisation of high-speed air-breathing engines in the future.

# Chapter 7

# Conclusions

## 7.1 Summary of the thesis

This thesis developed a high-order joint-velocity-scalar stochastic fields solver for simulation of high-speed air-breathing engine conditions.

First, Chapter 2 introduced a LES methodology that combines state-of-the-art numerical methods, including the high-order TENO scheme and HLLC Riemann solver. The SF solver utilises adaptive mesh refinement (AMR) and a novel approximate characteristic transformation to reduce computational costs while maintaining accuracy. Test cases demonstrated that the solver achieves low numerical dissipation and high-order accuracy. Subsequent test cases in Chapters 3 and 6 revealed that this solver alone, without any turbulence models, outperforms solvers with low-order numerics and is competitive with other state-of-the-art solvers extensively used for high-speed combustion studies.

Building on this underlying numerical solver, Chapter 3 developed a joint-velocity-scalar probability density function (VSPDF) formulation, providing a unified closure for all turbulent interactions, including turbulent transport, turbulence-chemistry interactions, and potentially non-ideal equation of state. It does not rely on assumptions about flame structure or combustion regime, and has only a few model constants. The VSPDF equation is solved using a stochastic fields (SF) approach that focuses on conservation and thermodynamic consistency, crucial for numerical stability in complex, underresolved flow fields. The SF was integrated with AMR to further reduce computational costs.

The method was then improved along two lines. In Chapter 4, the first enhancement introduced the tensor-based neural network (TBNN) architecture, which respects the physical symmetries of the Navier-Stokes equations by construction. The TBNN showed substantial improvements across all performance metrics in *a priori* tests compared to the conventional sub-grid scale (SGS) Langevin model. It also significantly outperformed a standard deep neural network that does not incorporate rotational symmetries.

In Chapter 5, the second line of improvement coupled an ODE wall model with the SF solver, allowing for a relaxed $y^+$ requirement on near-wall resolution. A supersonic channel flow case verified that this model accurately predicts wall shear stress and heat flux even with a much coarser grid. In addition, a limiter for the stochastic term was proposed to suppress spurious sub-grid pressure fluctuations near walls.

Finally, this wall-modelled stochastic fields approach was applied to study an experimental ramjet with a cavity flameholder in Chapter 6. The results agreed closely with experimental measurements, demonstrating the method's capability to predict both the diffusion flame in the jet-stabilised mode at high inlet temperature and the premixed flame in the cavity-stabilised mode at low inlet temperature. The position and length of the isolator shock train were captured accurately. Its propagation was also investigated, and an analytical model based on Fanno flow was proposed to predict the trajectory of the leading shock.

## 7.2 Key findings

Findings related to the VSPDF-SF-AMR model:

1. The Taylor-Green vortex case (subsection 3.4.2) demonstrated that the velocity PDF is an effective SGS model. A unique advantage of this model over conventional eddy-viscosity models is that it appears to be able to distinguish between laminar shear and turbulence, introducing dissipation only during the turbulent decay phase but not in the vortex stretching phase.
2. In the case of homogeneous isotropic turbulence (subsection 3.4.3), the VSPDF model correctly predicted autoignition, whereas the no model approach failed. This indicates that the VSPDF model is effective when sub-grid temperature fluctuations are large and when the case is sensitive to extreme, non-linear events such as extinction or ignition. Although only small improvements were observed in some other test cases considered in this thesis, it is believed that the VSPDF method will excel in cases near flammability limits. More research is needed to identify in what use cases the method will have the greatest impact.
3. Conservation and thermodynamics consistency were extremely important for numerical stability, especially in the presence of shocks and steep gradients, without which many test cases in this thesis would fail. Subsection 3.2.1 showed that replacing the mean pressure gradient in the PDF transport equation with the stochastic pressure does not affect the mean behaviour. It effectively introduced a stabilising stochastic force that is inversely proportional to the smoothness (measured by two-point correlation) of the fields.
4. When using SF with AMR sub-cycling, random numbers should be generated at the finest level and then summed up to the coarser levels. This procedure ensures that

the mean is zero and that the random numbers in each time step in all levels are independent. The Ornstein-Uhlenbeck process (subsection 3.4.1) demonstrated that this algorithm preserves accuracy across AMR boundaries.

Findings related to the ramjet combustor simulation:

1. If the temperature at the combustor inlet is too high, the cavity has limited stabilising effects, as a diffusion flame is established around the fuel jet. In contrast, if the inlet temperature is lower than the autoignition temperature, the flame requires the cavity to remain in place. However, the cavity plays a crucial role during the engine starting phase for both inflow temperatures, as the initial flame is developed in the cavity regardless of the inflow temperature.
2. In the propagation phase, the shock train motion is primarily driven by wall shear stress and pressure ratio. The boundary layer profile seems to influence only through the friction coefficient. However, as the shock system approaches its steady state position, the model becomes less accurate, indicating that other factor might become important. This could be due to the complex shock-boundary layer interaction pattern or that the shock can no longer be treated as a normal shock.
3. In the current settings, the sub-grid Damköhler number is small. This is because, although the chemical timescale is short due to the high temperature and the use of hydrogen, the flow timescale is even shorter due to the high sub-grid kinetic energy. Note that in both hot and cold inflow cases studied, the engine operates in ram mode. This conclusion may be different in scram mode.

## 7.3 Scientific contributions

This work produced the first SF-AMR study and the first application of VSPDF to ramjet simulation in the literature. The solver developed, Cerisse, is open source and publicly available on GitHub (Navarro-Martinez, Un, *et al.* 2025).

Part of the results presented in this thesis have been published in conferences and journals:

- T.-H. Un and S. Navarro-Martinez, "Large-eddy simulation of shock-train dynamics in a cavity-stabilised ramjet engine", 35$^{\text{th}}$ International Symposium on Shock Waves, Brisbane, Australia, July 2025
- T.-H. Un and S. Navarro-Martinez, "On the performance of PDF methods near walls", *Proceedings of the Combustion Institute* 41, 2025, pp. 105838 (Part of the special issue of the 12$^{\text{th}}$ European Combustion Meeting, Edinburgh, UK, April 2025)
- T.-H. Un and S. Navarro-Martinez, "Stochastic fields with adaptive mesh refinement for high-speed turbulent combustion", *Combustion and Flames* 272, 2025, pp. 113897

- T.-H. Un and S. Navarro-Martinez, "A high-order compressible Eulerian stochastic fields solver based on AMReX", 19$^{\text{th}}$ International Conference on Numerical Combustion, Kyoto, Japan, May 2024 (Oral presentation)
- T.-H. Un and S. Navarro-Martinez, "Large eddy simulation of a lean-hydrogen aeronautical combustor", 11$^{\text{th}}$ European Combustion Meeting, Rouen, France, April 2023
- T.-H. Un and S. Navarro-Martinez, "Machine-assisted subgrid-scale modelling for LES-PDF approaches", Direct and Large-Eddy Simulation 13, Udine, Italy, October 2022 (Oral presentation)
- T.-H. Un and S. Navarro-Martinez, "Machine-assisted subgrid-scale modelling for LES-PDF approaches", UK Fluid Conference, Sheffield, UK, September 2022 (Oral presentation)

## 7.4 Future outlooks

The author believes that the joint-velocity-scalar stochastic fields method still has significant potential for development. Below are several suggestions for future research directions.

**Neural-network Langevin model**: The neural network approach described in Chapter 4 should be examined in greater depth, particularly regarding its stability and accuracy improvements in *a posteriori* scenarios.

**New PDF formulation for variable density flows**: Appendix D proposes a novel VSPDF formulation, which is considered more consistent as it produces correctly filtered terms in a variable density flow and makes fewer assumptions. Introducing a Langevin-like model in the density could allow the system to return to thermodynamic equilibrium. Also, introducing a timescale linked to the velocity divergence may help account for compressibility effects.

**Adaptive stochastic fields**: Since the stochastic fields method can be computationally expensive, it would be beneficial to develop an adaptive approach that switches it off in regions where such capability is not needed. For example, it could target areas with high sub-grid kinetic energy or filtered vorticity. Transitioning from SF to a non-SF region can be performed by simply taking the mean. However, moving in the opposite direction may require careful consideration. A buffer zone could be defined to ensure that transitions always occur in regions with minimal sub-grid fluctuations, although the optimal width of this buffer zone needs to be determined.

**Non-ideal equation of state for trans- and supercritical fluids**: Modelling SGS interactions for non-ideal equations of state is challenging (*e.g.* Chung, Mishra, *et al.* 2021). However, since the non-ideal equation of state is a one-point phenomenon, in principle, it can be closed using the current one-point PDF without modification. The literature lacks documentation regarding the performance of stochastic fields under non-ideal equations of

state. Moreover, this topic is relevant for high-speed propulsion systems, which often use cryogenic hydrogen as fuel and high injection pressures to achieve sufficient jet penetration.

**Shock train-combustor coupling and dynamics**: Further investigation is required into the coupling and dynamics between the isolator shock train and the combustor. For instance, it is important to determine how the analytical model proposed performs under different inflow conditions, whether it can capture dynamics if the back pressure is a time-dependent variable, and if we can integrate other analytical models (*e.g.*, Smart 2015) to predict the entire isolator profile rather than just the leading shock position.

**Model limitations**: It is suspected that low SGS Mach and Damköhler numbers in the ramjet cases examined in this thesis may limit the improvements that the PDF method can provide. Future research could explore whether these low SGS Mach and Damköhler numbers are common in other ramjet/scramjet configurations and identify conditions under which the PDF method is most effective. This information could also be useful in refining the criteria for the adaptive SF concept mentioned earlier. Lastly, simulating the engine in scram mode operation and near flameout limits would be essential to fully validate the model's ability to simulate all operating conditions of a dual-mode ramjet engine, although such measurements are currently scarce.

# Bibliography


Almeida, Y. and Navarro-Martinez, S. (2021). "Joint-velocity scalar energy probability density function method for large eddy simulations of compressible flow". *Physics of Fluids* 33 (3), p. 035155.

Almeida, Y. (2019). "Large Eddy Simulation of Supersonic Combustion using a Probability Density Function method". PhD thesis. Imperial Collgee London.

Anderson Jr., J. D. (2019). *Hypersonic and High-Temperature Gas Dynamics, Third Edition*. American Institute of Aeronautics and Astronautics, Inc.

Andreadis, D. (2004). "Scramjets integrate air and space". *Industrial Physicist* 10.4, pp. 24–26.

Azarnykh, D., Litvinov, S., and Adams, N. A. (2016). "Numerical methods for the weakly compressible Generalized Langevin Model in Eulerian reference frame". *Journal of Computational Physics* 314, pp. 93–106.

Baccarella, D., Liu, Q., McGann, B., Lee, G., and Lee, T. (2021). "Isolator-combustor interactions in a circular model scramjet with thermal and non-thermal choking-induced unstart". *Journal of Fluid Mechanics* 917, A38.

Bailly, C. and Juve, D. (1999). "A stochastic approach to compute subsonic noise using linearized Euler's equations". *$5^{th}$ AIAA/CEAS Aeroacoustics Conference and Exhibit*. American Institute of Aeronautics and Astronautics, pp. 496–506.

Balsara, D. S., Bhoriya, D., Shu, C.-W., and Kumar, H. (2024). "Efficient Alternative Finite Difference WENO Schemes for Hyperbolic Conservation Laws". *Communications on Applied Mathematics and Computation*, pp. 1–54.

Beck, A., Flad, D., and Munz, C. D. (2019). "Deep neural networks for data-driven LES closure models". *Journal of Computational Physics* 398, p. 108910.

Ben-Yakar, A. (2000). "Experimental Investigation of Mixing and Ignition of Transverse Jets in Supersonic Crossflows". PhD thesis. Stanford University.

Berger, M. and Giuliani, A. (2021). "A state redistribution algorithm for finite volume schemes on cut cell meshes". *Journal of Computational Physics* 428, p. 109820.

Berger, M. and Oliger, J. (1984). "Adaptive mesh refinement for hyperbolic partial differential equations". *Journal of Computational Physics* 53 (3), pp. 484–512.

Bermejo-Moreno, I., Larsson, J., Bodart, J., and Vicquelin, D. R. (2013). "Wall-modeled large-eddy simulations of the HIFiRE-2 scramjet". *Center for Turbulence Research Annual Research Briefs*. Stanford University.

Bermejo-Moreno, I., Campo, L., Larsson, J., Bodart, J., Helmer, D., and Eaton, J. K. (2014). "Confinement effects in shock wave/turbulent boundary layer interactions through wall-modelled large-eddy simulations". *Journal of Fluid Mechanics* 758, pp. 5–62.

Bilger, R. W. (1993). "Conditional moment closure for turbulent reacting flow". *Physics of Fluids A: Fluid Dynamics* 5 (2), p. 436.

Bocher, M. (1906). "Introduction to the Theory of Fourier's Series". *The Annals of Mathematics* 7 (3), p. 81.

Boivin, P., Dauptain, A., Jiménez, C., and Cuenot, B. (2012). "Simulation of a supersonic hydrogen–air autoignition-stabilized flame using reduced chemistry". *Combustion and Flame* 159 (4), pp. 1779–1790.

Bose, S. T. and Park, G. I. (2018). "Wall-Modeled Large-Eddy Simulation for Complex Turbulent Flows". *Annual Review of Fluid Mechanics* 50 (1), pp. 535–561.

Bottin, B., Abeele, D. V., Magin, T., and Rini, P. (2006). "Transport properties of collision-dominated dilute perfect gas mixtures at low pressures and high temperatures". *Progress in Aerospace Sciences* 42 (1), pp. 38–83.

Bouheraoua, L., Domingo, P., and Ribert, G. (2017). "Large-eddy simulation of a supersonic lifted jet flame: Analysis of the turbulent flame base". *Combustion and Flame* 179, pp. 199–218.

Candler, G. V. (2019). "Rate Effects in Hypersonic Flows". *Annual Review of Fluid Mechanics* 51 (1), pp. 379–402.

Castro, M., Costa, B., and Don, W. S. (2011). "High order weighted essentially non-oscillatory WENO-Z schemes for hyperbolic conservation laws". *Journal of Computational Physics* 230 (5), pp. 1766–1792.

Chan, W. L. and Ihme, M. (2014). "Large-Eddy Simulations of a Dual-Mode Scramjet Combustor: Operating Point "A" of University of Virginia's Scramjet Experiments". *52nd Aerospace Sciences Meeting*. American Institute of Aeronautics and Astronautics.

Chapman, D. R. and Rubesin, M. W. (1949). "Temperature and Velocity Profiles in the Compressible Laminar Boundary Layer with Arbitrary Distribution of Surface Temperature". *Journal of the Aeronautical Sciences* 16 (9), pp. 547–565.

Chen, J. H., Choudhary, A., Supinski, B. de, DeVries, M., Hawkes, E. R., Klasky, S., Liao, W. K., Ma, K. L., Mellor-Crummey, J., Podhorszki, N., Sankaran, R., Shende, S., and Yoo, C. S. (2009). "Terascale direct numerical simulations of turbulent combustion using S3D". *Computational Science & Discovery* 2 (1), p. 015001.

Chen, P. E., Lv, Y., Xu, H. H., Shi, Y., and Yang, X. I. (2022). "LES wall modeling for heat transfer at high speeds". *Physical Review Fluids* 7 (1), p. 014608.

Cheng, T. S., Wehrmeyer, J. A., and Pitz, R. W. (1991). *Laser Raman Diagnostics in Subsonic and Supersonic Turbulent Jet Diffusion Flames*. Tech. rep. Vanderbilt University.

Cheng, T. S., Wehrmeyer, J. A., Pitz, R. W., Jarrett, O., and Northam, G. B. (1994). "Raman measurement of mixing and finite-rate chemistry in a supersonic hydrogen-air diffusion flame". *Combustion and Flame* 99 (1), pp. 157–173.

Choi, H. and Moin, P. (2012). "Grid-point requirements for large eddy simulation: Chapman's estimates revisited". *Physics of Fluids* 24 (1).

Chung, W. T., Akoush, B., Sharma, P., Tamkin, A., Jung, K. S., Chen, J., Guo, J., Brouzet, D., Talei, M., Savard, B., Poludnenko, A., and Ihme, M. (2023). "Turbulence in Focus: Benchmarking Scaling Behavior of 3D Volumetric Super-Resolution with BLASTNet 2.0 Data". *Advances in Neural Information Processing Systems*. Ed. by A. Oh, T. Naumann, A. Globerson, K. Saenko, M. Hardt, and S. Levine. Vol. 36. Curran Associates, Inc., pp. 77430–77484.

Chung, W. T., Mishra, A. A., and Ihme, M. (2021). "Interpretable data-driven methods for subgrid-scale closure in LES for transcritical LOX/GCH4 combustion". *Combustion and Flame*, p. 111758.

Clark, R. A., Ferziger, J. H., and Reynolds, W. C. (1979). "Evaluation of subgrid-scale models using an accurately simulated turbulent flow". *Journal of Fluid Mechanics* 91 (1), pp. 1–16.

Coffee, T. P. and Heimerl, J. M. (1981). "Transport algorithms for premixed, laminar steady-state flames". *Combustion and Flame* 43 (1), pp. 273–289.

Colin, O., Ducros, F., Veynante, D., and Poinsot, T. (2000). "A thickened flame model for large eddy simulations of turbulent premixed combustion". *Physics of Fluids* 12 (7), pp. 1843–1863.

Collin, C., Dessornes, O., and Magre, P. (1997). "Installations d'essais pour les recherches fondamentales en propulsion". *Tiré à part – Office national d'études et de recherches aerospatiales*.

Cordier, M., Bénard, P., Lybaert, P., Paepe, W. D., and Bricteux, L. (2022). "On the Need for Turbulence Chemistry Interaction Modelling in Highly Resolved Large-Eddy Simulations of Mild Combustion". *Flow, Turbulence and Combustion* 108 (2), pp. 509–538.

Corrsin, S. (1958). "Statistical Behavior of a Reacting Mixture in Isotropic Turbulence". *The Physics of Fluids* 1 (1), pp. 42–47.

Curran, E. T. (2001). "Scramjet Engines: The First Forty Years". *Journal of Propulsion and Power* 17 (6), pp. 1138–1148.

Curtiss, C. F. and Hirschfelder, J. O. (1949). "Transport Properties of Multicomponent Gas Mixtures". *The Journal of Chemical Physics* 17 (6), pp. 550–555.

Cutler, A., Magnotti, G., Cantu, L., Gallo, E., Danehy, P., Rockwell, R., Goyne, C., and McDaniel, J. (2012). "Dual-Pump CARS Measurements in the University of Virginia's Dual-Mode Scramjet: Configuration 'A'". *50$^{th}$AIAA Aerospace Sciences Meeting including the New Horizons Forum and Aerospace Exposition*. American Institute of Aeronautics and Astronautics.

Cutler, A., Magnotti, G., Cantu, L., Gallo, E., Danehy, P., Rockwell, R., Goyne, C., and McDaniel, J. (2013). "Dual-Pump CARS Measurements in the University of Virginia's Dual-Mode Scramjet: Configuration 'C'". *51st AIAA Aerospace Sciences Meeting including the New Horizons Forum and Aerospace Exposition*. American Institute of Aeronautics and Astronautics.

Danaila, I. and Boersma, B. J. (1998). "Mode interaction in a forced homogeneous jet at low Reynolds numbers". *Center for Turbulence Research Proceedings of the Summer Program*. Stanford University, pp. 141–158.

Delarue, B. J. and Pope, S. B. (1997). "Application of PDF methods to compressible turbulent flows". *Physics of Fluids* 9 (9), pp. 2704–2715.

Ding, T., Readshaw, T., Rigopoulos, S., and Jones, W. P. (2021). "Machine learning tabulation of thermochemistry in turbulent combustion: An approach based on hybrid flamelet/random data and multiple multilayer perceptrons". *Combustion and Flame* 231, p. 111493.

Domingo, P. and Vervisch, L., eds. (2025). *Numerical Modeling of Turbulent Combustion*. Elsevier.

Donde, P., Koo, H., and Raman, V. (2012). "A multivariate quadrature based moment method for LES based modeling of supersonic combustion". *Journal of Computational Physics* 231 (17), pp. 5805–5821.

Dopazo, C. (1975). "Probability density function approach for a turbulent axisymmetric heated jet. Centerline evolution". *The Physics of Fluids* 18 (4), pp. 397–404.

Dopazo, C. (1976). "A probabilistic approach to turbulent flame theory". *Acta Astronautica* 3 (9-10), pp. 853–878.

Dopazo, C. and O'Brien, E. E. (1974). "An approach to the autoignition of a turbulent mixture". *Acta Astronautica* 1 (9-10), pp. 1239–1266.

Dreeben, T. D. and Pope, S. B. (1997a). "Probability density function and Reynolds-stress modeling of near-wall turbulent flows". *Physics of Fluids* 9 (1), pp. 154–163.

Dreeben, T. D. and Pope, S. B. (1997b). "Wall-function treatment in pdf methods for turbulent flows". *Physics of Fluids* 9 (9), pp. 2692–2703.

Dreeben, T. D. and Pope, S. B. (1998). "Probability density function/Monte Carlo simulation of near-wall turbulent flows". *Journal of Fluid Mechanics* 357, pp. 141–166.

Drummond, J. P., Rogers, R. C., and Hussaini, M. Y. (1987). "A numerical model for supersonic reacting mixing layers". *Computer Methods in Applied Mechanics and Engineering* 64 (1-3), pp. 39–60.

Ducros, F., Ferrand, V., Nicoud, F., Weber, C., Darracq, D., Gacherieu, C., and Poinsot, T. (1999). "Large-Eddy Simulation of the Shock/Turbulence Interaction". *Journal of Computational Physics* 152 (2), pp. 517–549.

Edwards, J. R., Potturi, A., and Fulton, J. A. (2012). "Large Eddy/Reynolds-Averaged Navier-Stokes Simulations of Scramjet Combustor Flow Fields". *48th AIAA/ASME/SAE/ASEE Joint Propulsion Conference & Exhibit*. American Institute of Aeronautics and Astronautics.

Einstein, A. (1905). "Über die von der molekularkinetischen Theorie der Wärme geforderte Bewegung von in ruhenden Flüssigkeiten suspendierten Teilchen". *Annalen der Physik* 322 (8), pp. 549–560.

Emory, M. and Iaccarino, D. G. (2014). "Visualizing turbulence anisotropy in the spatial domain with componentality contours". *Center for Turbulence Research Annual Research Briefs*. Stanford University.

Ern, A. and Giovangigli, V. (1994). *Multicomponent Transport Algorithms*. Springer Berlin Heidelberg.

Ern, A. and Giovangigli, V. (1995). "Fast and Accurate Multicomponent Transport Property Evaluation". *Journal of Computational Physics* 120 (1), pp. 105–116.

Falempin, F. (2007). "Ramjet and Dual Mode Operation". *Advances on Propulsion Technology for High-Speed Aircraft*. Ed. by G. Paniagua and J. Steelant. Von Karman Institute.

Favre, A. (1965). *The equations of compressible turbulent gases*. Institut de Mecanique Statistique de la Turbulence, Marseille, France.

Fedkiw, R. P., Merriman, B., and Osher, S. (1997). "High Accuracy Numerical Methods for Thermally Perfect Gas Flows with Chemistry". *Journal of Computational Physics* 132 (2), pp. 175–190.

Forbes-Spyratos, S. O. (2020). "Trajectory Optimisation of a Partially-Reusable Rocket-Scramjet-Rocket Small Satellite Launch System". PhD thesis. University of Queensland.

Fotia, M. L. and Driscoll, J. F. (2013). "Ram-Scram Transition and Flame/Shock-Train Interactions in a Model Scramjet Experiment". *Journal of Propulsion and Power* 29 (1), pp. 261–273.

Fox, R. O. (2003). *Computational Models for Turbulent Reacting Flows*. Cambridge University Press.

Fry, R. S. (2004). "A Century of Ramjet Propulsion Technology Evolution". *Journal of Propulsion and Power* 20 (1), pp. 27–58.

Fu, L., Hu, X. Y., and Adams, N. A. (2016). "A family of high-order targeted ENO schemes for compressible-fluid simulations". *Journal of Computational Physics* 305, pp. 333–359.

Fu, L., Hu, X. Y., and Adams, N. A. (2019). "Improved five- And six-point targeted essentially nonoscillatory schemes with adaptive dissipation". *AIAA Journal* 57 (3), pp. 1143–1158.

Fu, L., Karp, M., Bose, S. T., Moin, P., and Urzay, J. (2021). "Shock-induced heating and transition to turbulence in a hypersonic boundary layer". *Journal of Fluid Mechanics* 909, pp. 8–9.

Fujiwara, Y., Tamaki, Y., and Kawai, S. (2023). "Fully conservative and pressure-equilibrium preserving scheme for compressible multi-component flows". *Journal of Computational Physics* 478, p. 111973.

Fulton, J. A., Edwards, J., Hassan, H. A., McDaniel, J. C., Goyne, C. P., Rockwell, R. D., Cutler, A. D., Johansen, C. T., and Danehy, P. M. (2014). "Large-Eddy/Reynolds-Averaged Navier–Stokes Simulations of Reactive Flow in Dual-Mode Scramjet Combustor". *Journal of Propulsion and Power* 30 (3), pp. 558–575.

Fureby, C., Nordin-Bates, K., Petterson, K., Bresson, A., and Sabelnikov, V. (2015). "A computational study of supersonic combustion in strut injector and hypermixer flow fields". *Proceedings of the Combustion Institute* 35 (2), pp. 2127–2135.

Fureby, C. and Nilsson, T. (2023). "Large Eddy Simulation of cavity stabilized ramjet combustion". *Aerospace Science and Technology* 141, p. 108503.

Gardner, A., Steelant, J., Paull, A., and Hannemann, K. (2004). "Ground Testing of the HyShot Supersonic Combustion Flight Experiment in HEG and Comparison with Flight Data". *40$^{th}$AIAA/ASME/SAE/ASEE Joint Propulsion Conference and Exhibit*. American Institute of Aeronautics and Astronautics.

Garnier, E., Adams, N., and Sagaut, P. (2009). *Large Eddy Simulation for Compressible Flows*. Springer Netherlands.

Génin, F. (2009). "Study of compressible turbulent flows in supersonic environment by large-eddy simulation". PhD thesis. Georgia Institute of Technology.

Génin, F., Chernyavsky, B., and Menon, S. (2003). "Large Eddy Simulation of Scramjet Combustion Using a Subgrid Mixing/combustion Model". *12$^{th}$ AIAA International Space Planes and Hypersonic Systems and Technologies*. American Institute of Aeronautics and Astronautics.

Génin, F. and Menon, S. (2010). "Simulation of Turbulent Mixing Behind a Strut Injector in Supersonic Flow". *AIAA Journal* 48 (3), pp. 526–539.

Gerlinger, P., Möbus, H., and Brüggemann, D. (2001). "An Implicit Multigrid Method for Turbulent Combustion". *Journal of Computational Physics* 167 (2), pp. 247–276.

Germano, M., Piomelli, U., and Moin, P. (1991). "A dynamic subgrid-scale eddy viscosity model". *Physics of Fluids A: Fluid Dynamics* 3, p. 1760.

Gicquel, L. Y., Givi, P., Jaberi, F. A., and Pope, S. B. (2002). "Velocity filtered density function for large eddy simulation of turbulent flows". *Physics of Fluids* 14 (3), pp. 1196–1213.

Giusti, A. and Mastorakos, E. (2019). "Turbulent Combustion Modelling and Experiments: Recent Trends and Developments". *Flow, Turbulence and Combustion* 103 (4), pp. 847–869.

Gong, C., Jangi, M., Bai, X.-S., Liang, J.-H., and Sun, M.-B. (2017). "Large eddy simulation of hydrogen combustion in supersonic flows using an Eulerian stochastic fields method". *International Journal of Hydrogen Energy* 42 (2), pp. 1264–1275.

Gonzalez-Juez, E. D., Kerstein, A. R., Ranjan, R., and Menon, S. (2017). "Advances and challenges in modeling high-speed turbulent combustion in propulsion systems". *Progress in Energy and Combustion Science* 60, pp. 26–67.

Gruber, M., Smith, S., and Mathur, T. (2011). "Experimental Characterization of Hydrocarbon-Fueled, Axisymmetric, Scramjet Combustor Flowpaths". *17$^{th}$AIAA International Space Planes and Hypersonic Systems and Technologies Conference*. American Institute of Aeronautics and Astronautics.

Han, W., Raman, V., and Chen, Z. (2016). "LES/PDF modeling of autoignition in a lifted turbulent flame: Analysis of flame sensitivity to differential diffusion and scalar mixing time-scale". *Combustion and Flame* 171, pp. 69–86.

Harten, A., Engquist, B., Osher, S., and Chakravarthy, S. R. (1987). "Uniformly high order accurate essentially non-oscillatory schemes, III". *Journal of Computational Physics* 71 (2), pp. 231–303.

Harten, A., Lax, P. D., and van Leer, B. (1983). "On Upstream Differencing and Godunov-Type Schemes for Hyperbolic Conservation Laws". *SIAM Review* 25 (1), pp. 35–61.

Haworth, D. C. (2010). "Progress in probability density function methods for turbulent reacting flows". *Progress in Energy and Combustion Science* 36 (2), pp. 168–259.

Haworth, D. C. and Pope, S. B. (1986). "A generalized Langevin model for turbulent flows". *The Physics of Fluids* 29 (2), pp. 387–405.

Hawthorne, W. R., Weddell, D. S., and Hottel, H. C. (1948). "Mixing and combustion in turbulent gas jets". *Symposium on Combustion and Flame, and Explosion Phenomena* 3 (1), pp. 266–288.

Heinz, S. (2003). *Statistical Mechanics of Turbulent Flows*. Springer Berlin Heidelberg.

Henry de Frahan, M. T., Rood, J. S., Day, M. S., Sitaraman, H., Yellapantula, S., Perry, B. A., Grout, R. W., Almgren, A., Zhang, W., Bell, J. B., and Chen, J. H. (2023). "PeleC: An adaptive mesh refinement solver for compressible reacting flows". *International Journal of High Performance Computing Applications* 37 (2), pp. 115–131.

Henry de Frahan, M. T., Yellapantula, S., King, R., Day, M. S., and Grout, R. W. (2019). "Deep learning for presumed probability density function models". *Combustion and Flame* 208, pp. 436–450.

Hindmarsh, A. C., Brown, P. N., Grant, K. E., Lee, S. L., Serban, R., Shumaker, D. E., and Woodward, C. S. (2005). "SUNDIALS: Suite of nonlinear and differential/algebraic equation solvers". *ACM Transactions on Mathematical Software* 31.3, pp. 363–396.

Horing, J. A., Boyd, I. D., and Maute, K. K. (2024). "Fully Coupled Analysis of Aerothermoelastic Deformation of a Scramjet Inlet". *Journal of Propulsion and Power* 40 (2), pp. 181–193.

Ihme, M. and Chung, W. T. (2024). "Artificial intelligence as a catalyst for combustion science and engineering". *Proceedings of the Combustion Institute* 40 (1-4), p. 105730.

Ihme, M., Schmitt, C., and Pitsch, H. (2009). "Optimal artificial neural networks and tabulation methods for chemistry representation in LES of a bluff-body swirl-stabilized flame". *Proceedings of the Combustion Institute* 32 (1), pp. 1527–1535.

Im, S., Baccarella, D., McGann, B., Liu, Q., Wermer, L., and Do, H. (2016). "Unstart phenomena induced by mass addition and heat release in a model scramjet". *Journal of Fluid Mechanics* 797, pp. 604–629.

Jackson, K., Gruber, M., and Buccellato, S. (2013). "An Overview of the HIFiRE Flight 2 Project (Invited)". *51$^{st}$AIAA Aerospace Sciences Meeting including the New Horizons Forum and Aerospace Exposition*. American Institute of Aeronautics and Astronautics.

Jain, R., Ullman, M., and Raman, V. (2025). "Flame Stabilization in an Axisymmetric Scramjet Combustor Flowpath". *AIAA Science and Technology Forum and Exposition, AIAA SciTech Forum 2025*.

Janicka, J., Kolbe, W., and Kollmann, W. (1978). "The Solution of a p.d.f.-Transport Equation for Turbulent Diffusion Flames". *Proceedings of the 1978 Heat Transfer and Fluid Mechanics Institute*. Ed. by C. T. Crowe and W. L. Grosshander. Stanford University Press, pp. 296–312.

Jiang, G. S. and Shu, C. W. (1996). "Efficient Implementation of Weighted ENO Schemes". *Journal of Computational Physics* 126 (1), pp. 202–228.

Jones, W. P. and Navarro-Martinez, S. (2007). "Large eddy simulation of autoignition with a subgrid probability density function method". *Combustion and Flame* 150, pp. 170–187.

Kawai, S. and Larsson, J. (2012). "Wall-modeling in large eddy simulation: Length scales, grid resolution, and accuracy". *Physics of Fluids* 24 (1), p. 015105.

Kawai, S. and Larsson, J. (2013). "Dynamic non-equilibrium wall-modeling for large eddy simulation at high Reynolds numbers". *Physics of Fluids* 25 (1), p. 15105.

King, R. N., Hamlington, P. E., and Dahm, W. J. (2016). "Autonomic closure for turbulence simulations". *Physical Review E* 93 (3), p. 031301.

Kloeden, P. E. and Platen, E. (1992). *Numerical Solution of Stochastic Differential Equations*. Springer Berlin Heidelberg.

Kolmogorov, A. N. (1962). "A refinement of previous hypotheses concerning the local structure of turbulence in a viscous incompressible fluid at high Reynolds number". *Journal of Fluid Mechanics* 13 (1), pp. 82–85.

Koo, H., Donde, P., and Raman, V. (2013). "LES-based Eulerian PDF approach for the simulation of scramjet combustors". *Proceedings of the Combustion Institute* 34 (2), pp. 2093–2100.

Kotov, D. V., Yee, H. C., Wray, A. A., Hadjadj, A., and Sjögreen, B. (2016). "High Order Numerical Methods for the Dynamic SGS Model of Turbulent Flows with Shocks". *Communications in Computational Physics* 19 (2), pp. 273–300.

Kraichnan, R. H. (1959). "The structure of isotropic turbulence at very high Reynolds numbers". *Journal of Fluid Mechanics* 5 (4), p. 497.

Lapeyre, C. J., Misdariis, A., Cazard, N., Veynante, D., and Poinsot, T. (2019). "Training convolutional neural networks to estimate turbulent sub-grid scale reaction rates". *Combustion and Flame* 203, pp. 255–264.

Larsson, J., Vicquelin, R., and Bermejo-Moreno, D. I. (2011). "Large eddy simulations of the HyShot II scramjet". *Center for Turbulence Research Annual Research Briefs*. Stanford University.

Larsson, J. (2010). "Effect of Shock-Capturing Errors on Turbulence Statistics". *AIAA Journal* 48 (7), pp. 1554–1557.

Larsson, J., Kawai, S., Bodart, J., and Bermejo-Moreno, I. (2016). "Large eddy simulation with modeled wall-stress: recent progress and future directions". *Mechanical Engineering Reviews* 3 (1), pp. 15–00418.

Larsson, J., Laurence, S., Bermejo-Moreno, I., Bodart, J., Karl, S., and Vicquelin, R. (2015). "Incipient thermal choking and stable shock-train formation in the heat-release region of a scramjet combustor. Part II: Large eddy simulations". *Combustion and Flame* 162 (4), pp. 907–920.

Lee, M. and Moser, R. D. (2015). "Direct numerical simulation of turbulent channel flow up to $Re_\tau \approx 5200$". *Journal of Fluid Mechanics* 774, pp. 395–415.

Lele, S. K. (1992). "Compact finite difference schemes with spectral-like resolution". *Journal of Computational Physics* 103 (1), pp. 16–42.

Leyva, I. A. (2017). "The relentless pursuit of hypersonic flight". *Physics Today* 70 (11), pp. 30–36.

Li, J., Zhao, Z., Kazakov, A., and Dryer, F. L. (2004). "An updated comprehensive kinetic model of hydrogen combustion". *International Journal of Chemical Kinetics* 36 (10), pp. 566–575.

Li, N., Chang, J., Xu, K., Yu, D., and Bao, W. (2021). "Instability of shock train behaviour with incident shocks". *Journal of Fluid Mechanics* 907, A40.

Li, Y., Perlman, E., Wan, M., Yang, Y., Meneveau, C., Burns, R., Chen, S., Szalay, A., and Eyink, G. (2008). "A public turbulence database cluster and applications to study Lagrangian evolution of velocity increments in turbulence". *Journal of Turbulence* 9.31.

Ling, J., Kurzawski, A., and Templeton, J. (2016). "Reynolds averaged turbulence modelling using deep neural networks with embedded invariance". *Journal of Fluid Mechanics* 807, pp. 155–166.

Liu, J. and Wang, H. (2022). "Machine learning assisted modeling of mixing timescale for LES/PDF of high-Karlovitz turbulent premixed combustion". *Combustion and Flame* 238, p. 111895.

Liu, W. and Jones, W. P. (2025). "LES of dual-swirl non-premixed H2 turbulent flame using Eulerian stochastic fields". *Combustion and Flame* 275, p. 114094.

Lumley, J. L. (1970). "Toward a turbulent constitutive relation". *Journal of Fluid Mechanics* 41 (2), pp. 413–434.

Lundgren, T. S. (1967). "Distribution Functions in the Statistical Theory of Turbulence". *Physics of Fluids* 10 (5), pp. 969–975.

Lundgren, T. S. (1969). "Model Equation for Nonhomogeneous Turbulence". *Physics of Fluids* 12 (3), p. 485.

Lusher, D. J. and Sandham, N. D. (2021). "Assessment of Low-Dissipative Shock-Capturing Schemes for the Compressible Taylor–Green Vortex". *AIAA Journal* 59 (2), pp. 533–545.

Magnussen, B. F. (1981). "On the structure of turbulence and a generalized eddy dissipation concept for chemical reaction in turbulent flow". *19$^{th}$ Aerospace Sciences Meeting*. American Institute of Aeronautics and Astronautics.

Magnussen, B. F. and Hjertager, B. H. (1977). "On mathematical modeling of turbulent combustion with special emphasis on soot formation and combustion". *Symposium (International) on Combustion* 16 (1), pp. 719–729.

Martín, M. P., Taylor, E. M., Wu, M., and Weirs, V. G. (2006). "A bandwidth-optimized WENO scheme for the effective direct numerical simulation of compressible turbulence". *Journal of Computational Physics* 220 (1), pp. 270–289.

Martín, M. P., Piomelli, U., and Candler, G. V. (2000). "Subgrid-Scale Models for Compressible Large-Eddy Simulations". *Theoretical and Computational Fluid Dynamics* 13 (5), pp. 361–376.

Mauery, T., Alonso, J., Cary, A., Lee, V., Malecki, R., Mavriplis, D., Medic, G., Schaefer, J., and Slotnick, J. (2021). *A Guide for Aircraft Certification by Analysis*. Tech. rep. NASA CR-20210015404.

Mcbride, B. J., Gordon, S., Cleveland, A., and Reno, M. A. (1993). *Coefficients for calculating thermodynamic and transport properties of individual species*. Tech. rep. NASA.

Menon, S. and Kerstein, A. R. (2011). "The Linear-Eddy Model". *Turbulent Combustion Modeling: Advances, New Trends and Perspectives*. Ed. by T. Echekki and E. Mastorakos. Dordrecht: Springer Netherlands, pp. 221–247.

Micka, D. J., Torrez, S. M., and Driscoll, J. F. (2009). "Heat Release Distribution in a Dual-Mode Scramjet Combustor-Measurements and Modeling". *16$^{th}$AIAA/DLR/DGLR International Space Planes and Hypersonic Systems and Technologies Conference*.

Micka, D. J. and Driscoll, J. F. (2008). "Dual-Mode Combustion of a Jet in Cross-Flow with Cavity Flameholder". *46$^{th}$AIAA Aerospace Sciences Meeting and Exhibit*. American Institute of Aeronautics and Astronautics.

Micka, D. J. and Driscoll, J. F. (2009). "Combustion characteristics of a dual-mode scramjet combustor with cavity flameholder". *Proceedings of the Combustion Institute* 32 (2), pp. 2397–2404.

Micka, D. J. (2010). "Combustion stabilization, structure, and spreading in a laboratory dual-mode scramjet combustor". PhD thesis. University of Michigan.

Millikan, R. C. and White, D. R. (1963). "Systematics of Vibrational Relaxation". *The Journal of Chemical Physics* 39 (12), pp. 3209–3213.

Möbus, H., Gerlinger, P., and Brüggemann, D. (2003). "Scalar and joint scalar-velocity-frequency Monte Carlo PDF simulation of supersonic combustion". *Combustion and Flame* 132 (1-2), pp. 3–24.

Modesti, D. and Pirozzoli, S. (2016). "Reynolds and Mach number effects in compressible turbulent channel flow". *International Journal of Heat and Fluid Flow* 59, pp. 33–49.

Moin, P., Squires, K., Cabot, W., and Lee, S. (1991). "A dynamic subgrid-scale model for compressible turbulence and scalar transport". *Physics of Fluids A: Fluid Dynamics* 3 (11), p. 2746.

Monin, A. S. (1967). "Equations for finite dimensional probability distributions of a field of turbulence". *Doklady Akademii Nauk SSSR* 177 (5), pp. 1036–1038.

Morkovin, M. V. (1962). "Effects of compressibility on turbulent flows". *Mécanique de la Turbulence* 367.380, p. 26.

Moser, R. D., Haering, S. W., and Yalla, G. R. (2021). "Statistical Properties of Subgrid-Scale Turbulence Models". *Annual Review of Fluid Mechanics* 53 (1), pp. 255–286.

Mottura, L., Vigevano, L., and Zaccanti, M. (1997). "An Evaluation of Roe's Scheme Generalizations for Equilibrium Real Gas Flows". *Journal of Computational Physics* 138 (2), pp. 354–399.

Moule, Y., Sabelnikov, V., and Mura, A. (2014). "Highly resolved numerical simulation of combustion in supersonic hydrogen–air coflowing jets". *Combustion and Flame* 161 (10), pp. 2647–2668.

Mustata, R., Valiño, L., Jiménez, C., Jones, W., and Bondi, S. (2006). "A probability density function Eulerian Monte Carlo field method for large eddy simulations: Application to a turbulent piloted methane/air diffusion flame (Sandia D)". *Combustion and Flame* 145 (1-2), pp. 88–104.

Navarro-Martinez, S., Kronenburg, A., and Mare, F. D. (2005). "Conditional moment closure for large eddy simulations". *Flow, Turbulence and Combustion* 75 (1-4), pp. 245–274.

Navarro-Martinez, S., Un, T.-H., and Patel, M. (2025). *Cerisse: A high-order LES/DNS solver for compressible turbulent reactive flows*. `https://github.com/salvadornm/cerisse`.

Nguyen, H. T., Barnaud, C., Domingo, P., Nguyen, P. D., and Vervisch, L. (2023). "Large-Eddy Simulation of flameless combustion with neural-network driven chemistry". *Applications in Energy and Combustion Science* 14, p. 100126.

Nguyen, P.-D., Vervisch, L., Subramanian, V., and Domingo, P. (2010). "Multidimensional flamelet-generated manifolds for partially premixed combustion". *Combustion and Flame* 157 (1), pp. 43–61.

Nicoud, F. and Ducros, F. (1999). "Subgrid-scale stress modelling based on the square of the velocity gradient tensor". *Flow, Turbulence and Combustion* 62 (3), pp. 183–200.

Nicoud, F., Toda, H. B., Cabrit, O., Bose, S., and Lee, J. (2011). "Using singular values to build a subgrid-scale model for large eddy simulations". *Physics of Fluids* 23 (8), p. 85106.

Nikolaou, Z., Vervisch, L., and Domingo, P. (2022). "Criteria to switch from tabulation to neural networks in computational combustion". *Combustion and Flame* 246, p. 112425.

Nista, L., Schumann, C., Grenga, T., Attili, A., and Pitsch, H. (2023). "Investigation of the generalization capability of a generative adversarial network for large eddy simulation of turbulent premixed reacting flows". *Proceedings of the Combustion Institute* 39 (4), pp. 5279–5288.

Nordin-Bates, K., Fureby, C., Karl, S., and Hannemann, K. (2017). "Understanding scramjet combustion using LES of the HyShot II combustor". *Proceedings of the Combustion Institute* 36 (2), pp. 2893–2900.

Ó Conaire, M., Curran, H. J., Simmie, J. M., Pitz, W. J., and Westbrook, C. K. (2004). "A comprehensive modeling study of hydrogen oxidation". *International Journal of Chemical Kinetics* 36 (11), pp. 603–622.

O'Brien, E. E. (1980). "The probability density function (pdf) approach to reacting turbulent flows". *Turbulent Reacting Flows*. Ed. by P. A. Libby and F. A. Williams. Springer Berlin Heidelberg, pp. 185–218.

Park, G. I. and Moin, P. (2014). "An improved dynamic non-equilibrium wall-model for large eddy simulation". *Physics of Fluids* 26 (1), p. 15108.

Pierce, C. D. and Moin, P. (2004). "Progress-variable approach for large-eddy simulation of non-premixed turbulent combustion". *Journal of Fluid Mechanics* 504, pp. 73–97.

Piomelli, U. (2008). "Wall-layer models for large-eddy simulations". *Progress in Aerospace Sciences* 44 (6), pp. 437–446.

Pirozzoli, S. (2011). "Numerical Methods for High-Speed Flows". *Annual Review of Fluid Mechanics* 43 (1), pp. 163–194.

Pitsch, H. and Steiner, H. (2000). "Large-eddy simulation of a turbulent piloted methane/air diffusion flame (Sandia flame D)". *Physics of Fluids* 12 (10), pp. 2541–2554.

Poinsot, T. and Veynante, D. (2012). *Theoretical and numerical combustion*. 3rd ed. The authors.

Pope, S. B. (1976). "The probability approach to the modelling of turbulent reacting flows". *Combustion and Flame* 27, pp. 299–312.

Pope, S. B. (1985). "PDF methods for turbulent reactive flows". *Progress in Energy and Combustion Science* 11 (2), pp. 119–192.

Pope, S. B. and Chen, Y. L. (1990). "The velocity-dissipation probability density function model for turbulent flows". *Physics of Fluids A: Fluid Dynamics* 2 (8), pp. 1437–1449.

Pope, S. B. (2000). *Turbulent Flows*. Cambridge University Press.

Pope, S. B. (2004). "Ten questions concerning the large-eddy simulation of turbulent flows". *New Journal of Physics* 6 (1), p. 35.

Prasad, V. N. (2011). "Large Eddy Simulation of Partially Premixed Turbulent Combustion". PhD thesis. Imperial College London.

Prat, A., Sautory, T., and Navarro-Martinez, S. (2020). "A Priori Sub-grid Modelling Using Artificial Neural Networks". *International Journal of Computational Fluid Dynamics* 34 (6), pp. 397–417.

Rathore, O. and Navarro-Martinez, S. (2023). "Flame Dynamics Modelling Using Artificially Thickened Models". *Flow, Turbulence and Combustion* 111 (3), pp. 897–927.

Readshaw, T., Ding, T., Rigopoulos, S., and Jones, W. P. (2021). "Modeling of turbulent flames with the large eddy simulation–probability density function (LES–PDF) approach, stochastic fields, and artificial neural networks". *Physics of Fluids* 33 (3), p. 035154.

Ribeiro, F. H. E., Boukharfane, R., and Mura, A. (2020). "Highly-resolved large-eddy simulations of combustion stabilization in a scramjet engine model with cavity flameholder". *Computers & Fluids* 197, p. 104344.

Ristorcelli, J. R. (1997). "A pseudo-sound constitutive relationship for the dilatational covariances in compressible turbulence". *Journal of Fluid Mechanics* 347, pp. 37–70.

Roe, P. (1981). "Approximate Riemann solvers, parameter vectors, and difference schemes". *Journal of Computational Physics* 43 (2), pp. 357–372.

Roy, A., Kumar, S., and Ghosh, S. (2025). "Direct Numerical Simulation and Implicit Large-Eddy Simulation of Shock Train in Channel Flow Using High Order Optimised Targeted Essentially Non-Oscillatory Schemes". *International Journal for Numerical Methods in Fluids* 97 (5), pp. 713–735.

Sabelnikov, V. and Fureby, C. (2013). "Extended LES-PaSR model for simulation of turbulent combustion". *Progress in Propulsion Physics*. Vol. 4. EDP Sciences, pp. 539–568.

Sagaut, P. (2001). *Large Eddy Simulation for Incompressible Flows*. Springer Berlin Heidelberg.

Särkkä, S. and Solin, A. (2019). *Applied Stochastic Differential Equations*. Cambridge University Press.

Segal, C. (2009). *The Scramjet Engine*. Cambridge University Press.

Seltz, A., Domingo, P., and Vervisch, L. (2021). "Solving the population balance equation for non-inertial particles dynamics using probability density function and neural networks: Application to a sooting flame". *Physics of Fluids* 33 (1).

Seltz, A., Domingo, P., Vervisch, L., and Nikolaou, Z. M. (2019). "Direct mapping from LES resolved scales to filtered-flame generated manifolds using convolutional neural networks". *Combustion and Flame* 210, pp. 71–82.

Sharma, S., Bielawski, R., Gibson, O., Zhang, S., Sharma, V., Rauch, A. H., Singh, J., Abisleiman, S., Ullman, M., Barwey, S., and Raman, V. (2025). "An AMReX-based Compressible Reacting Flow Solver for High-speed Reacting Flows relevant to Hypersonic Propulsion". *arXiv.2412.00900*.

Sheikhi, M. R. H., Givi, P., and Pope, S. B. (2007). "Velocity-scalar filtered mass density function for large eddy simulation of turbulent reacting flows". *Physics of Fluids* 19 (9).

Singh, A. P., Medida, S., and Duraisamy, K. (2017). "Machine-Learning-Augmented Predictive Modeling of Turbulent Separated Flows over Airfoils". *AIAA Journal* 55 (7), pp. 2215–2227.

Slessor, M. D., Zhuang, M., and Dimotakis, P. E. (2000). "Turbulent shear-layer mixing: growth-rate compressibility scaling". *Journal of Fluid Mechanics* 414, pp. 35–45.

Slotnick, J., Khodadoust, A., Alonso, J., Darmofal, D., Gropp, W., Lurie, E., and Mavriplis, D. (2014). *CFD Vision 2030 Study: A Path to Revolutionary Computational Aerosciences*. Tech. rep. NASA CR–2014-218178.

Smagorinsky, J. (1963). "General circulation experiments with the primitive equations". *Monthly Weather Review* 91 (3), pp. 99–164.

Smart, M. K. (2015). "Flow modeling of pseudoshocks in backpressured ducts". *AIAA Journal* 53 (12), pp. 3577–3588.

Smart, M. K., Hass, N. E., and Paull, A. (2006). "Flight Data Analysis of the HyShot 2 Scramjet Flight Experiment". *AIAA Journal* 44 (10), pp. 2366–2375.

Smart, M. K. and Tetlow, M. R. (2009). "Orbital Delivery of Small Payloads Using Hypersonic Airbreathing Propulsion". *Journal of Spacecraft and Rockets* 46 (1), pp. 117–125.

Soulard, O. and Sabel'nikov, V. (2006). "Eulerian Monte Carlo method for the joint velocity and mass-fraction probability density function in turbulent reactive gas flows". *Combustion, Explosion, and Shock Waves* 42 (6), pp. 753–762.

Spalart, P. R. (2009). "Detached-Eddy Simulation". *Annual Review of Fluid Mechanics* 41 (1), pp. 181–202.

Spalding, D. B. (1971). "Mixing and chemical reaction in steady confined turbulent flames". *Symposium (International) on Combustion* 13 (1), pp. 649–657.

Starikovskiy, A. and Aleksandrov, N. (2011). "Plasma-Assisted Ignition and Combustion". *Aeronautics and Astronautics*. Ed. by M. Mulder. Rijeka: IntechOpen.

Stolz, S. and Adams, N. A. (1999). "An approximate deconvolution procedure for large-eddy simulation". *Physics of Fluids* 11 (7), pp. 1699–1701.

Sun, M. B., Wang, H., Wang, Z., Geng, H., Liang, J., Liu, W., and Bai, X. (2009). "Experimental and Numerical Study on Flame Stabilization in a Supersonic Combustor with Hydrogen Injection Upstream of Cavity Flameholders". *45$^{th}$ AIAA/ASME/SAE/ASEE Joint Propulsion Conference & Exhibit*. American Institute of Aeronautics and Astronautics.

Sunami, T., Murakami, A., Kudo, K., Kodera, M., and Nishioka, M. (2002). "Mixing and Combustion Control Strategies for Efficient Scramjet Operation in Wide Range of Flight Mach Number". *AIAA/AAAF 11$^{th}$ International Space Planes and Hypersonic Systems and Technologies Conference*. American Institute of Aeronautics and Astronautics.

Tam, C. and Shen, H. (1993). "Direct computation of nonlinear acoustic pulses using high-order finite difference schemes". *15$^{th}$ Aeroacoustics Conference*. American Institute of Aeronautics and Astronautics.

Tan, R. and Ooi, A. (2022). "Two Dimensional Analysis and Optimization of Hybrid MDCD-TENO Schemes". *Journal of Scientific Computing* 90 (1), p. 64.

Tang, Q., Zhao, W., Bockelie, M., and Fox, R. O. (2007). "Multi-environment probability density function method for modelling turbulent combustion using realistic chemical kinetics". *Combustion Theory and Modelling* 11 (6), pp. 889–907.

Toro, E. F., Spruce, M., and Speares, W. (1994). "Restoration of the contact surface in the HLL-Riemann solver". *Shock Waves* 4 (1), pp. 25–34.

Tyliszczak, A., Kuban, L., and Stempka, J. (2022). "Numerical analysis of non-excited and excited jets issuing from non-circular nozzles". *International Journal of Heat and Fluid Flow* 94, p. 108944.

U.S. Government Accountability Office (2019). *Science & Tech Spotlight: Hypersonic Weapons*. http://www.gao.gov/products/gao-19-705sp.

Urzay, J. (2018). "Supersonic Combustion in Air-Breathing Propulsion Systems for Hypersonic Flight". *Annual Revew of Fluid Mechanics* 50 (1), pp. 593–627.

Valiño, L. (1998). "A field Monte Carlo formulation for calculating the probability density function of a single scalar in a turbulent flow". *Flow, turbulence and combustion* 60, pp. 157–172.

van Noordt, W., Ganju, S., and Brehm, C. (2022). "An immersed boundary method for wall-modeled large-eddy simulation of turbulent high-Mach-number flows". *Journal of Computational Physics* 470, p. 111583.

van Oijen, J., Lammers, F., and de Goey, L. P. H. (2001). "Modeling of complex premixed burner systems by using flamelet-generated manifolds". *Combustion and Flame* 127 (3), pp. 2124–2134.

Vanstone, L., Lingren, J., and Clemens, N. T. (2018). "Simple physics-based model for the prediction of shock-train location". *Journal of Propulsion and Power* 34 (6), pp. 1428–1441.

Vassilicos, J. C. (2015). "Dissipation in Turbulent Flows". *Annual Review of Fluid Mechanics* 47 (1), pp. 95–114.

Veeraragavan, A. (2025). *Applications of Hypersonic Shock Tunnels and Expansion Tubes*. Presentation at the UQ Short Course on Hypersonic Shock Tube Technology, Brisbane, Australia.

Veynante, D. and Vervisch, L. (2002). "Turbulent combustion modeling". *Progress in Energy and Combustion Science* 28 (3), pp. 193–266.

Vreman, B., Geurts, B., and Kuerten, H. (1995). "A priori tests of large eddy simulation of the compressible plane mixing layer". *Journal of Engineering Mathematics* 29 (4), pp. 299–327.

Wacławczyk, M., Pozorski, J., and Minier, J.-P. (2004). "Probability density function computation of turbulent flows with a new near-wall model". *Physics of Fluids* 16 (5), pp. 1410–1422.

Waidmann, W., Alff, F., Böhm, M., Brummund, U., Clauß, W., and Oschwald, M. (1996). "Supersonic Combustion of Hydrogen/Air in a Scramjet Combustion Chamber". *Space Technology* 15, No. 6, pp. 421–429.

Wang, H., Wang, Z., Sun, M., and Qin, N. (2014). "Simulations of combustion with normal and angled hydrogen injection in a cavity-based supersonic combustor". *Proceedings of the Institution of Mechanical Engineers, Part G: Journal of Aerospace Engineering* 228 (4), pp. 530–541.

Weatheritt, J. and Sandberg, R. (2016). "A novel evolutionary algorithm applied to algebraic modifications of the RANS stress–strain relationship". *Journal of Computational Physics* 325, pp. 22–37.

Weber, R. J. and Mackay, J. S. (1958). *An analysis of ramjet engines using supersonic combustion*. Tech. rep. NACA TN-4386.

Williams, F. A. (2000). "Progress in knowledge of flamelet structure and extinction". *Progress in Energy and Combustion Science* 26 (4-6), pp. 657–682.

Wu, J., Xiao, H., Sun, R., and Wang, Q. (2019). "Reynolds-averaged Navier–Stokes equations with explicit data-driven Reynolds stress closure can be ill-conditioned". *Journal of Fluid Mechanics* 869, pp. 553–586.

Xia, Y., Liu, Y., Vaithianathan, T., and Collins, L. R. (2010). "Eddy damped quasinormal Markovian theory for chemically reactive scalars in isotropic turbulence". *Physics of Fluids* 22 (4), pp. 1–14.

Yamashita, H., Shimada, M., and Takeno, T. (1996). "A numerical study on flame stability at the transition point of jet diffusion flames". *Symposium (International) on Combustion* 26 (1), pp. 27–34.

Yang, X. I., Urzay, J., Bose, S., and Moin, P. (2018). "Aerodynamic heating in wall-modeled large-eddy simulation of high-speed flows". *AIAA Journal* 56 (2), pp. 731–742.

Yang, X. I. and Griffin, K. P. (2021). "Grid-point and time-step requirements for direct numerical simulation and large-eddy simulation". *Physics of Fluids* 33 (1), p. 15108.

Yao, S., Wang, B., Kronenburg, A., and Stein, O. T. (2020). "Modeling of sub-grid conditional mixing statistics in turbulent sprays using machine learning methods". *Physics of Fluids* 32 (11), p. 115124.

Yetter, R. A., Dryer, F. L., and Rabitz, H. (1991). "A Comprehensive Reaction Mechanism For Carbon Monoxide/Hydrogen/Oxygen Kinetics". *Combustion Science and Technology* 79 (1-3), pp. 97–128.

Yoshizawa, A. (1986). "Statistical theory for compressible turbulent shear flows, with the application to subgrid modeling". *The Physics of Fluids* 29 (7), p. 2152.

Zeman, O. (1991). "On the decay of compressible isotropic turbulence". *Physics of Fluids A: Fluid Dynamics* 3 (5), pp. 951–955.

Zettervall, N. and Fureby, C. (2018). "A Computational Study of Ramjet, Scramjet and Dual-mode Ramjet Combustion in Combustor with a Cavity Flameholder". *2018 AIAA Aerospace Sciences Meeting*. American Institute of Aeronautics and Astronautics.

Zhang, W., Almgren, A., Beckner, V., Bell, J., Blaschke, J., Chan, C., Day, M., Friesen, B., Gott, K., Graves, D., Katz, M. P., Myers, A., Nguyen, T., Nonaka, A., Rosso, M., Williams, S., and Zingale, M. (2019). "AMReX: a framework for block-structured adaptive mesh refinement". *Journal of Open Source Software* 4 (37), p. 1370.

Zhong, Z., Wang, Z., Sun, M., and Wang, H. (2016). "Combustion characteristics in a supersonic combustor with ethylene injection upstream of dual parallel cavities". *Proceedings of the Institution of Mechanical Engineers, Part G: Journal of Aerospace Engineering* 230 (13), pp. 2515–2522.

Zhou, L., Song, Y., Ji, W., and Wei, H. (2022). "Machine learning for combustion". *Energy and AI* 7, p. 100128.

Zhu, R., Huang, Z., Xu, C., Fang, X., Zhang, H., and Davy, M. (2024). "Large eddy simulation of a supersonic lifted hydrogen flame: Impacts of Lewis, turbulent Schmidt and Prandtl numbers". *Physics of Fluids* 36 (7).

# Appendix A

# Eigen-system of the Euler equations

The Navier-Stokes equations without the diffusive fluxes are known as the Euler equations. It can be written in terms of the conservative variables, as in (2.1), or in terms of the primitive variables $\mathbf{Q}$. This appendix will follow the primitive variables approach and will be presented in one dimension.

The Euler equation can be recast into the quasi-linear form,

$$\frac{\partial \mathbf{Q}}{\partial t} + \mathbf{J}(\hat{\mathbf{Q}})\frac{\partial \mathbf{Q}}{\partial x} = \mathbf{0}, \tag{A.1}$$

where

$$\mathbf{Q} = \begin{bmatrix} \rho \\ u_n \\ u_t \\ p \\ Y_\alpha \end{bmatrix}, \quad \mathbf{J} = \left.\frac{\partial \mathbf{F}}{\partial \mathbf{Q}}\right|_{\mathbf{Q}=\hat{\mathbf{Q}}} = \begin{bmatrix} u_n & \rho & 0 & 0 & 0 \\ 0 & u_n & 0 & 1/\rho & 0 \\ 0 & 0 & u_n & 0 & 0 \\ 0 & \rho c^2 & 0 & u_n & 0 \\ 0 & 0 & 0 & 0 & u_n \end{bmatrix} = \begin{bmatrix} u_n & \rho & 0 & 0 & 0 \\ 0 & u_n & 0 & 1/\rho & 0 \\ 0 & 0 & u_n & 0 & 0 \\ 0 & \gamma p & 0 & u_n & 0 \\ 0 & 0 & 0 & 0 & u_n \end{bmatrix},$$

and $u_n$ and $u_t$ are the velocity component normal and tangent to direction $x$, respectively. The hat $\hat{\cdot}$ denotes a reference state that is constant and independent of $x$ and $t$.

The flux Jacobian matrix $\mathbf{J}$ can be decomposed into a product of the eigenvector matrix $\mathbf{L}$, a diagonal matrix of eigenvalues $\mathbf{\Lambda}$, and the right eigenvector matrix $\mathbf{R} = \mathbf{L}^{-1}$. The system of equations can therefore be decoupled into independent advection equations:

$$\frac{\partial \mathbf{Q}}{\partial t} + \mathbf{R}\mathbf{\Lambda}\mathbf{L}\frac{\partial \mathbf{Q}}{\partial x} = \mathbf{0} \iff \frac{\partial \mathbf{W}}{\partial t} + \mathbf{\Lambda}\frac{\partial \mathbf{W}}{\partial x} = \mathbf{0}\,. \tag{A.2}$$

where $\mathbf{W} = \mathbf{L}\mathbf{Q}$ is known as the characteristic variables, and the wave speeds are $\mathbf{\Lambda} = \mathrm{diag}(u_n + c,\ u_n,\ u_n,\ u_n,\ u_n - c)$. $\mathbf{L}$ can be viewed as a (linear) projection of $\mathbf{Q}$ to $\mathbf{W}$.

Similarly, the characteristic projection that maps the state variables $\mathbf{U}$ to $\mathbf{W}$ can be

defined, noting that $\mathbf{Q}$ is a function of $\mathbf{U}$:

$$\mathbf{P}(\mathbf{U}, \hat{\mathbf{U}}) = \mathbf{L}(\mathbf{Q}(\hat{\mathbf{U}}))\mathbf{Q}(\mathbf{U}) = \mathbf{W}\,. \tag{A.3}$$

Its inverse projection is

$$\mathbf{P}^{-1}(\mathbf{U}, \hat{\mathbf{U}}) = \mathbf{Q}^{-1}(\mathbf{R}(\hat{\mathbf{U}})\mathbf{W}) = \mathbf{U}\,. \tag{A.4}$$

They are central to the stability of WENO reconstruction schemes, see (2.33), (2.55)–(2.56).

In functional form, a thermodynamic variable is needed. If the speed of sound $c$ is used,

$$\mathbf{W}(\mathbf{U}, \hat{c}) = \begin{bmatrix} \frac{1}{2}(p/c + \rho u_n) \\ \rho - p/\hat{c}^2 \\ u_t \\ Y_\alpha \\ \frac{1}{2}(p/\hat{c} - \rho u_n) \end{bmatrix}, \qquad \mathbf{Q}(\mathbf{W}, \hat{c}) = \begin{bmatrix} w_2 + (w_1 + w_5)/\hat{c} \\ (w_1 - w_5)/\hat{\rho} \\ u_t \\ (w_1 + w_5)\hat{c} \\ Y_\alpha \end{bmatrix}, \tag{A.5}$$

where the second component of $\mathbf{Q}$ can be approximated using $\hat{\rho} \approx \rho = w_2 + (w_1 + w_5)/\hat{c}$.

Alternatively, if the specific heat ratio $\gamma$ is used,

$$\mathbf{W}(\mathbf{U}, \hat{\gamma}) = \begin{bmatrix} \frac{1}{2}(p + u_n\sqrt{\hat{\gamma}\rho p}) \\ \rho - \rho/\hat{\gamma} \\ u_t \\ Y_\alpha \\ \frac{1}{2}(p - u_n\sqrt{\hat{\gamma}\rho p}) \end{bmatrix}, \qquad \mathbf{Q}(\mathbf{W}, \hat{\gamma}) = \begin{bmatrix} w_1/(1 - 1/\hat{\gamma}) \\ (w_1 - w_5)/\sqrt{\hat{\gamma}\rho p} \\ u_t \\ w_1 + w_5 \\ Y_\alpha \end{bmatrix}. \tag{A.6}$$

A simple arithmetic average of the left and the right cells is used to calculate the reference states. The Roe average may be beneficial when stability is needed in more challenging cases (Roe 1981):

$$\hat{\rho} = \sqrt{\rho_L \rho_R}\,, \tag{A.7}$$

$$\hat{u} = \frac{\sqrt{\rho_L}u_L + \sqrt{\rho_R}u_R}{\sqrt{\rho_L} + \sqrt{\rho_R}}\,, \tag{A.8}$$

$$\hat{h} = \frac{\sqrt{\rho_L}h_L + \sqrt{\rho_R}h_R}{\sqrt{\rho_L} + \sqrt{\rho_R}}\,, \tag{A.9}$$

$$\hat{c} = \sqrt{(\gamma - 1)\big(\hat{h} - \hat{q}^2/2\big)}\,, \tag{A.10}$$

where $h = e - p/\rho$, $q^2 = u^2 + v^2 + w^2$. See *e.g.* Mottura *et al.* 1997 for extension to real gas.

# Appendix B

# Scripts for proving the order of the central difference schemes

```
from sympy import *
from sympy.tensor.array.expressions import ArraySymbol

# Here, we find sxx (Ds2) at the cell centre
h = symbols('h')
Ds = ArraySymbol('Ds', (7,)) # d^n s/dx^n
s = zeros(5,1) # stencil
# FD (s are point values)
# |___|___|_?_|___|___|
#   0   1   2   3   4
#         sm   sp

# Expand using Taylor series
for i in range(Ds.shape[0]):
  s[0] += Ds[i]*(-2*h)**i/factorial(i)
  s[1] += Ds[i]*(-1*h)**i/factorial(i)
  s[2] += Ds[i]*(0*h)**i/factorial(i)
  s[3] += Ds[i]*(1*h)**i/factorial(i)
  s[4] += Ds[i]*(2*h)**i/factorial(i)

sm = (-1*s[1]+1*s[2])/h # 2th order
sp = (-1*s[2]+1*s[3])/h # 2th order
print(simplify((sp-sm)/h))
# output: h**4*Ds[6]/360 + h**2*Ds[4]/12 + Ds[2]

sm = (1*s[0]-15*s[1]+15*s[2]-1*s[3])/(12*h) # 4th order
sp = (1*s[1]-15*s[2]+15*s[3]-1*s[4])/(12*h) # 4th order
print(simplify((sp-sm)/h))
# output: -h**4*Ds[6]/90 + Ds[2]
```

Listing B.1: Python script for proving the order of accuracy of the normal derivative schemes in (2.58) and (2.61).

```
from sympy import *
from sympy.tensor.array.expressions import ArraySymbol

# Here, we find sxy (Ds11) at the cell centre
hx, hy = symbols('h_x h_y')
Ds = ArraySymbol('Ds', (7,7)) # d^n s/dx^n
s = zeros(5,5) # stencil

# 2D Taylor series
def Sn(n, x, y):
  sn = 0
  for m in range(n+1):
    sn += factorial(n)/factorial(m)/factorial(n-m)*Ds[m,n-m]*x**m*y**(n-m)
  return sn

# 4 |___|___|___|___|___|
# 3 |___|___|___|___|___|
# 2 |___|___X_?_X___|___|
# 1 |___|___|___|___|___|
# 0 |___|___|___|___|___|
#     0   1   2   3   4
#           sm   sp
for i in range(s.shape[0]):
  for j in range(s.shape[1]):
    for n in range(Ds.shape[0]):
      s[i,j] += Sn(n, (-2+i)*hx, (-2+j)*hy)/factorial(n)

sm = (s[1,3]-s[1,1] + s[2,3]-s[2,1])/4/hy # 2nd order
sp = (s[2,3]-s[2,1] + s[3,3]-s[3,1])/4/hy # 2nd order
print(simplify((sp-sm)/hx))
# output: h_x**4*Ds[5, 1]/120 + h_x**2*h_y**2*Ds[3, 3]/36 + h_x**2*Ds[3,
    1]/6 + h_y**4*Ds[1, 5]/120 + h_y**2*Ds[1, 3]/6 + Ds[1, 1]

sm = (-(s[0,0]-8*s[0,1]+8*s[0,3]-s[0,4])
    +7*(s[1,0]-8*s[1,1]+8*s[1,3]-s[1,4])
    +7*(s[2,0]-8*s[2,1]+8*s[2,3]-s[2,4])
      -(s[3,0]-8*s[3,1]+8*s[3,3]-s[3,4]))/(12*hy)/12 # 4th order
sp = (-(s[1,0]-8*s[1,1]+8*s[1,3]-s[1,4])
    +7*(s[2,0]-8*s[2,1]+8*s[2,3]-s[2,4])
    +7*(s[3,0]-8*s[3,1]+8*s[3,3]-s[3,4])
      -(s[4,0]-8*s[4,1]+8*s[4,3]-s[4,4]))/(12*hy)/12 # 4th order
print(simplify((sp-sm)/hx))
# output: -h_x**4*Ds[5, 1]/30 - h_y**4*Ds[1, 5]/30 + Ds[1, 1]
```

Listing B.2: Python script for proving the order of accuracy of the transverse derivative schemes in (2.59) and (2.63).

# Appendix C

# Derivation of the PDF transport equation

This derivation follows the fine-grained PDF approach in Pope 2000, Appendix H.

### Fine-grained PDF

A fine-grained PDF is defined as

$$f^*(\boldsymbol{\varphi}; \mathbf{x}, t) = \delta(\boldsymbol{\phi}(\mathbf{x}, t) - \boldsymbol{\varphi}) = \prod_{m=1}^{N_V} \delta(\phi_m(\mathbf{x}, t) - \varphi_m)\,. \tag{C.1}$$

Using the filtering operation (3.3),

$$\overline{f^*} = \overline{\delta(\boldsymbol{\phi} - \boldsymbol{\varphi})} = \int_{-\infty}^{\infty} \delta(\boldsymbol{\psi} - \boldsymbol{\varphi}) f(\boldsymbol{\psi})\, \mathrm{d}\boldsymbol{\psi} = f(\boldsymbol{\varphi})\,, \tag{C.2}$$

where $\boldsymbol{\psi}$, $\boldsymbol{\varphi}$ are both variables representing the sample space of the random variable $\boldsymbol{\phi}$.

### Conditional expectation

For a random variable $Q$ whose sample space variable is $q$,

$$\begin{aligned} \overline{Qf^*} = \overline{Q\delta(\boldsymbol{\phi} - \boldsymbol{\varphi})} &= \iint_{-\infty}^{\infty} q\delta(\boldsymbol{\psi} - \boldsymbol{\varphi}) f_{Q\phi}(q, \boldsymbol{\psi})\, \mathrm{d}q\mathrm{d}\boldsymbol{\psi} \\ &= \int_{-\infty}^{\infty} q f_{Q\phi}(q, \boldsymbol{\varphi})\, \mathrm{d}q \\ &= \int_{-\infty}^{\infty} q f_{Q|\phi}(q, \boldsymbol{\varphi})\, \mathrm{d}q \;\; f_\phi(\boldsymbol{\varphi}) = \overline{Q \,|\, \boldsymbol{\phi}}\, f(\boldsymbol{\varphi})\,. \end{aligned} \tag{C.3}$$

$\overline{Q\,|\,\boldsymbol{\phi}}$ is known as the conditional expectation of $Q$ on $\boldsymbol{\phi}$. The last step is due to the Bayes' theorem

$$f_{\psi|\phi}(\boldsymbol{\psi},\boldsymbol{\varphi}) = \frac{f_{\psi\phi}(\boldsymbol{\psi},\boldsymbol{\varphi})}{f_{\phi}(\boldsymbol{\varphi})}\,, \tag{C.4}$$

with $f_{\psi\phi}$ being the joint PDF and $f_{\phi}$ the marginal PDF. Three possibilities exist for $\overline{Q\,|\,\boldsymbol{\phi}}$:

1. $\boldsymbol{\psi}$ is a function of $\boldsymbol{\phi}$: the joint PDF reduces to the marginal PDF $f_{\psi\phi} = f_{\phi}\delta(\boldsymbol{\psi}-\boldsymbol{\varphi})$. As a result, $\overline{Q\,|\,\boldsymbol{\phi}} = Q(\boldsymbol{\varphi})$, as in the case with the chemical source term.

2. $\boldsymbol{\psi}$ is independent of $\boldsymbol{\phi}$: the joint PDF is separable $f_{\psi\phi} = f_{\psi}f_{\phi}$ and $\overline{Q\,|\,\boldsymbol{\phi}} = \bar{Q}$. For instance, gravity or external heat source that do not depend on the flow states.

3. $\boldsymbol{\psi}$ is related to $\boldsymbol{\phi}$ but with some unknown interaction: $f_{\psi\phi}$ is unknown, leaving us with a closure problem for $\overline{Q\,|\,\boldsymbol{\phi}}$. Unfortunately, all the terms involving spatial derivatives in the PDF transport equation belong to this case, as spatial derivatives require two-point information that is lacking in our one-point PDF.

**PDF transport equation**

We first seek the temporal derivative of $f^*$:

$$\frac{\partial f^*}{\partial t} = \frac{\partial \delta(\boldsymbol{\phi}-\boldsymbol{\varphi})}{\partial t} = \frac{\partial \delta(\boldsymbol{\phi}-\boldsymbol{\varphi})}{\partial \phi_m}\frac{\partial \phi_m}{\partial t} \tag{C.5}$$

$$= -\frac{\partial \delta(\boldsymbol{\phi}-\boldsymbol{\varphi})}{\partial \varphi_m}\frac{\partial \phi_m}{\partial t} \tag{C.6}$$

$$= -\frac{\partial f^*}{\partial \varphi_m}\frac{\partial \phi_m}{\partial t} = -\frac{\partial}{\partial \varphi_m}\left(\frac{\partial \phi_m}{\partial t} f^*\right)\,, \tag{C.7}$$

where (C.5) uses the chain rule, (C.6) applies the identity (Pope 2000, p. 674)

$$\frac{\partial \delta(a-b)}{\partial a} = -\frac{\partial \delta(a-b)}{\partial b}\,, \tag{C.8}$$

and (C.7) is uses the fact that $\phi_m$ is independent of $\varphi_m$.

Similarly, the spatial derivative of $f^*$ is

$$\frac{\partial f^*}{\partial x_j} = -\frac{\partial}{\partial \varphi_m}\left(\frac{\partial \phi_m}{\partial x_j} f^*\right)\,. \tag{C.9}$$

Multiplying both sides by the velocity $u_j$ and adding (C.7), we have

$$\frac{\partial f^*}{\partial t} + u_j\frac{\partial f^*}{\partial x_j} = -\frac{\partial}{\partial \varphi_m}\left[\left(\frac{\partial \phi_m}{\partial t} + u_j\frac{\partial \phi_m}{\partial x_j}\right) f^*\right]\,. \tag{C.10}$$

Finally, filtering the above equation by (C.2)–(C.3) completes the derivation

$$\frac{\partial f}{\partial t} + \overline{u_j|\,\boldsymbol{\phi}}\frac{\partial f}{\partial x_j} = -\frac{\partial}{\partial \varphi_m}\left(\overline{\frac{D\phi_m}{Dt}\,\middle|\,\boldsymbol{\phi}}\, f\right)\,, \tag{C.11}$$

where

$$\frac{D}{Dt} = \frac{\partial}{\partial t} + u_j \frac{\partial}{\partial x_j} \tag{C.12}$$

denotes the total derivative, and $\overline{u_j | \boldsymbol{\phi}} = v_j$ can be invoked if the PDF contains velocity in its sample space.

### MDF transport equation

For variable density flows, recall the definition of the MDF (3.4),

$$\overline{\rho f^*} = F(\boldsymbol{\varphi}) \,, \tag{C.13}$$

$$\overline{\rho Q f^*} = \widetilde{Q \,|\, \boldsymbol{\phi}} \; F(\boldsymbol{\varphi}) = \frac{\overline{\rho Q \,|\, \boldsymbol{\phi}}}{\bar{\rho}} F(\boldsymbol{\varphi}) \,. \tag{C.14}$$

The MDF transport equation is obtained by multiplying (C.10) with density $\rho$

$$\rho \frac{\partial f^*}{\partial t} + \rho u_j \frac{\partial f^*}{\partial x_j} = \frac{\partial \rho f^*}{\partial t} + \frac{\partial \rho u_j f^*}{\partial x_j} - \underbrace{\left( \frac{\partial \rho}{\partial t} + \frac{\partial \rho u_j}{\partial x_j} \right)}_{=0} f^* \tag{C.15}$$

$$= -\frac{\partial}{\partial \varphi_m} \left( \rho \frac{D\phi_m}{Dt} f^* \right) . \tag{C.16}$$

The last step uses the fact that $\rho$ is independent of $\boldsymbol{\phi}$.

Finally, filtering the above equation by (C.13)–(C.14) gives (3.6):

$$\frac{\partial F}{\partial t} + \frac{\partial \widetilde{u_j | \boldsymbol{\phi}} F}{\partial x_j} = -\frac{\partial}{\partial \varphi_m} \left( \widetilde{\left. \frac{D\phi_m}{Dt} \right| \boldsymbol{\phi}} \; F \right) . \tag{C.17}$$

### Equivalence to stochastic differential equations

The PDF transport equation is a Fokker-Planck equation. In the general form,

$$\frac{\partial f}{\partial t} + \overline{u_j | \boldsymbol{\phi}} \frac{\partial f}{\partial x_j} = -\frac{\partial}{\partial \varphi_m} (a_m f) + \frac{\partial^2}{\partial \varphi_m \partial \varphi_n} \left( \frac{1}{2} b_{mn}^2 f \right) , \tag{C.18}$$

which corresponds to the stochastic differential equation (SDE)

$$\mathrm{d}\mathbf{x}(t) = \overline{u_j | \boldsymbol{\phi}} \, \mathrm{d}t \,, \tag{C.19}$$

$$\mathrm{d}\boldsymbol{\phi}(t) = \mathbf{a}(\boldsymbol{\phi}, t) \, \mathrm{d}t + \mathbf{b}(\boldsymbol{\phi}, t) \, \mathrm{d}\mathbf{W}(t) \,, \tag{C.20}$$

where $\mathbf{x}$ is the Lagrangian position, $\mathbf{a}$ is the drift vector, $\mathbf{b}$ is the diffusion coefficient matrix, and $\mathbf{W}(t)$ is a vector Wiener process which has the property

$$\langle W_i(t_k) W_j(t_l) \rangle = \delta_{ij} |t_k - t_l| \,, \tag{C.21}$$

where angled brackets $\langle\cdot\rangle$ denote time averaging.

Using the definition of total derivative, this can also be written as a stochastic partial differential equation (SPDE)

$$\mathrm{d}\boldsymbol{\phi}(\mathbf{x},t) + \overline{u_j|\boldsymbol{\phi}}\frac{\partial\boldsymbol{\phi}(\mathbf{x},t)}{\partial x_j}\,\mathrm{d}t = \mathbf{a}(\boldsymbol{\phi},t)\,\mathrm{d}t + \mathbf{b}(\boldsymbol{\phi},t)\,\mathrm{d}\mathbf{W}\,. \tag{C.22}$$

Note that since $\mathbf{W}$ is continuous but not differentiable in time, temporal derivatives can only be interpreted as a finite change in the variable $\mathrm{d}\boldsymbol{\phi}$ over a finite time step $\mathrm{d}t$ and an increment in $\mathbf{W}$, $\mathrm{d}\mathbf{W} = \mathbf{W}(t+\mathrm{d}t) - \mathbf{W}(t)$. However, conventional partial derivatives exist in space as $\mathbf{W}$ is independent of (constant in) space.

Similarly, an MDF transport equation

$$\frac{\partial F}{\partial t} + \frac{\partial\widetilde{u_j|\boldsymbol{\phi}}\,F}{\partial x_j} = -\frac{\partial}{\partial\varphi_m}\left(a_m F\right) + \frac{\partial^2}{\partial\varphi_m\partial\varphi_n}\left(\frac{1}{2}b_{mn}^2 F\right), \tag{C.23}$$

corresponds to a SPDE of

$$\mathrm{d}\boldsymbol{\phi}(\mathbf{x},t) + \frac{\partial\widetilde{u_j|\boldsymbol{\phi}}\,\boldsymbol{\phi}(\mathbf{x},t)}{\partial x_j}\,\mathrm{d}t = \mathbf{a}(\boldsymbol{\phi},t)\,\mathrm{d}t + \mathbf{b}(\boldsymbol{\phi},t)\,\mathrm{d}\mathbf{W}\,, \tag{C.24}$$

$$\frac{\partial\bar{\rho}}{\partial t} + \frac{\partial\bar{\rho}\tilde{u}_j}{\partial x_j} = 0\,. \tag{C.25}$$

The last equation recovers the mass conservation in the Navier-Stokes equations. It is obtained by integrating the transport equation in its sample space, and using the divergence theorem so that the right-hand-side terms are the MDF at infinity $F(\pm\infty;\mathbf{x},t)$, which are exactly zero.

# Appendix D

# An alternative VSPDF system

This appendix presents a PDF of $\boldsymbol{\phi} = [\rho\mathbf{Y}, \rho\mathbf{u}, \rho E]$ as a new formulation for the joint-velocity-scalar PDF (VSPDF). This ongoing work is considered more consistent than previous formulations and has potential applications in future studies.

The PDF transport equation is

$$\begin{aligned}\frac{\partial f}{\partial t} + v_j\frac{\partial f}{\partial x_j} = &-\frac{\partial}{\partial r\Upsilon_\alpha}\left[\left(-\overline{\rho Y_\alpha\frac{\partial u_j}{\partial x_j}} - \overline{\frac{\partial J_{\alpha,j}}{\partial x_j}} + \rho S_\alpha(\boldsymbol{\varphi}) + \mathcal{M}_1\right)f\right]\\ &-\frac{\partial}{\partial r v_i}\left[\left(-\overline{\rho u_i\frac{\partial u_j}{\partial x_j}} - \overline{\frac{\partial p}{\partial x_i}} + \overline{\frac{\partial \tau_{ij}}{\partial x_j}} + \mathcal{M}_2\right)f\right]\\ &-\frac{\partial}{\partial r\mathcal{E}}\left[\left(-\overline{\rho E\frac{\partial u_j}{\partial x_j}} - \overline{\frac{\partial q_j}{\partial x_j}} - \overline{\frac{\partial p u_j}{\partial x_j}} + \overline{\frac{\partial \tau_{ij}u_i}{\partial x_j}} + \mathcal{M}_3\right)f\right].\end{aligned} \tag{D.1}$$

The corresponding SPDE system is

$$\frac{\mathrm{d}\rho Y_\alpha}{\mathrm{d}t} + \frac{\partial \rho u_j Y_\alpha}{\partial x_j} = \rho Y_\alpha\frac{\partial u_j}{\partial x_j} - \overline{\rho Y_\alpha\frac{\partial u_j}{\partial x_j}} - \frac{\partial \bar{J}_{\alpha,j}}{\partial x_j} + \rho S_\alpha + \mathcal{M}_1\,, \tag{D.2}$$

$$\frac{\mathrm{d}\rho u_i}{\mathrm{d}t} + \frac{\partial \rho u_i u_j}{\partial x_j} = \rho u_i\frac{\partial u_j}{\partial x_j} - \overline{\rho u_i\frac{\partial u_j}{\partial x_j}} - \frac{\partial \bar{p}}{\partial x_i} + \frac{\partial \bar{\tau}_{ij}}{\partial x_j} + \mathcal{M}_2\,, \tag{D.3}$$

$$\frac{\mathrm{d}\rho E}{\mathrm{d}t} + \frac{\partial \rho u_j E}{\partial x_j} = \rho E\frac{\partial u_j}{\partial x_j} - \overline{\rho E\frac{\partial u_j}{\partial x_j}} - \frac{\partial \bar{q}_j}{\partial x_j} - \frac{\partial \overline{p u_j}}{\partial x_j} + \frac{\partial \overline{\tau_{ij}u_i}}{\partial x_j} + \mathcal{M}_3\,. \tag{D.4}$$

If we assume small-scale incompressibility or the Morkovin hypothesis, *i.e.*, velocity divergence is primarily large-scale,

$$\widetilde{\frac{\partial u_j}{\partial x_j}} \approx \frac{\partial \tilde{u}_j}{\partial x_j} \iff \frac{\partial u_j}{\partial x_j} \approx \frac{\partial \tilde{u}_j}{\partial x_j}\,. \tag{D.5}$$

This can also be understood as the divergence is a large-scale flow feature and is mostly associated with resolved motions.

And if the usual SGS model form is applied,

$$\mathcal{M} = -\frac{C}{\tau_{\text{sgs}}}(\phi - \bar{\phi}) + B\frac{\mathrm{d}W}{\mathrm{d}t}\,, \tag{D.6}$$

the SPDE can be rewritten as

$$\frac{\mathrm{d}\rho Y_\alpha}{\mathrm{d}t} + \frac{\partial \rho u_j Y_\alpha}{\partial x_j} = (\rho Y_\alpha - \overline{\rho Y_\alpha})\left(\frac{\partial \tilde{u}_j}{\partial x_j} - \frac{C_{\rho Y_\alpha}}{\tau_{\text{sgs}}}\right) - \frac{\partial \bar{J}_{\alpha,j}}{\partial x_j} + \rho S_\alpha + B_{\rho Y_\alpha}\frac{\mathrm{d}W}{\mathrm{d}t}\,, \tag{D.7}$$

$$\frac{\mathrm{d}\rho u_i}{\mathrm{d}t} + \frac{\partial \rho u_i u_j}{\partial x_j} = (\rho u_i - \overline{\rho u_i})\left(\frac{\partial \tilde{u}_j}{\partial x_j} - \frac{C_{\rho u_i}}{\tau_{\text{sgs}}}\right) - \frac{\partial \bar{p}}{\partial x_i} + \frac{\partial \bar{\tau}_{ij}}{\partial x_j} + B_{\rho u_i}\frac{\mathrm{d}W}{\mathrm{d}t}\,, \tag{D.8}$$

$$\frac{\mathrm{d}\rho E}{\mathrm{d}t} + \frac{\partial \rho u_j E}{\partial x_j} = (\rho E - \overline{\rho E})\left(\frac{\partial \tilde{u}_j}{\partial x_j} - \frac{C_{\rho E}}{\tau_{\text{sgs}}}\right) - \frac{\partial \bar{q}_j}{\partial x_j} - \frac{\partial \overline{p u_j}}{\partial x_j} + \frac{\partial \overline{\tau_{ij} u_i}}{\partial x_j} + B_{\rho E}\frac{\mathrm{d}W}{\mathrm{d}t}\,. \tag{D.9}$$

The mean pressure can be replaced by the stochastic pressure as in subsection 3.2.1, and $B_{\rho Y_\alpha}$ and $B_{\rho E}$ can be taken as zero. They are retained here for completeness. Note that the system is conservative without further modification.

This formulation is the most consistent, as it yields correct filtering in variable-density flow, carries no unreasonable assumptions, and has a form that closely resembles the constant-density PDF. Compressibility effects are manifested through the velocity divergence. The stochastic quantities return to their mean quicker when the flow is locally compressive ($\nabla \cdot \tilde{\mathbf{u}} < 0$), and *vice versa* when the flow is locally expanding ($\nabla \cdot \tilde{\mathbf{u}} > 0$). This aligns with the physical intuition that an expanding system stretches a PDF in its sample space. However, due to the additional divergence term, which could be positive, a limiting procedure is likely necessary to ensure the stability of the system.